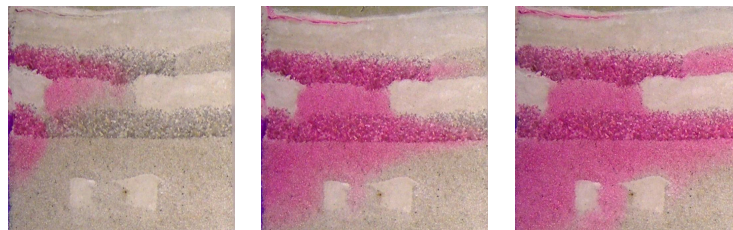Université catholique de Louvain
Faculté des Sciences Appliquées
Département d'Architure, d'Urbanisme
et de Génie Civil et Environnemental

Upscaling of solute transport in heterogeneous media

Theories and experiments to compare and validate Fickian and non-Fickian approaches

Thèse présentée en vue de l'obtention
du grade de Docteur en Sciences Appliquées par

Christophe Frippiat

Louvain-la-Neuve, Mai 2006

Acknowledgements

iv

cent et Stéphane, ainsi que Hassan, Eugène et Francis. Merci aussi à l'équipe du laboratoire d'électronique : Alex, Eric et André. Je ne voudrais pas oublier le plus important, le ciment liant le laboratoire et l'unité : Viviane et Marie-Rose, dont j'ai eu la chance et le plaisir d'occuper le bureau voisin, place stratégique pour les friandises et le café, pendant quatre ans.

From July 2005 to January 2006, I worked in the Department of Geology and Geological Engineering of the Colorado School of Mines, in Golden (Co, USA), in the team of Prof. David Benson. I must thank him for having welcomed me in his team and for everything I learned from him. The design of the physical experiment came out of long discussions with him. I'm just sorry not to have skied nor kayaked or biked with him. I also thank Prof. Tissa Illangasekare for the trust he gave us and for having let us use his facilities. I also thank him for all his human skills. A special thank goes to Nate, who managed to pull me out of the lab a couple of hours every week. I also thank him for the help he brought us for the experiment. I'm particularly grateful to Kent for the time he spent (lost ?) to explain me all he knew in the lab. He could always give the right piece of advice. I also thank Minie, Toshi, Derrick and Jose, as well as Rob and Yong. I thank Anushit and Paul for the good moments and a couple of long discussions together. Special thanks goes to Profs. Mike Gooseff and Eileen Poeter, for the fluorometer and for Modflow and Ucode. Debbie and Marylin are bringing much more than administrative support to the Geology and Geological Engineering Department of the CSM. It was a pleasure to meet them. Greg and Lara are now a bit like my american uncle and aunt. I loved to live in their house and I'm grateful for all that they shared with me. I finally would like to thank Kittie, who was the only one I could legitimately give love to while I was in there in Golden.

Les personnes les plus déterminantes dans un travail de l'envergure d'une thèse doctorale sont les personnes dont on est proche au quotidien : sa famille. Merci tout d'abord à mes beaux-parents, Claudine et Daniel, pour leur intérêt et leurs encourgaments répétés, ainsi qu'à mon beau-frère et ma belle-soeur, Michel et Marine. Merci à mes frères et soeur, Valérie, Sébastien et David, dont les encouragements prennent des formes moins explicites, mais qui sont tout aussi efficaces. Merci à Maman Zèzè, ma grand-mère, qui n'a à mon avis pas encore vraiment compris qu'une thèse doctorale pouvait être réalisée dans un domaine autre que la médecine mais qui m'a cependant toujours encouragé aussi. Merci surtout à mes parents, Martine et Claudy, pour leurs encouragements durant cette thèse, mais également pour tout ce qu'ils ont fait avant et tout ce qu'ils feront après.

Finalement, merci à Adeline pour m'avoir supporté et soutenu durant ces quatre années. Tout ne fut pas toujours facile, en particulier quand j'étais à l'autre bout de la planète pendant que tu affrontais seule tes soucis. Je pense que nous avons néanmoins réussi ces épreuves brillamment . . .

List of main symbols

Mathematical operators

$\langle \; \rangle$	Expected value
$E[\;\;]$	Expected value
$\hat{}$	Estimated value
$\tilde{}$	Fourier transform
$\mathcal{L}$	Laplace transform
$\| \;\; \|$	Norm
$*$	Complex conjugate

Variables

A	[m]	Characteristic longitudinal size of inclusions
B	[m]	Characteristic transversal size of inclusions
C	[g/m^3]	Solute concentration
C'	[g/m^3]	Solute concentration fluctuation
C_m	[g/m^3]	Solute concentration in the mobile zone
C_{im}	[g/m^3]	Solute concentration in the immobile zone
C_r	[-]	Concentration relative to injection
C_{YY}	[-]	Covariance function of Y
d	[-]	Fractal dimension of the space
D^d	[m^2/s]	Effective diffusion coefficient
D_{ij}	[m^2/s]	$(i,j)^{th}$ component of the mechanical dispersion tensor
D_{ij}^H	[m^2/s]	$(i,j)^{th}$ component of the hydrodynamical dispersion tensor
D_{ij}^*	[m^2/s]	$(i,j)^{th}$ component of the macrodispersion tensor
D_L	[m^2/s]	Longitudinal hydrodynamical dispersion coefficient
D_L^*	[m^2/s]	Longitudinal macrodispersion coefficient
D_T	[m^2/s]	Transverse hydrodynamical dispersion coefficient
Da	[-]	Damkholer number
e	[-]	Anisotropy ratio
e_u	[-]	Euclidian dimension of the space
H	[-]	Hurst coefficient
h	[m]	Aquifer thickness (perfectly stratified case)
K	[m/s]	Permeability
K_e	[m/s]	Effective permeability
K_g	[m/s]	Geometric mean of the permeability
L_m	[m]	Fractal cutoff limit
m_0	[m^{e_u} g/m^3]	Zero-order spatial moment of concentration distribution along direction i

m_i	$[\text{m}^{e_u+1} \text{ g/m}^3]$	First-order spatial moment of concentration distribution along direction i
m_{ij}	$[\text{m}^{e_u+2} \text{ g/m}^3]$	Second-order spatial moment of concentration distribution along directions i and j
m_{ij}^c	$[\text{m}^{e_u+2} \text{ g/m}^3]$	Second-order central spatial moment of concentration distribution along directions i and j
Pe	[-]	Peclet number
$\mathbf{q}$	[m/s]	Darcy velocity vector
q_i	[m/s]	i^{th} component of the Darcy velocity vector
q_i^A	$[\text{g/m}^2\text{s}]$	Advective solute mass flux in direction i
q_i^d	$[\text{g/m}^2\text{s}]$	Diffusive solute mass flux in direction i
q_i^D	$[\text{g/m}^2\text{s}]$	Dispersive solute mass flux in direction i
$\mathbf{s}$	[1/m]	Vector of Fourier-space coordinates
s_i	[1/m]	i^{th} component of the vector of Fourier-space coordinates
S_{YY}	[-]	Spectral density function of Y
t	[s]	Time
$\langle t \rangle$	[s]	Mean breakthrough time
U	[-]	Number of pore volumes
u	[1/s]	Laplace transform coordinate
$\mathbf{v}$	[m/s]	Solute velocity vector
$\mathbf{v}'$	[m/s]	Solute velocity fluctuation vector
v_i	[m/s]	i^{th} component of the velocity vector
v_i'	[m/s]	i^{th} component of the velocity fluctuation vector
v	[m/s]	Longitudinal velocity
V	[m/s]	Far field longitudinal velocity
V_a	[-]	Adimensional variance
v_β	$[\text{m/s}^{\beta_x}]$	Generalized velocity for temporally anomalous transport
v_F	[m/s]	Tracer front velocity
$\mathbf{x}$	[m]	Vector of spatial coordinates
x_i	[m]	i^{th} component of the vector of spatial coordinates
x	[m]	Longitudinal coordinate
Y	[-]	Natural logarithm of the permeability

Greek symbols

α_1/α_2	[-]	Fractal anistropy ratio
α_{ijkl}	[m]	$(i,j,k,l)^{th}$ component of the dispersivity tensor
α_L	[m]	Local longitudinal dispersivity
α_T	[m]	Local transverse dispersivity
α_L^*	[m]	Longitudinal macrodispersivity
β_x	[-]	Rational number characterizing spatially anomalous transport
β_t	[-]	Rational number characterizing temporally anomalous transport
$\mathcal{D}_x$	$[\text{m}^{\beta_x}/\text{s}]$	Generalized dispersion coefficient

		for spatially anomalous transport
$\mathcal{D}_t$	$[\mathrm{m}^2/\mathrm{s}^{\beta_t}]$	Generalized dispersion coefficient
		for temporally anomalous transport
ΔRMS_c	[-]	Indicator quantifying the best fit of predicted
		and measured BTC
ΔRMS_u	[-]	Indicator quantifying the general fit of predicted
		and measured BTC in an upscaling framework
ϵ_c	[-]	Indicator quantifying the best fit of predicted
		and measured longitudinal dispersivity
ϵ_u	[-]	Indicator quantifying the general fit of predicted
		and measured longitudinal dispersivity
		in an upscaling framework
γ	[-]	Stochastic flow factor
γ_a	[-]	Telegraph equation skewness parameter
γ_B	[-]	Space-fractional ADE skewness parameter
λ	[m]	One-dimensional spatial correlation length
		of the $ln(K)$ field
λ_e	[m]	Effective relaxation distance
λ_i	[m]	Spatial correlation length in direction i
λ_K	[m]	One-dimensional spatial correlation length
		of the K field
λ_S	[m]	Strack's characteristic length
μ_i	$[\mathrm{s}^{i+1}\mathrm{g}/\mathrm{m}^3]$	i^{th} temporal moment of BTC
μ_i^c	$[\mathrm{s}^{i+1}\mathrm{g}/\mathrm{m}^3]$	i^{th} central temporal moment of BTC
μ_Y	[-]	Mean of random variable Y
ν	[-]	Capacity ratio
ϕ	[m]	Piezometric head
θ	[-]	Total porosity
θ_m	[-]	Relative volumetric proportion of mobile fluid
θ_{im}	[-]	Relative volumetric proportion of immobile fluid
σ_Y	[-]	Standard deviation of random variable Y
σ_Y^2	[-]	Variance of random variable Y
τ_e	[s]	Effective relaxation time
ω	[1/s]	First-order exchange rate coefficient

Contents

II Application to synthetic examples   45

Chapter 1

Introduction

Groundwater is the world's largest reservoir of fresh water. Even considering the great lakes of North America and rivers like the Amazon and the Ganges, it represents over 97 % of the planet's fresh water resources [1]. In many parts of the world, groundwater is the main source of water. In Belgium, in the Walloon Region, more than 80 % of the fresh water supply comes from under the surface [2].

Groundwater is however a fragile resource. It is exposed to numerous pollutants, including pesticides and fertilizers from agriculture, heavy metals and mineral oils from industry or hydrocarbon compounds leaking from underground storage tanks. In the Walloon Region, the number of potentially contaminated sites is estimated at more than 6000, and 1207 of them are identified as requiring an intervention [2]. The Walloon Government plans to invest between 2.1 and 3.9 billions of euros over the next 30 years in the monitoring and the cleanup of these sites [2].

Within this context, there is a need for a better understanding of the mechanisms that control pollution migration in the soil, in order to improve efficiency of aquifer management, monitoring and cleanup strategies.

1.1 The classical model for solute transport in porous media

1.1.1 Basic definitions and transport processes

Before starting any developments, it is good practice to provide the reader with a clear view of the context of the study and general definitions of the key terms that will be used. The problem of interest is the movement (or transport) of solutes in natural soils. While the general concept of soil is well established, the definition of soil varies, hinging on the perspective of the discipline employing it as a resource. For example, agronomists consider it as the weathered material on the surface of a lithosphere, capable of supporting plant life [12]. In this work, soil will be defined as an inert material, made of aggregated solid particles in-between which gaz and liquids are present.

A solute is a chemical substance that dissolves in the liquid soil water phase [192]. In this study, only ideal inert solutes that do not undergo decay will be considered. Furthermore, the solute will be assumed to be present

---

[1]from http://www.iah.org/
[2]from http://mrw.wallonie.be/dgrne/

in sufficiently low concentration for density effects to be neglected. No chemical process such as hydrolysis, oxydation or interaction with other dissolved species will be considered, nor will biological processes (biodegradation, biotransformation, . . .). The solute will be assumed to move in a saturated porous medium, i.e. the presence of air as a third phase will not be considered neither. The study will focus on transport in heterogeneous porous media and will not consider fracture transport processes. However, at the limit for highly heterogeneous media, it will be shown that flow architecture tends to follow a network of preferential pathways that could be assimilated to a fracture network.

Basically, three main physical processes control solute transport in the soil : advection, diffusion and mechanical dispersion (see e.g. [13, 66, 72, 76]). Firstly, advection is mass transport caused by bulk movement of flowing groundwater. If no other process occurs, then contaminant plumes are simply translated at groundwater velocity. The driving force is the hydraulic gradient and the average transport velocity v_i $[m/s]$ in direction i ($i = 1 \ldots n$, n being the number of dimensions considered in space) can be calculated as the Darcy flux q_i $[m/s]$ divided by the volumetric proportion of mobile fluid in the soil θ_m $[-]$ (also called effective porosity). The advective solute mass flux in direction i (q_i^A, in $[g/m^2/s]$) can be written as

$$q_i^A = v_i C \tag{1.1}$$

where C $[g/m^3]$ is the solute concentration. This process will play an important role in heterogeneous formations, where velocity fluctuations cannot be neglected.

As spatial concentration gradients exist, diffusion is the net flux of solutes from zones of higher concentration to zones of lower concentration. Diffusion does not depend on any bulk movement of the solution and will occur even if pore water is at rest. The diffusive solute mass flux in direction i (q_i^d, in $[g/m^2/s]$) can be described by Fick's first law of diffusion

$$q_i^d = -D^d \frac{\partial C}{\partial x_i} \tag{1.2}$$

where x_i is the coordinate in direction i and D^d $[m^2/s]$ is an effective diffusion coefficient being related to the molecular diffusion coefficient in liquid phase. At low pore-water velocities, such as in clayey soils, solute transport is dominated by diffusion.

Finally, there is a tendency for solutes to spread out from the flow lines that it would be expected to follow according to the advective hydraulics of the flow system, leading to apparent diffusion coefficients that are higher by several orders of magnitude. This spreading phenomenon is usually called mechanical dispersion and is caused entirely by differential microscopic velocities in the pore space (due, for example, to the non-uniform velocity profile within a pore and to variations in pore diameter and in pore length, as described in e.g. [13, 72, 77] and illustrated on Fig. 1.1.a.). Dispersive solute flux is classically represented using a diffusion-like or Fickian law

$$q_i^D = -\sum_j D_{ij} \frac{\partial C}{\partial x_j} \tag{1.3}$$

where q_i^D $[g/m^2/s]$ is the dispersive solute mass flux in direction i and D_{ij} $[m^2/s]$ is a second-order tensor called mechanical dispersion. Eq. 1.3 is the starting point of the reflexion conducted in this dissertation, as it will be shown in Section 1.1.3 that the Fickian assumption may, most of the time, be questioned.

The solute mass transport equation can be set up by writing the mass balance on a representative elementary volume (R.E.V.) of soil (according to Bear's definition in [13]). Combining advective, diffusive and dispersive fluxes leads to

$$\frac{\partial C}{\partial t} = -\sum_i \frac{\partial}{\partial x_i} \left(q_i^A + q_i^d + q_i^D \right) \tag{1.4}$$

Diffusion and dispersion are usually combined in a single tensor $D_{ij}^H = D^d + D_{ij}$ called hydrodynamical dispersion. Subsituting it into Eq.1.4 and detailing the flux terms according to Eqs. 1.1, 1.2 and 1.3 yields

$$\frac{\partial C}{\partial t} = -\sum_i v_i \frac{\partial C}{\partial x_i} + \sum_i \sum_j \frac{\partial}{\partial x_i} \left(D_{ij}^H \frac{\partial C}{\partial x_j} \right) \tag{1.5}$$

which is usually called the advection-dispersion equation (ADE). In this study, this equation will also be referred to as the classical or Fickian model of solute transport in porous media. In a one-dimensional framework, it reads

$$\frac{\partial C}{\partial t} = -v \frac{\partial C}{\partial x} + D_L \frac{\partial^2 C}{\partial x^2} \tag{1.6}$$

where $v = v_1$ and $D_L = D_{11}^H$ $[m^2/s]$, called longitudinal hydrodynamical dispersion coefficient, is assumed to be constant.

1.1.2 Introducing dispersivity

The coefficient of mechanical dispersion is found to depend strongly on the advective velocity. The exact relationship between these two parameters can however only be obtained from theoretical considerations for simple or hypothetical pore systems [192]. Except in the case of very simple conceptual models, one can generally find that the coefficient of mechanical dispersion is linearly related to velocity [13]

$$D_{ij} = \sum_k \sum_l \alpha_{ijkl} \frac{v_k v_l}{||v||} \tag{1.7}$$

where α_{ijkl} $[m]$ is a fourth-order tensor called dispersivity assumed to depend only on soil properties and $||v||$ is the norm of the velocity vector. In the case of an isotropic homogeneous medium, owing to symmetry properties, the dispersivity tensor can be fully described by two parameters α_L and α_T, respectively called longitudinal and transverse dispersivity [13], both expressed in length units. In a uniform flow field, if the principal directions of the dispersion tensor are aligned with the principal directions of the velocity flow field, one can write

$$D_L = \alpha_L v + D^d \tag{1.8}$$
$$D_T = \alpha_T v + D^d \tag{1.9}$$

where D_L is already used in Eq. 1.6 and $D_T = D_{22}^H = D_{33}^H$ quantifies mechanical dispersion in a direction transverse to flow.

Extensive experimental validation of Eq. 1.7 has been performed. Reference books usually provide plots of the longitudinal dispersion versus velocity and show that in the laboratory, when diffusion can be neglected, Eqs. 1.8 and 1.9 are valid under typical groundwater flow conditions [13, 66, 72, 85]. Other studies were also conducted at larger scale. For example, Klotz et al. [111] investigated in the laboratory and in the field a more general relation $D_L = \alpha_L v^B + D^d$ and found that parameter B should be close to one. They also showed the dependency of longitudinal dispersivity to soil sedimentological properties.

1.1.3   Limitations

Although supported by several theoretical models and verified under well-controlled laboratory conditions, the Fickian model of dispersion has shown difficulties in predicting solute transport under certain other conditions. Dispersion is basically an advective process, as it is caused by variations in fluid velocity. However, this process does not only take place at the pore scale, but also occurs at larger scales, ranging from macroscopic to megascopic [66, 72]. At the field scale, commonly encountered geological structures influence contaminant transport drastically, leading to velocity variations over several orders of magnitude. As illustrated on Fig. 1.1, this includes the effects of stratification and the presence of lenses with higher or lower permeablity. At the megascopic scale, differences between geologic formations also cause non-ideality in solute transport. As the flow path increases in length, a solute cloud can encounter greater and greater variations in the aquifer, causing the variability of the velocity field to increase. Because dispersivity is related to the variability of the velocity, neglecting or ignoring the true velocity distribution (i.e. by replacing the heterogeneous medium by an equivalent homogeneous one) must be compensated for by a corresponding higher apparent (or effective) dispersivity, leading to what is commonly called the scale effect of dispersion [72, 77].

This scale effect first arose from the comparison of laboratory and field values of dispersivity. Whereas typical values of dispersivity from column experiments range between 0.01 and 0.1 m, values of macroscopic dispersivity (or macrodispersivity) are in general three to four orders of magnitude larger [82, 116]. It has also been widely observed that field-scale dispersion coefficients increase with distance and with time [160, 161].

However, it must be underlined that field dispersivity values reported in the literature are not always reliable. Inverse modelling is the usual tool to determine dispersivity. The latter is adjusted so that the experimental curve fits a given theoretical solution to the solute transport problem [3, 72]. When interpreting field observations of concentration, numerous factors, such as actual injection conditions, solute density effects or even temporal variations of the advective flow regime or biaised interpretation techniques, are likely to be interpreted as dispersion. For example, Domenico and Robbins [65] showed that interpreting the two- or three-dimensional spreading of a tracer with a one-dimensional model requires a spatially increasing dispersivity, whereas the
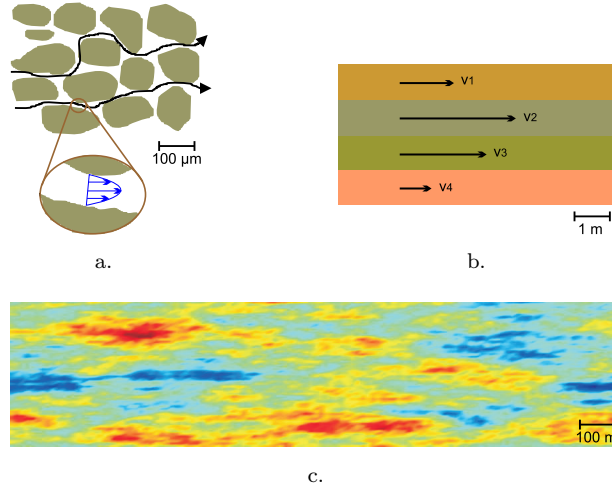
Figure 1.1: Velocity fluctuations at different scales. a. Pore-to-pore variations. b. Stratification as a cause of variation. c. Randomly heterogeneous two-dimensional anisotropic medium. *Adapted from Domenico and Schwartz [66].*

use of a dimensionally correct model does not show any dispersion scale-effect. In studies with insufficient data, the lack of field data is hidden in the dispersion term of the governing transport equation. This was mostly highlighted by Gelhar et al. [82] who classified results from field studies using a reliability criterion. Despite this criterion, they produced an experimental curve for longitudinal dispersivity versus measurement scale, reprinted on Fig. 1.2, clearly establishing the trend for dispersivity to increase with distance. Finally, this scale effect was demonstrated using controlled laboratory experiments (by e.g. Silliman and Simpson [174]).

1.2   Scope and outline of this thesis

Three main research directions have been investigated for the past 20 years in order to solve the problem of the scale effect. First, field and laboratory characterization methods have received a growing attention and are currently a fast-developing research area. Indeed, an accurate identification of the subsoil structure and a detailed knowledge of fine-scale hydraulic properties variations remain key requirements in the correct modelling of solute transport in field-scale situations. The advancing edge of geophysics provides new methods, such as time-domain reflectometry [108], ground penetrating radar [117] or electrical resistivity tomography [150], that are currently being applied to the characterization of subsuface transport problems. However, the fine spatial resolution needed to completely solve the scale effect is currently out of reach of available characterization methods, and will most likely remain so for some time.

Based on a partial characterization of the subsoil structure, many researchers have then tried to provide upscaling methods for the dispersivity. Most
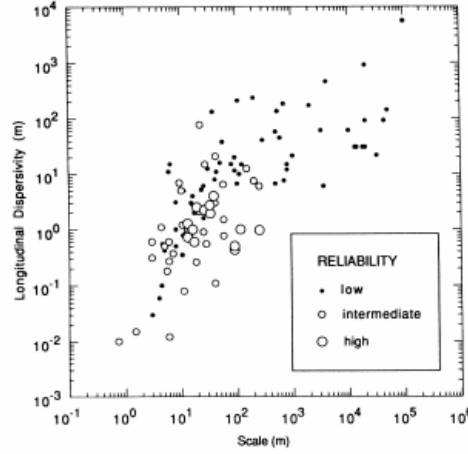
Figure 1.2: Experimental longitudinal dispersivity values versus measurement scale with data classified by reliability. *From Gelhar et al. [82].*

of these methods are generally based on a geostatistical description of the heterogeneity [51, 80], but fractal methods [197] and methods based on other particular parametrizations of subsoil structure have been developed [67]. This approach however relies on the main assumption that the classical advection-dispersion equation is valid at the scale of interest. Regarding this latter issue, a third main research area has been the upscaling of the transport equation itself. Higher-order and fractional-order transport equations have been either developed or brought to the field of hydrogeology [19, 24, 163].

Research aimed at solving the scale effect in dispersion has developed in an uncoordinated fashion. It is not always easy to discriminate which approach can be best adopted in a given situation and the relative performance of the various upscaling methodologies available has never been formally tested. Therefore, the main general objective of this study is the comparison of existing solute transport models, either resulting from the upscaling of Fickian transport parameters or resulting from the upscaling of the transport equation itself. Particular objectives of this research are

- To identify the most relevant upscaling methodologies and non-Fickian transport models for solute transport in heterogeneous media.

- To develop a methodology to compare their upscaling capacities.

- To apply the methodology to very simple synthetic examples in order to identify main tendencies. More precisely, to quantify the effect of the overall variability of hydraulic properties as well as the effect of the relative size of heterogeneities on prediction capacities of various solute transport models.

- To refine the numerical analysis in order to base the comparison of the methodologies on more complex heterogeneous situations. More precisely,

to identify the effect of anistropy, permeability distribution and flow orientation on prediction capacities of methods.

- To apply the methodology to an original intermediate-scale laboratory experiment.

As a result, this work is divided into three main parts. The first part is an overview of existing solute transport upscaling theories in heterogeneous media. Without trying to be exhaustive, some of the most used theories will be summarized, with an emphasis on their fundamental assumptions. Chapter 2 will summarize available upscaling methodologies for longitudinal dispersivity. The widespread stochastic approach will be first tackled, with a focus on the main contribution to this theory. Then, fractal methods and the particular case of a medium with inclusion of different material will be summarized. In Chapter 3, upscaled transport equations will be presented. It will be shown that telegraph equations can be a simple extension of the classical ADE but that fractional-order transport equations are more powerful tools. The special case of dual-porosity media will also be briefly reviewed.

In the second part of this dissertation, numerical examples will be set up in order to assess the upscaling capacities of each model. Therefore, Chapter 4 will first describe the general method that will be used to compare the different approaches. Characterization methods available to parametrize models to be tested will also be summarized. In Chapter 5, perfectly stratified examples will be first investigated. Due to their high level of conceptualization, they are ideal candidates to allow one to identify rough tendencies among models. Moreover, analytical solutions are easy to derive for this simple geometry and are widely available for the various models to be tested. Finally, in Chapter 6, the analysis will be refined by considering two-dimensional cases. It will be verified whether conclusions drawn from simplified situations can be extended to more complicated situations. The influence of other structural parameters, such as anisotropy or orientation of flow with respect to bedding, will also be assessed. It must be already stated that, unlike numerical investigations usually presented in the literature, these examples will not be designed to fit fundamental assumptions of analytical solutions of the various models. In particular, flow domains of limited extension will be investigated and boundary conditions will clearly play a role in flow and solute transport.

Synthetic examples are convenient because they allow one to perform a large number of parametric variations. However, they rely on several fundamental assumptions, like the validity of the ADE at small scale and the validity of the numerical code that is used. These limitations are circumvented when performing physical experiments. Therefore, in the third part of this work, models will be compared on the basis of an intermediate-scale laboratory experiment. This experiment was performed at the Colorado School of Mines (CSM, Golden, Colorado, USA) in collaboration with Prof. David Benson from the Department of Geology and Geological Engineering of the CSM and with Prof. Tissa Illangasekare from the Department of Environmental Science and Engineering of the CSM. The experiment took place in the facilities of the Center for Experimental Study of Subsurface Environmental Processes (CESEP), directed

by Prof. Illangasekare. A highly heterogeneous composite aquifer was created in a sandbox and a one-dimensional tracer test was performed. The design of the aquifer was chosen in order to create a preferential pathways architecture of the flow system, leading to diffusion-dominated transport characterized by (1) a relatively important scale effect in apparent dispersivity of the transversally-averaged BTC and (2) heavy tails of concentration distributions. This physical experiment was typically designed as complementary to numerical examples investigated in Part 2. Actually, numerical examples were used to determine a spatial structure of permeability that would be interesting to investigate in the laboratory. The physical experiment also allows one to compare upscaling methods and upscaled equations in a less artificial situation, in which only a partial information is available (as the full spatio-temporal concentration distribution could not be measured).

General conclusions and perspectives are drawn in Chapter 8.

Part I

Overview of upscaling approaches

Chapter 2

Upscaling of transport parameters

2.1 Introduction

In this chapter, it will be shown how transport parameters and in particular, the longitudinal dispersivity, can be upscaled based on different characterization methods for heterogeneous permeability fields. The major assumption that has to be drawn in this framework is that the classical Fickian transport model remains valid at every scale of interest, provided flow and transport parameters of the medium are properly adapted. Basically, this approach is equivalent to considering a macroscale R.E.V. and deriving equivalent macroscale flow and transport parameters.

As this work focuses on solute dispersion, theories on the upscaling of flow parameters will not be reviewed here. Basic considerations on effective permeability can be found e.g. in [53] or [79]. Three main approaches for the upscaling of solute transport will be reviewed in this chapter. First, the stochastic theory will be introduced. As the literature in this domain is relatively abundant, we will mainly focus on the general derivation by Gelhar and Axness [80]. Basically, this theory shows how fluctuations in permeability results in an increased spreading of solute plumes. Then, in Section 2.3, it will be shown how fractal geometry can give an insight into macrodispersivity. Finally, inclusion models will be introduced in Section 2.4. They allow one to deal with a medium composed of inclusions of given shapes and permeabilities and solve transport considering advection only.

It must be noted that the upscaling of longitudinal dispersivity is always possible in a deterministic framework. Assuming that the heteregeneous permeability field is fully determined, the corresponding transport problem can be solved at a local scale and apparent properties (i.e. effective tranport properties of an equivalent homogeneous medium) are obtained by subsequent averaging at a larger scale. In the case of a perfectly stratified aquifer (i.e. where the permeability only depends on the elevation with respect to an arbitrary datum), semi-analytical methods have been developped, based either on moment analysis [90] or on modal analysis [21, 89]. For more complicated problems, numerical methods such as finite elements, finite differences or particle tracking can be used. These approaches will not be reviewed here but will be used in Chapters 5 and 6 to provide an *exact* solution towards which tested methods should ideally tend.

2.2   The stochastic approach

Hydraulic properties of subsurface materials, such as hydraulic conductivity, will generally vary in complicated ways in space [79]. It cannot therefore be objectively fully characterized in a deterministic way. However, as subsurface heterogeneity usually results from formation processes (such as e.g. sedimentation), it is not fully random neither, and (geo)statistical methods can be used to identify and characterize its spatial structure [150]. Stochastic analysis enables then the variability in flow and transport to be related to variability and spatial structure associated to hydraulic properties of the heterogeneous medium considered.

In this section several results from stochastic theories applied to solute transport in heterogeneous porous media will be presented. As an introduction, basics of geostatistics and stochastic modelling will be reviewed, and the main assumptions required by the method will be presented. In Section 2.2.2, tools to characterize the spatial structure of heterogeneous permeability fields will be presented. Then, in Section 2.2.3, the analytical expression of macrodispersivity obtained by Gelhar and Axness [80] will be derived, based on an Eulerian description of the velocity field. In Section 2.2.4, a few analytical solutions to be used in the next chapters will be provided.

2.2.1   Definitions and fundamental assumptions

In a stochastic framework, the hydraulic properties of a heterogeneous medium are treated as random variables. A random variable R can be described in terms of its cumulative probability distribution function (CDF) $F_R(r) = P\,[R \leq r]$, which denotes the probability that R is less than some specified value r. For a continuous random variable, the probability density function (PDF) can also be used to describe it, and is linked to the CDF using $f_R(r) = dF/dr$ [79]. The mean or expected value and the variance of the variable R are

$$\mu_R \quad = \quad E\,[R] = \int_{-\infty}^{+\infty} r f_R(r)\,dr \tag{2.1}$$

$$\sigma_R^2 \quad = \quad E\left[(R - \mu_R)^2\right] = \int_{-\infty}^{+\infty} (r - \mu_R)^2 f_R(r)\,dr \tag{2.2}$$

μ_R (also noted $\langle R \rangle$) is a measure of the central tendency of the random variable and σ_R^2 is a measure of the variability associated with the variable. The square-root σ_R of the variance is called standard deviation.

A normal or Gaussian random variable is described by the PDF

$$f_R(r) = \frac{1}{\sqrt{2\pi\sigma_R^2}} \exp\left[\frac{-(r - \mu_R)^2}{2\sigma_R^2}\right] \tag{2.3}$$

A normal variable is thus entirely characterized by its mean and variance. A log-normal random variable R is such that $\ln(R)$ is a normal random variable. In subsurface hydrology, and more particularly in the stochastic approach of transport in heterogeneous formations, hydraulic conductivity is usually assumed to be log-normally distributed. Therefore, one defines $Y = \ln(K)$, where

the permeability K is expressed in $[m/s]$ and ln is the natural logarithm. This assumption will be adopted throughout this work but will be questioned in Chapter 6. This hypothesis has the advantage that negative values are excluded, which is consistent with the physical requirement that permeability is positive [79].

When we are dealing with more than one variable, it is necessary to consider how the variables are interrelated probabilistically. The joint CDF of two random variables R and S is $F(r, s) = P[R \leq r, S \leq s]$ and the corresponding joint density probability function is $f(r, s) = \partial^2 F(r, s)/\partial r \partial s$. The degree of linear relationship between R and S is quantified by the covariance

$$
\begin{aligned}
cov(R, S) &= E\left[(R - \mu_R)(S - \mu_S)\right] \\
&= \int_{-\infty}^{+\infty} \int_{-\infty}^{+\infty} (r - \mu_R)(s - \mu_S) f(r, s) \, dr ds
\end{aligned}
\tag{2.4}
$$

If R and S are independent, then the covariance is zero. However, the inverse statement is not correct : if the covariance is zero, then the random variables are not necessarily independent. They are said to be uncorrelated [79]. Another useful tool to quantify the correlation of two random variables is the variogram $\gamma(R, S) = 1/2 \, E\left[(R - S)^2\right] = \sigma_R \sigma_S - cov(R, S)$.

A random function (also called random field or stochastic process) can be viewed as a random variable with an infinite number of components [53]. For instance, hydraulic conductivity of soils can be considered as a spatial multidimensional stochastic process $K(\mathbf{x})$, where $\mathbf{x}$ is a vector of spatial coordinates [79]. For a fixed $\mathbf{x}$, the random field is a random variable, and is completely characterized by its joint PDF to any arbitrary order. A particular record of a stochastic process (e.g. the measured permeability field in a given situation) is referred to as a realization of the stochastic process, whereas the ensemble refers to the collection of all possible realizations of the stochastic process [79].

In applications related to flow through porous formations, the concept of ensemble is relatively abstract, as one only encounters one single realization of the process. The ensemble then reflects uncertainty in the depiction of the spatial structure of the formation, rather than a set of existing similar formations [53]. Moreover, this representation relies on a finite-length record composed of discrete values of data measured at some interval [79]. The statistical characterization of the random structure is then based on spatial averages over the single realization available, rather than over ensemble averages [53]. This might not induce a high bias if the ergodic hypothesis prevails and the single realization considered contains the whole information available in each realization of the ensemble [150].

Because a stochastic process is defined as a random variable at each point (in time or in space), the mean, the variance and the covariance are functions that may vary (in time or in space). In the case of the log-permeability field Y

of soils , one could calculate

$$\mu_Y(\mathbf{x}) \quad = \quad E\left[Y(\mathbf{x})\right] = \int_{-\infty}^{+\infty} y f_Y(y, \mathbf{x})\, dy \tag{2.5}$$

$$\sigma_Y^2(\mathbf{x}) \quad = \quad E\left[(Y(\mathbf{x}) - \mu_X)^2\right] = \int_{-\infty}^{+\infty} (y - \mu_Y)^2 f_Y(y, \mathbf{x})\, dy \tag{2.6}$$

where y are specified values of log-permeability. An important particular class of stochastic processes is that of stationary (or homogeneous) random functions [53], for which both mean and variance are constant (in time or in space). One will thus have $\mu_Y(\mathbf{x}) = \mu_Y$ and $\sigma_Y^2(\mathbf{x}) = \sigma_Y^2$. For a second-order or weakly stationary random field, the covariance (which is then a function) is moreover only dependent on the separation (in time or in space) of the two random variables considered.

2.2.2 Covariance function and spectral representation

Assuming two zero-mean weakly stationary random spatial fields $f(\mathbf{x})$ and $g(\mathbf{x})$, their covariance function is noted $C_{fg}(\mathbf{h})$ and only depends on the separation gap $\mathbf{h}$ (where a vector notation was adopted as the covariance can be dependent on the orientation, in the case of a macroscopically anisotropic random field). f and g could be either permeabilities, heads, velocities, concentrations or any variable of interest. C_{fg} is either called the autocovariance or the cross-covariance, depending on f and g being representative of a same random field or not. The covariance function cannot take any arbitrary parametric shape. It must meet several properties, some of them being difficult to verify. One found therefore convenient to adopt a set of simple covariance models that are known to be valid. One of the most used model is the exponential covariance model, expressed in the one-dimensional case as

$$C_{fg}(h) = \sigma_f \sigma_g \exp\left(-\frac{|h|}{\lambda}\right) \tag{2.7}$$

where λ is called correlation length or integral scale. Intuitively, λ is a measure of the separation required for two random variables to become uncorrelated [150]. Other one-dimensional covariance models are, among others, the Gaussian (Eq. 2.8) and the hole-effect covariance function (Eq. 2.9)

$$C_{fg}(h) \quad = \quad \sigma_f \sigma_g \exp\left(-\left(\frac{h}{\lambda}\right)^2\right) \tag{2.8}$$

$$C_{fg}(h) \quad = \quad \sigma_f \sigma_g \exp\left(-\frac{|h|}{\lambda}\right)\left(1 - \frac{5}{3}\frac{|h|}{\lambda} + \frac{1}{3}\frac{h^2}{\lambda^2}\right) \tag{2.9}$$

Fig. 2.1 illustrates these different models (in the case of autocovariance C_{ff}) and shows one realization of a corresponding stochastic process. Basically, the exponential model can be used to model small-scale sharp variability, whereas the Gaussian model produces softer variations and mild transitions. The hole-effect model can be used to represent alternating sequences, such as stratification [81].

If a process is stationary, it is virtually always possible to describe it in terms of its frequency content, which is accessible through a Fourier-transform of this process. The Fourier-transform of the covariance function is called the power density spectrum (or spectral density function), is noted S_{fg}, and is evaluated according to

$$S_{fg}(\mathbf{s}) = \tilde{f}(\mathbf{s})\tilde{g}^*(\mathbf{s}) \tag{2.10}$$

$$= \int_{-\infty}^{+\infty} C_{fg}(\mathbf{h}) \, \exp(-2\pi i \mathbf{h} \cdot \mathbf{s}) \, d\mathbf{h} \tag{2.11}$$

where $\mathbf{s}$ is the wave number (that has the same number of dimensions as $\mathbf{x}$), $\tilde{f}(\mathbf{s})$ is the Fourier-transform of function $f(\mathbf{x})$ and $\tilde{g}^*(\mathbf{s})$ is the complex conjugate of the Fourier-transform of function $g(\mathbf{x})$. Inversely, the covariance function can be obtained from the inverse Fourier-transform of the spectral density function

$$C_{fg}(\mathbf{h}) = \int_{-\infty}^{+\infty} S_{fg}(\mathbf{s}) \, \exp(2\pi i \mathbf{h} \cdot \mathbf{s}) \, d\mathbf{s} \tag{2.12}$$

2.2.3 Eulerian derivation of macrodispersion

In this section, the general three-dimensional derivation of macrodispersion performed by Gelhar and Axness [80] will be shortly summarized, following the lines of Gelhar [79] and Cirpka [43]. The starting point is the advection-dispersion equation, expressed with a constant local hydrodynamical dispersion tensor D_{ij}^H and assuming that concentration and migration velocity are stationary random functions

$$\begin{aligned} C &= \langle C \rangle + C' \\ \mathbf{v} &= \langle \mathbf{v} \rangle + \mathbf{v}' \end{aligned} \tag{2.13}$$

where bold symbols are vectors. $\langle C \rangle$, $\langle \mathbf{v} \rangle$, C' and $\mathbf{v}'$ are respectively mean concentration, mean velocity, concentration fluctuation and velocity fluctuation. Fluctuations are assumed to have a zero mean $\langle C' \rangle = \langle \mathbf{v}' \rangle = 0$. Substituting these expressions in Eq. 1.5 leads to

$$\frac{\partial \langle C \rangle}{\partial t} + \frac{\partial C'}{\partial t} = -\sum_i \left(\langle v_i \rangle \frac{\partial \langle C \rangle}{\partial x_i} + v_i' \frac{\partial \langle C \rangle}{\partial x_i} + \langle v_i \rangle \frac{\partial C'}{\partial x_i} + v_i' \frac{\partial C'}{\partial x_i} \right)$$
$$+ \sum_i \sum_j \left(\frac{\partial}{\partial x_i} \left(D_{ij}^H \frac{\partial \langle C \rangle}{\partial x_j} \right) + \frac{\partial}{\partial x_i} \left(D_{ij}^H \frac{\partial C'}{\partial x_j} \right) \right) \tag{2.14}$$

Taking expected values and dropping higher-order terms, yield the governing equation for the mean concentration

$$\frac{\partial \langle C \rangle}{\partial t} = -\sum_i \langle v_i \rangle \frac{\partial \langle C \rangle}{\partial x_i} - E \left[\sum_i v_i' \frac{\partial C'}{\partial x_i} \right] + \sum_i \sum_j \frac{\partial}{\partial x_i} D_{ij}^H \frac{\partial \langle C \rangle}{\partial x_j} \tag{2.15}$$
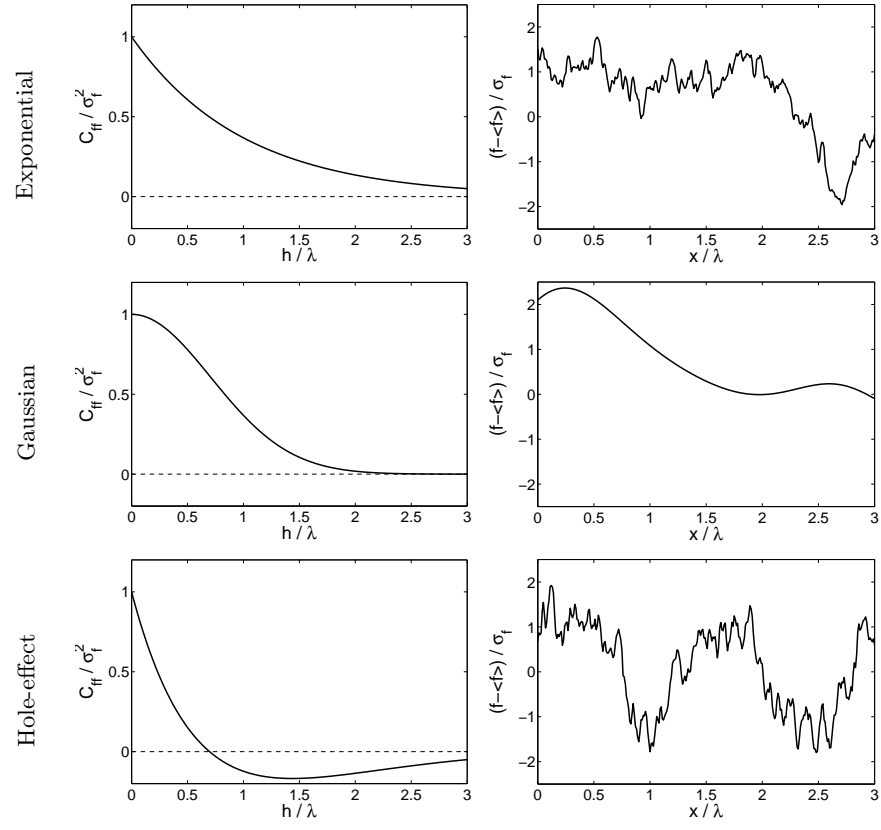
Figure 2.1: Models of covariance and one realization of a corresponding random field.

Considering the classical advection-dispersion equation, a new term arises here. It reflects additional mass transport due to correlation between specific discharge and concentration fluctuations. It produces a large-scale dispersion effect and can be approximated using a Fickian-like law

$$E\left[\sum_i v_i' \frac{\partial C'}{\partial x_i}\right] = \sum_i \frac{\partial}{\partial x_i}\langle v_i' C'\rangle \approx -\sum_i \sum_j \frac{\partial}{\partial x_i}\left(D_{ij}^* \frac{\partial\langle C\rangle}{\partial x_j}\right) \qquad (2.16)$$

D_{ij}^* is the macrodispersion tensor and is assumed to be proportionnal to the absolute value of migration velocity, as for the local dispersion tensor. It can be evaluated using the governing equation of concentration perturbations. The latter is obtained by substracting Eq. 2.15 from Eq. 2.14, which yields

$$\begin{aligned}
\frac{\partial C'}{\partial t} &+ \sum_i \left(v_i' \frac{\partial\langle C\rangle}{\partial x_i} + \langle v_i\rangle \frac{\partial C'}{\partial x_i}\right) - \sum_i \sum_j \frac{\partial}{\partial x_i}\left(D_{ij}^H \frac{\partial C'}{\partial x_j}\right) \\
&= \sum_i \frac{\partial}{\partial x_i}\left(v_i' C' - \langle v_i' C'\rangle\right) \approx 0
\end{aligned} \qquad (2.17)$$

The approximation in Eq. 2.17 is of crucial importance. Basically, it implies that velocity fluctuations are sufficiently small for second-order products to be neglected. For a log-normal permeability field, it can be shown based on a similar stochastic analysis of the flow equation that this condition on velocity perturbation requires a small variance of the Y field, so that it can be linearized [79]. Typically, these developments are assumed to be valid for $\sigma_Y^2 < 1$.

In general, Eqs. 2.15 and 2.17 must be solved simultaneously. However, a decoupling can be accomplished provided that concentration fluctuations occurs at a much smaller scale than variations associated to the mean concentration [79]. It is then possible to solve Eq. 2.17 to evaluate the macrodispersive flux and subsequently substitute it in Eq. 2.15. Assuming that the mean flow occurs in direction $i = 1$ and using the notations introduced in Eqs. 1.8 and 1.9, Eq. 2.17 simplifies to

$$\frac{\partial C'}{\partial t} = -v_1'|\nabla\langle C\rangle| - \langle v_1\rangle \frac{\partial C'}{\partial x_1} + D_L \frac{\partial^2 C'}{\partial x_1^2} + D_T \frac{\partial^2 C'}{\partial x_2^2} + D_T \frac{\partial^2 C'}{\partial x_3^2} \qquad (2.18)$$

where the notation $|\nabla\langle C\rangle|$ indicates that the gradient of the mean concentration is assumed to be constant in time and in space. This assumption may not be very realistic. But a mean gradient hardly varying over several correlation lengths of the hydraulic conductivity field may be achieved in the large-time limit under ordinary flow conditions, allowing one to apply the theory derived here in field conditions [43].

Eq. 2.18 may be transferred into the Fourier-space. Using some basic properties of the Fourier-transform, one obtains

$$\left(\frac{d}{dt} + b\right)\tilde{C}'(\mathbf{s}) = -\tilde{v}_1'(\mathbf{s})\,|\nabla\langle C\rangle| \qquad (2.19)$$

where $\tilde{\ }$ indicates the Fourier-transform and where $b = 2\pi i\langle v_1\rangle s_1 + 4\pi^2 D_L s_1^2 + 4\pi^2 D_T(s_2^2 + s_3^2)$. Eq. 2.19 is a linear non-homogeneous first-order time differential equation. Since the concentration gradient is taken as a constant and

assuming as initial condition a concentration distribution equal to the mean concentration (i.e. a concentration perturbation $C' = 0$), one obtains

$$\tilde{C}'(\mathbf{s}, t) = -\tilde{v}'_1(\mathbf{s})\, |\nabla\langle C\rangle| \int_0^t exp(b(\tau - t))d\tau \qquad (2.20)$$

$$= -\frac{\tilde{v}'_1(\mathbf{s})\, |\nabla\langle C\rangle|}{b}(1 - \exp(-bt)) \qquad (2.21)$$

Recalling Eq. 2.16 and the assumption of a constant concentration gradient, one can compute the longitudinal apparent dispersion coefficient according to

$$D_L^* = -\frac{1}{|\nabla\langle C\rangle|}\langle C'v'_1\rangle \qquad (2.22)$$

As $\langle C'v'_1\rangle$ is the integral of the cross-spectral density of concentration and longitudinal velocity fluctuations S_{Cv_1}, Eq. 2.22 can be transformed to

$$\alpha_L^* = -\frac{1}{|\nabla\langle C\rangle|\,\langle v_1\rangle}\int_{-\infty}^{+\infty} S_{Cv_1}(\mathbf{s})\, d\mathbf{s} \qquad (2.23)$$

where α_L^* is a macroscale longitudinal dispersivity. S_{Cv_1} is obtained from the product $S_{Cv_1} = \tilde{C}'\tilde{v}'^*_1$. Substitution of Eq. 2.21 into Eq. 2.23 yields

$$\alpha_L^*(t) = \frac{1}{\langle v_1\rangle}\int_{-\infty}^{+\infty}\frac{1 - \exp(-bt)}{b}\tilde{v}'_1(\mathbf{s})\tilde{v}'^*_1(\mathbf{s})\, d\mathbf{s} \qquad (2.24)$$

$$= \frac{1}{\langle v_1\rangle}\int_{-\infty}^{+\infty}\frac{1 - \exp(-bt)}{b}S_{v_1v_1}(\mathbf{s})\, d\mathbf{s} \qquad (2.25)$$

This equation establishes the link between velocity fluctuations and macrodispersivity. As the velocity spectrum is linked to log-permeability variations, macrodispersivity is basically found to be dependent on the permeability field. Moreover, macrodispersivity is also proved to be time-dependent and, as the exponential term in Eq. 2.25 vanishes for large time, macrodispersivity converges to a constant asymptotic value.

Similar derivations have been performed by Dagan [51, 52, 53] and by Neuman et al. [141]. Dagan used a Lagrangian framework, but had to use an approximate relationship between the Eulerian and the Lagrangian velocity covariance. Neuman et al. used a more abstract mathematical analysis based on semigroup theory. Basically, these derivations all require an assumption of relatively small perturbations, leading to little discrepancy among them and a domain of validity $\sigma_Y^2 < 1$.

2.2.4   A few analytical solutions

Most of available analytical solutions are based on exponential covariance models and assume that local dispersivities are negligible compared to correlation lengths. The asymptotic value of longitudinal dispersivity in an isotropic medium is given by [80]

$$\alpha_L^*(\infty) = \sigma_Y^2\frac{\lambda}{\gamma^2} \qquad (2.26)$$
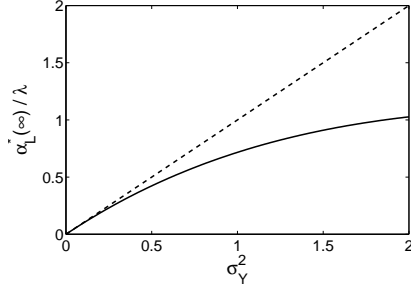
Figure 2.2: Asymptotic longitudinal dispersivity in the isotropic case. 3D (solid line) and 2D (dashed line) case. The solution by Dagan [51] in the 3D case corresponds to the dashed line.
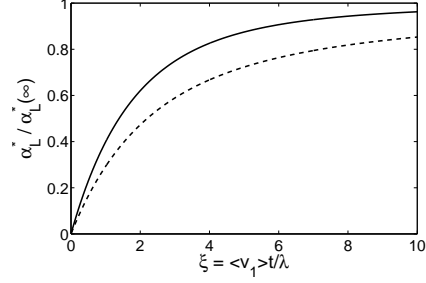
Figure 2.3: Convergence of longitudinal dispersivity in the isotropic case. 3D (solid line) and 2D (dashed line) cases.

where γ is a flow factor accounting for the dependence of effective permeability on dimensionality. In the two-dimensional case, $\gamma = 1$, whereas in the three-dimensional case, $\gamma = \exp(\sigma_Y^2/6)$. It must be noted that Dagan [53] obtained a similar result using a Lagrangian framework, but with $\gamma = 1$ in the three-dimensional case. Dagan [53] states that taking into account a value $\gamma \neq 1$ is not consistent with first-order approximations adopted, as it introduces a term of order σ_Y^4. Fig. 2.2 depicts the influence of the variance of the log-permeability field on the asymptotic value of longitudinal apparent dispersivity.

The three-dimensional isotropic solution for intermediate times is given by Gelhar [79], based on an expression derived by Dagan [51]

$$\frac{\alpha_L^*(t)}{\alpha_L^*(\infty)} = 1 - \frac{4}{\xi^2} + \frac{24}{\xi^4} - 8\left(\frac{1}{\xi^2} + \frac{3}{\xi^3} + \frac{3}{\xi^4}\right)\exp(-\xi) \tag{2.27}$$

where $\xi = \langle v_1 \rangle t/\lambda$. In a two-dimensional isotropic aquifer, it is given by [100]

$$\frac{\alpha_L^*(t)}{\alpha_L^*(\infty)} = 1 - \frac{3}{2\xi} + \frac{3}{\xi^3} - \frac{3}{\xi^2}\left(1 + \frac{1}{\xi}\right)\exp(-\xi) \tag{2.28}$$

Basically, these results express that the convergence to the asymptotic behavior is only controlled by the ratio of mean travel distance to correlation length. In the two-dimensional case, as the number of available paths to bypass low permeability zones is lower than in the three-dimensional case, convergence is less rapidly reached (Fig. 2.3).

In the case of a two-dimensional anisotropic situation with flow occuring in a direction at an angle θ with respect to the bedding of the permeability field, asymptotic dispersivity is given by [80]

$$\alpha_L^*(\infty) = \sigma_Y^2 \frac{\lambda_1 \lambda_2}{\gamma^2 \sqrt{\lambda_1^2 \sin^2\theta + \lambda_2^2 \cos^2\theta}} \tag{2.29}$$

where the flow factor is obtained from

$$\gamma = \frac{\exp\left[\sigma_Y^2(1/2 - g_{22})\right]}{\sin^2\theta + B\cos^2\theta} \tag{2.30}$$
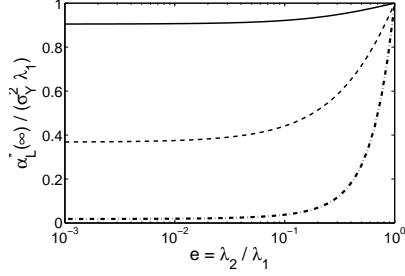
Figure 2.4: Influence of the anistropy on asymptotic longitudinal dispersivity for $\theta = 0$. $\sigma_Y^2 = 0.1$ (solid line), $\sigma_Y^2 = 1$ (dashed line) and $\sigma_Y^2 = 4$ (dot-dashed line).
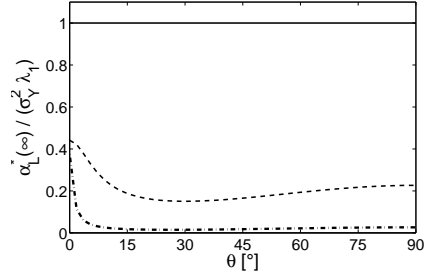
Figure 2.5: Influence of the flow direction on asymptotic longitudinal dispersivity for $\sigma_Y^2 = 1$. $e = 1$ (solid line), $e = 0.1$ (dashed line) and $e = 0.01$ (dot-dashed line).

with $B = \exp\left[\sigma_Y^2(g_{11} - g_{22})\right]$, $g_{11} = \lambda_2/(\lambda_1 + \lambda_2)$ and $g_{22} = \lambda_1/(\lambda_1 + \lambda_2)$. In the case of an isotropic field with flow oriented along the principal directions of the permeability field, Eq. 2.29 simplifies to Eq. 2.26 with a flow factor $\gamma = 1$ consistent with the theoretical effective permeability of two-dimensional isotropic media. Fig. 2.4 shows the effect of anisotropy on asymptotic longitudinal dispersivity. For high variance and high anisotropy, flow is mainly directed in the longitudinal direction and little transverse mixing can occur, leading to lower values of longitudinal dispersivity. As anisotropy decreases, transverse mixing increases, leading to higher apparent longitudinal dispersivities. Fig. 2.5 shows that, globally, when flow is not aligned with the main principal direction of the permeability field, apparent dispersivity tends to decrease. No analytical solution for transient apparent dispersivity in two-dimensional anisotropic situation could be found.

The perfectly stratified case could be obtained by solving Eq. 2.25 under appropriate conditions ($\lambda_1 \rightarrow \infty$, $\lambda_2 \rightarrow \infty$ and finite λ_3). However, a separate but similar analysis was conducted by Gelhar et al. [81]. They assumed a normal permeability distribution (instead of a log-normal one) and obtained

$$\alpha_L^* = \int_{-\infty}^{+\infty} \frac{S_{KK}(s)}{\langle K \rangle^2} \frac{1 - e^{-\alpha_T v t s^2}}{\alpha_T s^2} \, ds \tag{2.31}$$

in which $S_{KK}(s)$ is the power density spectrum of the hydraulic conductivity field, characterized by an integral scale λ.

Three different regimes can be identified from Eq. 2.31. At early times, transverse spreading has not caused any mixing yet and solute particles remain on their initial flow line. The concentration distribution behavior is fully controlled by longitudinal advection and apparent longitudinal dispersivity varies linearly in time

$$\alpha_L^* \rightarrow \frac{\sigma_K^2}{\langle K \rangle^2} v t \quad t \rightarrow 0 \tag{2.32}$$

After some time, spatial concentration gradients appear due to transverse velocity variations, causing diffusion and dispersion of particles from their initial

flow line. Particle velocities then change according to their new flow line, and new concentration gradients appear, causing new transfers of particles between flow lines. For intermediate times, transverse transport processes have ensured mixing over the respective layer thicknesses (or over the integral scale λ), but not over the overall aquifer thickness. In this case, it can be shown that longitudinal dispersivity increases according to the square-root of time [53, 132]. The third regime corresponds to full mixing of the solume plume over the aquifer thickness. This regime was first investigated by Taylor [179, 180] and Aris [5] for laminar flow through a tube, with a deterministic velocity distribution. They showed that in this regime, commonly referred to as the Taylor dispersion regime, the dispersive flux is Fickian with a constant asymptotic apparent dispersivity. In the stochastic approach of solute transport in perfectly layered soils, this regime only exists provided the covariance function of the permeability field is properly chosen. Using a hole-effect covariance model, Gelhar et al. [81] obtained

$$\alpha_L^*(\infty) = \frac{1}{3} \frac{\sigma_K^2}{\langle K \rangle^2} \frac{\lambda^2}{\alpha_T} \tag{2.33}$$

which basically exhibits similar tendencies as Eq. 2.26 or Eq. 2.29. Asymptotic apparent longitudinal dispersivity is directly proportional to the variance of the $\ln(K)$ field (as $\sigma_K^2/\langle K \rangle^2 \approx \sigma_Y^2$) but depends on the square of the correlation length. Moreover, its value is inversely proportional to the magnitude of transverse mixing.

2.3 Fractal models of heterogeneity

The main feature of a fractal object is that its degree of irregularity is independent of the scale. As long as one watches it closer and closer, new small-scale irregularities appear, although it is not possible to detect them from a larger-scale point of view. In normal Euclidian geometry, the length L of a line can be calculated with

$$L = n\epsilon \tag{2.34}$$

where n is the number of length units ϵ [197]. If the size of ϵ is diminished by 2, then the number of measuring units n increases by 2, keeping the length constant.

Many natural objects do not behave according to this simple relationship. If one attempts to apply Eq. 2.34 to an irregular line, such as a coastline, it can be found that the product $n\epsilon$ is not a constant, but grows without bounds as long as ϵ gets smaller. It has been found that, in the case of fractal lines such as coastal lines,

$$F = n\epsilon^d \tag{2.35}$$

where F is a measure of the fractal line length (which, contrary to L, is not expressed in $[m]$ but in $[m^d]$) and d is the dimension in which one has to measure the line length in order to obtain a constant value for F. d is called the fractal dimension. In the case of a line, this parameter may vary from 1 to 2. If $d = 1$, the measured line is geometrically simple, whereas if $d = 2$, the line
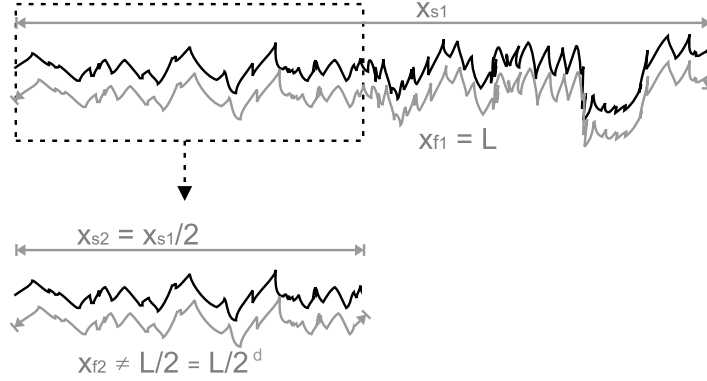
Figure 2.6: Schematic illustration of a fractal particle path.

is so irregular that it completely fills a plane. Combining Eqs. 2.34 and 2.35 leads to

$$L(\epsilon) = F\epsilon^{1-d} \tag{2.36}$$

which describes the dependence of a measured length with the measurement unit ϵ, according to fractal length F and fractal dimension d.

2.3.1   Application to solute transport

Fractal geometry was first introduced by Wheatcraft and Tyler [197] to describe solute particle travel paths in heterogeneous media. However, as the Euclidian length of a fractal line increases without bounds as long as the measurement unit decreases, particle travel path cannot be fully fractal. Indeed, water flow does not exactly follow the shape of the soil grains, otherwise some particules would have an infinite travel time. A cutoff limit ϵ_c was then introduced for the measurement unit, this limit being comprised between a mean pore size and the size of the R.E.V. for the smallest heterogeneity.

In a single fractal streamtube, if x_F is the actual distance travelled by a particle (in $[m]$) and if x_S is the longitudinal straight-line distance travelled by this same particle (also expressed in $[m]$), one has

$$F = x_S^d \tag{2.37}$$

where the measurement unit is equal to the straight-line path. Substituting this relationship into Eq. 2.36 and measuring at the fractal cutoff limit leads to

$$x_F = \epsilon_c^{1-d} x_S^d \tag{2.38}$$

which can be viewed as a scaling relationship between measurement scale x_S and real particle travel path x_F. This is illustrated in Fig. 2.6. If measurement scale is divided by 2, if particle travel path is fractal, it is not divided by 2 but by 2^d.

Provided the Fickian model is valid at some local scale, the spreading of a dissolved particle cloud in space, expressed as the variance of the particle position $\sigma_C^2 = E\left[(X - \langle X \rangle)^2\right]$, is given by

$$\sigma_C^2 = 2\alpha_L x_F \tag{2.39}$$

where α_L is the local longitudinal dispersivity. This variance can also be expressed in terms of measured variables

$$\sigma_C^2 = 2\alpha_L^* x_S \tag{2.40}$$

where α_L^* is the measured (apparent or effective) longitudinal dispersivity. Equating Eqs. 2.39 and 2.40, and using Eq. 2.38, leads to

$$\alpha_L^* = \alpha_L \epsilon_c^{1-d} \, x_S^{d-1} \tag{2.41}$$

which allows the upscaling of longitudinal dispersivity based on a fractal description of the heterogeneous medium. For an homogeneous non-fractal medium ($d = 1$), field-scale dispersivity remains equal to local dispersivity. Wheatcraft and Tyler [197] and Zhou and Selim [204] extended this latter equation to transport in a soil composed of a set of fractal streamtubes. However, this approach is rather conceptual, and one could expect a real aquifer to behave somehow differently than a set of disconnected fractal streamtubes. Zhan and Wheatcraft [201] proposed another approach, combining fractal geometry and spectral analysis, that could be more adapted to real field-scale situations.

2.3.2 Fractal geometry and spectral analysis

Whereas classical stochastic approaches involve $\ln(K)$ covariance functions that have a finite correlation length, in order to have a rapid decrease of hydraulic conductivity autocorrelation (see Section 2.2), this assumption is not necessary anymore when using concepts of fractal geometry. Zhan and Wheatcraft [201] proposed to use a power-law covariance model $C_{YY} = |h|^{2H}$ (using the same notations as in Section 2.2), where $0 < H < 1$ is called Hurst coefficient and link with the fractal dimension according to $H = 1 + e_u - d$ (e_u being the Euclidian dimension). $H = 1$ corresponds thus to a non-fractal medium. For this type of heterogeneity, Fickian behavior will never be achieved if the aquifer is not bounded, and longitudinal macrodispersivity will monotonically increase with plume scale to infinity. However, for most geological formations, physical boundaries always exist. A generally encountered situation is that no-flow boundaries enclosing the fractal porous medium define the field scale at which contaminants will disperse. Zhan and Wheatcraft [201] then introduced a macroscale cutoff limit L_m, having the same role as the correlation length used in classical stochastic analysis, but being linked to a physical boundary rather than to the structure of the permeability field.

Zhan and Wheatcraft [201] showed that, in the case of a stratified fractal aquifer, asymptotic macrodispersivity can be computed from

$$\alpha_L^*(\infty) = \frac{\sigma_Y^2}{\alpha_T} \frac{2 - d}{3 - d} \left(\frac{L_m}{2\pi}\right)^2 \tag{2.42}$$

where $1 < d < 2$ and L_m is representative of the aquifer thickness. Eq. 2.42 is very similar to Eq. 2.33, $\alpha_L^*(\infty)$ being inversely proportional to α_T and with a linear dependence on the variance of the $\ln(K)$ field and on the square of a characteristic length. Relative macrodispersivity can be computed according to

$$
\begin{aligned}
\frac{\alpha_L^*}{\alpha_L^*(\infty)} &= 1 - \exp\left[-\frac{\xi}{(2\pi)^2}\right] \\
&+ \frac{1}{2-d}\frac{\xi}{(2\pi)^2}\exp\left[-\frac{\xi}{(2\pi)^2}\right] \\
&- \frac{1}{2-d}\left[\frac{\xi}{(2\pi)^2}\right]^{3-d}\Gamma\left(d-1,\frac{\xi}{(2\pi)^2}\right)
\end{aligned}
\tag{2.43}
$$

where $\xi = \alpha_T\langle v_1\rangle t/L_m^2$ and $\Gamma(a,x)$ is the incomplete Gamma function. In two- and three-dimensional problems, asymptotic dispersivity is given by

$$
\alpha_L^*(\infty) = \frac{\sigma_Y^2}{\gamma^2}\frac{6-2d}{7-2d}\left(\frac{L_m}{2\pi}\right) \quad \text{(2D)}
\tag{2.44}
$$

$$
\alpha_L^*(\infty) = \frac{\pi}{2}\frac{\sigma_Y^2}{\gamma^2}\frac{8-2d}{9-2d}\left(\frac{L_m}{2\pi}\right) \quad \text{(3D)}
\tag{2.45}
$$

where $\gamma = 1$ and $\gamma = 1+\sigma_Y^2/6$ in two- and three-dimensional cases respectively. Fig. 2.7 shows the dependency of asymptotic dispersivity on Hurst coefficient for two- and three-dimensional problems. These results are qualitatively consistent with results from stochastic theories, as an increase in the correlation of the medium (i.e. an increase of the Hurst coefficient or an increase of the correlation length) results in a higher asymptotic longitudinal apparent dispersivity and that an increase in the Euclidian dimension of the problem results in a decrease of the dispersivity. It should be noted that a totally fractal medium ($H = 0$) yields a macroscopic dispersivity equal to zero, which is again consistent with stochastic theories ($\alpha_L^* = 0$ for $\lambda = 0$) but contradictory with results of streamtubes models developed in the previous section. Fig. 2.8 shows the transient development of apparent longitudinal dispersivity in the case of a perfectly stratified aquifer.

In the anisotropic case, Zhan and Wheacraft [201] also developed two- and three-dimensional analytical solutions for asymptotic apparent dispersivity. In the two-dimensional case for flow parallel to the bedding, they propose

$$
\begin{aligned}
\alpha_{L,\parallel}^*(\infty) &= \frac{\sigma_Y^2}{\gamma^2}\frac{6-2d}{7-2d}\left(\frac{L_m}{2\pi}\right)\left(\frac{\alpha_1}{\alpha_2}\right)^{8-2d} \\
&\times \left(\sum_{n=0}^{\infty}\frac{(3-d+n)!}{(3-d)!}\left(1-\frac{\alpha_2^2}{\alpha_1^2}\right)^n\frac{(2n)!}{2^{2n}(n!)^3}\right)^{-1}
\end{aligned}
\tag{2.46}
$$

and for flow perpendicular to the bedding

$$
\begin{aligned}
\alpha_{L,\perp}^*(\infty) &= \frac{\sigma_Y^2}{\gamma^2}\frac{6-2d}{7-2d}\left(\frac{L_m}{2\pi}\right) \\
&\times \left(\sum_{n=0}^{\infty}\frac{(3-d+n)!}{(3-d)!}\left(1-\frac{\alpha_1^2}{\alpha_2^2}\right)^n\frac{(2n+2)!}{2^{2n}(n!)^3}\right)^{-1}
\end{aligned}
\tag{2.47}
$$
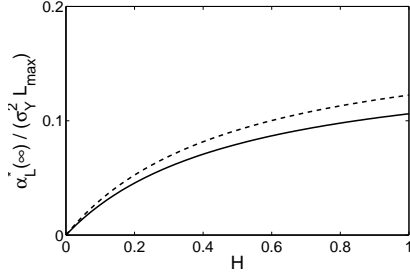
Figure 2.7: Influence of Hurst coefficient on asymptotic dispersivity for two-dimensional (solid line) and three-dimensional (dashed line) medium. $\sigma_Y^2 = 1$.
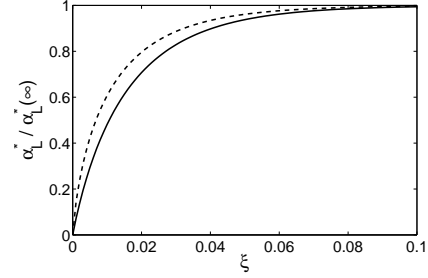
Figure 2.8: Influence of fractal dimension on the transient behavior of apparent longitudinal dispersivity in a perfectly stratified aquifer. $d \to 1$ (solid line) and $d \to 2$ (dashed line).
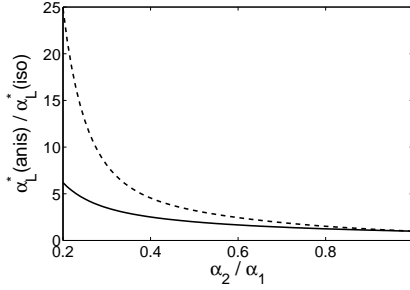
Figure 2.9: Influence of the anisotropy ratio on apparent longitudinal dispersivity in a two-dimensional aquifer for flow parallel to the bedding. $H \to 0$ (solid line) and $H \to 1$ (dashed line).
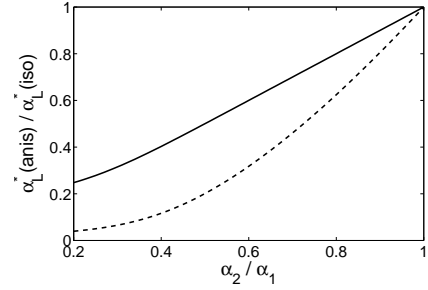
Figure 2.10: Influence of the anisotropy ratio on apparent longitudinal dispersivity in a two-dimensional aquifer for flow perpendicular to the bedding. $H \to 0$ (solid line) and $H \to 1$ (dashed line).

where α_1 and α_2 reflect relative hydraulic conductivity variations in direction 1 and 2. It must be noted that a depiction of the anisotropy in terms of correlation lengths is not possible in a fractal framework, as they are assumed to be infinite. Figs. 2.9 and 2.10 show the influence of anisotropy ratio on asymptotic longitudinal dispersivity for different Hurst coefficients.

2.4 Inclusion models

Transport in aquifers made of inclusions of highly contrasted permeabilities has only been very recently investigated. Desbarats [62] performed pioneering numerical simulations using a binary medium with inclusions of low permeability and showed that permeability contrast and inclusion volumetric proportion were the main controlling parameters for transport. Rubin [152] proposed a first-order stochastic approach and derived analytical results in the case of bimodal isotropic media. Like other results from stochastic theories, Rubin's results are only valid for low permeability contrasts. Eames and Bush [67] and later Dagan and Lessoff [56] and Lessoff and Dagan [120] studied transport

properties of two- and three-dimensional bimodal fields composed of inclusions of fixed size and of constant permeability, disposed at random in an homogeneous matrix. Their developments were conducted under the assumption of low volumetric proportion of inclusions (i.e. in the dilute system limit) so that advective transport could be solved by isolating one inclusion and the dispersive effect of a collection of lenses was determined subsequently in a simple additive manner. Dagan et al. [55] and Fiori et al. [74] further refined the analysis by considering distributions of ellipses of different size and of different permeabilities, and by computing the transient development of apparent dispersivity. They released the dilute system approximation by considering instead the self-consistent approach, in which the flow and transport problems are solved for a single inclusion embedded in a equivalent homogeneous medium replacing the neighbouring inclusions. However, they limited their analysis to isotropic media and compared the results with numerical simulations [105]. Dagan and Fiori [54] and Fiori and Dagan [73] studied transport properties of media with composite inclusions, that allowed them to derive results without relying neither on the dilute system nor on the self-consistent approach. However, they also conducted their analysis in the isotropic case. Fiori et al. [75] and Jankovic et al. [106] performed extensive numerical simulations on bimodal isotropic medium for different volumetric proportions of inclusions (ranging from 5 to 40%) and for different permeability ratios (ranging from 0.01 to 10). They found that the self-consistent approach could be reasonably adopted in each of their tested case.

In this section, it is thus proposed to further study the model suggested by Dagan et al. [55], developped under the self-consistent approximation, and to extend it to anistropic formations using the results proposed by Dagan and Lessoff [56] and Lessoff and Dagan [120].

2.4.1   Conceptual model

Dagan et al. [55] have suggested to model heterogeneous formations as multiphasic ones, made up of M types of block geometry and of N different types of material. Blocks are assumed not to overlap (Fig. 2.11 a.). A point of the medium lies in the block i, j of shape i ($i = 1 \ldots M$) and of material j ($j = 1 \ldots N$) with a known probability p_{ij}. p_{ij} thus denotes the volumetric proportion of blocks of size i and of material j in the medium. Centroid positions of blocks $\overline{\mathbf{x}}_{ij}$ are however not known and are treated as random variables. If K_j is the permeability of material j, the overall conductivity field is given by [55]

$$K(\mathbf{x}) = \sum_i \sum_j K_j I(\mathbf{x} - \overline{\mathbf{x}}_{ij}) \qquad (2.48)$$

where the indicator function $I(\mathbf{x} - \overline{\mathbf{x}}_{ij})$ is equal to 1 for $\mathbf{x}$ belonging to the inclusion (i, j) and is equal to zero otherwise. It is emphasized that permeabilities of two neighbouring blocks remain uncorrelated. Mean and variance of the
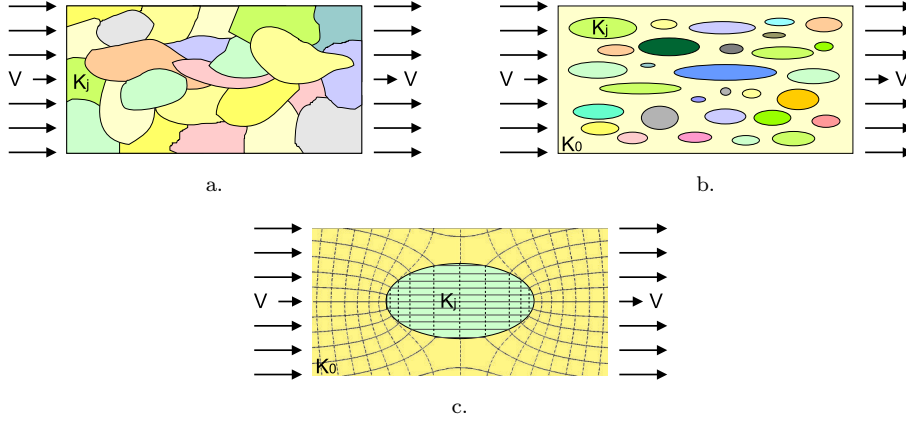
Figure 2.11: Conceptual model and the self-consistent approximation. a. Statistically homogeneous but anisotropic heterogeneous permeability field. b. Model of inclusions of regular shape disposed at random in a matrix. c. Single inclusion embedded in a matrix. *Adapted from Dagan et al. [55].*

log-permeability field can be computed from

$$\ln(K_g) = \sum_i \sum_j p_{ij} m_j \tag{2.49}$$

$$\sigma_Y^2 = \frac{1}{2} \sum_i \sum_j \sum_{k \neq j} (m_j - m_k)^2 p_{ij} p_{ik} \tag{2.50}$$

where $m_j = \ln(K_j)$. It appears from Eq. 2.50 that the variance of such media can be very high, well above the classical limit $\sigma_Y^2 < 1$ established for the validity of first-order stochastic theories.

To further simplify the model, Dagan et al. [55] propose to represent blocks as inclusions of regular size, such as ellipses or spheroids, and to assume that they are submerged in a matrix of arbitrary conductivity K_0 to be determined below (Fig. 2.11 b.). Dagan et al. [55] state that, despite these limitations and provided the distribution of sizes and permeabilities is properly chosen, this type of permeability field can properly mimic any given permeability distribution and any two-point anisotropic covariance function.

In a given heterogeneous formation of this geometry, the solution of the flow field can be represented as a distribution of singularities of source type, each source corresponding to a given block. The self-consistent approach proceeds by isolating one inclusion of shape i and permeability K_j and by suppressing the remaining ones in the matrix of permeability K_0 (Fig. 2.11 c.). The flow and transport problems are then solved assuming there is no interaction between each block. As K_0 could be any reference permeability somehow linked to the effective permeability K_e of the medium, the self-consistent approach assumes $K_0 = K_e$ and K_0 reflects the presence of neighbourings blocks that have been suppressed. The derivation of K_e for two- and three-dimensional isotropic media is given by Dagan [50] and extended to three-dimensional anisotropic media

in [53]. The case of two-dimensional anisotropic media is given in Appendix A.

2.4.2   Advective transport by the Lagrangian approach

Under ergodic condition, the spatial moments of a solute plume can be computed from the statistical moments of the trajectory of a single particle. One will then consider a solute particle injected at time $t = 0$ and at position $\mathbf{x}_0$. The trajectory of this particle is $\mathbf{x} = \mathbf{X}(t, \mathbf{x}_0)$ and is given by

$$\mathbf{X}(t, \mathbf{x}_0) = \mathbf{x}_0 + \mathbf{V}t + \sum_i \sum_j \mathbf{X}'_{ij} \tag{2.51}$$

where $\mathbf{V}$ is the far field velocity and $\mathbf{X}'_{ij}$ is the trajectory fluctuation caused by block (i, j). Trajectory second moments are given by

$$X_{ms}(t) = \sum_i \sum_j E\left[X'_{ij,m}(\mathbf{x}_0 - \overline{\mathbf{x}}_{ij})\ X'_{ij,s}(\mathbf{x}_0 - \overline{\mathbf{x}}_{ij}) \right] \tag{2.52}$$

where m and s refer to the components of the vectors of the trajectory fluctuations. Following the work of Dagan et al. [55], one will further consider the continuous limit for permeability and for inclusion size. The volumetric proportion of blocks of size i and of material j will tend to $p_{ij} \to pf(K, A)dKdA$. $p = \sum_i \sum_j p_{ij} \leq 1$ is the total volumetric proportion of inclusions and A is a characteristic size of inclusion (e.g. the longitudinal semi-axe). $f(K, A)$ is then the distribution of permeability and ellipse size. It will be assumed that anisotropy ratio is identical for each inclusion. In this case, and particularizing Eq. 2.52 to longitudinal fluctuations yields

$$X_{11}(t) = p \int \int \int \frac{X_1'^2(t, \mathbf{x}_0, K, A)}{V(A)} f(K, A)\ d\mathbf{x}_0 dK dA \tag{2.53}$$

where $V(A)$ is the volume occupied by the ellipse of size A. The longitudinal apparent dispersivity is obtained from

$$\alpha_L^* = \frac{1}{2V} \frac{dX_{11}(t)}{dt} \tag{2.54}$$

One will only consider the two-dimensional problem, as it is the one of main interest in this study and as extension to three-dimensional cases follows the same lines. Flow is assumed to be uniform at infinity, of velocity V aligned in the longitudinal direction (although the developments could be easily extended to flow in any direction [56]). The head field ϕ for an inclusion of characteristic size A and of permeability K in the situation depicted on Fig. 2.11 c. is given by Eqs. A.4 and A.5. Longitudinal trajectory fluctuations are computed according to

$$X_1'(t, \mathbf{x}_0, K, A) = \int_0^t (\nabla \phi(K, A) - V) dt \tag{2.55}$$

Details of the computation method are given by Lessoff and Dagan [120] and by Fiori et al. [74].
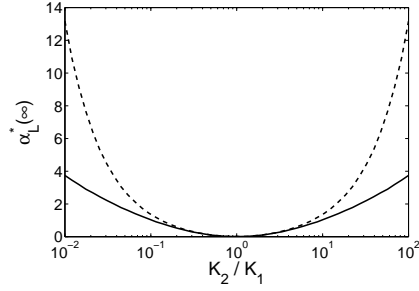
Figure 2.12: Influence of permeability contrast on apparent longitudinal dispersivity. Proportions of inclusions are $p_1 = p_2 = 0.5$. $e = 1$ (solid line) and $e = 1/4$ (dashed line).
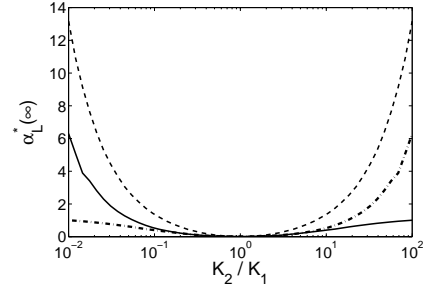
Figure 2.13: Influence of permeability contrast on apparent longitudinal dispersivity. Anisotropy ratio is $e = 1/4$ and proportions of inclusions are $p_2 = 0.1$ (solid line), $p_2 = 0.5$ (dashed line) and $p_2 = 0.9$ (dot-dashed line).

Figs. 2.12 to 2.15 show the behavior of the asymptotic dispersivity for a two-facies permeability field (facies 1 and 2) of varying permeability contrast, anisotropy ratio and volumetric proportion. Each point on these figures requires computation of effective permeability according to Eq. A.21 and computation of asymptotic dispersivity using Eqs. 2.53 and 2.54. It appears that for equal volumetric proportion of facies, curves are symmetric. For higher anisotropy ratio, apparent longitudinal dispersivity increases, which is in accordance with results obtained by Lessof and Dagan [120] under the dilute assumption. When the medium is mainly composed of a low-permeability facies, apparent dispersivity increases when permeability decreases. However, as discussed qualitatively by Dagan and Lessoff [56] and Dagan et al. [55], the behavior for low permeability inclusions is altered by transverse dispersivity and molecular diffusion, which provide a cutoff in asymptotic longitudinal macrodispersivity. When the medium is predominantly composed of high permeability inclusions, apparent dispersivity converges to a constant value for increasing permeability. Apparent dispersivity is maximum for a volumetric proportion of inclusions close to 50 %.

2.5 Conclusion

In this chapter, three methods for the upscaling of longitudinal dispersivity in heterogeneous media were detailed. These methods allow one to compute apparent (or effective) values of longitudinal dispersivity to be used in the ADE for an equivalent homogeneous medium.

The stochastic method is relatively popular but is bound to a strong limitation of low permeability variability. The other limitation of this method is that it is based on a statistical characterization of the permeability field. This characterization ideally requires vast amounts of data, that are generally not available in field-scale problems. The fractal method that has been presented does not require an assumption low variability. However, it basically requires
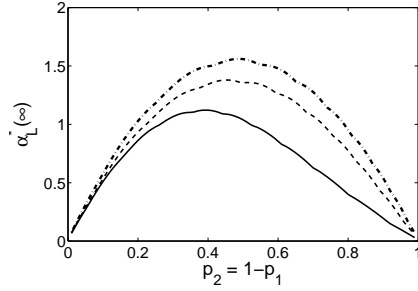
Figure 2.14: Influence of facies volumetric proportion on apparent longitudinal dispersivity. Permeability ratio is $K_2/K_1 = 1/10$. $e = 1$ (solid line), $e = 1/4$ (dashed line) and $e = 1/10$ (dot-dashed line).
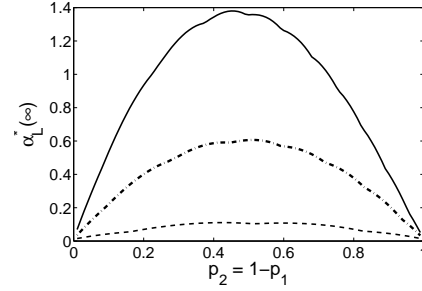
Figure 2.15: Influence of facies volumetric proportion on apparent longitudinal dispersivity. Anisotropy ratio is $e = 1/4$ and permeability ratios are $K_2/K_1 = 1/10$ (solid line), $K_2/K_1 = 1/5$ (dashed line) and $K_2/K_1 = 1/2$ (dot-dashed line).

similar characterization methods as the stochastic approach, as the transport problem is parametrized using a covariance function for the permeability field and a large scale cutoff distance. Finally, the self-consistent approach allowed one to derive apparent dispersivity values in the case of highly heterogeneous media. The main limitation of this approach is that diffusive and local-scale dispersive transport are not considered, which might induce a serious bias when considering media with relatively low permeabilities.

The basic approach for modelling large-scale solute transport consists then to use the upscaled dispersion coefficients in the classical advection-dispersion equation and solve it at the scale of interest. However, as the time needed to reach the asymptotic large-scale Fickian behavior turns out to be extremely long, the assumption of a constant macrodispersion coefficient can still be questionable in most of the case. The remaining solution consists in solving the ADE with time- or space-dependent dispersion coefficients, either numerically [146] or analytically [4, 101, 102, 103, 124, 143, 199, 207].

Chapter 3

Upscaling of the transport equation

3.1 Introduction

The advection-dispersion equation was obtained assuming a Fickian dispersive flux. A first way of departing from this assumption consists in obtaining a more elaborate model of the dispersive flux and substituting it in the mass balance equation. Most of the time, a non-Fickian dispersive flux can be obtained by solving the effect of heterogeneities on transport in highly conceptualized situations, such as perfectly stratified formations [21, 35, 81]. Other approaches have however been investigated, being probabilistic [163] or heuristic [176]. In Section 3.2, third- and fourth-order transport models will first be evoked, then telegraph equations will be more extensively presented, as they represent a more useful alternative to the ADE.

Probabilistic models of solute transport in heterogeneous formations yield a second way of deriving non-Fickian transport equations. In Section 3.3, Continuous Time Random Walk (CTRW) will be presented as an extension to Brownian motion, for particle movements correlated in time or in space. It will also be shown that this approach can yield fractional-order partial differential equations that are a direct extension of the ADE.

Finally, the particular case of transport in a two-region medium will be studied in Section 3.4. In the literature, this type of model is usually referred to as mobile-immobile models (MIM). The heterogeneous medium is partitionned into two zones, one of them having a negligible velocity. Exchange between mobile and immobile phases is quantified either using a rate coefficient or using a diffusion model, and a source term is added to the classical ADE. Whereas this type of model was developped to account for long tails and slowly converging concentration distributions, effective dispersion coefficients can be expressed in terms of MIM transport parameters [186] and simulations based on field-scale data showed that rate-limited models could correctly explain macrodispersion [69, 97].

As this work focuses on longitudinal apparent dispersion, and in order to use simple analytic expressions, upscaled transport equations will be presented in their one-dimensional form. They have thus to be compared with Eq. 1.6.

31

3.2 Higher-order and telegraph equations

3.2.1 Higher-order equations

In this section, the problem of Taylor dispersion is adressed. Assuming a one-dimensional velocity profile (such as the velocity in a perfectly stratified aquifer, the velocity profile in a tube or the velocity profile between parallel plates) and transverse transport processes (being either diffusion only or hydrodynamical dispersion), authors have tried to incorporate attributes of this velocity profile as a description of macrodispersive processes in the transport equation without relying on the Fickian assumption.

Camacho [35, 36, 37] studied laminar flow between parallel plates. He deduced using Fourier analysis to average the advection-diffusion equation, a non-Fickian relaxation equation for the macrodispersive flux

$$\frac{\partial q^D}{\partial t} + \frac{q^D}{\tau_e} + (1 + \gamma_a)v\frac{\partial q^D}{\partial x} - D^d\frac{\partial^2 q^D}{\partial x^2} = -\sigma_v^2\frac{\partial C}{\partial x} \tag{3.1}$$

where q^D is the mass flux due to diffusion, τ_e $[s]$ is an effective relaxation time characterizing exponential degradation towards Fickian behavior and γ_a $[-]$ is an asymmetry term. σ_v^2 $[m^2/s^2]$ is the variance of the velocity profile. Incorporating this constitutive equation in the mass balance equation leads to a fourth-order transport model that can account for molecular diffusion, macrodispersion due to transverse mixing in non-uniform one-dimensional flow fields and that can yield asymmetric concentration distributions

$$
\begin{aligned}
&\frac{\partial C}{\partial t} + v\frac{\partial C}{\partial x} - D^d\frac{\partial^2 C}{\partial x^2} \\
+ \quad &\tau_e\left[\frac{\partial^2 C}{\partial t^2} + \left((1+\gamma_a)v^2 - \sigma_v^2\right)\frac{\partial^2 C}{\partial x^2} + (2+\gamma_a)v\frac{\partial^2 C}{\partial x\partial t}\right] \\
= \quad &\tau_e\left[2D^d\frac{\partial^3 C}{\partial x^2\partial t} + (2+\gamma_a)vD^d\frac{\partial^3 C}{\partial x^3} - D^d\frac{\partial^4 C}{\partial x^4}\right]
\end{aligned}
\tag{3.2}
$$

Gelhar et al. [81] studied solute transport in a randomly heterogeneous but perfectly stratified aquifer. Using a method similar to that described in Section 2.2.3, they obtained an analytical solution for concentration fluctuations that could be injected in the governing equation of the mean concentration. They truncated the latter to the third-order term, which resulted in

$$
\begin{aligned}
\frac{\partial C}{\partial t} \quad + \quad &v\frac{\partial C}{\partial x} - \left((\alpha_L^* + \alpha_L)v + D^d\right)\frac{\partial^2 C}{\partial x^2} \\
- \quad &\gamma_G\frac{\partial^3 C}{\partial t\partial x^2} - \gamma_G v\frac{\partial^3 C}{\partial x^3} = 0
\end{aligned}
\tag{3.3}
$$

where α_L^* is given by Eq. 2.31 and

$$\gamma_G = \int_{-\infty}^{+\infty} \frac{S_{KK}(s)}{\langle K\rangle^2}\frac{1 - e^{-\alpha_T vts^2}(1 + \alpha_T vts^2)}{\alpha_T^2 s^4}\,ds \tag{3.4}$$

Gelhar et al. [81] provide an analytical solution to Eq. 3.3 in terms of a moment series expansion.

A third- or a fourth-order transport equation is much more difficult to solve analytically, even for very simple initial and boundary conditions, and therefore does not represent a valuable alternative to the classical and easy to handle advection-dispersion equation. It will be however shown in the next section how Eq. 3.2 can be simplified to obtain a second-order equation that could be much more useful.

3.2.2 Telegraph equations

The advection-dispersion equation is a parabolic differential equation. No downstream condition is needed for concentration whereas solute front velocity is theoretically infinite. This means that, after a small time step, concentration at infinity is non-zero. Regarding this physical inconsistency, a few authors have turned to telegraph equations to model solute transport. Telegraph equations are second-order hyperbolic differential equations, meaning that the relative increase in complexity compared to the ADE remain reasonable, while these equations yield finite front velocities.

In order to depart from the Fickian assumption of a totally uncorrelated random movement of solute particles, Scheidegger [163] introduced an exponential correlation function for particle velocities, with a correlation time τ_e [s]. This approach could be compared to the stochastic approach, in which the velocity density spectrum is introduced to quantify apparent dispersion. Scheidegger also showed that this approach ended up in adding a term to Eq. 1.6, leading to a telegraph equation that can be written as

$$\frac{\partial C}{\partial t} = -v\frac{\partial C}{\partial x} + D_L\frac{\partial^2 C}{\partial x^2} - \tau_e\left(v^2\frac{\partial^2 C}{\partial x^2} + 2v\frac{\partial^2 C}{\partial x\partial t} + \frac{\partial^2 C}{\partial t^2}\right) \qquad (3.5)$$

Analytical solutions to this equation lead however to sharp cutoffs at tailing edges of concentration fronts [162, 163], which does not fit experimental results. This is illustrated on Fig. 3.1 for a continuous injection. $U = vt/x$ is the number of pore volumes and $C_r = C/C_0$ is the relative concentration of solute. Numerical values are $v = 10^{-7}$ m/s, $\alpha_L = 1$ cm, $D^d = 0$ and $x = 1$ m (so that mean breakthrough time is $\langle t \rangle = 10^7$ s). It can be easily checked that Eq. 3.5 is a particular case of the fourth-order model of Camacho presented in previous section. In case molecular diffusion can be neglected while a significant transverse variation in the velocity field is present, Eq. 3.2 reduces to a second-order telegraph equation

$$\tau_e\frac{\partial^2 C}{\partial t^2} + \frac{\partial C}{\partial t} + v\frac{\partial C}{\partial x} + \tau_e(2+\gamma_a)v\frac{\partial^2 C}{\partial x\partial t} - \tau_e\left(\sigma_v^2 - (1+\gamma_a)v^2\right)\frac{\partial^2 C}{\partial x^2} = 0 \ (3.6)$$

which, when γ_a is set to zero, reduces to Eq. 3.5, with an apparent longitudinal dispersivity being expressed according to $\alpha_L^* = \tau_e\sigma_v^2/v$.

Strack [176] proposed to solve the problem of infinite front velocities by including an inertia term in the constitutive equation of the dispersive flux

$$q^D = -D_L\frac{\partial C}{\partial x} - \frac{\lambda_S}{v}\frac{\partial q_D}{\partial t} \qquad (3.7)$$
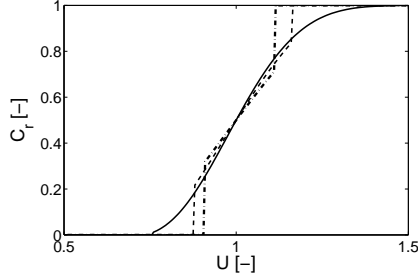
Figure 3.1: Solution of Scheidegger's telegraph equation for a continuous injection. $\tau_e/\langle t \rangle = 0.1$ (solid line), $\tau_e/\langle t \rangle = 0.5$ (dashed line) and $\tau_e/\langle t \rangle = 1$ (dash-dotted line).
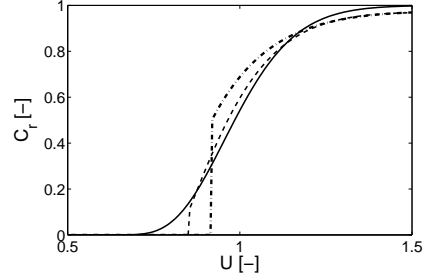
Figure 3.2: Solution of Strack's telegraph equation for a continuous injection. $\lambda_S/\alpha_L = 1$ (solid line), $\lambda_S/\alpha_L = 2$ (dashed line) and $\lambda_S/\alpha_L = 10$ (dash-dotted line).

where λ_S is a parameter having the dimension of a length. Strack [176] found from experimental evidence λ_S to be inversely proportionnal to solute velocity. Incorporating this term into Eq. 1.4 leads to an equation slightly different from the advection-dispersion equation and somehow comparable to Eq. 3.5

$$\frac{\partial C}{\partial t} = -v\frac{\partial C}{\partial x} + D_L\frac{\partial^2 C}{\partial x^2} - \frac{\lambda_S}{v}\left(v\frac{\partial^2 C}{\partial x \partial t} + \frac{\partial^2 C}{\partial t^2}\right) \tag{3.8}$$

As in Scheidegger's theory, one obtains analytical solutions charaterized by sharp breakthroughs, with the difference that late-time edges are smoothened. Fig. 3.2 shows the analytical solution of Eq. 3.8 in the case of a one-dimensional continuous injection, for the same set of transport parameters used in Fig. 3.1.

Strack [176] also showed that first and second temporal moments of Eq. 3.8 under null initial concentration and for a unit step variation in concentration are similar to those of the advection-dispersion equation. The main implication of this result is that Strack's telegraph equation has no upscaling capacities regarding dispersion of solute plumes.

Tompson and Gray [183] used a volumetric averaging technique to derive large-scale balance equations. Their work was further simplified by Tompson [182], who derived another relationship for the dispersive solute flux, the latter being written in the one-dimensional case as

$$\tau_e\frac{\partial q^D}{\partial t} = -D_L\frac{\partial C}{\partial x} - \tau_e v\frac{\partial q^D}{\partial x} - q^D \tag{3.9}$$

where τ_e is somehow similar to Scheidegger's autocorrelation time. Tompson [182] also derived a transport telegraph equation, that can be shown to be a generalization of Eq. 3.5, accounting for diffusion effects.

Hassanizadeh [98] also used a volumetric averaging technique to scale up microscopic flow and transport equations. Solute dispersive flux was described using physical and chemical properties, such as chemical potentials or solute Helmholtz free energy. Hassanizadeh showed his model to be a more general form of Scheidegger's, Tompson's and Strack's models.

Most of other non-Fickian models are obtained by similar flow and transport upscaling technique, as reported from Whittaker by Peters and Smith [145]. Some of them are evoked in [98, 176, 182, 183]. Although they provide strong theoretical bases to understand non-Fickian effects in solute dispersion, most of these models are inapplicable. Indeed, parameters involved in these equations are generally very difficult to evaluate at the field scale, while their physical meaning may remain unclear.

3.3 Fractional-order transport equations

Recently, new probabilistic formulations of solute transport have been introduced to describe solute particle movements in heterogeneous media. These formulations, called Continuous Time Random Walk (CTRW), were first introduced to describe the random movement of a particle on a lattice [139] and, for instance, are already used in the field of electricity (to calculate impurity conduction in semi-conductors) [164]. They are found to be powerful tools to model situations where anomalous transport occurs [16, 18, 23, 26, 121].

First, the general framework of CTRW will be presented in Section 3.3.1. A new type of probability distribution, that will be shown to be a generalization of the Gaussian PDF, will be described. Then, in Section 3.3.2, it will be shown that fractional-advection dispersion equation can be obtained in several particular cases of CTRW, and a few one-dimensional analytical solutions will be illustrated. Finally, aspects linked to apparent dispersivity will be studied in Section 3.3.3.

3.3.1 Probabilistic random walk formulations

In a heterogeneous medium, dissolved particles are transported along different paths at varying velocities. Under ergodic conditions, this kind of transport can in general be represented using a coupled time-space PDF $p(\mathbf{x}, t)$, describing particle transitions in space (jumps) and in time (pausing times between jumps) [16, 24]. Fundamental properties of transport are governed by the asymptotic behavior of $p(\mathbf{x}, t)$. Simple asymptotic forms of $p(\mathbf{x}, t)$ include exponential and power-law (algebraic) decay [23]. Adoption of an exponential form leads to all moments of $p(\mathbf{x}, t)$ to be finite. In that case, the Central Limit Theorem applies and $p(\mathbf{x}, t)$ is Gaussian [184]. The limit process for particle movement is then a Brownian motion governed by Fick's law [6]. However, the movement of a particle in an aquifer generally does not follow uncorrelated Brownian motion, since geological material is deposited in sequenced and correlated units. A particle travelling faster than the mean at some instant is much more likely to be still travelling faster at later times, due to spatial correlation in aquifer hydraulic conductivity (see Section 2.2). This also means that particles travelling at velocities significantly different from the mean velocity may occur more often than Brownian motion can model [16, 169].

In the CTRW framework, moving particles undergo random transitions according to a probability density function that decays algebraically. This type of PDF is called a Lévy distribution, as they were first shown to ex-
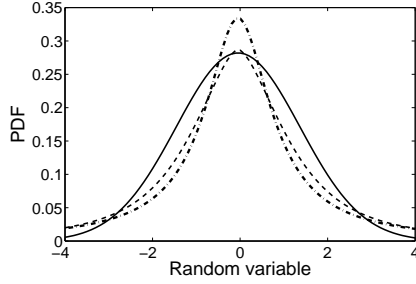
Figure 3.3: Plots of symmetric Lévy's density distributions. $\beta = 2$ (solid line), $\beta = 1.5$ (dashed line) and $\beta = 0.9$ (dot-dashed line).
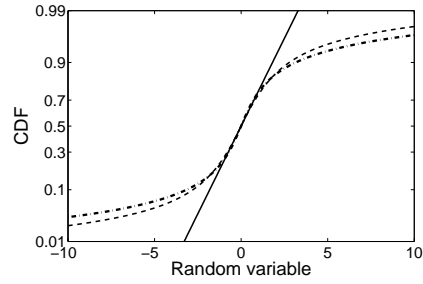
Figure 3.4: Plots of symmetric Lévy's cumulative distributions. $\beta = 2$ (solid line), $\beta = 1.5$ (dashed line) and $\beta = 0.9$ (dot-dashed line).

ist by Paul Lévy [18]. For infinite-variance jumps, tails of the corresponding PDF fall off according to an algebraic-in-space decay $p(\mathbf{x}, t) \rightarrow |\mathbf{x}|^{-1-\beta_x}$. In that case, transport is said to be spatially anomalous. Similarly, for infinite-mean pausing times, PDF tails fall off according to an algebraic-in-time decay $p(\mathbf{x}, t) \rightarrow t^{-1-\beta_t}$ and transport is said to be temporally anomalous. β_x and β_t are positive numbers, since the integral of the probability density function must be finite. For $\beta_x \geq 2$ and $\beta_t \geq 2$, the first two spatial and temporal moments of $p(\mathbf{x}, t)$ exist and particles exhibit Gaussian behavior. If $1 < \beta_x < 2$, the second spatial moment of $p(\mathbf{x}, t)$ diverge. Similarly, if $1 < \beta_t < 2$, its second temporal moment diverges too. The case $\beta_x < 1$ or $\beta_t < 1$ respectively correspond to infinite mean jump and infinite mean pausing time. Margolin and Berkowitz [129] showed that the case $\beta_t = 1$ corresponds to a purely advective transport behavior (each particle remains on its initial flow line and apparent dispersion grows without bounds). Fig. 3.3 shows a few examples of Lévy distributions, and Fig. 3.4 shows corresponding CDF plotted on probability paper.

For transport in heterogeneous media with highly conductive layers or fractures, the distribution of jump lengths is relatively broad, as particles may remain in low velocity channels whereas other particles travel at a velocity much higher than the mean. In that case, one could expect β_x to be lower than 2. Reciprocally, transport in a medium with low permeability inclusions could be characterized by $\beta_t < 2$, as particles captured in inclusions exhibit sensitively longer pausing times [135].

It must be noted that, in fact, β_x and β_t are functions of the length scale (or the time needed to traverse this length scale). The CTRW theory can be applied when β_x or β_t are constant or slowly varying over a number of orders of magnitude in length or in time [127]. Geological systems can encounter heterogeneities over different hierarchical scales, and the characteristic length of the largest heterogeneity is likely to influence β_x and β_t the most [127]. However, this largest heterogeneity must be small enough compared to the full travel distance of the particle cloud, so that the ergodic hypothesis is valid and probability distributions correctly approximate concentration distributions. If it is not the case, then large heterogeneities must be treated deterministically [127]. Moreover, as travel distance increases, the size of the largest heterogeneity must

also increase. Otherwise, provided that the domain is large enough, full averaging take place and tracer plumes become Gaussian. In this case, β_x and β_t increase to the threshold of 2 [127].

3.3.2 Fractional-order transport equations

In this section, special cases of CTRW are presented, that can lead to extended transport equations involving fractional derivatives. Mathematical developments are not derived here but can be found in [16, 19, 22, 137].

The word fractional refers to the occurence of fractional order differentiation in time or in space, or both. Introduction to fractional calculus can be found e.g. in [16, 19, 48, 169] and references therein. An easy way to understand how fractional derivatives work is to extend the action of Fourier-transforms on integer derivatives to rational order

$$\widetilde{\frac{d^\beta}{dr^\beta} f(r)} = (is)^\beta \tilde{f}(s) \tag{3.10}$$

where $\tilde{}$ indicates the Fourier-transform, r is the spatial or temporal coordinate, s is the Fourier-coordinate and β is a rational number. By inverse-transforming this equation, one can find one-dimensional expressions for fractional derivatives. The main feature of these fractional derivatives is that, unlike integer derivatives, they are non-local operators and incorporate an integral from $-\infty$ to r. This can be interpreted as a memory-effect (or as a correlation in time or in space of particle displacement), allowing one to take into account long particle jumps or long pausing times.

Considering spatial anomalous transport, with $\beta_t = 2$ and $0 < \beta_x < 2$, Benson [16, 19] showed that describing the dispersive flux of solute particles as proportional to a fractional derivative allows the magnitude of particle velocities (or the size of particle jumps) to be unconstrained. This is an extension of Fick's second law, where the variation of concentration in time can be modelled using

$$\frac{\partial C}{\partial t} = \mathcal{D}_x \frac{\partial^{\beta_x} C}{\partial x^{\beta_x}} \tag{3.11}$$

where β_x is the parameter of the Levy probability density function and $\mathcal{D}_x$ is comparable to the classical longitudinal dispersion coefficient D_L but is expressed in $[m^{\beta_x}/s]$. If advection and Eq. 3.11 are incorporated in the mass balance, one obtains a spatial fractional advection-dispersion equation, which can be expressed in the one-dimensional case as

$$\frac{\partial C}{\partial t} = -v \frac{\partial C}{\partial x} + \left(\frac{1+\gamma_B}{2}\right) \mathcal{D}_x \frac{\partial^{\beta_x} C}{\partial x^{\beta_x}} + \left(\frac{1-\gamma_B}{2}\right) \mathcal{D}_x \frac{\partial^{\beta_x} C}{\partial (-x)^{\beta_x}} \tag{3.12}$$

where γ_B is a skewness parameter allowing a forward jump probability distribution different from the backward jump PDF. A complete derivation of this equation can be found in [16, 18]. It can be easily checked that in the case of $\beta_x = 2$, one finds back Eq. 1.6. As soil heterogeneity is captured by parameter β_x, $\mathcal{D}_x$ may remain constant and does not need to be scale-dependent anymore. Figs. 3.3 and 3.4 show typical solutions of Eq. 3.12 without skewness,

respectively corresponding to a Dirac injection and a continuous injection. In
the case of spatial concentration distributions, the random variable to be con-
sidered is position x. In the case of temporal distributions, the random variable
is $(t - \langle t \rangle)/(t \langle t \rangle)^{1/2}$.

In the multidimensional case, a multiscaling fractional operator was in-
troduced to encompass different scaling rates of dispersion in different direc-
tions [133, 134, 168]. In that case, β_x is no longer a scalar but rather a tensor
whose principal directions may not be aligned with the principal directions of
the flow field and whose eigenvalues may not be equal in all directions.

Considering now temporal anomalous transport, with $0 < \beta_t < 1$ and $\beta_x =
2$, it can be shown that a fractional-in-time advection-dispersion equation can
be obtained [22, 137]. In the one-dimensional case, it reads

$$\frac{\partial^{\beta_t} C}{\partial t^{\beta_t}} = -v_\beta \frac{\partial C}{\partial x} + \mathcal{D}_t \frac{\partial^2 C}{\partial x^2} \tag{3.13}$$

where v_β is a generalized velocity expressed in $[m/s^{\beta_t}]$ and $\mathcal{D}_t$ is expressed in
$[m^2/s^{\beta_t}]$. Instead of using Eq. 3.13 as a starting point, Margolin and Berkowitz
[127, 129, 130] go back to the Laplace transform of the probability density
function $\psi(u) = \mathcal{L}(\psi(t))$, with $\psi(t) = \int_{-\infty}^{+\infty} p(\mathbf{x}, t) d\mathbf{x}$. In the case $0 < \beta_t < 1$,
$\psi(u)$ can be expanded in polynomial series and truncated after the third term

$$\psi(u) \approx 1 - c_\beta u^{\beta_t} + c_1 u \tag{3.14}$$

where c_β and c_1 are constant and where c_β is found to be positive [130]. It
should be noted that in early developments of CTRW theory, only two terms
were taken into account, and c_1 was systematically set equal to zero for $\beta_t < 1$
[22, 25, 26, 129]. Margolin and Berkowitz [130] showed that this approximation
becomes questionable as β_t approaches 1 from below.

This method also allows one to derive solutions in the case $1 < \beta_t < 2$. $\psi(u)$
is then expressed as

$$\psi(u) \approx 1 + c_\beta u^{\beta_t} - c_1 u \tag{3.15}$$

where, in this case, c_1 can be interpreted as a mean transition time [127, 129].
Laplace inversion of Eqs. 3.14 and 3.15 allows one to obtain analytical solutions
for temporal and spatial concentration distributions, either under continuous or
under instantaneous injection [26, 127, 129, 130]. These solutions are expressed
in terms of two parameters C_β and C_1 which are linked to c_β and c_1 via mean
transition length $\langle l \rangle$

$$C_\beta = \frac{c_\beta}{\langle l \rangle} \tag{3.16}$$

$$C_1 = \frac{c_1}{\langle l \rangle} \tag{3.17}$$

where C_1 can be expressed as the inverse of a velocity, in $[s/m]$. Margolin and
Berkowitz [130] have defined a set of new parameters in order to efficiently
compute spatial concentration distributions (SCD) and breakthrough curves
(BTC). These parameters are summarized in Table 3.1.

	$0 < \beta_t < 1$	$1 < \beta_t < 2$
SCD	$R = \frac{t^{\beta_t}}{C_\beta}$	$R = \frac{t}{C_1}$
	$\kappa = \frac{C_1 t^{\beta_t - 1}}{C_\beta}$	$\kappa = \frac{C_\beta t^{\beta_t - 1}}{C_1}$
BTC	$T = (L C_\beta)^{1/\beta_t}$	$T = L C_1$
	$r = \frac{C_1}{C_\beta^{1/\beta_t}} L^{1 - 1/\beta_t}$	$r = \frac{C_\beta^{1/\beta_t}}{C_1} L^{-1 - 1/\beta_t}$

Table 3.1: Parameters of CTRW distributions in the case of temporally anomalous transport
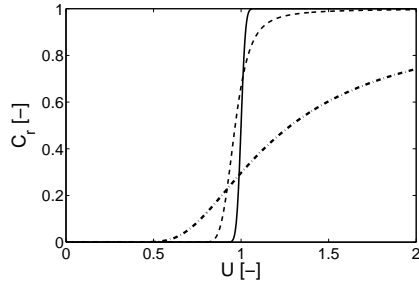
Figure 3.5: Influence of β_t on breakthrough curve. $\beta_t = 2$ (solid line), $\beta_t = 1.5$ (dashed line) and $\beta_t = 0.9$ (dot-dashed line).
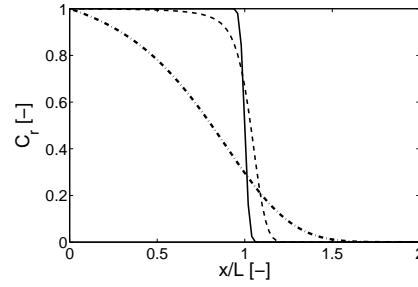
Figure 3.6: Influence of β_t on spatial distribution. $\beta_t = 2$ (solid line), $\beta_t = 1.5$ (dashed line) and $\beta_t = 0.9$ (dot-dashed line).

In addition to being dependent on β_t, spatial distributions are expressed in terms of parameters R and κ, whereas temporal distributions depends on parameters T and r. R represents the mean position of particle clouds and T is the mean breakthrough time. κ and r are both linked to apparent dispersivity. Analytical solutions involving these parameters are not presented here, but can be found in [127, 130] and are available as Matlab© functions (at http://www.weizmann.ac.il/ESER/People/Brian/CTRW/). Figs 3.5 and 3.6 show breakthrough curves and spatial concentration distributions for various values of β_t in the case of a continous injection.

Finally, it should be mentioned that other fractional-order equations have been proposed in the literature. Baeumer et al. [7] proposed an equation similar to Eq. 3.12 without skewness but with an advection term described using a space-fractional derivative of order $\beta_x/2$. Equations with fractional temporal derivatives of an order up to 2 have also been proposed [6, 17, 168], as well as equations involving both time- and space-fractional derivatives [6, 135, 137].

3.3.3 Apparent dispersivity

In this section, consequences of considering spatial or temporal anomalous transport are described with respect to apparent dispersivity. In the case of Gaussian distributions, the mean displacement of a particle cloud $\langle x \rangle$ as well as its spatial variance σ_C^2 are growing linearly with time t, so that $\sigma_C / \langle x \rangle \sim$

$t^{-1/2}$. This means that a relative narrowing of the particle plume occurs with time [23, 26, 127, 128]. As time increases, the spreading of a particle cloud around its mean position decreases compared to its mean position. The corresponding apparent dispersion coefficient, that can be computed as half of the time derivative of the spatial variance, is indeed constant, as well as apparent dispersivity.

Considering spatial anomalous transport, with $0 < \beta_x < 2$ and $\beta_t = 2$, Benson [16, 19] showed that the standard deviation of concentration distributions grows proportionally to t^{1/β_x}. As mean travel distance is directly proportional to time, $\sigma_C/\langle x \rangle \sim t^{1/\beta_x - 1}$ and the relative narrowing of concentration plumes occurs more slowly than in the case of Fickian dispersion. This situation is usually referred to as super-diffusion, as the variance of the particle plume grows faster than in the Fickian case. Apparent dispersivity follows the trend

$$\alpha_L^* = \frac{D_L^*}{v} \sim t^{2/\beta_x - 1} \sim \langle x \rangle^{2/\beta_x - 1} \tag{3.18}$$

In the case of temporally anomalous transport, for $0 < \beta_t < 1$ and $\beta_x = 2$, it can be shown that the mean displacement of a particle cloud is not linearly depending on time anymore. This is the direct consequence of having a first moment of $\psi(t)$ that is infinite. In this case, $\langle x \rangle \sim t^{\beta_t}$. It can also be shown that $\sigma_C^2 \sim t^{2\beta_t}$, so that the ratio $\sigma_C/\langle x \rangle$ is constant, and concentration distributions remain similar over different scales. There is no relative narrowing of plume distributions. This universality property is called self-similarity, and is linked to the fractal behavior of the medium. Apparent dispersion coefficient is in this case $D_L^* \sim t^{2\beta_t - 1}$. Moreover, as $\langle x \rangle \sim t^{\beta_t}$, mean particle velocity is a decreasing function of mean travel distance $v = \frac{\langle x \rangle}{t} \sim t^{\beta_t - 1} \sim \langle x \rangle^{1 - 1/\beta_t}$. Physical arguments can be used to justify this behavior [127] : considering a step injection, faster flow paths are initially filled faster by particles. The mean velocity of a particle cloud at this time is representative of the mean velocity of the fluid in these faster flow paths, and is higher than the mean flow velocity. Over time, mixing occurs with slower paths, and the average velocity of the particle cloud decreases. Combining dispersion coefficient and velocity allows one to obtain an apparent dispersivity that grows without bound linearly in space [129]

$$\alpha_L^* = \frac{D_L^*}{v} \sim t^{\beta_t} \sim \langle x \rangle \tag{3.19}$$

When $1 < \beta_t < 2$, $\langle x \rangle \sim t$ and $\sigma_C^2 \sim t^{3-\beta_t}$, so that $D_L^* \sim t^{2-\beta_t}$. Concentration distributions become narrower with growing scales but, in this case too, the relative narrowing is slower than in the Gaussian case, allowing apparent dispersivity to grow with scale [16, 23, 26, 127, 129].

$$\alpha_L^* = \frac{D_L^*}{v} \sim t^{2-\beta_t} \sim \langle x \rangle^{2-\beta_t} \tag{3.20}$$

Finally, Eqs. 3.18, 3.19 and 3.20 could be related to Eq. 2.43, were the apparent macrodispersivity was found to be proportional to $\langle x \rangle^{d-1}$ (with d being the fractal dimension of the medium), or to similar equations derived considering the soil as a set of fractal streamtubes [197, 204]. This could highlight the link

between the fractal model and the CTRW theory, establishing an equivalence between the fractal dimension d and parameters β_x and β_t [133].

3.4 Transport in dual-region media

Early in the study of solute transport in porous media, it was realized that a fraction of the fluid present in the pore space of a medium could remain immobile [44, 189]. These immobile zones could be either dead-end pores in a porous medium, the rock matrix in a saturated fractured media or clay lenses. Three different approaches can be adopted to account for the influence of these immobile zones. First, an assumption of local equilibrium can be invoked. It supposes transfer processes to occur instantaneously. The second approach uses first-order rate-limited exchange, using models borrowed from non-equilibrium chemical theories. The third approach considers diffusion to quantify exchange between mobile and immobile zones. In this section, one will only consider rate-limited and diffusion models. Local equilibrium is an asymptotic case of rate-limited transfer.

More elaborate models, accounting for two and more subdivisions of the flow system and considering advection or not in each of the subdivision have been developed [83, 107] but will not be reviewed here.

3.4.1 Single-rate and diffusion models

In the case of a two-region model, solutes are divided into a mobile and an immobile region in soils. Solutes present in the mobile zone undergo advection, diffusion and dispersion, while solutes present in the immobile zone only undergo diffusion (i.e. flow velocity in the immobile zone is assumed to be negligible compared that in the mobile zone). One defines C_m and C_{im} the concentrations in mobile and immobile phases respectively. The ADE, as it includes advection and dispersion, is used to describe C_m. It must be however augmented by a term expressing exchange with the stagnant zone. In the one-dimensional case, it reads [44, 91, 167]

$$\frac{\partial C_m}{\partial t} + \nu \frac{\partial C_{im}}{\partial t} = -v \frac{\partial C_m}{\partial x} + D_L \frac{\partial^2 C_m}{\partial x^2} \qquad (3.21)$$

where $\nu = \theta_{im}/\theta_m$ [-] is the capacity ratio, with θ_m [$-$] and θ_{im} [$-$] the volumetric fractions of mobile and immobile zones respectively. As an additional unknown appears in Eq. 3.21, an additional relationship is required to solve the problem. It usually comes from the assumption of linear non-equilibrium mass transfer [31, 44, 91, 167, 188]

$$\frac{\partial C_{im}}{\partial t} = \omega \left(C_m - C_{im} \right) \qquad (3.22)$$

where ω is a first-order rate coefficient [$1/s$]. Figs. 3.7 and 3.8 show the influence of volumetric proportion of the mobile phase and of exchange rate coefficient on evolution of concentration in the mobile phase (which is actually the concentration that can usually be measured). The transport problem was solved using the
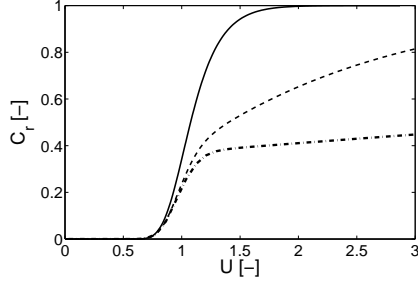
Figure 3.7: Influence of the volumetric proportion of mobile phase on total concentration. $\theta_{im}/\theta = 0.1$ (solid line), $\theta_{im}/\theta = 0.5$ (dashed line) and $\theta_{im}/\theta = 0.9$ (dot-dashed line). $Da = 1$.
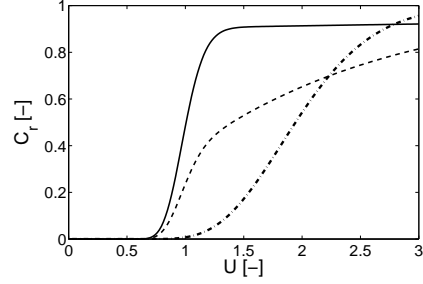
Figure 3.8: Influence of the rate coefficient on total concentration. $Da = 0.1$ (solid line), $Da = 1$ (dashed line) and $Da = 10$ (dot-dashed line). $\theta_m/\theta = 0.5$.

program STANMOD (ver. 2.2, available at http://typhoon.mines.edu/software/ igwmcsoft/stanmod.htm) for the same set of parameters, initial and boundary conditions as used for Figs. 3.1 and 3.2. The adimensional number $Da = \frac{\omega x}{\theta_m v}$ is the Damkohler number. It quantifies the rate of exchange between mobile and immobile phases compared to advective velocity in the mobile phase. As θ_{im} increases, transport exhibits anomalous behavior, with breakthrough curves characterized by longer tails (Fig. 3.7). For low Da, exchange has no time to occur and transport behaves as if there were no immobile phase (Fig. 3.8). On the contrary, for high Da, concentrations in mobile and immobile phase have time to reach local equilibrium and transport could be properly characterized using an appropriate retardation factor [8, 91, 144, 186].

The key issue is to properly characterize the exchange rate ω. Diffusion models are more convenient as exchange between mobile and immobile zones is directly quantified using Fick's first law for a given immobile zone geometry [31, 94, 95, 149, 187]. The average concentration in the immobile zone is calculated as [91]

$$C_{im} = \frac{n}{A^n} \int_0^A r^{n-1} c_r \ dr \tag{3.23}$$

where n is the dimensionality of the immobile zone ($n = 1$ for layers, $n = 2$ for cylinders and $n = 3$ for spheres) and A is its characteristic length (thickness or radius). c_r is the concentration in the immobile zone and is obtained by solving [91]

$$\frac{\partial c_r}{\partial t} = \frac{D^d}{r^{n-1}} \frac{\partial}{\partial r} \left(r^{n-1} \frac{\partial c_r}{\partial r} \right) \tag{3.24}$$

subject to

$$\frac{\partial c_r}{\partial r} = 0 \quad \text{at } r = 0 \tag{3.25}$$

$$c_r = C_m \quad \text{at } r = A \tag{3.26}$$

Approximate apparent exchange rate coefficients have been derived based on Eqs. 3.24 to 3.26, that are generally proportional to $\omega \sim D^d/A^2$ [31, 91, 94, 95, 144, 149].

3.4.2 Extension to multirate mass transfer

Although several experimental results show an equivalence between both modelling approaches [142], a few authors are relatively mitigated regarding the general applicability of single-rate models [9, 86, 87]. Haggerty and Gorelick [91] extended the single-rate model to a multirate solute transport equation

$$\frac{\partial C_m}{\partial t} + \sum_{i=1}^{N} \nu_i \frac{\partial (C_{im})_i}{\partial t} = -v \frac{\partial C_m}{\partial x} + D_L \frac{\partial^2 C_m}{\partial x^2} \tag{3.27}$$

with N additional equations

$$\frac{\partial (C_{im})_i}{\partial t} = \omega_i \left(C_m - (C_{im})_i \right) \quad i = 1 \ldots N \tag{3.28}$$

In this case, $\nu_i = \frac{(\theta_{im})_i}{\theta_m}$ includes the volumetric proportion of immobile zone i. In case ω is continuously distributed, the sum in Eq. 3.27 must be replaced by an integral [193]. Haggerty and Gorelick [91] demonstrated the equivalence between diffusion and multirate models by deriving a series solutions for ω_i and ν_i that could match diffusion models. Moreover, multirate mass transport models were recently shown to be equivalent to temporal CTRW [49, 61, 167].

In the case of single-rate exchange, Eq. 3.22 can also be expressed as [167]

$$\frac{\partial C_{im}}{\partial t} = f(t) * C_m + f(t) \left(C_m(x,0) - C_{im}(x,0) \right) \tag{3.29}$$

where $f(t) = \omega e^{-\omega t}$ is a memory function and $*$ denotes convolution. Haggerty et al. [92] showed that the memory function can take many forms, considering various diffusion models or multirate exchange with various exchange rate distributions. In the latter case, $f(t)$ is a sum of exponential functions, each corresponding to a single rate. Haggerty et al. [92] used the properties of the memory function to discern between single- and multirate transport by considering the late-time behavior of breakthrough curves. For single-rate exchange between mobile and immobile zones, late-time behavior is governed by a single exponential in time, and the plot of $\log(C)$ versus time should be linear for $t >> \langle t \rangle$ (Fig. 3.9). In the case of multirate mass transport, late-time behavior is governed by a sum of exponential, that are actually equivalent to an algebraic tail. Therefore, the plot of $\log(C)$ versus $\log(t)$ should be linear for $t >> \langle t \rangle$ (Fig. 3.10). Figs. 3.9 and 3.10 were produced using the software STAMMT-L [93] for a Dirac injection of a unit mass of tracer, considering a similar situation as previous figures. $\theta_m/\theta = 0.5$ for the non-equilibrium cases and $Da = 1$ for single-rate transport. Multirate transport was solved considering a log-normal distribution of exchange rates, with a mean corresponding to $Da = 1$ and a standard deviation of 3. Results are shown for the mobile phase only.

3.5 Conclusion

In this chapter, potential alternatives to the ADE are reviewed. Higher-order partial differential equations are not found to be valuable options due to their
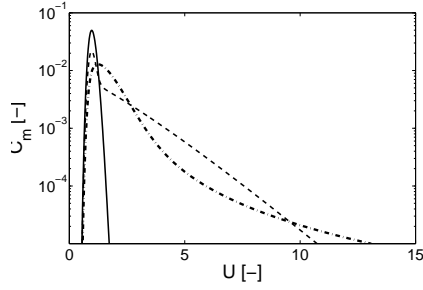
Figure 3.9: Influence of immobile phase and exchange rate distribution on transport. Single-porosity media (solid line), dual-porosity media with single rate exchange (dashed line) and dual-porosity media with multiple rate exchange (dot-dashed line). Linear late-time behavior of the single rate system.
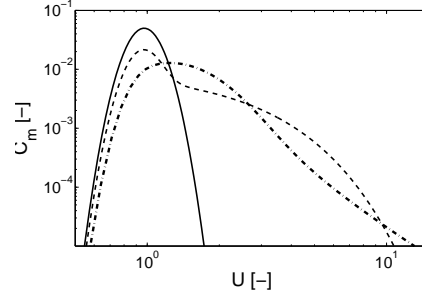
Figure 3.10: Influence of immobile phase and exchange rate distribution on transport. Single-porosity media (solid line), dual-porosity media with single rate exchange (dashed line) and dual-porosity media with multiple rate exchange (dot-dashed line). Linear late-time behavior of the multiple rate system.

increased complexity, but telegraph equations could be more appropriate. CT-RW and fractional-order partial differential equations have been recently brought to the field of hydrogeology and, although requiring a relatively unusual mathematical formalism, could also be more appropriate to model solute transport. Finally, MIM are found to be a third class of transport equations that could also account for non-Fickian effects in dispersive processes.

Chapters 2 and 3, far from being exhaustive in the review of solute dispersion models in heterogeneous media, give an insight into some of the main explanations to scale-dependent dispersion. One may however wonder which approach is best : using more complex non-Fickian mathematical transport models, or going along with the classical ADE and using upscaled parameters in order to simulate super-Fickian dispersion ? Peters and Smith [145] showed that non-Fickian models such as the one suggested by Hassanizadeh [98] could be efficiently approximated using the ADE with a spatially varying dispersivity. In the next chapters of this dissertation, this issue will be investigated through various solute transport problems, allowing upscaling methodologies to be confronted to each other.

Part II

Application to synthetic examples

Chapter 4

Methods of analysis

4.1 Introduction

In Part 1, a set of upscaling methods for apparent dispersivity and a set of upscaled transport models have been reviewed. In Part 2, it is proposed to apply them to synthetic numerical examples, in order to test them under various conditions of heterogeneity. In Part 3, using observations and conclusions from Part 2, a laboratory experiment will be designed and performed to test methods and models under real conditions. This will allow one to verify whether conclusions drawn from synthetic cases can be extended to physical situations (at least at the laboratory scale) and to identify other processes that could potentially complicate upscaling.

Application of upscaling methods and transport equations proceeds in two steps. First, an appropriate set of transport parameters has to be determined based on given available data. As the aim of this study is to assess model upscaling capacities, only information obtained at a local scale is used for this purpose. Then, methods and models are used in a forward mode, to predict apparent dispersivity and concentration distributions at a larger scale. Analytical solutions of forward models have already been presented and illustrated in Chapter 2 and Chapter 3. It is proposed to introduce in this chapter inverse modelling methods that will be used to estimate transport parameters. The general methodology adopted to compare methods and models will also be presented here.

As a large number of different cases are investigated in the sequel, the comparison of methods and models cannot rely on qualitative observations, and numerical indicators are defined in Section 4.2 to quantify the efficiency of upscaling. In particular, one indicator focuses on apparent dispersivity. As the latter cannot be directly measured, methods to determine longitudinal dispersivity from concentration distributions are introduced in Section 4.3.

Upscaling methods for dispersivity are based on descriptions of heterogeneity. The stochastic method uses a geostatistical description of soil heterogeneity (variance and correlation length) that can be obtained by variogram analysis [28]. As this type of method is relatively common and as an important part of investigated numerical examples uses lognormal permeability fields, that are created based on a known set of geostatistical parameters, geostatistical characterization methods are not recalled in this dissertation. Similarly, inclusion models are based on a description of soil heterogeneity that is also theoretically known when creating the corresponding synthetic cases. Therefore, only a method to obtain a measure of the fractal dimension of random fields will be

presented in Section 4.4.1.

A general method to parametrize a transport equation using concentration data is bulk curve-fitting. However, this method cannot always be used as analytical solutions may not be available and as accurate numerical solutions may take time to be processed. Moreover, data series may not be sufficiently informative to estimate the whole set of transport parameters. This leads to the need for other methods. In Section 4.4.2, a method to estimate parameters to be used in Scheidegger's telegraph equation is presented. This method is only applicable to perfectly stratified cases and uses a modal decomposition of the permeability profile. In Section 4.4.3, methods to parametrize temporal and spatial CTRW are presented. Unlike other methods presented in this chapter, they are not based on permeability spatial distribution but use concentration data. Mobile-immobile models will only be used in Part 3 for a limited portion of the analysis, and will therefore not be presented here. Other models (i.e. third- and fourth-order equations and other telegraph equations) will not be investigated due to their expected limited applicability.

4.2 Comparison of models

For the sake of generality, models will be compared in relatively simple conditions : only one-dimensional flow and transport problems will be investigated. The quality of model predictions will be evaluated from two different points of view, using two different indicators. First, only transient apparent dispersivity will be examined. Actual values will be compared with theoretical predictions using the average value of the relative difference between observed and predicted dispersivity, called here ϵ_u

$$\epsilon_u = \frac{1}{N} \sum_{i=1}^{N} \frac{|\alpha^*_{L,i,th} - \alpha^*_{L,i,exp}|}{\alpha^*_{L,i,exp}} \tag{4.1}$$

where subscript u stands for *upscaling*, N is the number of data points in the apparent dispersivity curve, $\alpha^*_{L,i,th}$ are predicted values of macrodispersivity and $\alpha^*_{L,i,exp}$ are experimental values (obtained either from a numerical or a physical experiment). In order to evaluate whether discrepancies are due to an unadapted model or to unadapted parameter values, a coupled indicator ϵ_c will be defined similarly to ϵ_u

$$\epsilon_c = \frac{1}{N} \sum_{i=1}^{N} \frac{|\alpha^*_{L,i,th,opt} - \alpha^*_{L,i,exp}|}{\alpha^*_{L,i,exp}} \tag{4.2}$$

where subscript c stands for *characterization* and where $\alpha^*_{L,i,th,opt}$ is the prediction of macrodispersivity obtained by least-square fitting of the corresponding analytical solution to the experimental curve. A value of ϵ_c smaller than ϵ_u would highlight that better inverse methods could yield more adapted transport parameters. On the contrary, $\epsilon_c \approx \epsilon_u$ would reveal adequate characterizing methods, as obtained transport parameters would allow a correct prediction of macrodispersivity.

Then, the global prediction of concentration distributions will be quantified using the root-mean-square of the difference between experimental and predicted concentration. The improvement resulting from the use of a non-Fickian model will be evaluated using the ΔRMS_u indicator, defined as

$$\Delta RMS_u = RMS_{nF,u} - RMS_F \tag{4.3}$$

where $RMS_{nF,u}$ corresponds to the root-mean-square of the difference between experimental BTC and non-Fickian prediction. RMS_F is a similar indicator that involves the solution of the ADE. These indicators are computed according to

$$RMS = \sqrt{\frac{1}{N} \sum_{i=1}^{N} \left(C_{i,th} - C_{i,exp}\right)^2} \tag{4.4}$$

where N is the number of data points available for the BTC of interest, $C_{i,th}$ are theoretical concentration values (computed either from the Fickian or from a non-Fickian model) and $C_{i,exp}$ are experimental concentration values. A negative value of ΔRMS_u indicates that the non-Fickian model yields a better fit to experimental data, whereas a positive value indicates that the classical advection-dispersion equation provides better results. If concentration are expressed relative to injection value, RMS indicators vary between 0 and 1, so that ΔRMS varies between -1 and 1. A ΔRMS_c indicator will also be used as a measure of the best achievable results for non-Fickian models.

4.3   Determination of apparent dispersivity

Different methods are available in order to determine effective dispersion coefficients based on concentration distributions in time or in space. These methods include curve-fitting methods and moments methods. Curve-fitting methods are very versatile methods and can be used either with analytical or with numerical solutions, allowing one to infer transport parameter values even for highly complex flow systems. They also allow one to obtain an estimation of parameter uncertainty. They are however rather artificial and may depend on the optimization algorithm and the convergence criteria that is used.

Instead, moments method only rely on a statistical analysis of the concentration distribution. For simple (one-dimensional) systems, an analytical solution is generally available for these statistics and transport parameters are obtained by inverting that solution. Aris [5] first introduced this method to analyze solute dispersion in fluids flowing through tubes. In this study, both temporal and spatial concentrations will be considered, as it will be shown that their results might sensitively differ.

4.3.1   Temporal moment analysis

Temporal moments are defined according to [43]

$$\mu_i(x,y,z) \quad = \quad \int_{t=0}^{\infty} t^i C(x,y,z,t)dt \tag{4.5}$$

$$\langle t(x,y,z)\rangle \quad = \quad \frac{\mu_1(x,y,z)}{\mu_0(x,y,z)} \tag{4.6}$$

$$\mu_i^c(x,y,z) \quad = \quad \int_{t=0}^{\infty} (t - \langle t(x,y,z)\rangle)^i C(x,y,z,t)dt \tag{4.7}$$

where μ_i and μ_i^c are respectively i^{th} non-central and central temporal moments. Multiplying the advection dispersion equation (Eq. 1.5) by t^i and integrating it allow one to obtain governing equations for temporal moments. These equations can be solved for a specific set of initial and boundary conditions, in order to quantify the link between the shape of a given breakthrough curve and effective transport parameters at measurement location.

For example, temporal moments of the one-dimensional ADE (Eq. 1.6) in the case of a Dirac-type injection applied to a sample submitted to a mean gradient in its longitudinal direction are [114, 119, 200]

$$\langle t\rangle \quad = \quad \frac{x}{\hat{v}} \tag{4.8}$$

$$\frac{\mu_2^c}{\mu_0} \quad = \quad \left(\frac{x}{\hat{v}}\right)^2 \frac{2\hat{D}_L^*}{\hat{v}x} \tag{4.9}$$

where $\hat{\ }$ indicate estimated parameters and where it was assumed that injection and measurement were both performed in flux-mode (first-type injection boundary condition). These expressions can be easily inverted to obtain transport parameters on the basis of temporal moments

$$\hat{v} \quad = \quad \frac{x}{\langle t\rangle} \tag{4.10}$$

$$\hat{D}_L^* \quad = \quad \frac{\mu_2^c}{\mu_0}\frac{x\hat{v}}{2\langle t\rangle^2} \tag{4.11}$$

and apparent dispersivity is computed using

$$\hat{\alpha_L^*} = \frac{\hat{D}_L^* - D^d}{\hat{v}} - \alpha_L \tag{4.12}$$

In the case of a one-dimensional step input of concentration, temporal moments become infinite. Yu et al. [200] propose to solve that issue by exploiting the link between the Dirac function $\delta(t - t_0)$ and the Heaviside distribution (step variation function) $u(t - t_0)$

$$\frac{d\left[u(t - t_0)\right]}{dt} = \delta(t - t_0) \tag{4.13}$$

The ADE is a linear model for concentrations. If two sources terms are related by a linear operator, outputs are similarly related. So, if C_1 is the breakthrough

curve recorded at a given location in response to a step input and C_2 is the breakthrough curve at the same location in response to a Dirac delta input, then C_1 and C_2 are related by

$$\frac{\partial C_1}{\partial t} = C_2 \tag{4.14}$$

and time moments for C_1 can be calculated from those of C_2

$$\langle t \rangle = \frac{\int_{t=0}^{\infty} t \frac{\partial C_1}{\partial t} dt}{\int_{t=0}^{\infty} \frac{\partial C_1}{\partial t} dt} = \int_0^1 t \, dC_1 \tag{4.15}$$

$$\mu_2^c = \int_{t=0}^{\infty} (t - \langle t \rangle)^2 \frac{\partial C_1}{\partial t} dt = \int_0^1 (t - \langle t \rangle)^2 \, dC_1 \tag{4.16}$$

with, for a unit step injection,

$$\int_0^1 dC_1 = 1 \tag{4.17}$$

These moments can be used with Eqs. 4.10 and 4.11 to predict transport parameters based on cumulative BTC. Leij and Dane [119] proposed another method to analyze cumulative BTC, using the complementary relative concentrations $1 - C(t)$, but had to derive specific analytical solutions for temporal moments.

4.3.2 Spatial moment analysis

The same way time averaging techniques have been applied to calculate temporal moments, spatial averaging techniques can also be applied in order to obtain expressions for spatial moments. Zeroth, first and second moments are defined by [43]

$$m_0(t) = \int_V C(x, y, z, t) dV \tag{4.18}$$

$$m_i(t) = \int_V x_i C(x, y, z, t) dV \tag{4.19}$$

$$m_{ij}(t) = \int_V x_i x_j C(x, y, z, t) dV \tag{4.20}$$

The zeroth moment $m_0(t)$ is the total mass of solute in the flow domain. The jth component of the first moment represents the position of the center of gravity of a particle cloud $\langle x_j \rangle$ along the jth direction, times the total mass of solute. Mostly, second non-central moments are not used, and second central moments are used instead

$$m_{ij}^c(t) = \int_V (x_i - \langle x_i \rangle)(x_j - \langle x_j \rangle) C(x, y, z, t) dV \tag{4.21}$$

They describe the amount of spreading of a solute plume around its center of gravity.

Instead of using Eq. 1.5 with given initial and boundary conditions, more general auxiliary conditions can be used : it can be assumed that concentration C decreases at least exponentially in the large-distance limit. Additionnally, a known initial concentration distribution that satisfies the auxiliary conditions must be defined. A valid condition would be a bounded volume with a fixed concentration within an infinite domain [43]. Integrating Eq. 1.5 under these conditions over the entire flow domain leads to a governing equation for the zeroth-moment, that can be written under the form

$$\frac{\partial m_0}{\partial t} = 0 \qquad (4.22)$$

The latter expresses conservation of solute mass, as no decay was accounted for in Eq. 1.5. Similarly, multiplying Eq. 1.5 by x_i and integrating it over the spatial domain allow one to obtain governing equations for first-order spatial moments

$$\frac{\partial m_i}{\partial t} = v_i m_0 \qquad (4.23)$$

stating that the center of gravity of a particle cloud moves at a constant velocity $\mathbf{v}$ through the whole domain. Finally, multiplying the ADE by $(x_i - \langle x_i \rangle)(x_j - \langle x_j \rangle)$ and integrating it leads to governing equations for second central moments

$$\frac{\partial m_{ij}^c}{\partial t} = 2D_{ij}^* m_0 \qquad (4.24)$$

The latter expresses that the dispersion tensor equals half the rate of change of the second central moment, normalized by total mass.

In the case of a step variation in concentration at injection, auxiliary conditions are not verified and it is not possible to apply this method. The same way Yu et al. [200] proposed to deduce transport parameters from time-moments analysis of temporal gradients of concentration, Landman [118] proposed to evaluate apparent dispersion coefficients from an analysis of the moments of the spatial gradients of concentration. In this case, an effective longitudinal dispersion coefficient can be computed according to

$$D_L(t) = -\frac{1}{2}\frac{\partial I_{xx}}{\partial t} \qquad (4.25)$$

where I_{xx} is the second central spatial moment of the concentration gradient

$$I_{xx} = \int_{-\infty}^{+\infty} \frac{\partial C}{\partial x} (x - \langle x \rangle)^2 \, dx \qquad (4.26)$$

Eqs. 4.22 and 4.23 can be extended to zeroth- and first-order spatial moments of concentration gradients in case of a step input. Mean apparent transport parameters are then computed according to [118]

$$\hat{v} = \frac{1}{t}\int_0^t \frac{1}{m_0}\frac{\partial m_1}{\partial t}dt = \frac{m_1(t) - m_1(0)}{m_0 t} \qquad (4.27)$$

$$\hat{D}_L^* = \frac{1}{t}\int_0^t \frac{1}{2m_0\hat{v}}\frac{\partial m_2^c}{\partial t}dt = \frac{m_2^c(t) - m_2^c(0)}{2m_0\hat{v}t} \qquad (4.28)$$
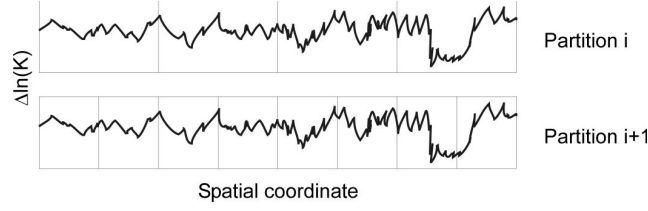
Figure 4.1: Signal partitioning for dispersional analysis

4.4 Parametrization of non-Fickian methods and models

4.4.1 Determination of Hurst coefficient

In this work, dispersional analysis is used to infer values of H [34]. This method involves a three-step procedure. First, a sequence of partitions is considered for the data series to be analyzed (Fig. 4.1). Typically, if a partition i includes N bins of length $2K$, the partition $i + 1$ includes $2N$ bins of length K. Each partition isolates thus a scale of observation. Then, a single-scale statistic is used to characterize data contained in each bin. In a dispersional analysis, the latter is the mean of the variable of interest in each partition. Finally, the standard deviation of the bin means is used as a transcale statistic. H is then obtained as 1 plus the slope of the plot of the log of the transcale statistics versus the log of the number of bins (Figs. 4.2 and 4.3). It must be noted that data series to be analyzed in a dispersional analysis are not $\ln(K)$ values themselves, but their increments $\Delta \ln(K) = \ln(K(x + dx)) - \ln(K(x))$.

In order to reduce bias and variance in estimations of H, Caccia et al. [34] propose to ignore measures from several of the longest bins (e.g. the three longest bins). They also propose to use bin shifting in order to increase accuracy of $\hat{H}$. Multiple estimates of the standard deviation of bin means are obtained from additional partitions resulting from the shifting of partition starting positions. Figs. 4.2 and 4.3 show the results of the analysis of some of the permeability profiles presented in Chapter 5. As data series are relatively short, no bin was dropped and bin shifting was used to increase the number of points to use in the linear regression. Expectively, Hurst coefficients are not influenced by variance (Fig. 4.2) but increase when correlation length increases (Fig. 4.3).

Other methods to estimate Hurst coefficients are spectral analysis [159] and rescale range analysis. Spectral analysis was found to be less reliable and Caccia et al. [34] indicate that dispersional analysis yields better results than rescale range analysis.

4.4.2 Parametrization of Scheidegger's telegraph equation

It was shown in Section 3.2.2 that various telegraph equations could be derived to model solute transport in the soil. Most of them have no practical applicability as they use parameters that are difficult to quantify at the field scale,
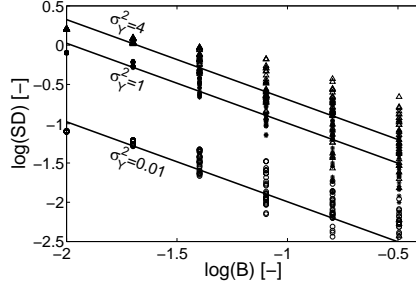
Figure 4.2: Results of the dispersional analysis of stratified examples K_{13}, K_{33} and K_{53}. B is the bin length and SD is the transcale statistic.
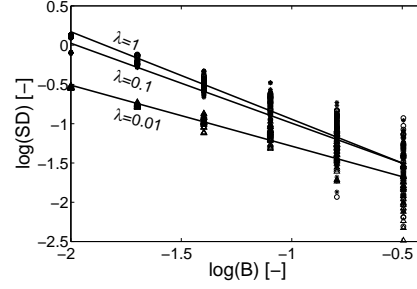
Figure 4.3: Results of the dispersional analysis of stratified examples K_{31}, K_{33} and K_{35}. B is the bin length and SD is the transcale statistic.

or have upscaling properties similar to the ADE. Only Scheidegger's telegraph equation could be more useful, as it incorporates the variance of the velocity field and a correlation time for particle velocities.

Berentsen [20] proposed an upscaling method for Scheidegger's equation by extending the approach of Camacho [35, 36, 37]. The latter was initially aimed to model diffusion of solutes in a flow between parallel plates and was extended to model solute transport in a perfectly stratified porous media. Berentsen [20] started by expanding concentration and velocity in cosine Fourier series

$$C(y,t) = C_0(x,t) + \sum_{n=1}^{\infty} C_n(t) \cos\left(\frac{n\pi y}{h}\right) \tag{4.29}$$

$$v(y,t) = v_0(x,t) + \sum_{n=1}^{\infty} v_n(t) \cos\left(\frac{n\pi y}{h}\right) \tag{4.30}$$

where h is the thickness of the aquifer and subscripts 0 and n respectively refer to fundamental (average) and n^{th} modes of the variable of interest. Longitudinal and transverse dispersion coefficients are then computed from

$$D_L(y) = D^d + \alpha_L\, v(y) = D_{L,0} + \sum_{n=1}^{\infty} D_{L,n} \cos\left(\frac{n\pi y}{h}\right) \tag{4.31}$$

$$D_T(y) = D^d + \alpha_T\, v(y) = D_{T,0} + \sum_{n=1}^{\infty} D_{T,n} \cos\left(\frac{n\pi y}{h}\right) \tag{4.32}$$

Substituting Eqs. 4.29 to 4.32 in the two-dimensional advection-dispersion equation and integrating over the transverse direction, yields a governing equation for transversely averaged concentrations

$$\frac{\partial C_0}{\partial t} = -v_0 \frac{\partial C_0}{\partial x} + D_{L,0} \frac{\partial C_0}{\partial x^2} - \frac{1}{2} \sum_{n=1}^{\infty} \left(v_n \frac{\partial C_n}{\partial x} - D_{L,n} \frac{\partial^2 C_n}{\partial x^2} \right) \tag{4.33}$$

which is similar to the one-dimensional form of the ADE, with an additionnal source term that appeared due to the interaction of longitudinal dispersion,

	$m = n$	$m \neq n$
$\beta_{n,m} =$	$v_{2n}/2$	$\left[v_{m+n} + v_{|m-n|}\right]/2$
$D_{L_{n,m}} =$	$D_{L,0} + D_{L,2n}/2$	$\left[D_{L,m+n} + D_{L,|m-n|}\right]/2$
$D_{T_{n,m}} =$	$(n\pi/d)^2(D_{T,0} + D_{T,2n}/2)$	$nm(\pi/d)^2\left[-D_{T,m+n} + D_{T,|m-n|}\right]/2$

Table 4.1: Definition of modal dispersion coefficients

transverse dispersion and advection in the higher-order modes $n \geq 1$. This term can be interpreted as the spatial derivative of an additional flux term J called *Taylor flux*

$$J = -\frac{1}{2}\sum_{n=1}^{\infty}\left(v_n C_n - D_{L,n}\frac{\partial C_n}{\partial x}\right) \tag{4.34}$$

Similarly, multiplication of the two-dimensional advection-dispersion equation with $\cos(n\pi y/h)$ and integration over the transverse direction gives a constitutive relationship for the nth concentration mode. Due to transverse variations of the dispersion tensor, concentration modes are however coupled with each other, resulting in a system that can be expressed under a matrix form as

$$\frac{\partial C_0}{\partial t} + v_0\frac{\partial C_0}{\partial x} - D_{L,0}\frac{\partial C_0}{\partial x^2} = -\frac{1}{2}\boldsymbol{v}^t\frac{\partial \boldsymbol{C}}{\partial x} + \boldsymbol{d_{L,n}}^t\frac{\partial^2 \boldsymbol{C}}{\partial x^2}$$

$$\frac{\partial \boldsymbol{C}}{\partial t} + (v_0\boldsymbol{I} + \boldsymbol{\beta})\frac{\partial \boldsymbol{C}}{\partial x} + \boldsymbol{D_T}\boldsymbol{C} - \boldsymbol{D_L}\frac{\partial^2 \boldsymbol{C}}{\partial x^2} = -\boldsymbol{v}\frac{\partial C_0}{\partial x} + \boldsymbol{d_{L,n}}\frac{\partial C_0}{\partial x^2} \tag{4.35}$$

where $\boldsymbol{C}$, $\boldsymbol{v}$ and $\boldsymbol{d_{L,n}}$ are a column vectors containing modal concentrations C_n, velocities v_n and longitudinal dispersion coefficients $D_{L,n}$ respectively. $\boldsymbol{I}$ is the unit matrix. Matrices $\boldsymbol{\beta}$, $\boldsymbol{D_T}$ and $\boldsymbol{D_T}$ contain $\beta_{m,n}$, $D_{L_{n,m}}$ and $D_{T_{n,m}}$ terms respectively, computed as expressed in Table 4.1. $\boldsymbol{D_L}$ and $\boldsymbol{D_T}$ are symmetric and have thus real eigenvalues.

In order to obtain a set of uncoupled equations, Berentsen [20] proposed to diagonalise $\boldsymbol{D_T}$ and replace it with

$$\boldsymbol{D_T} = \boldsymbol{T}^t\boldsymbol{\Lambda}\boldsymbol{T} \tag{4.36}$$

where $\boldsymbol{T}$ is a transformation matrix the columns of which are the eigenvectors of $\boldsymbol{D_T}$, and $\boldsymbol{T}^t$ is its transpose. $\boldsymbol{\Lambda}$ is a diagonal matrix containing the eigenvalues λ_n sorted by increasing magnitude. Berentsen [20] showed that $\tilde{\tau}_n = 1/\lambda_n$ is a characteristic time describing the relaxation of mode n to the fundamental mode.

An independent governing equation for each concentration mode could be obtained by applying the transformation matrix to the system in Eq. 4.35. Berentsen [20] showed that, by summing them according to Eq. 4.34, an approximate governing equation for J was given by Eq. 3.1. The effective relaxation time to be used was however found to be time-dependent itself. In order to correctly model apparent dispersion in the long time limit, Berentsen showed

that an appropriate expression for the effective relaxation time was

$$\tau_e = \frac{\sum_{n=1}^{\infty} \tilde{v}_n^2 \tilde{\tau}_n}{\sum_{n=1}^{\infty} \tilde{v}_n^2} \tag{4.37}$$

In that case, apparent dispersion coefficients computed from the second spatial moment of Eq. 3.2 are converging exponentially to their asymptotic value

$$D_L^* = \sigma_v^2 \tau_e \left(1 - \exp\left(-\frac{t}{\tau_e} \right) \right) \tag{4.38}$$

This methodology allows one to link the velocity profile in the case of a perfectly stratified aquifer to the effective relaxation time to be used in the fourth-order model described in Section 3.2 and, more practically, in Scheidegger's telegraph equation. Unfortunately, to the author's knowledge, no such method is available for two- or three-dimensional problems. The effective relaxation time must then be estimated from measured breakthrough curves using curve-fitting methods [163]. It must be finally noted that, as this method is based on a modal analysis and provides an analytical expression for apparent longitudinal dispersivity, it will be also referred to as the modal upscaling method.

4.4.3   Parametrization of CTRW models

Temporally anomalous transport

Berkowitz et al. [23] noted that the probabilistic formulation of tracer distribution used in the CTRW theory was equivalent to that of flux-averaged concentrations. As a consequence, the CTRW formalism could be used to analyze experimental results, and has already been successfully applied to the interpretation of breakthrough curves recorded either at the laboratory scale [26, 27, 174] or in the field [23].

Parameters used to characterize temporally anomalous transport are usually obtained by least-square fitting of one-dimensional analytical solutions to experimental data [23, 26, 27, 174]. The determination of β_t ideally requires at least two sets of concentration measurements at different scales. In this case, β_t can be estimated from the rate of narrowing of the distribution [23, 127]. Moreover, it is also possible to determine whether there is a decrease in tracer velocity or not. In such case, one must have $\beta_t < 1$ and β_t can be determined from the rate of decrease of the velocity [127]. When only a single breakthrough curve is available, β_t can be estimated from the tailing behavior of the distribution.

Margolin and Berkowitz [130] proposed a set of analyzing tools, available under the form of Matlab© functions (http://www.weizmann.ac.il/ESER/People/Brian/CTRW/). These tools will be used in the next part of this study. It must be noted that a Matlab© CTRW toolbox was recently released [45]. It basically extends the flexibility of the functions used in this study by allowing one to choose between different transition rate probability density functions [46]. The functions used in Eqs. 3.14 and 3.15 correspond to the asymptotic model in Eq. 28 of [46].
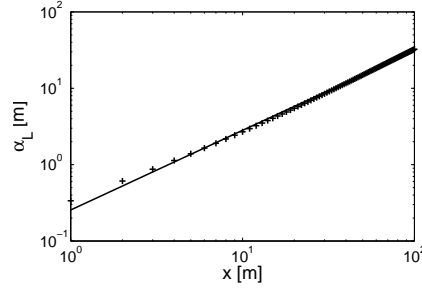
Figure 4.4: Determination of β_x based on the scale-effect. Stratified example K_{44}.

Spatially anomalous transport

This theory was also successfully applied to laboratory and field experiments [16, 18], and Benson et al. [18] proposed a basic methodology to determine β_x and $\mathcal{D}_x$ from breakthrough curve analysis.

First, when plotting apparent dispersivity versus measurement scale on a log-log scale graph (Fig. 4.4), Benson [16] showed that one should obtain a linear curve, with a slope m that is linked to β_x according to

$$\beta_x = \frac{2}{m+1} \tag{4.39}$$

Then, if the breakthrough curves are shifted by the mean travel time and if the temporal scale is divided by t^{1/β_x}, one should obtain a set of curves that are scale-invariant. Figs. 4.5 and 4.6 show the difference between standard Fickian scaling and non-Fickian scaling in the case of a perfectly stratified aquifer (case K_{33} investigated in Chapter 5). Whereas sensitive differences appear between the curves plotted on Fig. 4.5, mostly in the tails of the distributions, a better agreement can be reached by using the proper scaling.

Finally, once the proper scaling is found, $\mathcal{D}_x$ and γ_B can be found by fitting of the solution of Eq. 3.12 to any experimental BTC (as these parameters are scale-invariant). In order to avoid the influence of potential boundary effects, data available at the largest scale will be used for this purpose (i.e. if for example two BTC are used in the inverse modelling process - the first one measured at $x = 1$ m and the second one measured at $x = 10$ m, the latter will be used to compute $\mathcal{D}_x$ and γ_B).

However, Zhou and Selim [205] argue that this methodology may lead to incorrect results, as the use of two separately estimated parameters would not necessary mimic the whole variance of the particle cloud pattern. Instead, they propose to start from the plot of the spatial variance of the particle cloud versus time and propose to fit on this plot a non-linear model of the type $\sigma_C^2 = At^B$, and simultenously relate A and B to β_x and $\mathcal{D}_x$. Theoretically, parameters obtained from joint estimation should model more accurately the variance-time dependence. To assess the validity of their method, Zhou and Selim applied it to the same example as Benson et al. [18] and showed an improvement in the modelling results. However, the variance of the solute particle cloud is a
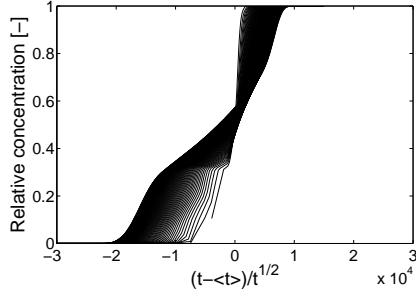
Figure 4.5: Inadequate Fickian scaling of BTC. Stratified example K_{44}.
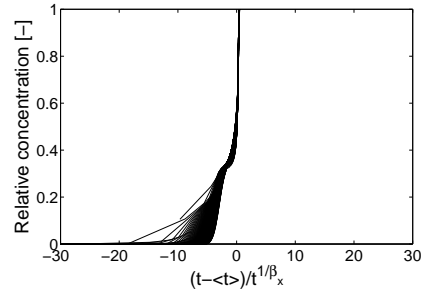
Figure 4.6: Proper non-Fickian scaling of BTC. Stratified example K_{44}.

parameter that cannot be directly obtained from standard tracer tests and the method cannot be used easily. It was moreover found from previous modelling attempts that this method does not allow one to obtain reasonable values of $\mathcal{D}_x$, due to an unadapted sensitivity of the non-linear model [78]. As a consequence, this method will not be used in this study.

4.5   Conclusion

In this chapter, the methodology used to compare upscaling methods and upscaled models in Chapter 5 and Chapter 6 was presented, as well as inverse methods to determine appropriate transport parameters. It will be shown in Chapter 5 and Chapter 6 that the application of these methods to synthetic examples is relatively straightforward, as required information is theoretically available. However, in the case of a physical experiment, it will be shown in Part 3 that the applicability of some of these methods raises issues.

Chapter 5

Solute transport in stratified media

5.1 Introduction

Theoretical models have highlighted the dependence of the dispersive mechanisms of transport in aquifers to the spatial variability of the hydraulic conductivity K. One of the simplest models of heterogeneity is that of stratified formations, for which K only varies in the vertical direction [158]. Natural aquifers often exhibit stratification, both geologically and in the geostatistical sense, leading to considerably smaller correlation lengths along the vertical direction than along the horizontal directions [175]. A perfectly stratified aquifer corresponds to the limiting case where horizontal correlation lengths tend to infinity. Geostatistical tools then only require two parameters to characterize this situation : the vertical correlation length and the variance [79]. The simplicity of this model makes it convenient to explore new theoretical approaches and derive closed-forms analytical solutions [175].

Historically, vertical heterogeneity has been indeed the first type of heterogeneity to be investigated as a possible cause of the scale effect in apparent dispersion, either in deterministic [90, 131, 138, 147] or stochastic [81, 89, 132, 136] approaches.

Naturally, in a first step, this study will focus on this type of heterogeneity as well, in order to (re-)establish the effects of correlation length and variance on apparent dispersivity. In Section 5.2, the geometry of the problem will be presented, as well as numerical values adopted for the structure of the permeability field, numerical tools to be used and, eventually, numerical results in terms of apparent dispersivity will be shown. Then, theories presented in Chapter 2 and 3 will be applied in Section 5.3 and 5.4 respectively. General conclusions on this relatively conceptual case will be finally drawn in Section 5.5. It must be noted that figures and tables that contain secondary information related to this analysis are shown in Appendix B.

5.2 Synthetic examples

5.2.1 Problem description

The synthetic example that will be analyzed in this chapter consists in a perfectly stratified aquifer with a thickness $h = 1$ m (Fig. 5.1). The longitudinal
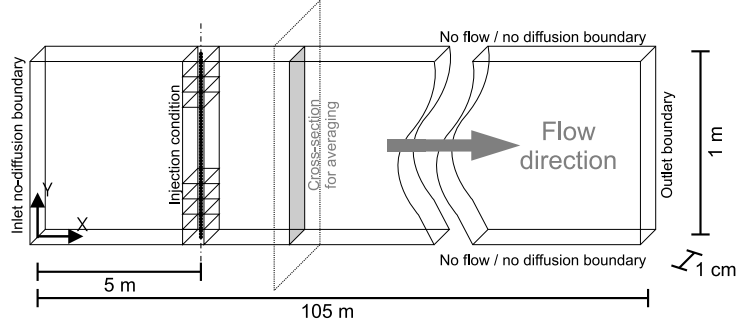
Figure 5.1: Schemtatic representation of the geometry and boundary conditions of perfectly stratified cases (not to scale).

extent of the flow domain is 105 m, and it is discretized in cubic cells of 1 cm long sides (leading to a two-dimensional numerical grid of 1,050,000 cells). The vertical permeability profile is assumed to be random and log-normally distributed (with log referring to the natural logarithm and the permeability being expressed in m/s) with a geometric mean $K_g = \exp(-10)$ and a spatial correlation characterized by

$$\gamma_Y(s) = \sigma_Y^2 \left(1 - \exp\left(-\frac{3|s|}{\lambda} \right) \right) \tag{5.1}$$

where the same notations as in Chapter 2 are used. The factor 3 appearing in the numerator of Eq. 5.1 was introduced so that correlation corresponding to separation gaps larger than λ is negligible (i.e. less than 5 %).

The structure of the log-permeability profile is fully characterized by its variance and its correlation length. Therefore, the influence of these parameters on solute transport can be investigated in a systematic fashion through 25 different permeability profiles. Table 5.1 summarizes the various parameters sets that are adopted for this study. Basically, the variance is ranging from 0.01 to 4 and the correlation length from 0.01 to 1. The case $\lambda = 0.01$ tends to correspond to a totally uncorrelated field, whereas $\lambda = 1$ corresponds to permeability values correlated over the entire aquifer thickness. The fully correlated limit is the case of an aquifer of constant permeability.

Permeability profiles were generated using a spectral method (implemented as a Matlab© routine, available at http://matlabdb.mathematik.uni-stuttgart.de). Profiles were composed of 100 points (according to the grid size) and were extracted from larger data sets (in order to avoid frequency cutoffs when correlation length is large compared to domain size). The sequence of 100 data points to be extracted was chosen so that its corresponding experimental variogram best reproduces the theoretical one. Each profile extracted was afterwards shifted and rescaled so that means and variances effectively correspond to announced values. The same set of random numbers was used for each permeability profile. This means that, once properly scaled, profiles with the same correlation length perfectly surperimpose. Fig. 5.2 shows the corresponding scaled log-permeability profiles. Experimental and theoretical variograms

K_{ij}	$j = 1$	$j = 2$	$j = 3$	$j = 4$	$j = 5$
$i = 1$	$\sigma_Y^2 = 0.01$ $\lambda/h = 0.01$	$\sigma_Y^2 = 0.01$ $\lambda/h = 0.05$	$\sigma_Y^2 = 0.01$ $\lambda/h = 0.1$	$\sigma_Y^2 = 0.01$ $\lambda/h = 0.5$	$\sigma_Y^2 = 0.01$ $\lambda/h = 1$
$i = 2$	$\sigma_Y^2 = 0.1$ $\lambda/h = 0.01$	$\sigma_Y^2 = 0.1$ $\lambda/h = 0.05$	$\sigma_Y^2 = 0.1$ $\lambda/h = 0.1$	$\sigma_Y^2 = 0.1$ $\lambda/h = 0.5$	$\sigma_Y^2 = 0.1$ $\lambda/h = 1$
$i = 3$	$\sigma_Y^2 = 1$ $\lambda/h = 0.01$	$\sigma_Y^2 = 1$ $\lambda/h = 0.05$	$\sigma_Y^2 = 1$ $\lambda/h = 0.1$	$\sigma_Y^2 = 1$ $\lambda/h = 0.5$	$\sigma_Y^2 = 1$ $\lambda/h = 1$
$i = 4$	$\sigma_Y^2 = 2$ $\lambda/h = 0.01$	$\sigma_Y^2 = 2$ $\lambda/h = 0.05$	$\sigma_Y^2 = 2$ $\lambda/h = 0.1$	$\sigma_Y^2 = 2$ $\lambda/h = 0.5$	$\sigma_Y^2 = 2$ $\lambda/h = 1$
$i = 5$	$\sigma_Y^2 = 4$ $\lambda/h = 0.01$	$\sigma_Y^2 = 4$ $\lambda/h = 0.05$	$\sigma_Y^2 = 4$ $\lambda/h = 0.1$	$\sigma_Y^2 = 4$ $\lambda/h = 0.5$	$\sigma_Y^2 = 4$ $\lambda/h = 1$

Table 5.1: $\ln(K)$ field structures adopted for the stratified case

are shown in Appendix B (Fig. B.1). Experimental variograms were computed using BMELib [42]. Correlation lengths larger than the aquifer thickness were not investigated, as corresponding experimental variograms would not have correctly reproduced theoretical ones.

It must be noted that early (stochastic) theories on solute transport in perfectly stratified aquifers generally assume the permeability profile to be described as a normal random variable (instead of a lognormal one), so that effective permeability only depends on the mean of the variable [81, 132]. However, this approach was not adopted in this study as it does not allow the simulation of highly heterogeneous formations, in which a high variance would not ensure the positiveness of the permeability field.

Flow is directly computed from the permeability profile according to Darcy's law, using a constant mean gradient of 1 %. Transport is solved using the particle tracking software RWHet [115]. $100,000$ particles were set evenly along a line passing by the center of the cells at a distance of 5 m from the domain boundary (Fig. 5.1). Assuming that each particle carry a given mass of contaminant, this type of injection corresponds to a Dirac condition. Ideally, in order to avoid numerical boundary effects, injection should be performed at a distance of 4 to 5 correlation lengths away from boundaries [153]. However, in case of a perfectly stratified medium, this criteria cannot be fulfilled as longitudinal correlation length is infinite. Instead, injection was performed at a distance of about $5h$ from the domain boundary.

Effective porosity is 40 %. Local longitudinal and transverse dispersivities are respectively equal to 1 cm and 0.5 mm. Effective molecular diffusion is 10^{-9} m^2/s. It must be emphasized that no ensemble-realizations were performed, as the aim of this study is mainly to understand the upscaling capacities of the various models in particular and well-defined cases.

5.2.2 Apparent longitudinal dispersivity

Cumulative breakthrough curves were obtained by summing the number of particles beyond a control plane located at the longitudinal position of interest (Fig. 5.1). Therefore, concentration are averaged over the full cross-section of
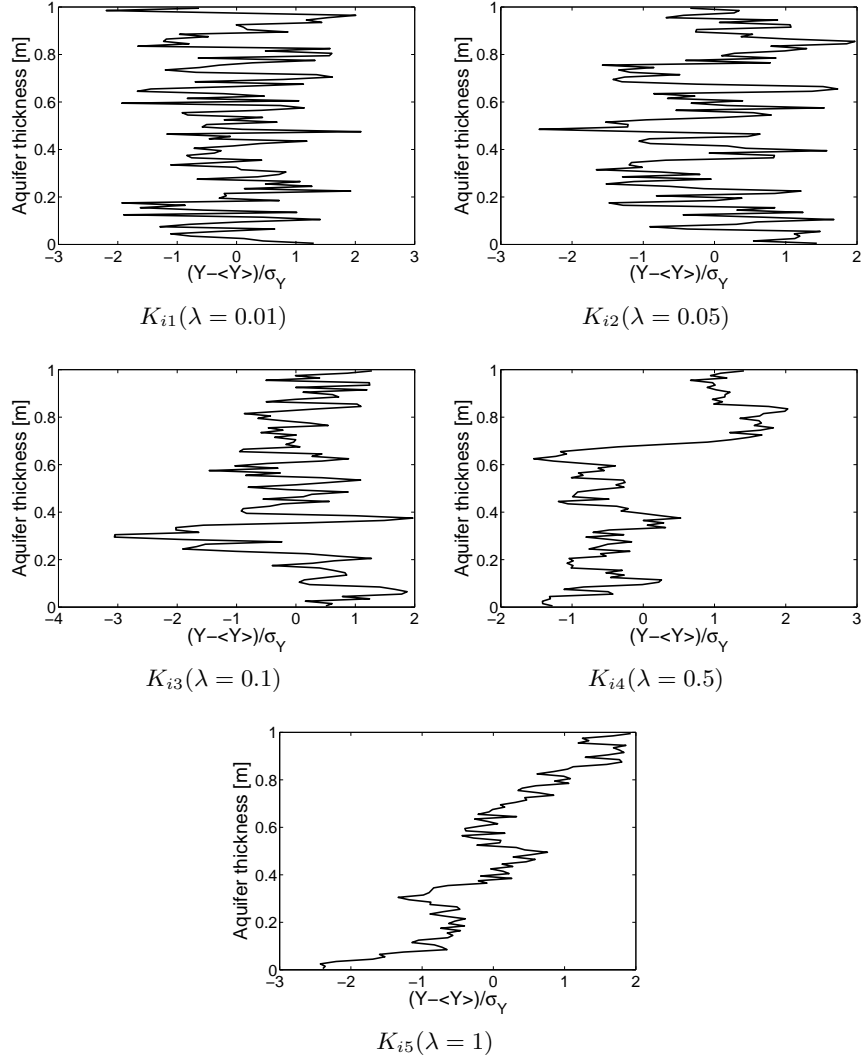
Figure 5.2: Vertical ln(K) profiles adopted for the stratified case.

the flow domain. The method proposed by Yu et al. [200] for step-injections is used to compute apparent transport parameters from temporal moment analysis. Fig. 5.3 shows observed macrodispersivity values for the set of numerical examples considered. Migration velocities are shown in Appendix B (Fig. B.2).

Spatial moments of particle clouds are directly obtained from particle positions at a given time. First-order and second-order central longitudinal spatial moments are computed according to

$$m_1(t) \quad = \quad M \sum_{i=1}^{N} X_i(t) \tag{5.2}$$

$$m_2^c(t) \quad = \quad M \sum_{i=1}^{N} \left(X_i(t) - \langle x \rangle(t)\right)^2 \tag{5.3}$$

where M is the mass of a particle, N is the number of particles, $X_i(t)$ is the longitudinal position of particle i at time t and $\langle x(t) \rangle = m_1(t)/m_0$ is the mean position of the plume, with $m_0 = NM$ the total mass of tracer. Mean migration velocity is computed from Eq. 4.27 and is shown in Appendix B (Fig. B.3). Model boundaries can potentially cause an increase in apparent plume velocity for early times, due to reflected particles on the no-diffusion boundary. For high variance, a small boundary effect can then be observed on Fig. B.3, but the relative difference between initial and asymptotic value of plume velocity remains reasonable.

Apparent longitudinal dispersivities are obtained from Eqs. 4.28 and 4.12, and are illustrated in Fig. 5.4. Macrodispersivity has been rescaled according to Eqs. 2.31 and 2.42. Theoretically, all 25 curves should be surperimposed. This tendency is indeed reasonably observed, except for small correlation lengths. The reason for this is that analytical stochastic results are strictly valid for negligible local dispersivities compared to correlation lengths. When local longitudinal dispersivity is equal to λ, the scaling of α_L^* with respect to variance and correlation length is expected to be more complex. No particular discrepancy appears for high variance (larger than 1) in Fig. 5.4. Data for spatial moments are limited to times for which no particle has exited the flow domain yet. This limitation does not appear in temporal moment analysis.

The most noticeable feature of the curves plotted in Figs. 5.3 and 5.4 is that they do not converge to a constant value (although this could be discussed for a few curves). The question of the convergence to an asymptotic Fickian plume behavior in heterogeneous formations has always remained a widely debated issue, particularly in the case of stratified flow. Whereas Güven et al. [90] implicitly assume that this convergence always exists (through setting the temporal derivative of the second moment of the solute concentration plume to zero for large times), Matheron and de Marsily [132] gave two conditions to ensure convergence : (1) one needs to characterize the velocity field using a hole-effect covariance function, so that the integral of this function is zero and (2) the Laplace transform of the velocity covariance function must behave linearly close to its origin. Typically, these conditions cannot be fulfilled when using an exponential covariance function for the log-permeability field.

Using a modal approach similar to that described in Section 4.4.2, Berentsen

Figure 5.3: Macrodispersivity values obtained from temporal moment analysis. $i = 1$ - $\sigma_Y^2 = 0.01$ (continuous line), $i = 2$ - $\sigma_Y^2 = 0.1$ (dashed line), $i = 3$ - $\sigma_Y^2 = 1$ (dot-dashed line), $i = 4$ - $\sigma_Y^2 = 2$ (small-dotted line) and $i = 5$ - $\sigma_Y^2 = 4$ (large-dotted line). Maximum and minimal values for the $j - 1$ case are also plotted (thin line).
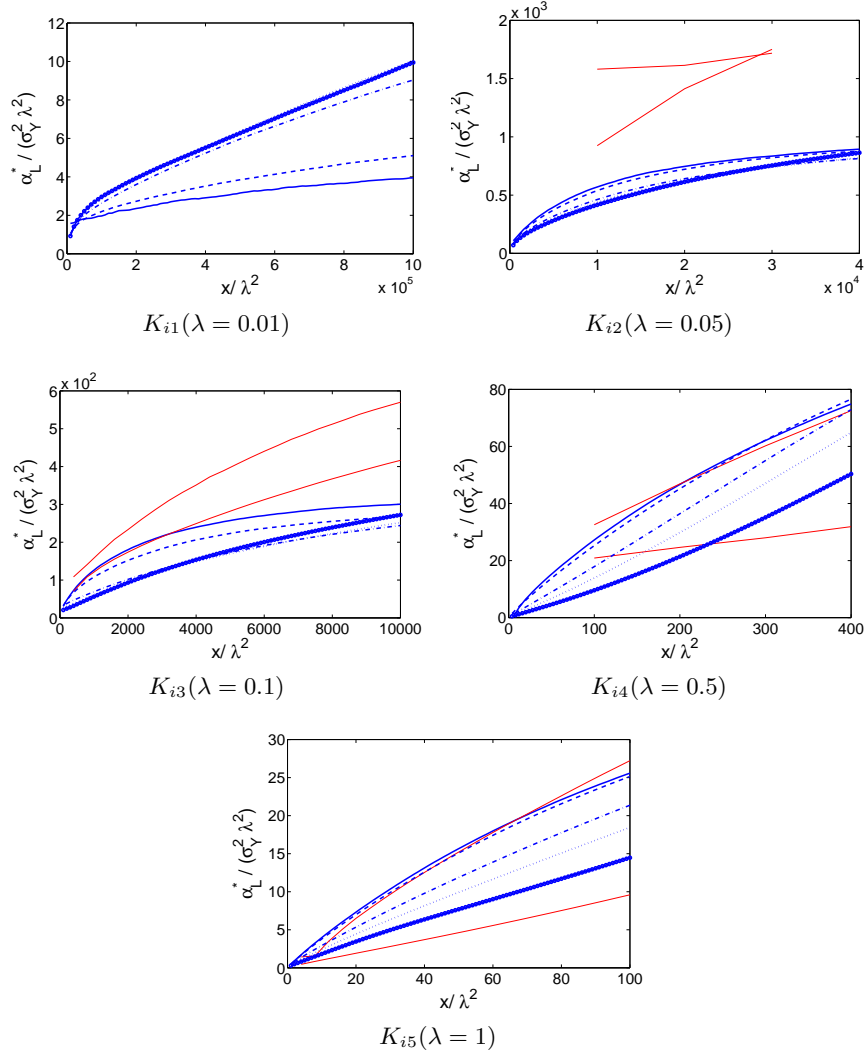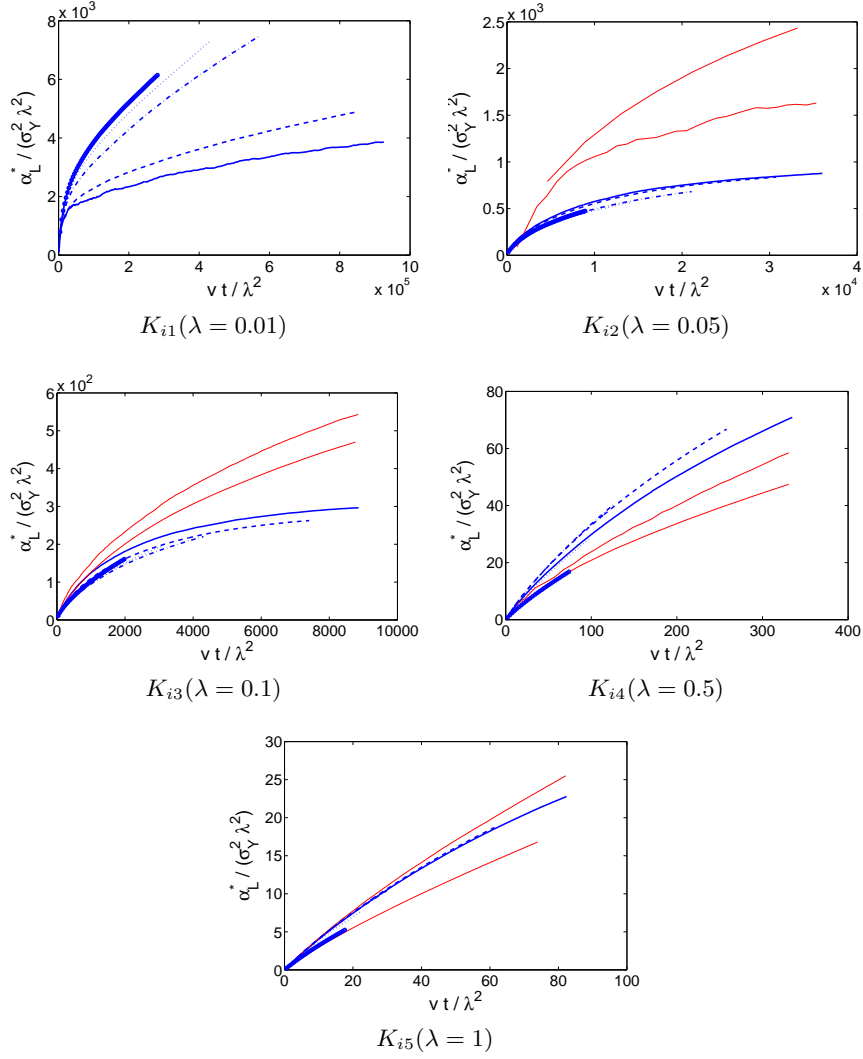
Figure 5.4: Macrodispersivity values obtained from spatial moment analysis. $i = 1$ - $\sigma_Y^2 = 0.01$ (continuous line), $i = 2$ - $\sigma_Y^2 = 0.1$ (dashed line), $i = 3$ - $\sigma_Y^2 = 1$ (dot-dashed line), $i = 4$ - $\sigma_Y^2 = 2$ (small-dotted line) and $i = 5$ - $\sigma_Y^2 = 4$ (large-dotted line). Maximum and minimal values for the $j - 1$ case are also plotted (thin line).

[20] and Berentsen et al. [21] showed that in the case of isotropic hydrodynamical dispersion coefficients (i.e. for low permeability formations, where dispersion can be neglected compared to diffusion), convergence was always ensured. However, in the case of a faster flow, if the ratio of longitudinal versus transverse dispersion becomes too important, no macroscale Fickian behavior can be reached. Peclet numbers characterizing transport systems used in this chapter are relatively high, and hydrodynamic dispersion tensors are anisotropic.

5.3   Upscaling methods for dispersivity

In a first step, one will focus on the predictive modelling of the scale effect in apparent dispersivity. Upscaling methods presented in Chapter 2 will be applied, excepted for the inclusion model, which is typically not suited for this problem as it assumes a two- or three-dimensional flow system. For the sake of brevity, stochastic and fractal methods will be referred to using letters S and F respectively.

   One already expects upscaling methods for longitudinal dispersivity to yield relatively poor results, as they generally predict convergence to a constant asymptotic value of macrodispersivity, whereas numerical values shown on Figs. 5.3 and 5.4 do not exhibit convergence.

5.3.1   Stochastic analysis

The stochastic asymptotic macrodispersivity in Eq. 2.33 was obtained assuming a hole-effect covariance function, but Eq. 2.31 can be used with the actual covariance function corresponding to permeability profiles illustrated on Fig. 5.2. In a first step, experimental variograms were determined for each permeability field, using again BMELib [42]. As numerical values of apparent dispersivity do not converge to an asymptotic constant value and as it was not obvious from experimental data whether a hole-effect variogram was indicated or not, numerical values for variance σ_K^2 and correlation length λ_K were determined by least-square fitting of an exponential covariance model on data (Table B.1). Values are in accordance with the theoretical geostatistical description of the $\ln(K)$ field, as $V_a = \sigma_K^2/\langle K \rangle^2 \approx \sigma_Y^2$ and $\lambda_K \approx \lambda$ (which is supposed to be relatively accurate for low variance and low correlation length).

   In order to compute transient macrodispersivity, Eq. 2.31 was integrated numerically using a trapezoïdal rule, after having substituted the analytical expression of the spectrum of the exponential covariance function

$$S_{KK}(s) = \frac{\sigma_K^2 \lambda_K}{3\pi \left(1 + \frac{\lambda_K^2 s^2}{9} \right)} \tag{5.4}$$

Upscaling results from the stochastic approach are expressed in terms of the ϵ_u indicator, shown in Figs. 5.5 and 5.6 and in Table B.1. As molecular diffusion is not included in Eq. 2.31, the effective local transverse dispersivity was taken equal to $\alpha_T + D^d/v$.
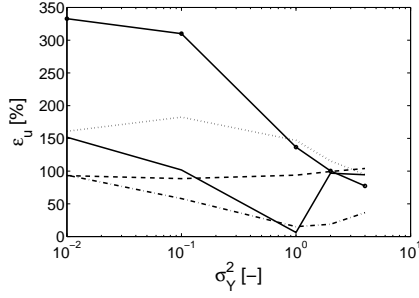
Figure 5.5: Efficiency of S. $\lambda = 0.01$ (continuous line), $\lambda = 0.05$ (dashed line), $\lambda = 0.1$ (dot-dashed line), $\lambda = 0.5$ (small-dotted line) and $\lambda = 1$ (large-dotted line).
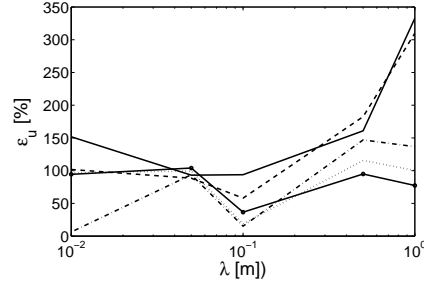
Figure 5.6: Efficiency of S. $\sigma_Y^2 = 0.01$ (continuous line), $\sigma_Y^2 = 0.1$ (dashed line), $\sigma_Y^2 = 1$ (dot-dashed line), $\sigma_Y^2 = 2$ (small-dotted line) and $\sigma_Y^2 = 4$ (large-dotted line).

A precision of 100 % seems to be a representative value for the stochastic upscaling method. Predicted and actual apparent longitudinal dispersivities thus usually differ by a factor of 2, which could be found relatively reasonable regarding the overall practical difficulty of finding a meaningful apparent value different from one tenth of the spatial scale. ϵ_u was also computed using $V_a = \sigma_Y^2$ and $\lambda_K = \lambda$, but no sensitive difference could be observed.

A first observation is that the method does not yield poorer results for high-variance cases. Typically, stochastic methods are said to be best applicable when $\sigma_Y^2 < 1$. Higher variance values usually yield flow domains containing stagnant zones, resulting in heavy-tailed transport processes (see Section 5.4). Although these processes cannot be modelled using a stochastic approach, longitudinal dispersivity appears to be reasonably upscalable. Whether this result is case-dependent or can be generalized to every high-variance perfectly stratified aquifer could be confirmed e.g. by a Monte Carlo analysis.

The second main noticeable feature of the curves on Figs. 5.5 and 5.6 is that higher discrepancies occur for $\lambda = 1$. Stochastic analysis requires the ergodic condition to be fulfilled, so that the statistical characterization of the structure can be performed based on spatial averages. Typically, the ergodic condition is fulfilled provided that the flow domain is at least 5 to 10 times larger than the correlation length, which is obviously not the case when $\lambda = h$.

Least-square fitting was then used to determine optimal values for V_a and λ_K. The fitting indicator ϵ_c ranges between 1 and 7 % (Table B.2), meaning that stochastic models can properly characterize the scale effect in apparent dispersion. Optimal values for geostatistical parameters are shown in Figs. 5.7 and 5.8. The adimensional variance V_a is always found too high compared to its optimal value $V_{a,opt}$. On the contrary, there is no clear tendency for correlation lengths, but higher discrepancies are observed. This is linked to the higher uncertainty on correlation lengths. Whereas variogram analysis can usually yield reliable variance values, confidence on correlation lengths obtained using this method is indeed known to be lower, due to variogram scatter [28].

Finally, ΔRMS_u (Fig. 5.9) was computed using the solution of the clas-
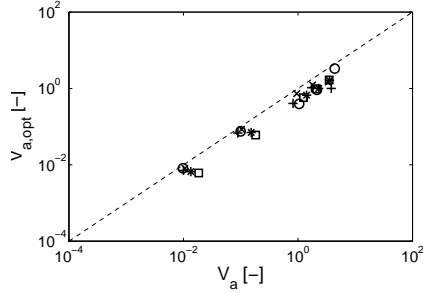
Figure 5.7: Optimal variance required by S. $\lambda = 0.01$ (circle), $\lambda = 0.05$ (x-mark), $\lambda = 0.1$ (plus), $\lambda = 0.5$ (star) and $\lambda = 1$ (square).

Figure 5.8: Optimal correlation length required by S. $\sigma_Y^2 = 0.01$ (circle), $\sigma_Y^2 = 0.1$ (x-mark), $\sigma_Y^2 = 1$ (plus), $\sigma_Y^2 = 2$ (star) and $\sigma_Y^2 = 4$ (square).

sical ADE with upscaled values of longitudinal dispersivity. This indicator is found to be negative most of the time (except for K_{11}), demonstrating that the method brings an improvement. The slope of the curves in Fig. 5.9 is found to be monotonic, except in a few low variance cases where the stochastic method probably exaggerates apparent dispersivity, leading to worse result than the ADE with local parameters. For other cases, as long as the observation scale increases, whatever be the level of heterogeneity, the stochastic method continues to yield better results than the ADE. ΔRMS_c (Fig. B.4) was computed using optimal transport parameters given in Table B.2, but only a slight improvement could be observed compared to ΔRMS_u.

5.3.2   Fractal methods

To determine Hurst coefficients, a dispersional analysis was performed using bin shifting. As the number of data to be processed must be a power of 2, 36 sets of 64 consecutive data were extracted from the original 100 points K fields. Dispersional analysis was performed on each of these 36 data sets and all of them were incorporated at the same time in the linear regression required to estimate H. Fig. 5.10 shows the values of the Hurst coefficient, as well as their corresponding 95 % confidence interval. Results are relatively consistent, as H tends to increase with λ. However, negative H values found for small λ have no physical significance. The best realistic value of H for $\lambda = 0.01$ is 0, which corresponds to a totally uncorrelated field. In the case $\lambda = 0.1$, one could reasonably assume that an appropriate H value lies in the positive part of the confidence interval.

Zhan and Wheatcraft [201] indicate that, in the case of a perfectly stratified medium, L_m simply corresponds to the aquifer thickness. As molecular diffusion is not included in Eqs. 2.42 and 2.43, effective local transverse dispersivity was again taken equal to $\alpha_T + D^d/v$.

Figs. 5.11 and 5.12 show the values obtained for ϵ_u using results from dispersional analysis. For $\lambda = 0.01$ and $\lambda = 0.1$, the fractal method does not predict any scale effect in apparent dispersivity. For smaller correlation lengths,

Figure 5.9: Improvement of S compared to the classical ADE. $i = 1$ - $\sigma_Y^2 = 0.01$ (continuous line), $i = 2$ - $\sigma_Y^2 = 0.1$ (dashed line), $i = 3$ - $\sigma_Y^2 = 1$ (dot-dashed line), $i = 4$ - $\sigma_Y^2 = 2$ (small-dotted line) and $i = 5$ - $\sigma_Y^2 = 4$ (large-dotted line).
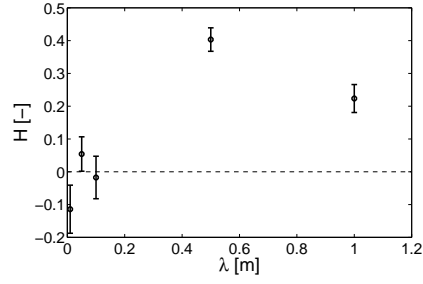
Figure 5.10: Hurst coefficient H as a measure of $\ln(K)$ correlation.
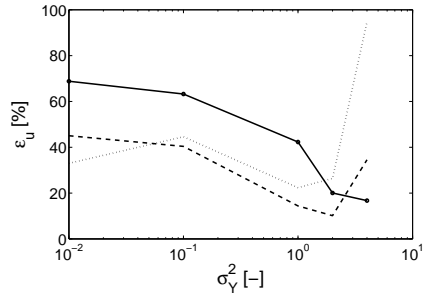
Figure 5.11: Efficiency of F. $\lambda = 0.05$ (dashed line), $\lambda = 0.5$ (small-dotted line), $\lambda = 1$ (large-dotted line). ϵ_u for $\lambda = 0.01$ and $\lambda = 0.1$ is 100 %.

Figure 5.12: Efficiency of F. $\sigma_Y^2 = 0.01$ (continuous line), $\sigma_Y^2 = 0.1$ (dashed line), $\sigma_Y^2 = 1$ (dot-dashed line), $\sigma_Y^2 = 2$ (small-dotted line) and $\sigma_Y^2 = 4$ (large-dotted line).
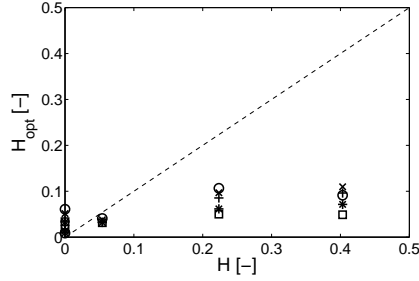
Figure 5.13: Optimal Hurst coefficient required by F. $\sigma_Y^2 = 0.01$ (circle), $\sigma_Y^2 = 0.1$ (x-mark), $\sigma_Y^2 = 1$ (plus), $\sigma_Y^2 = 2$ (star) and $\sigma_Y^2 = 4$ (square).
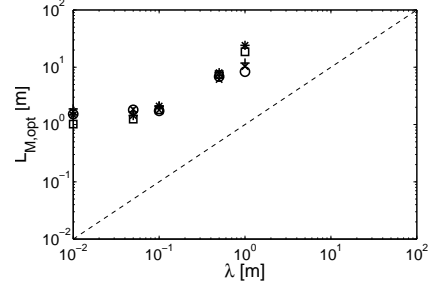
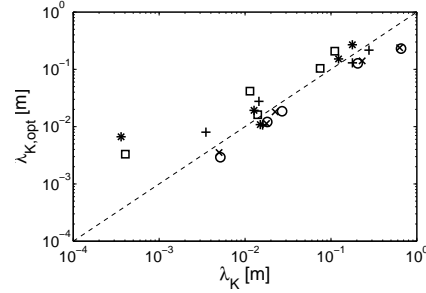**Figure 5.14:** Optimal L_m value required by F. $\sigma_Y^2 = 0.01$ (circle), $\sigma_Y^2 = 0.1$ (x-mark), $\sigma_Y^2 = 1$ (plus), $\sigma_Y^2 = 2$ (star) and $\sigma_Y^2 = 4$ (square).

correlation is almost zero and cannot be detected using dispersional analysis. However, correlation exist as a scale effect could be detected in apparent longitudinal dispersivity. In the case $\lambda = 0.1$, the error simply lies in the estimation of H. For larger correlation lengths, better results than the stochastic method are achieved, as the mean value of ϵ_u is about 40 %.

H and L_m were also determined by fitting of Eq. 2.43 on the curves in Fig. 5.4. Results for all stratified examples are shown in Figs 5.13 and 5.14 and are summarized in Table B.3. The ϵ_c indicator lies between 0.1 and 7 %, meaning that the model could be well-suited, provided better characterization methods are available for H and L_m. Optimal Hurst coefficients H_{opt} are relatively low and do not reach values obtained from dispersional analysis. They however tend to increase with correlation length, as already observed from analysis of K fields.

The question of the physical meaning of L_m is also raised, as Zhan and Wheatcraft [201] state that it is linked to a physical boundary of the flow domain. L_m is found to sensitively vary over the range of investigated examples, which are all characterized by a similar flow domain. L_m tends to increase both with variance and correlation length, and does not seem to be representative of a geometrical feature of the problem.

ΔRMS_u (Fig. 5.15) and ΔRMS_c (Fig. B.5) were computed using the solution of the ADE with upscaled values of longitudinal dispersivity. When Hurst coefficient is found to be equal to zero, no scale effect is predicted and ΔRMS_u is equal to zero as well. Global trends are similar to what was observed for the stochastic method. However, results seem to be of slightly worse quality, as ΔRMS_u (absolute) values are smaller here.

5.4 Application of upscaled transport equations

In this section, one will focus on the modelling of the full observed breakthrough curves, using upscaled transport equations. Theories presented in Chapter 3 will be applied and compared to numerical results. First, Scheidegger's telegraph equation will be tested in Section 5.4.1. CTRW models will then be evaluated in

$K_{i2}(\lambda = 0.05)$
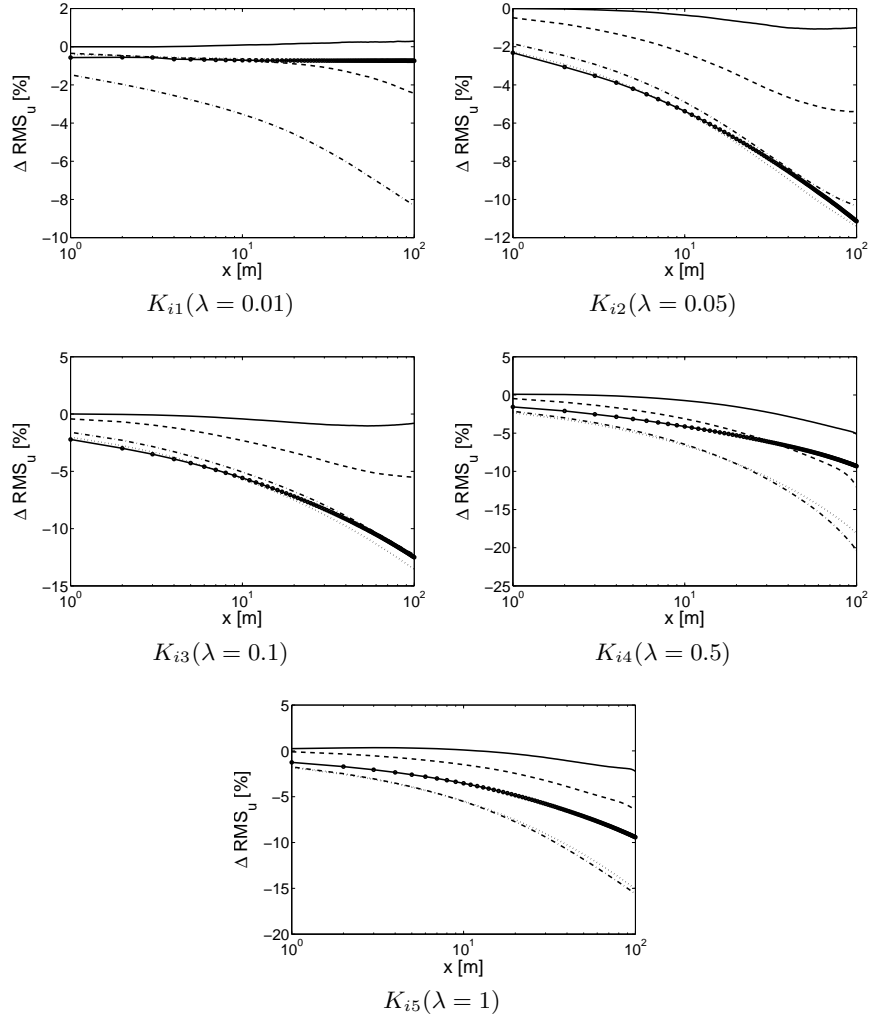
$K_{i4}(\lambda = 0.5)$

$K_{i5}(\lambda = 1)$

Figure 5.15: Improvement of F compared to the classical ADE. $i = 1$ - $\sigma_Y^2 = 0.01$ (continuous line), $i = 2$ - $\sigma_Y^2 = 0.1$ (dashed line), $i = 3$ - $\sigma_Y^2 = 1$ (dot-dashed line), $i = 4$ - $\sigma_Y^2 = 2$ (small-dotted line) and $i = 5$ - $\sigma_Y^2 = 4$ (large-dotted line).

K_{ij}	$j = 1$	$j = 2$	$j = 3$	$j = 4$	$j = 5$
$i = 1$	$\lambda_e = 2.96$ $\epsilon_u = 914.9$	$\lambda_e = 2.70$ $\epsilon_u = 81.6$	$\lambda_e = 2.23$ $\epsilon_u = 34.7$	$\lambda_e = 24.9$ $\epsilon_u = 119.1$	$\lambda_e = 31.9$ $\epsilon = 64.4$
$i = 2$	$\lambda_e = 2.07$ $\epsilon_u = 519.9$	$\lambda_e = 2.88$ $\epsilon_u = 105.4$	$\lambda_e = 2.95$ $\epsilon_u = 46.8$	$\lambda_e = 37.1$ $\epsilon_u = 130.1$	$\lambda_e = 48.4$ $\epsilon_u = 96.4$
$i = 3$	$\lambda_e = 3.24$ $\epsilon_u = 623.6$	$\lambda_e = 3.08$ $\epsilon_u = 160.4$	$\lambda_e = 5.21$ $\epsilon_u = 203.5$	$\lambda_e = 46.4$ $\epsilon_u = 157.2$	$\lambda_e = 47.0$ $\epsilon_u = 111.0$
$i = 4$	$\lambda_e = 4.65$ $\epsilon_u = 884.7$	$\lambda_e = 3.63$ $\epsilon_u = 241.1$	$\lambda_e = 7.03$ $\epsilon_u = 335.1$	$\lambda_e = 57.7$ $\epsilon_u = 182.0$	$\lambda_e = 44.6$ $\epsilon_u = 117.3$
$i = 5$	$\lambda_e = 7.75$ $\epsilon_u = 1492.1$	$\lambda_e = $ - $\epsilon_u = $ -	$\lambda_e = $ - $\epsilon_u = $ -	$\lambda_e = $ - $\epsilon_u = $ -	$\lambda_e = 42.1$ $\epsilon_u = 129.2$

Table 5.2: Upcaling results from modal analysis.

Section 5.4.2. Mobile-immobile models will not be investigated in this chapter. Again, symbols will be used to refer to upscaled models : telegraph equation (TE), temporal CTRW (TC) and spatial CTRW (SC).

5.4.1   Telegraph equation

Assuming that the vertical velocity profile is fully determined, it is possible to compute an effective relaxation time and an effective longitudinal dispersion coefficient according to Eqs. 4.37 and 4.38. Results for the various numerical examples are summarized in Table 5.2 and are shown in Figs 5.16 and 5.17. $\lambda_e = \langle v \rangle \tau_e$ is an effective relaxation distance corresponding to the effective relaxation time. The variance of the velocity field can be computed from the variance of the permeability field (which is given in Table B.1) as $\sigma_v^2 / \langle v \rangle^2 = \sigma_K^2 / \langle K \rangle^2$ for a stationary flow regime.

These results were computed for 700 modes, determined using a refined permeability field of 1000 data points (obtained by interpolating linearly between the 100 initial data points). Effective correlation distance is found to increase with geostatistical correlation length and does not depend on variance. It is moreover found that the method yields unphysical negative relaxation times in a few high-variance cases. Actually, Berentsen [20] did not provide a formal proof of the positiveness of the eigenvalues of the matrix $\boldsymbol{D_T}$. He simply observed that, for every case he tested, he obtained realistic (i.e. positive) values for τ_e. The numerical examples tested in this study reveal that the method might fail in highly heterogeneous cases.

Results in terms of the ϵ_u indicator also indicate that the modal method gives worse results than stochastic and fractal methods. For small correlation lengths, the predicted apparent dispersivity is up to 10 times larger than the actual one. For larger correlation lengths and variances below 1, the accuracy is about the same as for the stochastic method.

Optimal transport parameters are given in Table B.4 and are plotted in Figs. 5.18 and 5.19. In general, ϵ_c is higher than values obtained using the stochastic and the fractal methods, meaning that a simple exponential model is less suited to describe the temporal development of macrodispersivity. The op-

Figure 5.16: Efficiency of TE. $\lambda = 0.01$ (continuous line), $\lambda = 0.05$ (dashed line), $\lambda = 0.1$ (dot-dashed line), $\lambda = 0.5$ (small-dotted line) and $\lambda = 1$ (large-dotted line).
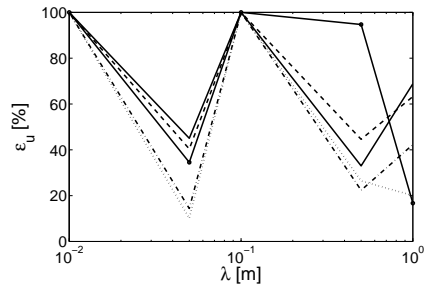

Figure 5.17: Efficiency of TE. $\sigma_Y^2 = 0.01$ (continuous line), $\sigma_Y^2 = 0.1$ (dashed line), $\sigma_Y^2 = 1$ (dot-dashed line), $\sigma_Y^2 = 2$ (small-dotted line) and $\sigma_Y^2 = 4$ (large-dotted line).
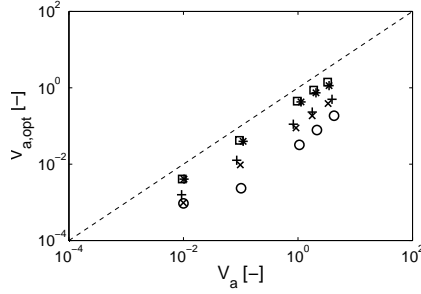

Figure 5.18: Optimal velocity variance required by TE. $\lambda = 0.01$ (circle), $\lambda = 0.05$ (x-mark), $\lambda = 0.1$ (plus), $\lambda = 0.5$ (star) and $\lambda = 1$ (square).
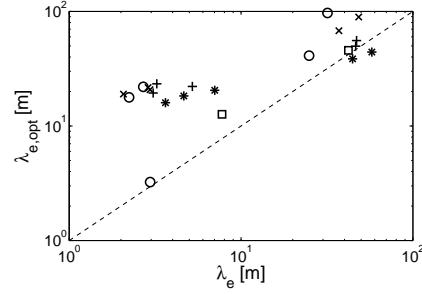
Figure 5.19: Optimal effective relaxation length required by TE. $\sigma_Y^2 = 0.01$ (circle), $\sigma_Y^2 = 0.1$ (x-mark), $\sigma_Y^2 = 1$ (plus), $\sigma_Y^2 = 2$ (star) and $\sigma_Y^2 = 4$ (square).

timal variance is always smaller than the actual one, as it was already observed for the stochastic method. Relaxation processes seem to be underestimated, as optimal values of λ_e are systematically greater than values estimated using the velocity profile.

The analytical solution of Scheidegger's telegraph equation was then confronted to experimental BTC. ΔRMS_u indicator is plotted in Fig. 5.20, whereas ΔRMS_c is given in Fig. B.6. It was highlighted in Section 4.4.2 that τ_e is scale-dependent itself and that Eq. 4.37 used to compute it from the velocity profile is best valid to model large-scale behavior. The consequence is that the prediction for intermediate-scale is worse than the ADE with local-scale parameters, as ΔRMS_u is generally positive for $x < 10$ m. However, large-scale behavior ($10 < x < 100$ m) is modelled with an improvement comparable to stochastic and fractal methods. Scatter is due to numerical problems appearing when computing the analytical solution of the telegraph equation. Finally, the difference between ΔRMS_u and ΔRMS_c is found to be limited, meaning that the use of optimal parameters from the point of view of apparent dispersivity does not usually yield a sensitive improvement in BTC modelling.
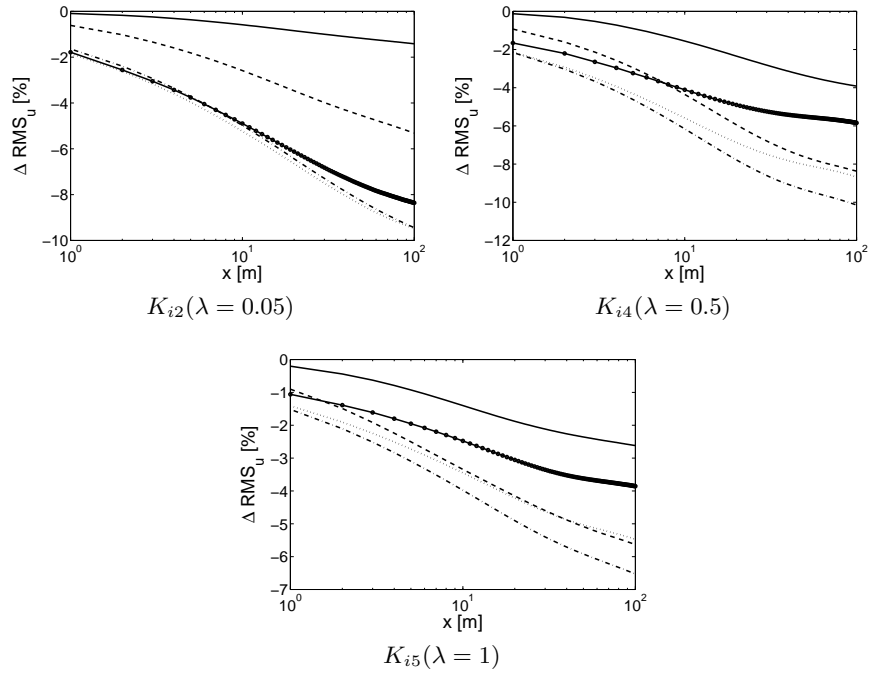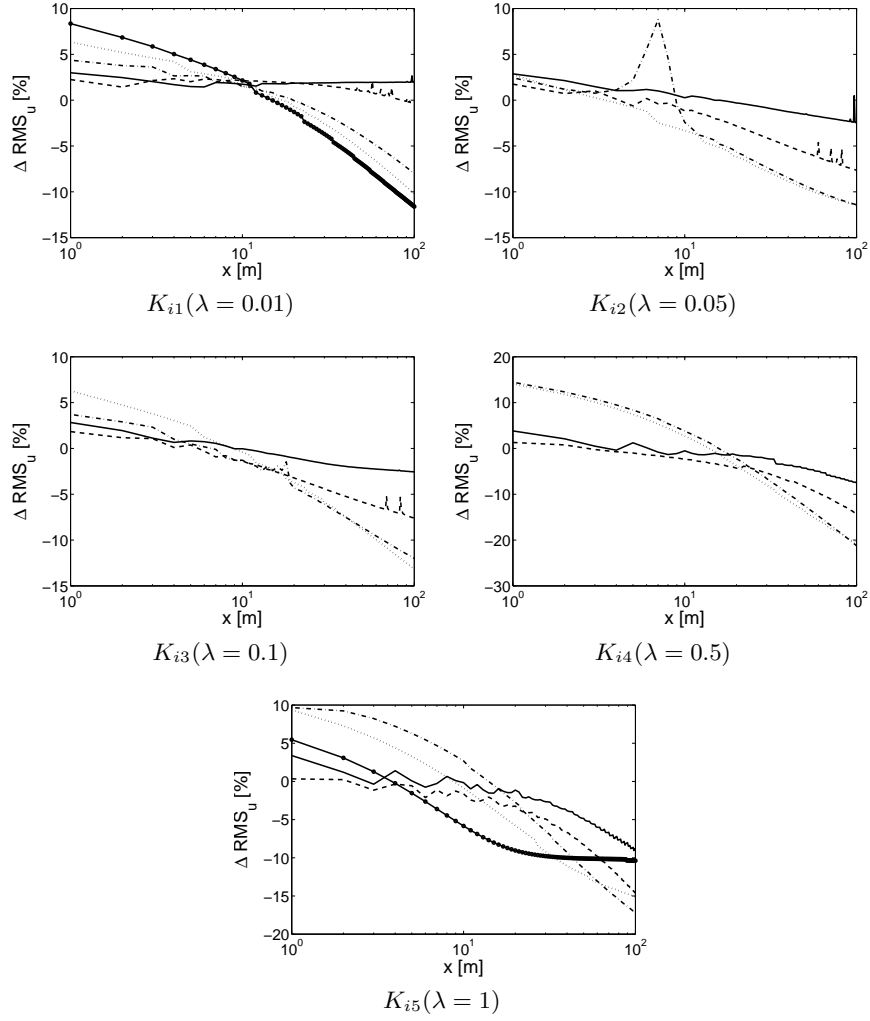
Figure 5.20: Improvement of TE compared to the classical ADE. $i = 1$ - $\sigma_Y^2 = 0.01$ (continuous line), $i = 2$ - $\sigma_Y^2 = 0.1$ (dashed line), $i = 3$ - $\sigma_Y^2 = 1$ (dot-dashed line), $i = 4$ - $\sigma_Y^2 = 2$ (small-dotted line) and $i = 5$ - $\sigma_Y^2 = 4$ (large-dotted line).

K_{ij}	$j = 1$	$j = 2$	$j = 3$	$j = 4$	$j = 5$
$i = 1$	$\beta_t = 1.70$	$\beta_t = 1.70$	$\beta_t = 1.66$	$\beta_t = 1.88$	$\beta_t = 1.73$
	$v_a = 1.02$	$v_a = 1.02$	$v_a = 1.02$	$v_a = 1.02$	$v_a = 1.02$
	$\epsilon_u = 141.7$	$\epsilon_u = 13.60$	$\epsilon_u = 16.16$	$\epsilon_u = 63.83$	$\epsilon = 65.33$
$i = 2$	$\beta_t = 1.64$	$\beta_t = 1.59$	$\beta_t = 1.48$	$\beta_t = 1.96$	$\beta_t = 1.65$
	$v_a = 1.04$	$v_a = 1.06$	$v_a = 1.08$	$v_a = 1.10$	$v_a = 1.12$
	$\epsilon_u = 6.87$	$\epsilon_u = 27.14$	$\epsilon_u = 22.45$	$\epsilon_u = 74.18$	$\epsilon_u = 66.25$
$i = 3$	$\beta_t = 1.37$	$\beta_t = 1.23$	$\beta_t = 1.24$	$\beta_t = 1.78$	$\beta_t = 1.32$
	$v_a = 1.29$	$v_a = 1.60$	$v_a = 1.58$	$v_a = 2.08$	$v_a = 2.65$
	$\epsilon_u = 11.14$	$\epsilon_u = 8.42$	$\epsilon_u = 8.21$	$\epsilon_u = 67.26$	$\epsilon_u = 49.92$
$i = 4$	$\beta_t = 1.25$	$\beta_t = 1.14$	$\beta_t = 0.93$	$\beta_t = 1.71$	$\beta_t = 1.21$
	$v_a = 1.70$	$v_a = 2.49$	$v_a = 1.42$	$v_a = 3.72$	$v_a = 5.94$
	$\epsilon_u = 10.68$	$\epsilon_u = 10.88$	$\epsilon_u = 54.01$	$\epsilon_u = 64.06$	$\epsilon_u = 43.05$
$i = 5$	$\beta_t = 1.16$	$\beta_t = 1.08$	$\beta_t = 1.12$	$\beta_t = 1.71$	$\beta_t = 1.57$
	$v_a = 3.00$	$v_a = 5.53$	$v_a = 4.25$	$v_a = 8.97$	$v_a = 8.99$
	$\epsilon_u = 16.32$	$\epsilon_u = 8.00$	$\epsilon_u = 21.24$	$\epsilon_u = 63.06$	$\epsilon_u = 53.87$

Table 5.3: Upcaling results of TC. $v_a = \langle v \rangle * C_1$ is an adimensional velocity

5.4.2   CTRW and fractional-order equations

Temporally anomalous transport

The application of CTRW in a temporally anomalous transport framework requires breakthrough curve analysis. Therefore, in order to capture early development of the scale effect and include it in the modelling, transport parameters were obtained from the joint analysis of the BTC recorded at $x = 1$ m and at $x = 10$ m. β_t values are shown in Table 5.3. Basically, β_t is not found to be sensitive to correlation in the permeability field, but is found to decrease when the variance increases. Indeed, when σ_Y^2 is high, the corresponding distribution of migration velocity is skewed and heavy-tailed, leading to lower β_t values.

For the sake of convenience, characteristic velocity $1/C_1$, also obtained from the BTC analysis, is expressed under an adimensional form as $v_a = \langle v \rangle C_1$ in Table 5.3. $1/C_1$ is found to be always smaller than $\langle v \rangle$, and decreases both when correlation length and variance increase.

ϵ_u values were calculated by (1) computing apparent dispersivity from analytical breakthrough curves obtained using parameters showed in Table 5.3 and (2) comparing these values with apparent longitudinal dispersivities obtained from actual synthetic curves. Temporal moment analysis is not indicated to obtain apparent Fickian transport parameters from analytical curves computed using the temporal CTRW framework, as temporal moments of BTC are theoretically infinite. Instead, fitting of the corresponding analytical solution of the ADE on the analytical CTRW curve was used to obtain apparent dispersivity values. Figs. 5.21 and 5.22 show that the model gives better results than previous methods for small correlation lengths (except when $\sigma_Y^2 = 0.01$). For larger correlation lengths, predictions of apparent longitudinal dispersivity are of a precision of a similar order of magnitude as using e.g. the fractal upscaling method.
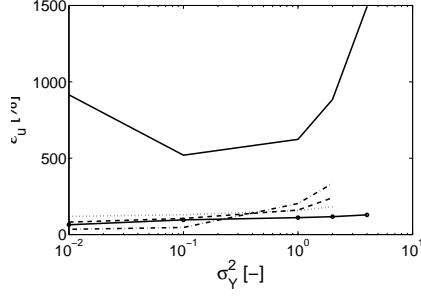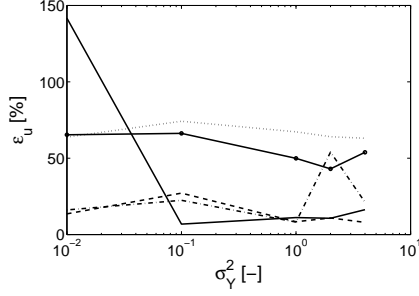
Figure 5.21: Efficiency of TC. $\lambda = 0.01$ (continuous line), $\lambda = 0.05$ (dashed line), $\lambda = 0.1$ (dot-dashed line), $\lambda = 0.5$ (small-dotted line) and $\lambda = 1$ (large-dotted line).
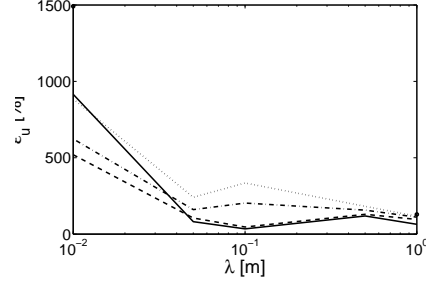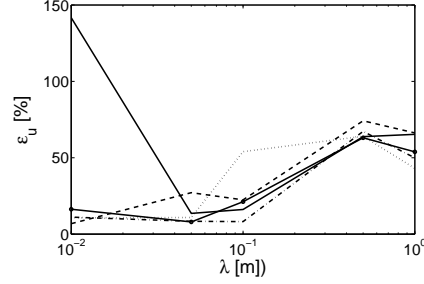
Figure 5.22: Efficiency of TC. $\sigma_Y^2 = 0.01$ (continuous line), $\sigma_Y^2 = 0.1$ (dashed line), $\sigma_Y^2 = 1$ (dot-dashed line), $\sigma_Y^2 = 2$ (small-dotted line) and $\sigma_Y^2 = 4$ (large-dotted line).

Optimal CTRW transport parameters were also obtained for each breakthrough curve. Fig. 5.23 shows optimal β_t values and illustrate that it is also scale-dependent. It can be seen on Fig. 5.23 that, for small variance and small correlation length, this situation is reached at intermediate scales, as β_t converges to its threshold value of 2. For larger correlation length and larger variance, this situation does not happen and β_t stabilizes at a value smaller than 2. In the particular case $\lambda = 0.5$, breakthrough curves all have a Gaussian shape as the best value for β_t is 2 at every scale.

Fig. 5.24 shows the results of the upscaling procedure in terms of ΔRMS_u indicators. Most of the time, the latter is found to be negative, indicating that temporal CTRW yields a better prediction of concentration distributions than the ADE with local parameters. However, for small variances and small correlation lengths, ΔRMS_u occurs to be positive. In these cases, the scale effect has a relatively limited amplitude and BTC obey quasi-normal distributions. Therefore, the Fickian model yields relatively good results, even with local parameters, and CTRW predicts heavy-tailed concentration distributions that do not match actual data, leading to worse upscaling results.

For small correlation lengths, as for other upscaling methods, the improvement of the temporal CTRW model globally increases with the variance (i.e. when the scale effect is stronger) and seems to stabilize to a constant level at about $x = 30$ m. In the case of higher correlation lengths, contrary to other results shown in this chapter, ΔRMS_u usually reaches a peak at that distance and then tends to become positive for large distance. Considering this, the upscaling capacities of the CTRW model seem to remain limited to about $1/3$ of order of magnitude. The problem might lie in the scale-dependence of β_t itself (Fig. 5.23). Inference of the transport parameters based on early behavior of the concentration distributions leads to an over-estimation of the scale-effect, that finally leads to worse upscaling results than the no-upscaling model.

ϵ_c indicator was not computed here. Other methods tested provide explicit analytical expressions to compute apparent dispersivity, that were used to obtain optimal transport parameters and calculate ϵ_c. In the temporal CTRW

$K_{i1}(\lambda = 0.01)$ $K_{i2}(\lambda = 0.05)$

$K_{i3}(\lambda = 0.1)$ $K_{i4}(\lambda = 0.5)$

$K_{i5}(\lambda = 1)$
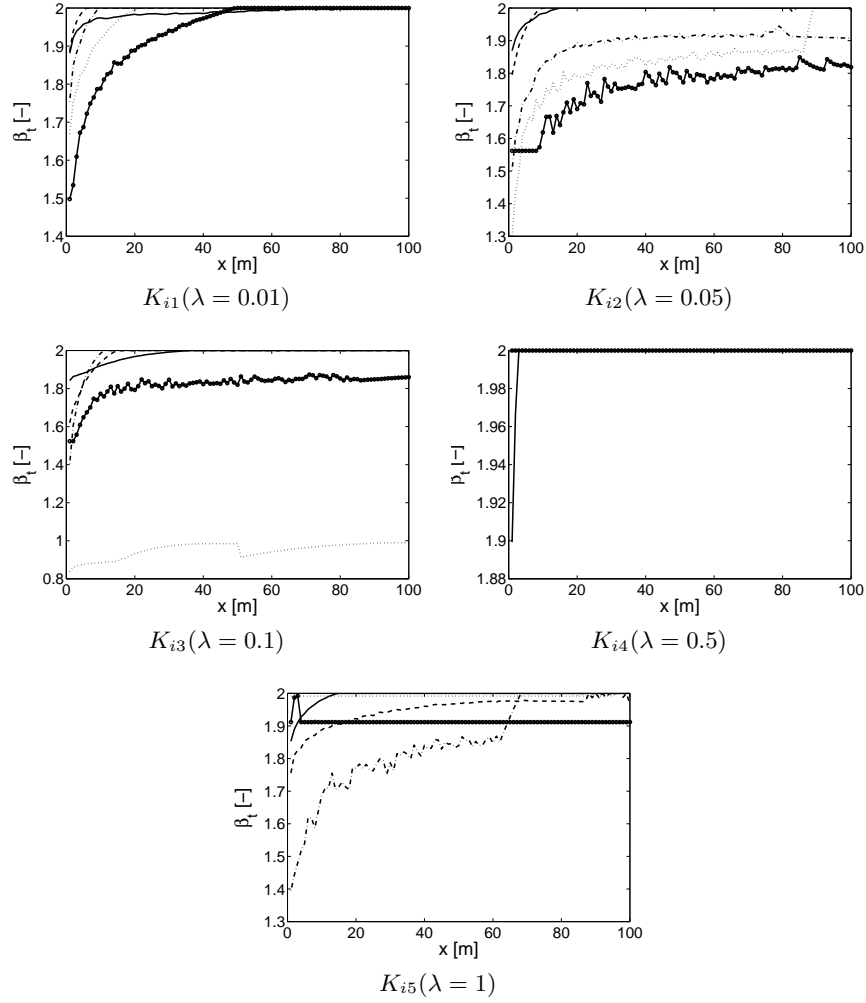
Figure 5.23: Optimal values of β_t. $i = 1$ - $\sigma_Y^2 = 0.01$ (continuous line), $i = 2$ - $\sigma_Y^2 = 0.1$ (dashed line), $i = 3$ - $\sigma_Y^2 = 1$ (dot-dashed line), $i = 4$ - $\sigma_Y^2 = 2$ (small-dotted line) and $i = 5$ - $\sigma_Y^2 = 4$ (large-dotted line).
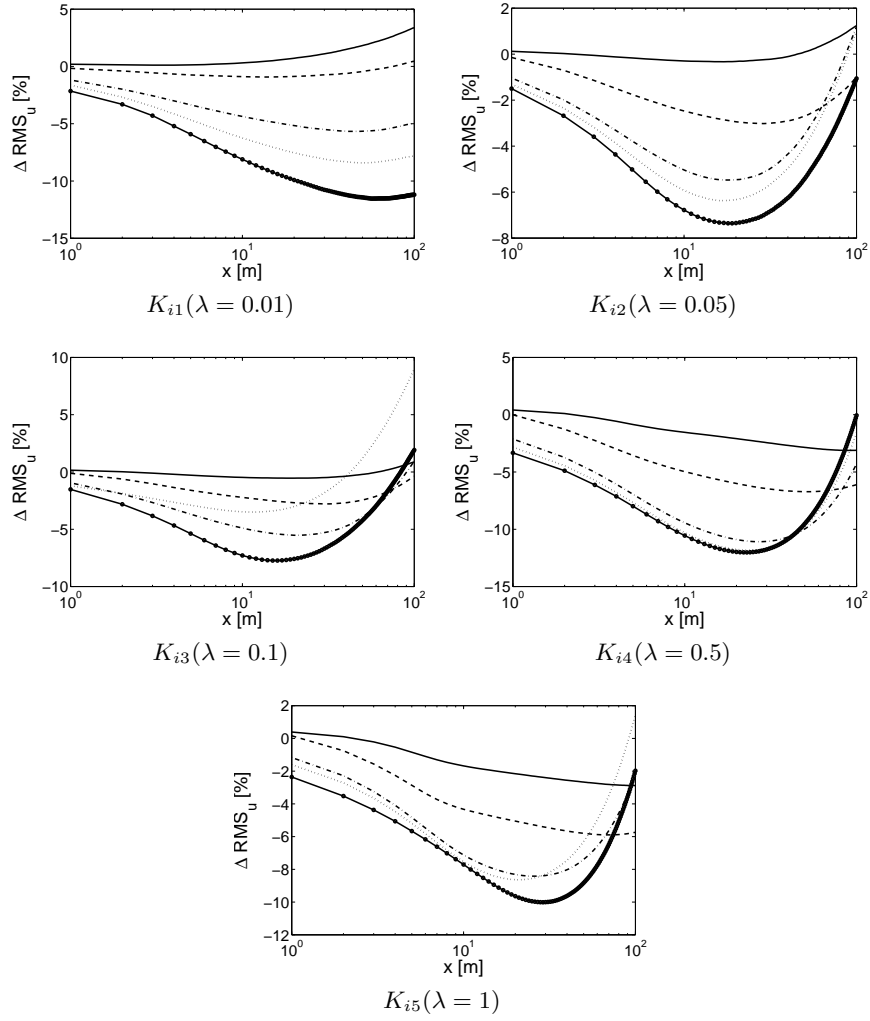
Figure 5.24: Improvement of TC compared to the classical ADE. $i = 1$ - $\sigma_Y^2 = 0.01$ (continuous line), $i = 2$ - $\sigma_Y^2 = 0.1$ (dashed line), $i = 3$ - $\sigma_Y^2 = 1$ (dot-dashed line), $i = 4$ - $\sigma_Y^2 = 2$ (small-dotted line) and $i = 5$ - $\sigma_Y^2 = 4$ (large-dotted line).

framework, transport parameters are fitted to mimic the whole BTC, not only its apparent dispersion. Therefore, ϵ_c values that could have been calculated would have been different and a comparison with other methods would not have been meaningful.

Finally, as expected since Fickian transport is a particular case of CTRW, values of ΔRMS_c indicator (Fig. B.7) were systematically found to be negative, indicating an improvement in the (non-predictive) modelling. For small correlation lengths, the improvement goes up to about three times ΔRMS_c values obtained with other upscaling methods ($\Delta RMS_c \approx 30$ % for K_{51}), meaning the temporal CTRW can better describe concentration distributions than the stochastic or the fractal methods. The drawback of this method thus lies in its parametrization, as parameter values inferred from small-scale data analysis yield upscaling results much poorer than results obtained with optimal parameters.

Spatially anomalous transport

In order to keep a level of small-scale information similar to what was used in previous section, the methodology proposed by Benson et al. [16, 18] and described in Section 4.4.3 was applied to simulated breakthrough curves at $x = 1$ m and $x = 10$ m. Therefore, β_x is estimated from Eq. 4.39 using

$$m = \frac{\log\left(\alpha_L^*|_{x=10}\right) - \log\left(\alpha_L^*|_{x=1}\right)}{\log(10) - \log(1)} = \log\left(\frac{\alpha_L^*|_{x=10}}{\alpha_L^*|_{x=1}}\right) \tag{5.5}$$

and the BTC recorded at $x = 10$ m was afterwards fitted with the analytical solution of Eq. 3.12 for a continuous injection to determine $\mathcal{D}_x$ and γ_B. The results of this procedure are summarized in Table 5.4. ϵ_u indicators, also shown in Table 5.4 and graphically presented in Figs. 5.26 and 5.27, were computed as in previous section, by first calculating theoretical BTC and by analyzing them using an adequate method. In this case, the temporal moment method could be used as temporal moments remain finite (but spatial moments are infinite). However, as theoretical BTC are characterized by long tails and as an accurate evaluation of temporal moments would require temporal scales to be several orders of magnitude larger, the curve-fitting method was again used to compute apparent Fickian transport parameters.

Contrary to temporal CTRW, β_x is found to vary with correlation length, but dependence on variance is less obvious. The characteristic length $\lambda_B = (\mathcal{D}_x/\langle v \rangle)^{1/(1-\beta_x)}$ incorporates a generalized dispersion coefficient, supposed to be scale-invariant. λ_B increases both with correlation length and variance, and could therefore be interpreted as a measure of the overall magnitude of the scale-effect. The bias increases with the variance, as velocity distribution are skewer for higher σ_Y^2. Considering ϵ_u, results seem to be much more homogeneous than previous methods. All values are below 80 % for the whole range of correlation lengths and variances.

As a point of comparison, optimal values for β_x were computed from the slope of the apparent dispersivity obtained from the regression over the 100 available BTC. It therefore embodies a description of the scale-effect over the

K_{ij}	$j=1$	$j=2$	$j=3$	$j=4$	$j=5$
$i=1$	$\beta_x = 1.83$ $\lambda_B = 0.006$ $\gamma_B = 0.18$ $\epsilon_u = 17.65$	$\beta_x = 1.32$ $\lambda_B = 0.000$ $\gamma_B = 0.05$ $\epsilon_u = 63.31$	$\beta_x = 1.26$ $\lambda_B = 0.000$ $\gamma_B = 0.02$ $\epsilon_u = 56.00$	$\beta_x = 1.03$ $\lambda_B = 0.000$ $\gamma_B = 0.02$ $\epsilon_u = 24.99$	$\beta_x = 1.06$ $\lambda_B = 0.000$ $\gamma_B = 0.02$ $\epsilon_u = 39.74$
$i=2$	$\beta_x = 1.52$ $\lambda_B = 0.003$ $\gamma_B = 0.40$ $\epsilon_u = 7.51$	$\beta_x = 1.26$ $\lambda_B = 0.001$ $\gamma_B = 0.17$ $\epsilon_u = 9.64$	$\beta_x = 1.30$ $\lambda_B = 0.002$ $\gamma_B = 0.19$ $\epsilon_u = 16.33$	$\beta_x = 1.05$ $\lambda_B = 0.001$ $\gamma_B = 0.19$ $\epsilon_u = 70.89$	$\beta_x = 1.05$ $\lambda_B = 0.089$ $\gamma_B = 0.07$ $\epsilon_u = 71.02$
$i=3$	$\beta_x = 1.41$ $\lambda_B = 0.038$ $\gamma_B = 0.81$ $\epsilon_u = 13.00$	$\beta_x = 1.29$ $\lambda_B = 0.091$ $\gamma_B = 0.50$ $\epsilon_u = 22.75$	$\beta_x = 1.48$ $\lambda_B = 0.216$ $\gamma_B = 0.85$ $\epsilon_u = 29.97$	$\beta_x = 1.78$ $\lambda_B = 2.190$ $\gamma_B = 0.56$ $\epsilon_u = 83.71$	$\beta_x = 1.12$ $\lambda_B = 0.894$ $\gamma_B = 0.58$ $\epsilon_u = 71.55$
$i=4$	$\beta_x = 1.36$ $\lambda_B = 0.119$ $\gamma_B = 0.95$ $\epsilon_u = 6.58$	$\beta_x = 1.30$ $\lambda_B = 0.305$ $\gamma_B = 0.70$ $\epsilon_u = 24.89$	$\beta_x = 1.47$ $\lambda_B = 0.607$ $\gamma_B = 0.99$ $\epsilon_u = 28.14$	$\beta_x = 1.05$ $\lambda_B = 0.392$ $\gamma_B = 0.84$ $\epsilon_u = 77.61$	$\beta_x = 1.13$ $\lambda_B = 2.196$ $\gamma_B = 0.86$ $\epsilon_u = 59.02$
$i=5$	$\beta_x = 1.33$ $\lambda_B = 0.645$ $\gamma_B = 0.99$ $\epsilon_u = 36.01$	$\beta_x = 1.29$ $\lambda_B = 1.067$ $\gamma_B = 0.88$ $\epsilon_u = 20.84$	$\beta_x = 1.40$ $\lambda_B = 1.821$ $\gamma_B = 0.99$ $\epsilon_u = 26.85$	$\beta_x = 1.05$ $\lambda_B = 1.546$ $\gamma_B = 0.97$ $\epsilon_u = 56.73$	$\beta_x = 1.12$ $\lambda_B = 9.073$ $\gamma_B = 0.94$ $\epsilon_u = 45.14$

Table 5.4: Upcaling results of SC. $\lambda_B = (\mathcal{D}_x / \langle v \rangle)^{1/(1-\beta_x)}$ is a characteristic length.

full range of distances investigated. Most of the time, the estimation of β_x using only the BTC at $x = 1$ m and at $x = 10$ m is relatively close to the value quantifying the slope of the full apparent dispersivity curve versus scale on a log-log-scale graph.

Prediction in terms of the full BTC is quantified in Fig. 5.28 using the ΔRMS_u indicator. It appears to be relatively good, compared to other methods. The order of magnitude is similar to what was previously obtained, except for small variance cases. As for the temporal CTRW, situations of low heterogeneity are not well predicted and tailing behavior is generally exaggerated, leading to positive values of ΔRMS_u.

Optimal values of $\mathcal{D}_x$ and γ_B are determined for each BTC by curve-fitting, using values of β_x shown in Fig. 5.25. ϵ_c was not computed here, for similar reasons as in previous section and Fig. B.8 shows the values of ΔRMS_c. The latter are found to be relatively close to ΔRMS_u, and it must be noted that for small variance cases, the indicator remains positive, meaning that the standard ADE is better indicated to model transport in mildly heterogeneous cases.

5.5 Conclusion

A few general conclusions can already be drawn from the analysis carried out in this chapter, regarding the general applicability and the capacities of tested upscaling procedures.

First, the lack of reliability of characterization methods appeared through
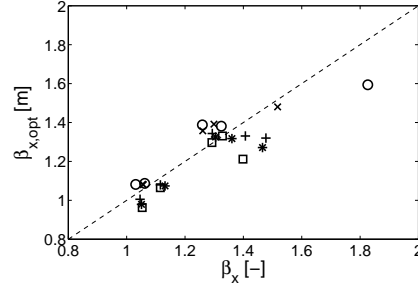
Figure 5.25: β_x value obtained from the
analysis of the full dispersivity-scale curve.
$\sigma_Y^2 = 0.01$ (circle), $\sigma_Y^2 = 0.1$ (x-mark),
$\sigma_Y^2 = 1$ (plus), $\sigma_Y^2 = 2$ (star) and $\sigma_Y^2 = 4$
(square).
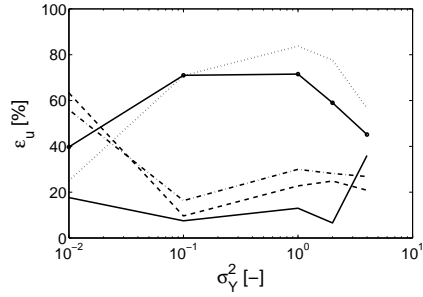
Figure 5.26: Efficiency of SC. $\lambda = 0.01$
(continuous line), $\lambda = 0.05$ (dashed line),
$\lambda = 0.1$ (dot-dashed line), $\lambda = 0.5$ (small-
dotted line) and $\lambda = 1$ (large-dotted line).
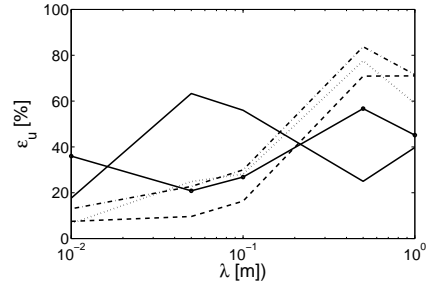
Figure 5.27: Efficiency of SC. $\sigma_Y^2 = 0.01$
(continuous line), $\sigma_Y^2 = 0.1$ (dashed line),
$\sigma_Y^2 = 1$ (dot-dashed line), $\sigma_Y^2 = 2$ (small-
dotted line) and $\sigma_Y^2 = 4$ (large-dotted
line).
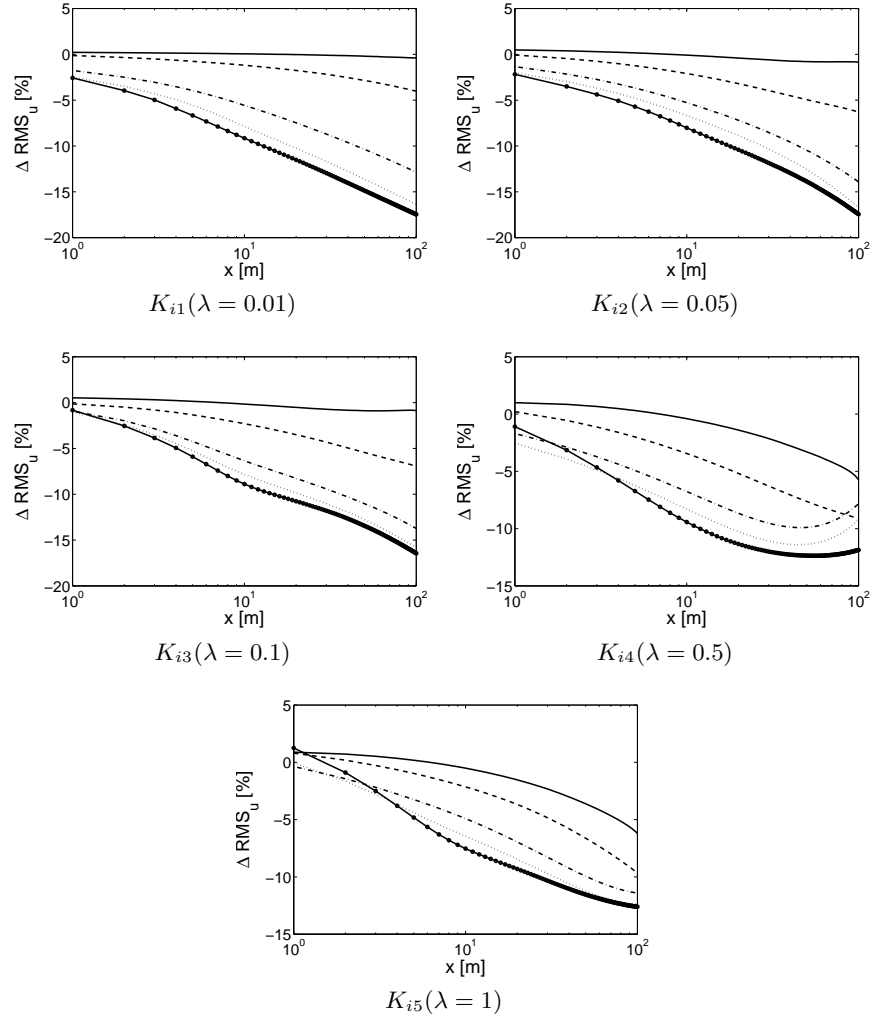
Figure 5.28: Improvement of SC compared to the classical ADE. $i = 1$ - $\sigma_Y^2 = 0.01$ (continuous line), $i = 2$ - $\sigma_Y^2 = 0.1$ (dashed line), $i = 3$ - $\sigma_Y^2 = 1$ (dot-dashed line), $i = 4$ - $\sigma_Y^2 = 2$ (small-dotted line) and $i = 5$ - $\sigma_Y^2 = 4$ (large-dotted line).

results obtained in this chapter. For example, estimation of Hurst coefficient H was subject to a relatively large uncertainty, resulting in large confidence intervals for apparent dispersivity. In the temporal CTRW approach, parameters inferred at small-scale are in a few cases so unadapted that the model gives worse results than the ADE with local parameters. It must also be noted that, if the stochastic method yielded relatively accurate estimations of transport parameters, K fields were generated according to a log-normal distribution. One could wonder if this observation could have been done with K fields generated using e.g. a fractal model. Moreover, the prediction of apparent dispersivity and concentration distributions is not really worse using other methods, meaning that the sensitivity of these non-Fickian models to their parameters is not really high.

Then, as scaling effects increase with the variance of the $\ln(K)$ field, efficiency of each non-Fickian method and model increased with σ_Y^2 compared to the classical ADE (almost systematic negative values for ΔRMS_u). However, absolute model efficiency seems to remain comparable for each tested model.

Other conclusions will be structured in order to distinguish features of upscaling methods from those of upscaled transport equation, with an emphasis on expected and surprising results.

5.5.1   Upscaling methods for dispersivity

Fig. 5.29 shows a table indicating which method yielded the best results with respect to upscaling of apparent dispersivity (i.e. which method yielded the smallest ϵ_u). Stochastic (S) and fractal (F) methods are considered, as well as the modal method used to parametrize Scheidegger's telegraph equation (TE) since it also provides an analytical expression for transient dispersivity. Actually, all methods gave upscaling results of a relatively similar quality, with at best a relative error of 40 % and an improvement that seems to stabilize for large scale.

It appears that S is the most efficient for intermediate correlation lengths. For smaller correlation lengths, upscaling capacities of the stochastic method decrease because local dispersivity becomes of a similar order of magnitude as correlation length (which violates assumptions under which stochastic analytical solutions are derived). For larger correlation length, the fulfillment of the ergodic condition becomes questionable and, expectively, the efficiency of S decreases. A surprising result is that the variance does not seem to influence the capacities of the stochastic method.

For the fractal method, the relative error on $\hat{H}$ was found to be lower for $\lambda > 0.1$ (see Fig. 5.10) and the sensitivity of the analytical solution of α_L^* decreases for high H (i.e. an error on $\hat{H}$ has less influence on upscaling when $\hat{H}$ is high). This could explain that F generally yields the best results for larger correlation lengths. For small correlation lengths, the problem might lie in the method used to obtain $\hat{H}$, as unreasonable negative values were obtained. Variance does not seem to influence upscaling capacities of F, but contrary to S, no assumption of low variability has to be made in a fractal framework and σ_Y^2 should indeed have no influence on efficiency of F.
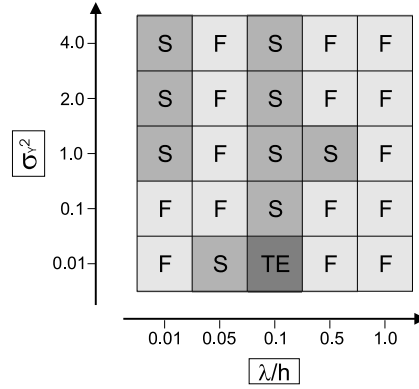
Figure 5.29: Prediction of apparent dispersivity for stratified media : best non-Fickian model with respect to ϵ_u (excluding models not based on a description of the soil structure).

Finally, the modal upscaling method appeared to be the best method in only one isolated case.

5.5.2 Upscaled transport equations

Upscaled transport equations have the advantage of allowing the prediction of non-symmetric concentration distributions, with heavy tails. Available analytical solutions are however relatively difficult to compute compared to solutions of the ADE, as numerical instabilities may appear for given combinations of numerical values for transport parameters. This is reflected by the more scattered ΔRMS curves of upscaled equations.

Fig. 5.30 show a table similar to Fig. 5.29 except that all tested models are considered. Temporally and spatially anomalous transport models are relatively equivalent regarding upscaling of dispersivity and usually yield the best results. This observation could simply be explained by the parametrization method of the models. Both temporal and spatial CTRW require a priori information on concentration and apparent dispersivity in order to be applied, whereas other methods are only based on a description of soil structure.

In Fig. 5.31, the models that yielded the best prediction in terms of the whole outlet breakthrough curve (i.e. the models that yielded the largest negative ΔRMS_u at 100 m from injection) are presented. Two models appear to have the best upscaling capacities : the spatial CTRW model for large variance and Scheidegger's telegraph equation for large correlation length. Moreover, for this indicator, a clear difference appears between spatial and temporal CTRW, as temporal CTRW was found to have a limit scale beyond which upscaling capacities decreased.

CTRW models are typically suited to situations were long-tailed BTC are observed. This explains why these models are relatively efficient for high vari-
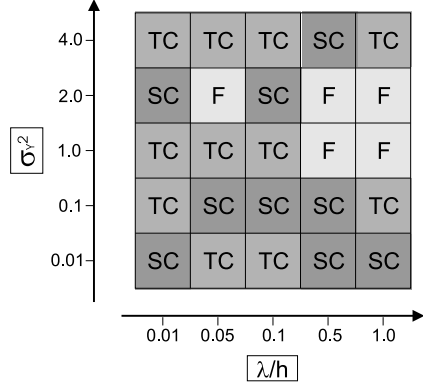
Figure 5.30: Prediction of apparent dispersivity for stratified media : best non-Fickian model with respect to ϵ_u.
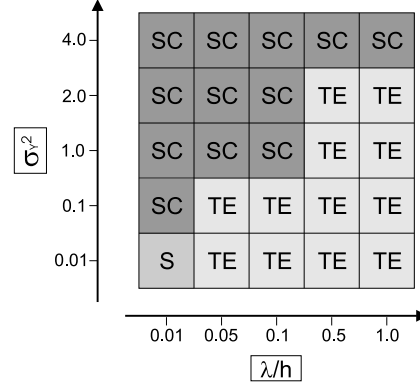
Figure 5.31: Prediction of concentration distributions for stratified media : best non-Fickian model with respect to ΔRMS_u.

ance cases and yield poorer results for small variance cases. The difference between temporal and spatial CTRW models investigated here might originate from a different scale-dependency of β_t and β_x. It could also be explained by the difference in the description of advective transport. Whereas SC embodies a classical description of advection, TC do not allow a parametrization using a mean migration velocity. Advective transport is estimated from BTC analysis using a curve-fitting method, that can yield a biased information.

Finally, TE turned out to be the most efficient model for high correlation lengths. Compared to its relatively low efficiency in upscaling of apparent dispersivity, this result would highlight that (1) a single exponential is a too simplified model for transient dispersivity but (2) the quality of the predicition of apparent dispersivity is sufficient to allow a correct prediction of concentration distributions. However, the drawback linked to the modal upscaling method used to parametrize TE is that it requires the full permeability profile, which is generally not practically accessible.

Chapter 6

Solute transport in 2D heterogeneous media

6.1 Introduction

In Chapter 5, efficiency of upscaling methods and upscaled equations was investigated for highly conceptual heterogeneous cases. The aim was to establish tendencies with respect to variance and correlation length, in situations were no other parameter is required to describe medium structure. It is propose to refine the analysis by considering in this chapter more complex 2D situations were longitudinal correlation lengths are finite and were flow is not parallel to the bedding.

Two-dimensional problems are generally well developed in the literature, mainly due to computational reasons [184]. There is indeed a trade-off between simulating flow and transport for a high number of different two-dimensional K fields and simulating more complex flow and transport problems in a few different three-dimensional systems. The approach adopted in this investigation is to perform a relatively high number of parametric variations, therefore leading to the need for restricting to two-dimensional problems. Another reason for focusing on 2D problems is that the physical experiment performed in Part 3 uses a two-dimensional laboratory tank. As conclusions drawn in this chapter should be used to design that experiment, it is necessary to investigate cases of a geometry comparable to the experimental device presented in Chapter 7.

In Section 6.2, the design of the various examples that are investigated is first detailed. Additional models to characterize heterogeneity are presented and used to generate synthetic aquifers exhibiting multimodal permeability distributions. Flow is solved numerically and compared to a few common analytical results available in the literature in Section 6.3. Transport is then solved using similar numerical tools as in Chapter 5. In Section 6.4 and 6.5, non-Fickian models are applied and compared to numerical values of apparent dispersivity and to concentration distributions.

It must be noted that model parameters will not be optimized for this set of examples, and neither ϵ_c nor ΔRMS_c will be calculated here. The number of parameters needed to describe the structure of 2D permeability fields becomes important and it is not possible to reasonably optimize all of them to correctly simulate apparent dispersivity. Moreover, it is believed that if only some of them are determined by bulk curve-fitting, their values might be completely meaningless.

6.2   Design of numerical simulations

6.2.1   Models of heterogeneity

Two- and three-dimensional Gaussian $\ln(K)$ fields can be easily generated by extending the methodology that was used for vertical permeability profiles (see Chapter 5). However, the scope of this work is to evaluate transport models in physically-consistent situations. That is, one could not limit this analysis to log-Gaussian permeability fields, which are well-suited to stochastic analysis but may be unadapted in most real field-scale situations [84, 113]. Other methodologies have emerged to represent heterogeneity of natural media in hydrogeology, being either descriptive, process-imitating or structure-imitating [60, 113].

Descriptive methods couple geologic conceptual models with hydrostratigraphic units of given geologic and hydraulic properties to divide an aquifer into zones characterized by constant effective parameters, neglecting smaller-scale heterogeneities [113]. These methods are however subjective, may depend on the experience of the modeller [113] and the zonated image of the subsurface can sometimes highly differ from real subsoil structure.

Process-imitating methods aim at simulating a medium by reproducing its formation processes. They include geologic processes model, combining sediment transport processes to simulate spatial patterns in grain size distribution, and thermomechanical mechanisms for large-scale tectonic deformations [29, 60, 112, 113, 181]. However, highly uncertain factors such as Paleoclimatic trends play a key role in these methods [112], which makes them currently impossible to apply to realistic models [60]. From this point of view, these methods will not be further considered in this study.

Structure-imitating methods rely on available information to constrain the geometry of spatial patterns of hydraulic properties. Koltermann and Gorelick [113] divided these methods into (1) spatial statistical methods and (2) sedimentation pattern methods. The latter could be linked to process-imitating methods and are of smaller extension compared to spatial statistical methods. The generation of Gaussian log-permeability fields based on a geostatistical analysis is typically a spatial statistical structure-imitating method. However, non-Gaussian methods are much more powerful tools, allowing the generation of multifacies and fractured media (although Gaussian methods can be adapted to produce discrete permeability fields). These methods include indicator-based methods, Boolean methods and Markov chains. Indicator random function models are particularly well suited to characterize categorical (binary) variables [63, 110]. Indicator models can thus be used e.g. to characterize the spatial pattern of a given facies of constant hydraulic conductivity (correlation lengths being in this case an image of mean facies lengths). Boolean methods involve generating objects in space that have a deterministic shape, but with random positions and dimensions. The traditional object used to model a fractured medium is a disk [60], but more complex structures can be adopted [64] . This method is however rather conceptual and as Markov chains will be shown to be more powerful than indicator variogram models, one will further focus on this latter approach.

In practical applications of continuous and categorical geostatistical ap-

proaches, geologic data sets are most of the time too sparse (or the geology is too complicated) to fully support the development of an accurate experimental variogram [38, 39, 84]. Yet, in the case of categorical variables, Markov chains provide a tool can fully and directly take into account volumetric proportions, mean length, juxtapositional tendencies and anisotropy [38, 39], by the use of transition probabilities. For a one-dimensional spatial application, a Markov chains model assumes that the permeability at a specified location depends entirely on the permeability of the nearest datum. Markov chains models can be either discrete [68] or continuous [40]. Mathematically, a one-dimensional continuous Markov chains applied to a categorical variable in a direction ϕ assumes a transition probability matrix $\mathbf{T}_\phi$ of exponential form [38, 40]

$$\mathbf{T}(h_\phi) = \exp\left(\mathbf{R}_\phi h_\phi\right) \tag{6.1}$$

were $\mathbf{R}_\phi$ is a transition rate square matrix of the size of the number of categories to be considered for the variable of interest and h_ϕ is the lag (separation) between two points in direction ϕ. Term $t_{ij}(h_\phi)$ in matrix $\mathbf{T}(h_\phi)$ represents the probability of finding category j at a distance h in direction ϕ from a location where category i is observed. Expectively, $\mathbf{T}(0)$ is a unit matrix. It can be shown that for a stationnary random field

$$\lim_{h_\phi \to \infty} t_{ij}(h_\phi) = p_j \qquad \forall i \tag{6.2}$$

The transition rate corresponds to the slope of the transition probability plot as the lag tends to zero. Consequently, transition rates for diagonal elements are negative whereas non-diagonal transition rates are (usually) positive. Diagonal transition rates are related to mean lengths of categories through [38, 40]

$$r_{jj,\phi} = -\frac{1}{L_\phi} \tag{6.3}$$

Other noticeable properties of the transition rate matrix are [38, 40]

$$\sum_{j=1}^{K} r_{ij,\phi} = 0 \tag{6.4}$$

$$\sum_{i=1}^{K} p_i r_{ij,\phi} = 0 \tag{6.5}$$

These two latter equations can be used to define a background category, whose properties are inferred from those of other categories. Fig. 6.1 shows transition probabilities for a three-category model, with approximatively $p_1 = 0.6$ (background category), $p_2 = 0.3$, $p_3 = 0.1$, and characterized by the transition rate matrix

$$\mathbf{R} = \begin{bmatrix} -0.8 & -0.1667 & 0.9667 \\ 0.6 & \frac{-1.0}{0.5} & \frac{0.7}{0.5} \\ 3 & \frac{0.7}{0.1} & \frac{-1.0}{0.1} \end{bmatrix} \tag{6.6}$$

were fractions were not computed so that mean lengths and superimposition tendencies are highlighted. Mean lengths of category 2 and 3 are respectively
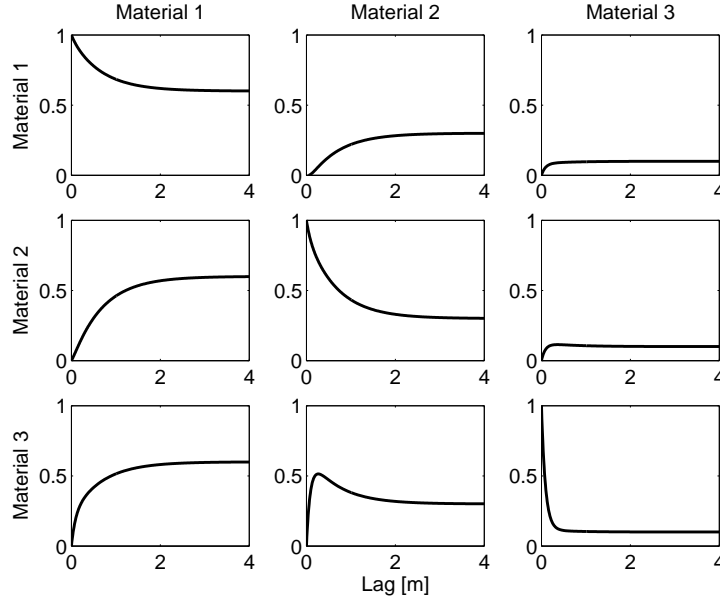
Figure 6.1: Example of transition probabilities for a three-category model

$L_2 = 0.5$ m and $L_3 = 0.1$ m and the probability of finding category 2 above 3 is equal to the probability of finding 3 above 2 and equals 0.7 (i.e category 3 is mainly embedded in category 2). Elements of the first row and the first column were obtained using Eqs. 6.4 and 6.5. The negative transition rate appearing on a non-diagonal element on the first line is caused by the strong juxtapositional tendency that was imposed between category 2 and 3 [38].

Due to properties of the matrix exponential operator in Eq. 6.1, it can be shown that a Markov chains model consists of linear combinations of exponential structures, that could generate non-exponential-looking Gaussian and hole-effect transition probabilities [38, 40], as illustrated on Fig. 6.1.

Multidimensional Markov chains models are obtained through elliptical interpolation between one-dimensional Markov chains models in principal directions [38, 40]. Simulation of multifacies models based on transition probabilities can then be achieved using the program T-Progs (Transition Probability Geostatistical Software [38]). Although Markov chains are defined very simply in theoretical and mathematical terms, they have shown remarkable applicability to the characterization of facies (hydrostratigraphic units) spatial variability in alluvial and fluvial depositional systems [39, 40, 57, 126, 194, 195].

6.2.2   Synthetic two-dimensional examples

This section aims at briefly presenting the geometry, initial and boundary conditions adopted for the investigation of two-dimensional problems, as well as the particular set of K fields that will be tested. The geometry of the model is inspired from an experimental setup available in the Laboratory of Civil Engi-
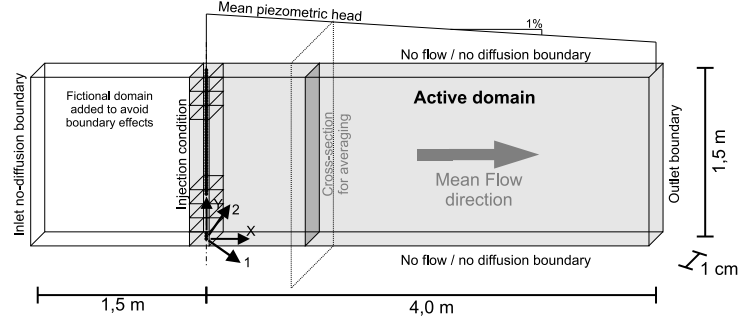
Figure 6.2: Geometry and boundary conditions of the 2D synthetic examples. X and Y refer to the coordinate system attached to the flow system, whereas 1 and 2 refer to the coordinate system attached to the principal directions of the permeability field.

neering of the Université catholique de Louvain (that will however not be used in Part 3 of this study). Flow and transport take place in a two-dimensional domain of 4 m long by 1.5 m wide, in confined conditions (Fig. 6.2). Left and and right boundaries are fixed-head boundaries in order to impose a mean gradient of 1 % in the longitudinal direction, whereas upper and lower boundaries are no-flow/no-diffusion boundaries. Initial concentration is null everywhere and purely one-dimensional transport problems are investigated through uniform concentration injection along the inlet boundary (Fig. 6.2).

The reason for a domain of such a limited extension is twofold. First, numerical results presented in the literature usually correspond to very large domains, in which boundary conditions are supposed to have no influence on solute transport, in order to validate semi-analytical models (see e.g. the results of Trefry et al. [184]). Perfectly stratified examples investigated in Chapter 5 pursued a rather similar objective, as these simulations were aimed at identifying tendencies between models for systematic parametric variations. However, general motivations of this study are oriented towards the practical use of non-Fickian models, under realistic conditions and for transport over finite distances. A domain of limited extension was therefore adopted. Secondly, as already mentioned, one of the objective of this chapter is to identify cases in which modelling problems are encountered. As the final part of this study involves laboratory experiments, the results obtained in this chapter must be used to design the physical experiment to perform. Therefore, a domain of a size similar to that of the setup that will be used in Chapter 7 is chosen.

First, a set a Gaussian log-permeability fields are generated using similar spectral tools as in Chapter 5. Table 6.1 summarizes parameter values adopted for each $\ln(K)$ field. Actual (observed) values of the geometric mean and the variance are slightly different than the theoretical values, and will be used in the remaining part of the analysis. Fig. 6.3 shows the 8 examples that were generated.

Then, a set of two-facies models were generated using T-Progs. A background category of permeability $K_1 = 10^{-5}$ m/s was assigned a probability occurrence of 60 % and a second facies of permeability $K_2 = 10^{-7}$ m/s was assigned a probability occurrence of 40 %. As background categories do not
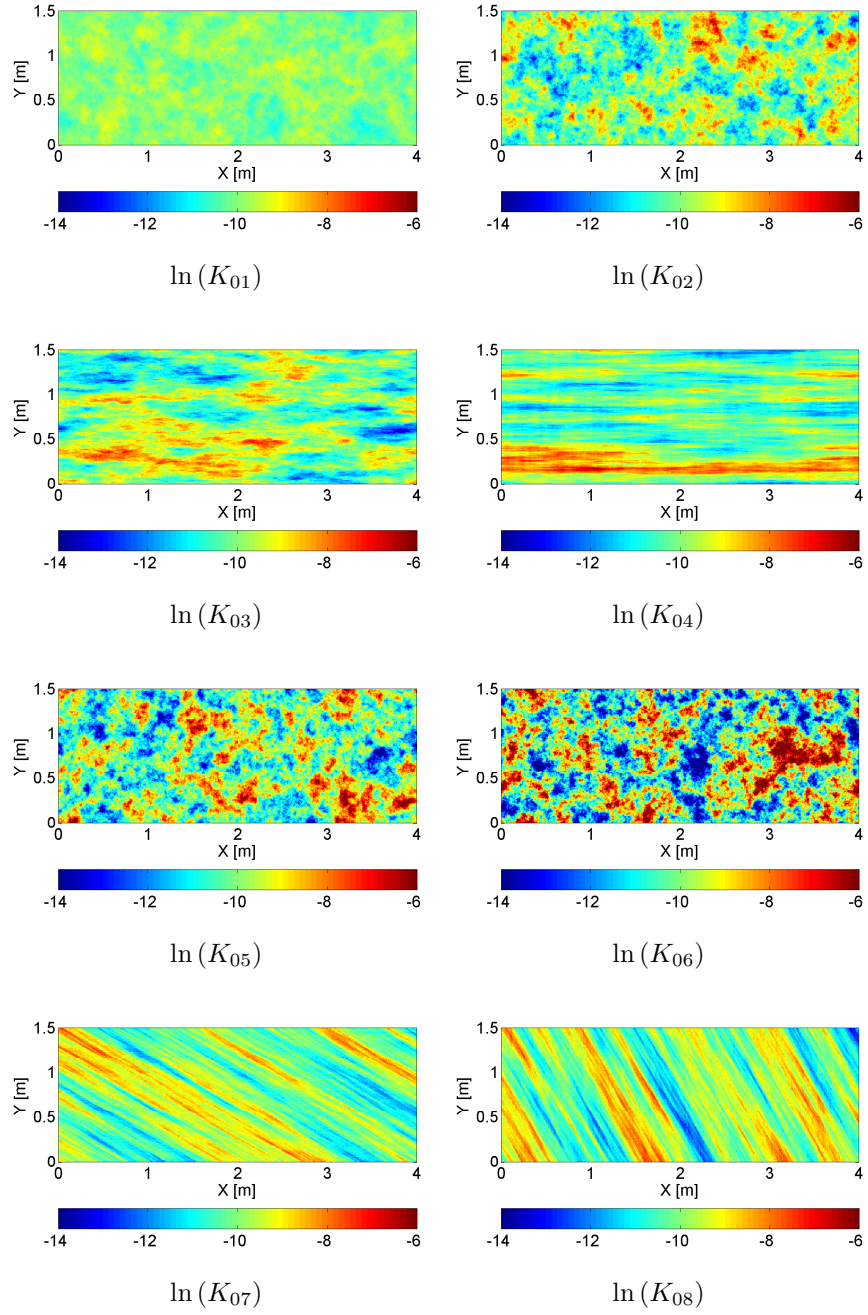
Figure 6.3: Set of Gaussian log-permeability fields

		K_{01}	K_{02}	K_{03}	K_{04}	K_{05}	K_{06}	K_{07}	K_{08}
K_g	$[10^{-5}$ m/s]	4.54	4.54	4.54	4.54	4.54	4.54	4.54	4.54
σ_Y^2	[-]	0.1	1.0	1.0	1.0	2.0	4.0	1.0	1.0
λ_1	[m]	0.1	0.1	0.5	2.0	0.1	0.1	2.0	2.0
λ_2	[m]	0.1	0.1	0.1	0.1	0.1	0.1	0.1	0.1
θ	[°]	0	0	0	0	0	0	30	60
$K_{g,o}$	$[10^{-5}$ m/s]	4.54	4.54	4.54	4.54	4.54	4.54	4.92	5.16
$\sigma_{Y,o}^2$	[-]	0.099	0.990	0.950	0.911	1.979	3.958	0.734	0.954

Table 6.1: Geometric mean K_g, variance σ_Y^2, correlation lengths λ_1 and λ_2 in direction 1 and 2 respectively, azimuth angle θ (counted positive if induces a clockwise rotation), observed geometric mean $K_{g,o}$ and observed variance $\sigma_{Y,o}^2$ of the Gaussian set of ln(K) fields

require a priori values of mean lengths, Table 6.2 only shows mean length and azimuth angle adopted for the second category (K_{09} to K_{13}). Fig. 6.4 shows the various examples generated.

Three-facies models are generated similarly, assuming a refinement in the second category of two-facies models. For that purpose, background categories were kept the same probability occurrence (i.e. 60 %) but second facies were this time assigned a probability occurrence of 30 %. Third facies have thus a probability occurrence of 10 % and were assigned a low permeability of 10^{-9} m/s. Moreover, transitions probabilities were chosen to ensure that third facies are mainly incorporated in second ones. The probability of having facies 2 just before or just after facies 3 was set to 70 % (in each principal direction). This yields a transition rate matrix of the form

$$T = \begin{bmatrix} * & * & * \\ * & -1/L_{i2} & 0.7/L_{i2} \\ * & 0.7/L_{i3} & -1/L_{i3} \end{bmatrix} \tag{6.7}$$

where i stands either for direction 1 or 2, L is the mean length and $*$ stands for background category data. Table 6.2 shows mean lengths adopted for each of the secondary facies. Azimuth angles are kept equal to 0 in each case. It can be observed that the Markov chains model for K_{14} in direction 1 corresponds to the example shown in Section 6.2.1. Its transition rate matrix is detailed in Eq. 6.6 and corresponding transition probabilities are shown in Fig. 6.1. The various examples generated are shown in Fig. 6.4.

Finally, a 17th example was set up from the two-facies example K_{11}. Two independent realizations of a ln(K) field with a zero mean, a variance of 0.5 and an isotropic exponential covariance function with a correlation length of 0.1 m were generated and each of them were added to one of the two facies, yielding a ln(K) field as shown in Fig. 6.5. Examples exhibiting non-stationarity in the variance or in the correlation length could also have been investigated [68], as well as other types of heterogeneous media [15, 58, 60, 125], but these are beyond the scope of the present study. It must be noted that, in order to avoid artifacts and boundary effects when generating highly correlated medium, each example was sampled in the center of a larger simulated medium (of a size being at least 5 times the mean/correlation lengths).
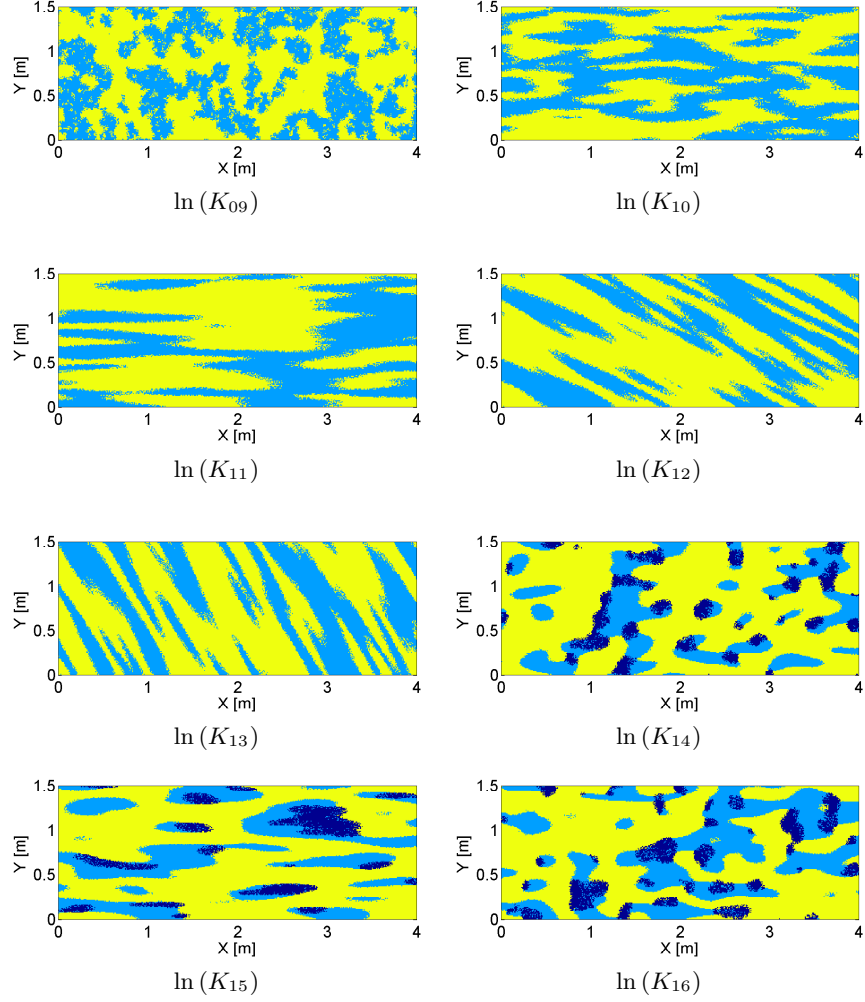
Figure 6.4: Set of two- and three-facies Markovian permeability fields. Light-colored region corresponds to first (background) material, intermediate-colored region corresponds to second material and dark-colored region corresponds to third material.
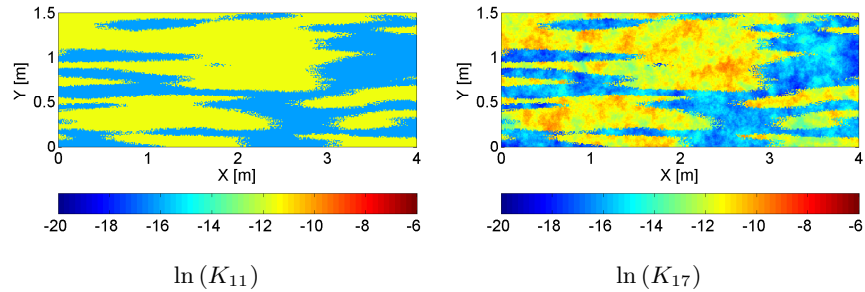
Figure 6.5: Two-facies model with and without intra-facies variability

		K_{09}	K_{10}	K_{11}	K_{12}	K_{13}	K_{14}	K_{15}	K_{16}	K_{17}
p_1	[%]	57.8	53.2	58.3	59.1	57.9	66.8	63.9	57.8	58.3
p_2	[%]	42.2	46.6	41.7	40.9	42.1	23.6	27.2	31.4	41.7
p_3	[%]	-	-	-	-	-	9.6	8.9	10.8	-
K_1	$[10^{-5}$ m/s]	1.00	1.00	1.00	1.00	1.00	1.00	1.00	1.00	1.00
K_2	$[10^{-7}$ m/s]	1.00	1.00	1.00	1.00	1.00	1.00	1.00	1.00	1.00
K_3	$[10^{-9}$ m/s]	-	-	-	-	-	1.00	1.00	1.00	-
L_{12}	[m]	0.1	0.5	1.0	1.0	1.0	0.5	0.5	1.0	1.0
L_{22}	[m]	0.1	0.1	0.1	0.1	0.1	0.1	0.1	0.1	0.1
L_{13}	[m]	-	-	-	-	-	0.1	0.5	0.1	-
L_{23}	[m]	-	-	-	-	-	0.1	0.1	0.1	-
θ	[°]	0	0	0	30	60	0	0	0	0
K_g	$[10^{-6}$ m/s]	1.43	1.20	1.47	1.52	1.44	1.39	1.26	0.87	1.47
σ_Y^2	[-]	5.17	5.26	5.16	5.13	5.17	9.26	9.02	9.86	5.66
$K_{g,o}$	$[10^{-6}$ m/s]	1.43	1.16	1.47	1.52	1.44	1.39	1.26	0.87	1.52
$\sigma_{Y,o}^2$	[-]	5.17	5.28	5.16	5.13	5.17	9.28	9.03	9.87	5.65
λ_1	[cm]	5.78	26.6	58.3	59.1	57.9	38.2	36.4	68.6	58.3
λ_2	[cm]	5.78	5.32	5.83	5.91	5.79	7.64	7.28	6.86	5.83

Table 6.2: Parameters sets used for the generation of Markovian permeability fields. K_g and σ_Y^2 are the theoretical values of the geometric mean and the variance, and $K_{g,o}$ and $\sigma_{Y,o}^2$ are the corresponding actual values. λ_1 and λ_2 are equivalent correlation lengths.

Geometric mean and variance of K fields exhibiting a multimodal distribution are computed from [152]

$$K_g = \exp\left(p_1 m_1 + p_2 m_2\right) \tag{6.8}$$
$$\sigma_Y^2 = p_1 \sigma_1^2 + p_2 \sigma_2^2 + (m_1 - m_2)^2 p_1 p_2 \tag{6.9}$$

where p_j, σ_j^2 and m_j are volumetric proportion, variance and mean of $\ln(K)$ of facies j. In the case of constant hydraulic conductivity inclusions, it reduces to [62]

$$\sigma_Y^2 = (m_1 - m_2)^2 p_1 p_2 \tag{6.10}$$

For a three-facies medium, Eqs. 6.8 and 6.10 extent to

$$K_g = \exp\left(p_1 m_1 + p_2 m_2 + p_3 m_3\right) \tag{6.11}$$
$$\sigma_Y^2 = (m_1 - m_2)^2 p_1 p_2 + (m_1 - m_3)^2 p_1 p_3 + (m_2 - m_3)^2 p_2 p_3 \tag{6.12}$$

Theoretical values are generally close to actual (observed) values, as shown in Table 6.2. In order to remain consistent with the approach adopted for K_{01} to K_{08}, only actual values will however be used in the remaining part of the analysis.

In order to apply stochastic theories to Markovian fields, it is necessary to establish the link between the mean length of a facies and an equivalent geo-statistical correlation length. It can be easily verified that a one-dimensional bimodal Markov chains model characterized by an inclusion length L and an

inclusion volumetric proportion p is equivalent to an exponential indicator co-variance model with a variance $p(1-p)$ and a correlation length $L(1-p)$. Therefore, in the case of an anisotropic bimodal Markovian field, equivalent correlation lengths are $\lambda_1 = p_1 L_{12}$ and $\lambda_2 = p_1 L_{22}$ (using the same notations adopted in Table 6.2). In the case of three-facies media, it will be assumed that the material with the largest volumetric proportion (besides the background formation) controls flow and transport. Volumetric proportions of remaining materials are then summed to compute equivalent correlation lengths. Effective permeability of tilted and subvertical formations such as K_{12} and K_{13} is computed according to Eq. 6.14. In the case of variable permeability within inclusions, as inclusions may be anisotropic while within-facies permeability variations may be isotropic (or vice-versa), it will also be assumed that the material with the largest volumetric proportion (which, in this case, is also the material with the largest correlation length) controls flow and transport.

The domain was discretized in 1 cm^3 cubic cells. Flow was solved using MODFLOW 2000 [96]. Transport was solved using the same particle tracking code that was used in Chapter 5, RWHet [115]. 1.000.000 particles are released uniformly over the cross-section $X = 0$ at time $t = 0$. As done in Chapter 5, particles are set evenly on a line crossing cell centers along the transverse direction (Fig. 6.2). In order to avoid particle reflexions on the upstream no-diffusion boundary, the flow domain is extended upwards over a distance of 1.5 m (Fig. 6.2), as was done in Chapter 5. Velocities in that zone are set equal to the velocities at the inlet boundary. Local dispersivities are both set equal to 1 cm and effective diffusion coefficient is $D^d = 10^{-9}$ m^2/s. Effective porosity is assumed constant and equal to 40 %.

6.3   Upscaling of flow

In this section, a few common analytical expressions from flow theories in heterogeneous media are confronted to numerical results. Whereas statistics of the velocity field in perfectly stratified aquifers are similar to those of the permeability field, this is not the case anymore in general two-dimensional heterogeneous situations. Therefore, before moving towards transport theories, one will first assess discrepancies between flow observations and corresponding theories, which might account for part of the potential discrepancy between observed and predicted concentration data.

6.3.1   Effective permeability

The permeability tensor of a two-dimensional $\ln(K)$ field characterized by an exponential correlation function is computed as [79]

$$K_i = K_g \left(1 + \sigma_Y^2 \left(\frac{1}{2} - g_i \right) \right) \quad i = 1, 2 \tag{6.13}$$

where $g_1 = \lambda_2/(\lambda_1 + \lambda_2)$ and $g_2 = \lambda_1/(\lambda_1 + \lambda_2)$. λ_1 and λ_2 are correlation lengths in direction 1 and 2 respectively. In the case of isotropic lognormal conductivity fields, variance has no influence on effective permeability and $K_{e,th}$ is equal to

		K_{01}	K_{02}	K_{03}	K_{04}	K_{05}	K_{06}	K_{07}	K_{08}
$K_{e,o}$	$[10^{-5}$ m/s$]$	4.54	4.38	5.76	7.10	4.27	3.56	5.43	4.00
$K_{e,t}$	$[10^{-5}$ m/s$]$	4.54	4.54	5.98	6.41	4.54	4.54	5.73	4.04

Table 6.3: Observed effective permeability $K_{e,o}$ of the Gaussian set of $\ln(K)$ fields. $K_{e,t}$ is the theoretical value computed using observed geometric mean and variance.

the geometric mean of the field K_g. Off-diagonal terms of the permeability tensor are null provided the principal directions of the flow field are aligned with the principal directions of the permeability tensor. If not, the effective permeability tensor in the flow coordinate systems reads [68]

$$\begin{bmatrix} K_X & K_{XY} \\ K_{YX} & K_Y \end{bmatrix} = \\ \begin{bmatrix} \cos(\theta) & \sin(\theta) \\ -\sin(\theta) & \cos(\theta) \end{bmatrix} \begin{bmatrix} K_1 & 0 \\ 0 & K_2 \end{bmatrix} \begin{bmatrix} \cos(\theta) & -\sin(\theta) \\ \sin(\theta) & \cos(\theta) \end{bmatrix} \quad (6.14)$$

where θ is given in Table 6.1.

Table 6.3 shows observed effective permeability values $K_{e,o}$ for each example. Theoretical values $K_{e,t}$ are also indicated. Classical limitations of first-order stochastic theories already appear for variances higher than 1 and when correlation length increases compared to domain length. For high variance, first-order approximations are not valid anymore and for high correlation length, the ergodic assumption is not fulfilled anymore. The discrepancy then increases between numerical and theoretical values. The general agreement between observed and theoretical values is however relatively good, with a mean and a maximum discrepancy of about 7 % and 27 % respectively.

Formally, it can also be shown that effective permeability is bounded by its arithmetic and harmonic means [53]. The arithmetic mean corresponds to a perfectly stratified aquifer oriented in the direction of flow and expresses for a log-normal field as $K_A = K_g \exp(\sigma^2/2)$. The harmonic mean corresponds to an aquifer perfectly stratified in a direction perpendicular to flow and expresses for a log-normal field as $K_H = K_g \exp(-\sigma^2/2)$. For long correlations, these expressions could also give a good approximation (or, at least upper and lower bounds) of effective permeability. Looking at K_{04}, for which the ratio of longitudinal to transverse correlation lengths is very high, one observes indeed that $K_{e,o} = 7.10\ 10^{-5} < K_A = 7.16\ 10^{-5}$ m/s and, looking at K_{08}, one observes that $K_{e,o} = 4.00\ 10^{-5} > K_H = 2.82\ 10^{-5}$ m/s.

In the case of Markovian fields, no analytical solution exists to compute effective permeability. So far, the latter has been only investigated through Monte Carlo simulations and no striking conclusion could be drawn from it, as ensemble-PDF of effective permeability were very discontinuous [68]. However, Rubin [152] proposed to use results from first-order stochastic theories developed for single-mode permeability distributions as a first approximation to effective permeability in a bimodal permeability field. Table 6.4 shows that the prediction of effective permeability of Markovian fields is worse than that of log-Gaussian field. Elfeki et al. [68] had already underlined that the char-

		K_{09}	K_{10}	K_{11}	K_{12}	K_{13}	K_{14}	K_{15}	K_{16}	K_{17}
$K_{e,o}$	$[10^{-6}$ m/s]	1.49	2.42	2.15	1.96	0.53	1.22	9.00	3.77	1.96
$K_{e,t1}$	$[10^{-6}$ m/s]	1.43	3.20	4.56	3.11	< 0	5.68	5.04	4.38	5.04
$K_{e,t2}$	$[10^{-6}$ m/s]	2.04	4.46	5.47	4.24	1.56	6.05	5.71	5.40	5.47

Table 6.4: Observed $K_{e,o}$ effective permeability of the Markovian set of K fields. $K_{e,t1}$ is the theoretical result from stochastic theories and $K_{e,t2}$ is the theoretical result obtained using the self-consistent approach.

acterization of Markovian field using Gaussian distributions could not yield valuable predictions. The results showed in Table 6.2 confirm this assertion, as the ratio of predicted to observed permeability goes up to 400 %. Even, a negative value of effective permeability was found for one of the tilted formations, meaning that flow should occur in the upgradient direction ! A clue to understanding such a bad behavior lies in the high variances calculated for Markovian fields. As two-facies models already had a variance of more than 5, adding a third facies of minor volumetric proportion led to a variance of 9. In this case, first-order stochastic theories suited to small variance problems cannot help anymore.

Another definition of K_e which does not require an assumption of low variability can be obtained using the self-consistent approach [53], described in Section 2.4. The effective permeability of a two-dimensional media computed using this model is given in Appendix A. An analytical expression to compute the effective permeability of a medium composed of two facies of constant permeability is given in Eq. A.21, whereas the corresponding solution for a three-facies medium is given in Eq. A.22. Results in Table 6.4 are not better, as the mean error on predicted effective permeability is about 100 %. The theoretical value computed for K_{17} neglects second-order variability of the field and is therefore supposed to underestimate K_e. It must be noted that the self-consistent approach is not really adapted to compute effective permeability of three-facies fields K_{14} to K_{16}, as clay inclusions are assumed to be embedded in facies 2, and do not constitute a separate family of inclusions in the background domain.

6.3.2 Velocity distributions

Uncertainty (or unpredictability) of effective permeability is tightly linked to uncertainty of mean longitudinal advective transport. Other features of the velocity distributions might however be of importance with respect to solute transport. First, the variance of the velocity field is directly linked to the scale effect in apparent dispersion, and controls the overall macroscale plume spreading. Then, global shapes of velocity distributions might reveal how biased and heavy-tailed concentration distributions could potentially be.

Statistics of the velocity fields are summarized in Table 6.5 and 6.6. A theoretical value of expected longitudinal velocity $\langle v_X \rangle$ can be found from effective permeability and mean gradient. For log-Gaussian permeability fields, $\langle v_Y \rangle$ is theoretically equal to zero, and can be indeed generally neglected compared

	K_{01}	K_{02}	K_{03}	K_{04}	K_{05}	K_{06}	K_{07}	K_{08}
$\langle v_{X,o}\rangle$ [10^{-7} m/s]	4.54	4.38	5.76	7.10	4.27	3.56	5.43	4.00
$\langle v_{Y,o}\rangle$ [10^{-9} m/s]	1.78	-1.45	21.2	8.48	-11.3	-16.8	-39.9	-35.2
$\sigma^2_{v_X,o}$ [10^{-13} m^2/s^2]	0.07	0.72	2.37	8.53	1.64	2.25	1.33	0.21
$\sigma^2_{v_Y,o}$ [10^{-13} m^2/s^2]	0.02	0.25	0.17	0.06	0.60	0.99	0.42	0.30
$\langle v_{X,t}\rangle$ [10^{-7} m/s]	4.54	4.54	5.98	6.41	4.54	4.54	-	-
$\langle v_{Y,t}\rangle$ [10^{-9} m/s]	0	0	0	0	0	0	-	-
$\sigma^2_{v_X,t}$ [10^{-13} m^2/s^2]	0.08	0.77	1.27	1.40	1.53	3.06	-	-
$\sigma^2_{v_Y,t}$ [10^{-13} m^2/s^2]	0.03	0.26	0.42	0.47	0.51	1.02	-	-

Table 6.5: Statistics of the velocity field of 2D log-Gaussian permeability fields. Subscript o refers to actual (observed) values and subscript t refers to theoretical values.

	K_{09}	K_{10}	K_{11}	K_{12}	K_{13}	K_{14}	K_{15}	K_{16}	K_{17}
$\langle v_{X,o}\rangle$ [10^{-8} m/s]	1.49	2.42	2.15	1.96	0.53	0.55	4.86	1.81	1.96
$\langle v_{Y,o}\rangle$ [10^{-9} m/s]	-0.98	-1.44	-0.12	-3.66	-0.63	-1.70	-6.33	-5.09	-0.48
$\sigma^2_{v_X,o}$ [10^{-16} m^2/s^2]	6.46	9.73	8.10	5.38	0.39	0.35	21.4	8.17	6.06
$\sigma^2_{v_Y,o}$ [10^{-16} m^2/s^2]	2.10	1.01	0.49	1.55	0.45	0.15	2.49	2.44	0.58
$\langle v_{X,t}\rangle$ [10^{-8} m/s]	1.43	3.20	4.57	3.11	< 0	5.69	5.05	4.38	5.03
$\langle v_{Y,t}\rangle$ [10^{-9} m/s]	0	0	0	-	-	0	0	0	0
$\sigma^2_{v_X,t}$ [10^{-16} m^2/s^2]	3.96	20.3	40.4	18.6	0.01	112	86.4	71.1	53.7
$\sigma^2_{v_Y,t}$ [10^{-16} m^2/s^2]	1.32	6.76	13.5	6.22	0.00	37.5	28.8	23.7	17.9

Table 6.6: Statistics of the velocity field of 2D Markovian permeability fields. Subscript o refers to actual (observed) values and subscript t refers to theoretical (stochastic) values.

to $\langle v_X\rangle$. For Markovian fields, $\langle v_Y\rangle$ cannot be negelected with respect to $\langle v_X\rangle$ anymore. This can be explained by the structure of the field itself. In heterogeneous media, flow is meandering between the zones of low permeability. In the case of Markovian fields, for values of mean length adopted in this study, only a few meanders can take place in the flow domain, and mean transverse velocity cannot converge to a null value. This effect can also be observed for log-Gaussian fields with a high variance. For tilted formations, expectively, $\langle v_Y\rangle$ is found to be negative (due to the inclination of the formations towards the negative part of the Y axis.

For a two-dimensional isotropic medium, first-order stochastic theories predict a longitudinal and a transverse velocity variance respectively equal to $\sigma^2_{v_X} = 3q^2\sigma^2_Y/8$ and $\sigma^2_{v_Y} = q^2\sigma^2_Y/8$, q being the specific discharge (or Darcy velocity) [79]. This leads to a ratio of 3/1 for longitudinal to transverse velocity variance, which is indeed the case for K_{01} (which is the only example that could correctly fit this theoretical result regarding ergodicity and variance value) and, to a lesser extent, for K_{02}, K_{05} and K_{06}. On the contrary, velocity variance of Markovian fields is totally mispredicted. If the ratio 3/1 is observed in a few cases (i.e. K_{09}, K_{12}, K_{14} and K_{16}), predicted velocity variance can exagerate the actual value by up to three orders of magnitude.

Figs. 6.6 to 6.8 illustrate several typical tendencies for velocity fields of log-
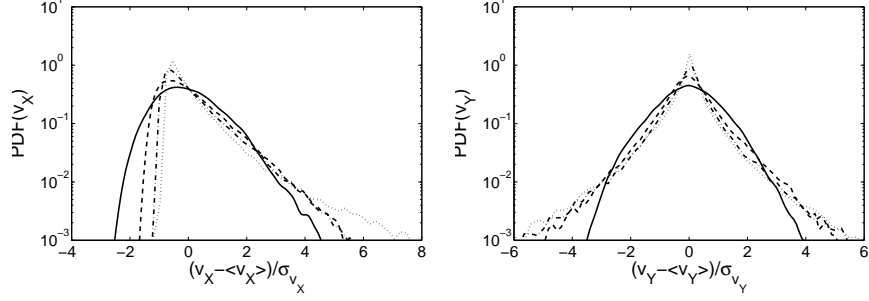
Figure 6.6: Influence of $\ln(K)$ variance on velocity distribution of log-Gaussian fields. $\sigma_Y^2 = 0.1$ (K_{01} - continuous line), $\sigma_Y^2 = 1$ (K_{02} - dashed line), $\sigma_Y^2 = 2$ (K_{05} - dot-dashed line) and $\sigma_Y^2 = 4$ (K_{06} - dotted line).
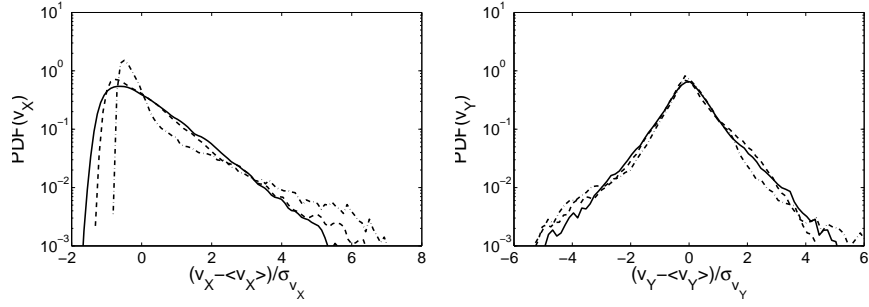
Figure 6.7: Influence of $\ln(K)$ correlation length on velocity distribution of log-Gaussian fields. $\lambda_1 = 0.1$ (K_{02} - continuous line), $\lambda_1 = 0.5$ (K_{03} - dashed line) and $\lambda_1 = 2.0$ (K_{04} - dot-dashed line).
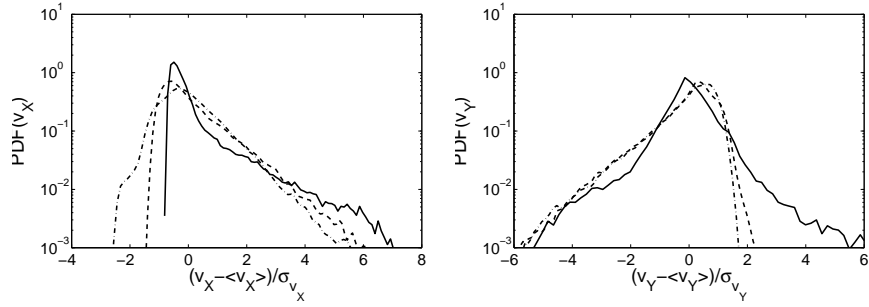
Figure 6.8: Influence of $\ln(K)$ orientation on velocity distribution of log-Gaussian fields. $\theta = 0°$ (K_{04} - continuous line), $\theta = 30°$ (K_{07} - dashed line) and $\theta = 60°$ (K_{08} - dot-dashed line).
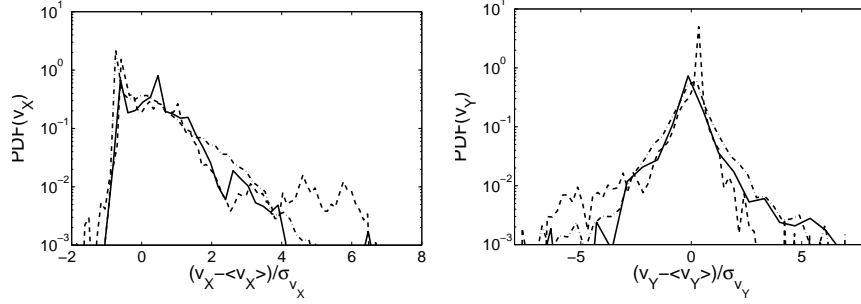
Figure 6.9: Influence of $\ln(K)$ variance on velocity distribution of Markovian fields. Two-facies without local variability (K_{11} - continuous line), Three-facies (K_{16} - dashed line) and two-facies with local variability (K_{17} - dot-dashed line).
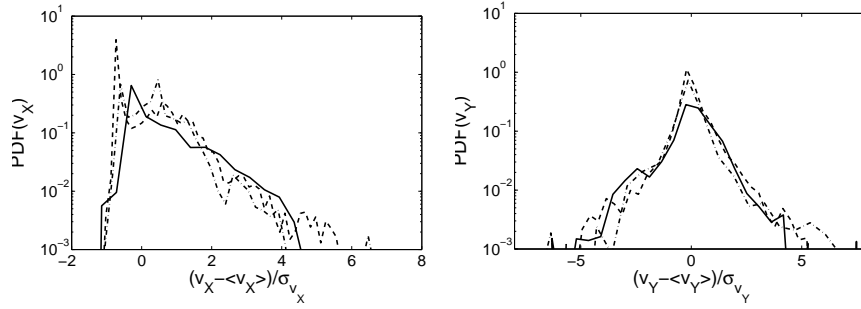
Figure 6.10: Influence of facies mean length on velocity distribution. $L_{12} = 0.1$ (K_{09} - continuous line), $L_{12} = 0.5$ (K_{10} - dashed line) and $L_{12} = 1.0$ (K_{11} - dot-dashed line).
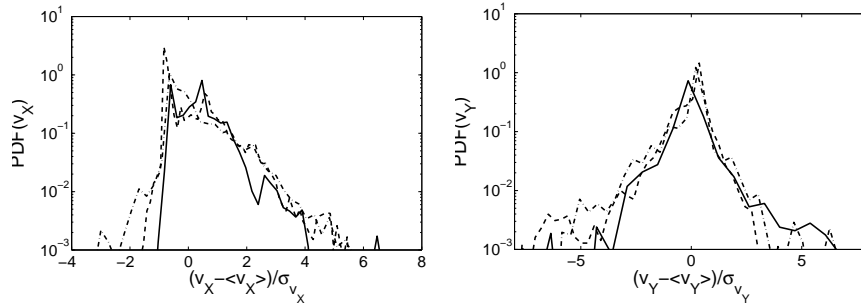
Figure 6.11: Influence of K field orientation on velocity distribution. $\theta = 0°$ (K_{11} - continuous line), $\theta = 30°$ (K_{12} - dashed line) and $\theta = 60°$ (K_{13} - dot-dashed line).
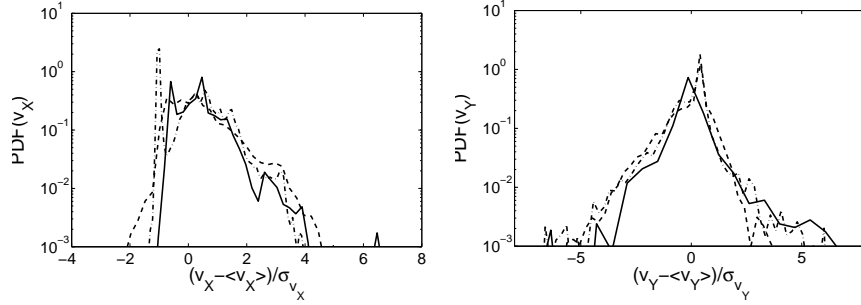
Figure 6.12: Influence of a third facies on velocity distribution. No facies (K_{11} - continuous line), Isotropic third facies (K_{14} - dashed line) and anisotropic third facies (K_{15} - dot-dashed line).

Gaussian cases. First, Fig. 6.6 shows that an increase of the variance yields a shift of longitudinal velocity distributions towards high velocities. The bias is sensitively increased, leading to non-Gaussian distributions [14, 157, 184]. The shape of transverse velocity distributions is relatively not influenced by the variance provided it is higher than 1 and, like in the simulations of Trefry et al. [184] and unlike those of Bellin et al. [14], does not exhibit a Gaussian shape (except for a small variance).

It can also be observed that longitudinal correlation length has an influence on the regularity of longitudinal velocity distributions (Fig. 6.7). A high correlation length means non-ergodic flow and biased distributions. On the contrary, for small lateral correlation lengths, no sensitive influence can be noticed on transverse velocity distributions. Fig. 6.8 also illustrates the effect of rotating the principal directions of K fields. Both longitudinal and transverse velocities tend to decrease for flow perpendicular to the formation.

Fig. 6.9 to 6.12 show velocity distributions of Markovian cases. Distributions are less smooth and less heavy-tailed, due to the discrete distribution of permeability. It is moreover difficult to identify tendencies.

Looking at figures and graphs shown it this section, it should be already possible to detect cases in which apparent dispersivity will reach a constant asymptotic value. For Gaussian longitudinal velocity distributions (i.e. with a strong downwards curvature), a large-scale fictional diffusion coefficient should be able to correctly model solute macroscale dispersion. When velocity distributions exhibit heavy tails, dispersivity is likely not to converge to an aymptotic value and CTRW models should be more appropriate to describe concentration distributions. Intermediate situations correspond to a longitudinal dispersivity that is likely to converge to an asymptotic macroscale value in the long run.

6.4   Upscaling of longitudinal dispersivity

In this section, upscaling methods and upscaled equations reviewed in Chapter 2 and Chapter 3 will be applied. A methodology similar to what was done

in Chapter 5 will be used. First, apparent dispersivity will be computed and presented. Then, efficiency of upscaling methods for apparent longitudinal dispersivity will be investigated. All of the methods presented in Chapter 2 will be investigated : stochastic (S), fractal (F) and inclusion (I) models (using a similar notation as in Chapter 5). Finally, upscaled transport equations derived in temporal and spatial CTRW frameworks (respectively TC and SC) will be applied. As no method to parametrize telegraph equations in 2D media could be identified in the literature, this type of model will not be used here, nor will mobile-immobile models (which were actually introduced in an attempt to analyze data presented in Part 3).

6.4.1   Numerical results

Due to the reduced domain size, it is not possible to use spatial moments to compute apparent dispersivity. The same method as in Chapter 5 is used to perform temporal moment analysis. Concentrations are averaged over the full aquifer cross-section (Fig. 6.2) and cumulative breakthrough curves are calculated. As stated previously, the aim of this study is not to apply theories under theoretical situations designed to validate them. On the contrary, boundary effects are present in real situations (e.g. due to the presence of the bedrock or impervious layers) and have an influence on flow and transport. Therefore, they will not be removed from this analysis. Apparent longitudinal dispersivity values obtained from BTC analysis is shown in Figs. 6.13 and 6.14 for log-Gaussian and Markovian fields respectively.

Compared to perfectly stratified examples investigated in Chapter 5, apparent dispersivity in log-Gaussian fields is less monotonic and it is not easy to discern whether macroscale Fickian behavior occurs or not. It must be noted that Trefry et al. [184] performed similar computations for much larger domains (over 200 correlation lengths) for similar variance values and did not obtain smoother curves. General theoretical trends are however observed in Fig. 6.13. For isotropic fields, normalized asymptotic dispersivity should be equal to 1 in Figs. 6.13.a. and b. In Fig. 6.13.c., it is observed that apparent dispersivity decreases when flow is tilted with respect to bedding, as predicted by theoretical models.

Apparent dispersivity of Markovian fields, like that of log-Gaussian fields, is found to be linearly proportional to variance (Fig. 6.14.a.). However, trends for other parameters are less obvious : it is difficult to conclude whether curves in Fig. 6.14.b. are surperimposed or not, there is no general trend for tilted formations and the influence of a third facies is not straigthforward to establish. It must be noted that negative apparent dispersivity values observed close to injection are probably due to numerical artifacts linked to spatial and temporal discretizations adopted.

6.4.2   Stochastic analysis

Asymptotic dispersivity computed within a stochastic framework is given in Eq. 2.29 for a general anisotropic situation, with a flow oriented at an angle θ with respect to the bedding. An analytical solution for transient dispersivity

a.

b.

c.
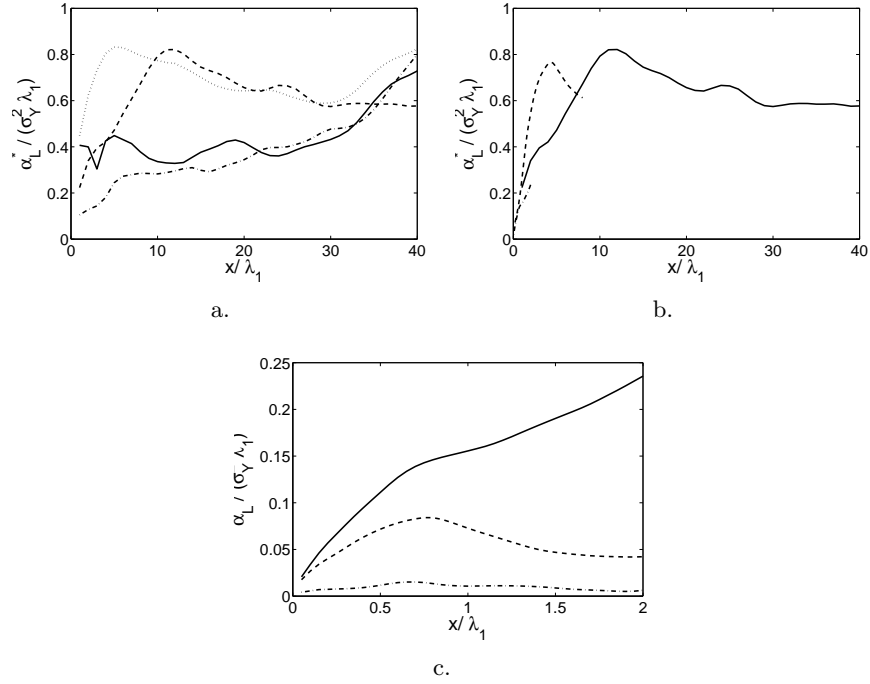
Figure 6.13: Apparent dispersivity of log-Gaussian fields. a. Influence of the variance (K_{01} : $\sigma_Y^2 = 0.1$, continuous line ; K_{02} : $\sigma_Y^2 = 1.0$, dashed line ; K_{05} : $\sigma_Y^2 = 2.0$, dot-dashed line and K_{06} : $\sigma_Y^2 = 4.0$, dotted line). b. Influence of the correlation length (K_{02} : $\lambda_1 = 0.1$, continuous line ; K_{03} : $\lambda_1 = 0.5$, dashed line and K_{04} : $\lambda_1 = 1.0$, dot-dashed line). c. Influence of the orientation angle (K_{04} : $\theta = 0°$, continuous line ; K_{07} : $\theta = 30°$, dashed line and K_{08} : $\theta = 90°$, dot-dashed line).
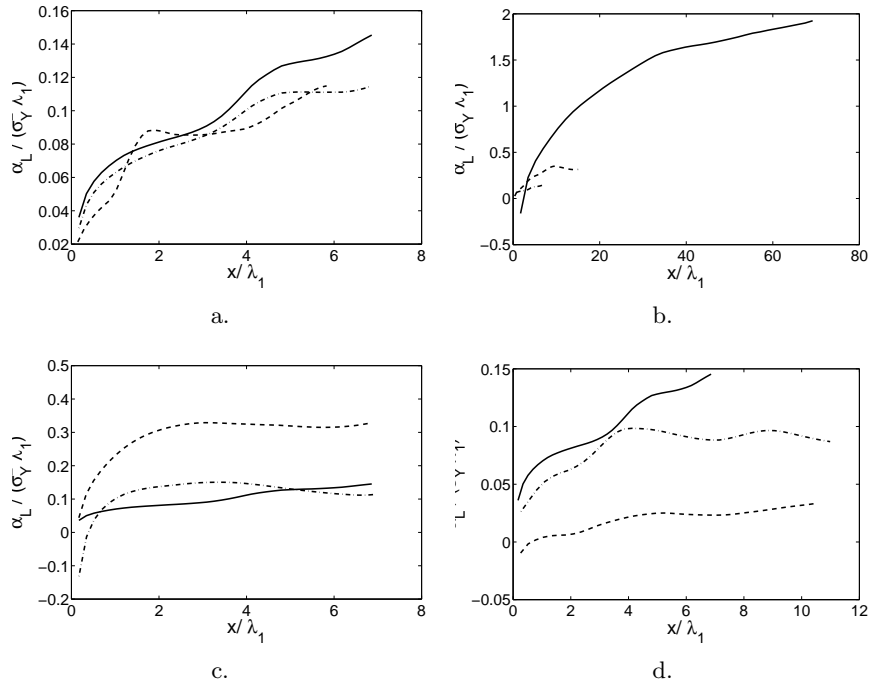
Figure 6.14: Apparent dispersivity of Markovian fields. a. Influence of the variance (K_{11} : $\sigma_Y^2 = 5.16$, continuous line ; K_{16} : $\sigma_Y^2 = 9.16$, dashed line and K_{17} : $\sigma_Y^2 = 5.66$, dot-dashed line). b. Influence of the mean length (K_{09} : $L_{12} = 0.5$, continuous line ; K_{10} : $L_{12} = 0.5$, dashed line and K_{11} : $L_{12} = 1.0$, dot-dashed line). c. Influence of the orientation angle (K_{11} : $\theta = 0°$, continuous line ; K_{12} : $\theta = 30°$, dashed line and K_{13} : $\theta = 90°$, dot-dashed line) d. Influence of a third facies (K_{11} : no third facies, continuous line ; K_{14} : isotropic third facies, dashed line and K_{15} : anisotropic third facies, dot-dashed line).

j	α_j	η_j	σ_j^2
1	λ_{in1}	p_1^2	σ_1^2
2	$\lambda_I \lambda_{in1} + (\lambda_I + \lambda_{in1})$	1	$p_1 p_2 \sigma_1^2$
3	λ_{in2}	p_b^2	σ_2^2
4	$\lambda_I \lambda_{in2} + (\lambda_I + \lambda_{in2})$	1	$p_1 p_2 \sigma_2^2$
5	λ_I	$(m_1 - m_2)^2$	$p_1 p_2$

Table 6.7: Coefficients for Eq. 6.15

is however only available in the isotropic case, for a flow parallel to the main principal direction of the permeability field (Eq. 2.28). It is proposed to assume that anistropy and flow orientation have a negligible effect on temporal development of macrodispersivity and that they only influence its asymptotic value. Theoretical parameters to be used with these equations are given in Tables 6.1 and 6.2.

For Markovian fields, the analytical solution of transient dispersivity proposed by Rubin [152] is also evaluated. This solution assumes that the permeability distribution is bimodal, that the global spatial structure is described by an exponential indicator variogram, and that intra-facies permeability is lognormally distributed and characterized by an exponential covariance function. The solution is derived in a two-dimensional isotropic case and reads [152]

$$\alpha_L^* = \sum_{j=1}^{5} \alpha_j \eta_j \sigma_j^2 \left[1 + \frac{3}{2 \exp(\tau_j) \tau_j^3} \left(2(\exp(\tau_j) - \tau_j - 1) - \exp(\tau_j) \tau_j^2 \right) \right] \quad (6.15)$$

where $\tau_j = vt/\alpha_j$ and with α_j, η_j and σ_j^2 defined in Table 6.7. λ_I is the (isotropic) correlation length of the indicator variogram (and therefore corresponds to $\lambda_1$ in Table 6.2. λ_{in1} and λ_{in2} are intra-facies (isotropic) correlation lengths, both equal to 0.1 m for K_{17} and zero otherwise. As done previously, subscripts 1 and 2 refer to facies number.

In the case of facies of constant permeability, $j = 5$ is the only remaining term in Eq. 6.15. Rubin [152] suggests that each of these terms represents a different source of spreading for solutes. $j = 1$ and $j = 3$ terms represent spreading due to intra-facies variability, $j = 2$ and $j = 4$ terms represent spreading due to irregularity of inclusions in space and $j = 5$ term represents spreading due to permeability contrasts at inclusion boundaries.

Table 6.8 shows computed values of ϵ_u. Values are of a similar order of magnitude as perfectly stratified cases, except for tilted formations and for long correlation lengths. For Markovian fields, the bimodal stochastic method provides however better upscaling results than the classical stochastic method with respect to apparent dispersivity. As in the perfectly stratified case, upscaling results do not seem to degrade for high variance. Results could not be plotted under graphical form, as parametric variations are less systematic than in Chapter 5.

Figs. 6.15 and 6.16 show ΔRMS_u for log-Gaussian and Markovian fields respectively. The mean migration velocity used to compute that indicator is the one characterizing the BTC measured at $X = 0.4$ m. The stochastic method

	K_{01}	K_{02}	K_{03}	K_{04}	K_{05}	K_{06}	K_{07}	K_{08}	
ϵ_u [%]	107	42.7	44.9	22.9	150	32.7	58.3	244	
	K_{09}	K_{10}	K_{11}	K_{12}	K_{13}	K_{14}	K_{15}	K_{16}	K_{17}
ϵ_{u1} [%]	30.2	91.1	92.1	68.1	1810	81.5	98.1	99.8	94.0
ϵ_{u2} [%]	61.3	61.9	57.2	85.2	52.3	101	52.8	76.3	55.9

Table 6.8: Results of the stochastic upscaling method. For Markovian fields, ϵ_{u1} is computed using the general analytical expression of dispersivity and ϵ_{u2} is computed using a bimodal stochastic framework.
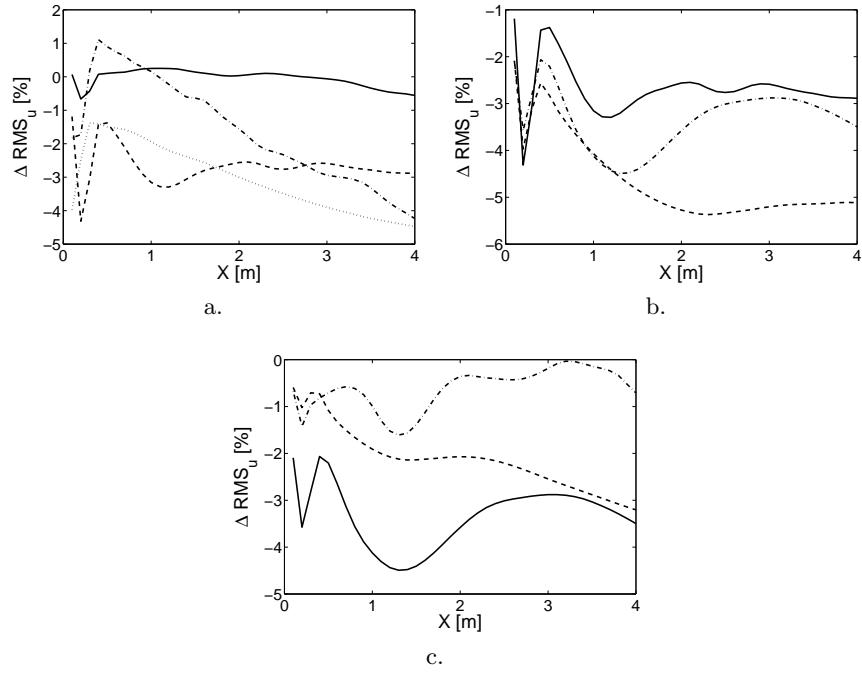
Figure 6.15: Improvement of S compared to the classical ADE for log-Gaussian fields. a. Influence of the variance ($K_{01} : \sigma_Y^2 = 0.1$, continuous line ; $K_{02} : \sigma_Y^2 = 1.0$, dashed line ; K_{05} : $\sigma_Y^2 = 2.0$, dot-dashed line and $K_{06} : \sigma_Y^2 = 4.0$, dotted line). b. Influence of the correlation length ($K_{02} : \lambda_1 = 0.1$, continuous line ; $K_{03} : \lambda_1 = 0.5$, dashed line and $K_{04} : \lambda_1 = 1.0$, dot-dashed line). c. Influence of the orientation angle ($K_{04} : \theta = 0°$, continuous line ; $K_{07} : \theta = 30°$, dashed line and $K_{08} : \theta = 90°$, dot-dashed line).

Figure 6.16: Improvement of S compared to the classical ADE for Markovian fields. a. Influence of the variance (K_{11} : $\sigma_Y^2 = 5.16$, continuous line ; K_{16} : $\sigma_Y^2 = 9.16$, dashed line and K_{17} : $\sigma_Y^2 = 5.66$, dot-dashed line). b. Influence of the mean length (K_{09} : $L_{12} = 0.1$, continuous line ; K_{10} : $L_{12} = 0.5$, dashed line and K_{11} : $L_{12} = 1.0$, dot-dashed line). c. Influence of the orientation angle (K_{11} : $\theta = 0°$, continuous line ; K_{12} : $\theta = 30°$, dashed line and K_{13} : $\theta = 90°$, dot-dashed line) d. Influence of a third facies (K_{11} : no third facies, continuous line ; K_{14} : isotropic third facies, dashed line and K_{15} : anisotropic third facies, dot-dashed line).

allow the upscaling of permeability, but the latter can induce an additional error on transport prediction (see Section 6.3). Temporal and spatial CTRW need local-scale BTC to be applied, and have therefore a direct access to actual effective permeability through concentration data. In order to keep upscaling results comparable, it was decided to use a direct measurement of advective transport. ΔRMS_u is found to be almost systematically negative, meaning that there is an improvement in model predictions compared to the classical ADE with local parameters. For log-Gaussian cases, the improvement increases when the variance of the correlation length increases, but decreases when flow is not oriented with the principal directions of the permeability field. For Markovian fields, ΔRMS_u is relatively small compared to values found for other examples, and it is decreasing when heterogeneity and complexity of soil structure increases. For tilted formations (i.e. K_{13}), ΔRMS_u is positive at each scale of observation.

		K_{01}	K_{02}	K_{03}	K_{04}	K_{05}	K_{06}	K_{07}	K_{08}
H_X	[-]	0.04	0.13	0.14	0.29	0.06	0.09	0.06	0.12
95 % CI [± %]		190	35.1	70.3	17.7	151	67.0	170	47.6
H_Y	[-]	0.08	0.14	0.10	0.13	0.08	0.06	0.02	0.15
95 % CI [± %]		55.5	31.5	63.2	35.8	70.6	86.6	383	38.9
$\hat{H}$	[-]	0.06	0.14	0.12	0.21	0.07	0.07	0.04	0.13
α_X/α_Y [-]		1.00	1.00	1.21	1.50	1.00	1.00	1.75	0.09

Table 6.9: Hurst coefficient estimates of log-Gaussian permeability fields in X and Y directions

		K_{09}	K_{10}	K_{11}	K_{12}	K_{13}	K_{14}	K_{15}	K_{16}	K_{17}
H_X	[-]	0.04	0.07	0.04	0.08	0.09	0.09	0.06	0.10	0.15
95 % CI [± %]		89.7	49.4	111	48.5	52.5	67.8	110	47.2	24.7
H_Y	[-]	0.09	0.12	0.14	0.12	0.07	0.11	0.11	0.13	0.06
95 % CI [± %]		43.1	28.2	24.4	30.8	70.0	70.1	43.5	37.1	74.4
$\hat{H}$	[-]	0.06	0.09	0.09	0.10	0.08	0.10	0.09	0.12	0.10
α_X/α_Y [-]		1.00	0.76	0.53	0.82	1.12	0.90	0.73	0.87	1.46

Table 6.10: Hurst coefficient estimates of Markovian permeability fields in X and Y directions

6.4.3 Fractal methods

Methods for the estimation of Hurst coefficients of multidimensional fields are relatively scarce in the literature. The straightforward method adopted here consists in sampling all rows and columns from the field and applying one-dimensional methods [15]. Tables 6.9 and 6.10 show the results of the dispersional analysis. As the number of data was sufficient, there was no need to use bin shifting to multiply to number of data series to include in the analysis.

For log-Gaussian fields, H estimates are found to be close to 0. They seem to increase with λ and seem to be relatively independent of the variance. Uncertainty is higher for low $\hat{H}$, which can also be observed from anisotropy. Indeed, as H increases when correlation increases, one expects the ratio H_X/H_Y to follow the same trend as λ_X/λ_Y. For small correlation, it is not the case (see e.g. K_{01} and K_{06}), whereas it is for larger correlation (see e.g. K_{03}, K_{04}, K_{07} and K_{08}).

Markovian fields with constant permeability inclusions are more difficult to characterize using fractal tools. Indeed, for small bins, permeability increments are null. The corresponding bin mean is zero for all bins, yielding a standard deviation equal to zero that cannot accomodate a logarithmic transformation. The solution to this issue is to exclude smallest bins from the analysis.

The analytical solution of transient dispersivity is only available in the perfectly stratified case (Eq. 2.43). This solution will be used for anisotropic cases only. Asymptotic theoretical values are available in the isotropic case (Eq. 2.44) and in the anisotropic case for flow parallel and perpendicular to the bedding (respectively Eqs. 2.46 and 2.46). Intermediate orientation cases K_{07},

	K_{01}	K_{02}	K_{03}	K_{04}	K_{05}	K_{06}	K_{07}	K_{08}	
ϵ_u [%]	63.4	139	62.0	42.1	145	15.9	32.4	30.2	

	K_{09}	K_{10}	K_{11}	K_{12}	K_{13}	K_{14}	K_{15}	K_{16}	K_{17}
ϵ_u [%]	44.8	48.3	33.2	62.0	20.2	1300	90.6	51.7	153

Table 6.11: Results of the fractal upscaling method.

K_{08}, K_{12} and K_{13} will be solved by assuming $\theta = 30° \approx 0°$ and $\theta = 60° \approx 90°$.

Strictly speaking, Eqs. 2.46 and 2.47 are valid for anisotropic fractal media with equal fractal dimensions along horizontal and vertical directions. The fractal anisotropy ratio α_X/α_Y represents the ratio of relative hydraulic conductivity variation in direction X and Y. Zhan and Wheatcraft [201] indicate that in general, if $\alpha_X > \alpha_Y$, the statistical hydraulic conductivity variation in direction X is smaller than in direction Y or, in other words, the medium exhibits a more pronounced fractal behavior in the transverse direction and should be characterized using a smaller Hurst coefficient in that direction. As, moreover, $\alpha_X^2 + \alpha_Y^2 = 1$, it is proposed to adopt $\hat{H} = (H_X + H_Y)/2$, $\alpha_X = \sqrt{(H_X/(H_X + H_Y))}$ and $\alpha_Y = \sqrt{(H_Y/(H_X + H_Y))}$. In the case of isotropic medium, the ratio α_X/α_Y was forced to 1.00. It must be noted that if α_X/α_Y is positively correlated with λ_X/λ_Y for log-Gaussian permeability fields, it is correlated with its inverse for Markovian field. Fractal cutoff limit L_m will be set equal to 4.

Table 6.11 shows the results of the fractal upscaling method. Prediction of apparent dispersivity is of a similar accuracy as the stochastic method, and yields much better results than the stochastic method for tilted formations (at least for log-Gaussian fields). It must be emphasized that stronger assumptions than in the stochastic framework are made to compute analytical expressions of dispersivity. As in Chapter 5, although uncertainty on fractal parameters is higher than uncertainty on stochastic parameters, upscaling of apparent dispersivity is of a similar quality.

Figs. 6.17 and 6.18 show values of ΔRMS_u. The modelling improvement increases in highly heterogeneous cases and decreases when flow is not oriented with the principal directions of the permeability field. For log-Gaussian fields, ΔRMS_u is always negative, whereas for Markovian fields, ΔRMS_u is positive at short distances, but decreases and eventually becomes negative at large distance. Thus, there seems to be a scale limit under which the fractal upscaling method is not efficient, this limit being in this case between 1/10 to 1/2 of the total domain length.

6.4.4 Inclusion models

As already mentioned, Dagan et al. [55] state that, provided the distribution of ellipse sizes and permeabilities is correctly chosen, any permeability distribution and any covariance function can be approximated by an inclusion model. As the determination of this appropriate ellipse distribution is beyond the scope of this study, inclusion models will only be applied to Markovian fields.
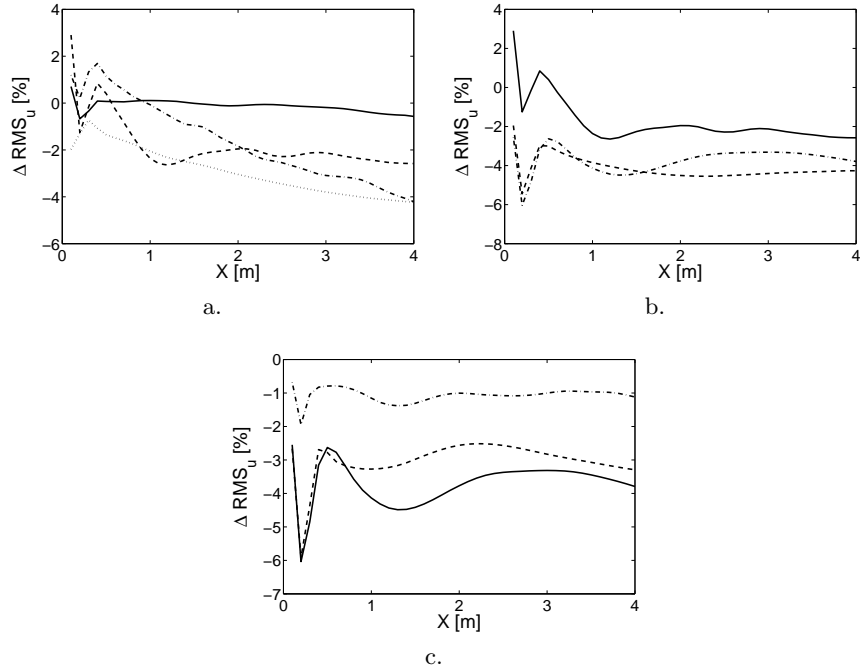
Figure 6.17: Improvement of F compared to the classical ADE for log-Gaussian fields. a. Influence of the variance ($K_{01} : \sigma_Y^2 = 0.1$, continuous line ; $K_{02} : \sigma_Y^2 = 1.0$, dashed line ; K_{05} : $\sigma_Y^2 = 2.0$, dot-dashed line and $K_{06} : \sigma_Y^2 = 4.0$, dotted line). b. Influence of the correlation length ($K_{02} : \lambda_1 = 0.1$, continuous line ; $K_{03} : \lambda_1 = 0.5$, dashed line and $K_{04} : \lambda_1 = 1.0$, dot-dashed line). c. Influence of the orientation angle ($K_{04} : \theta = 0°$, continuous line ; K_{07} : $\theta = 30°$, dashed line and $K_{08} : \theta = 90°$, dot-dashed line).
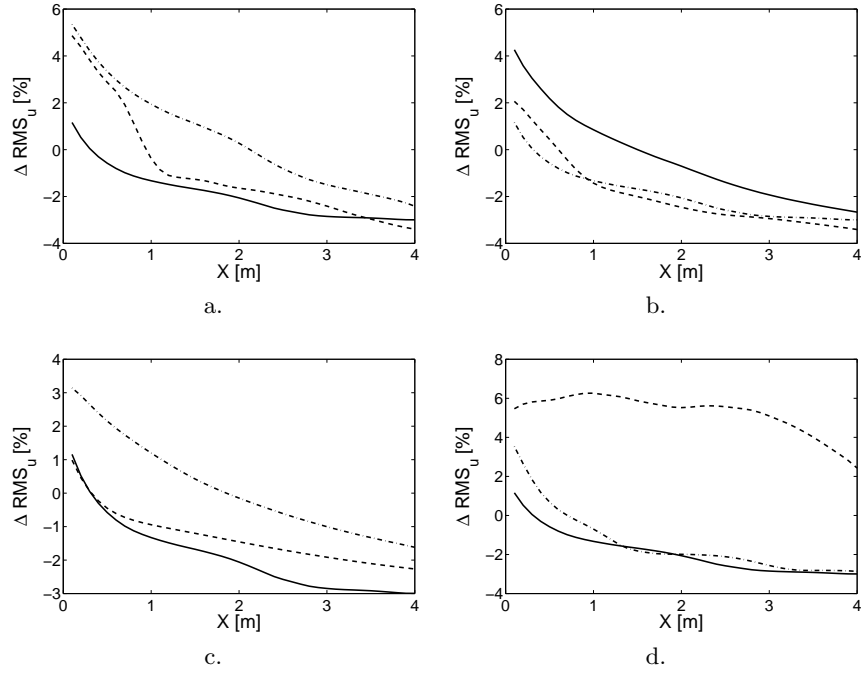
Figure 6.18: Improvement of F compared to the classical ADE for Markovian fields. a. Influence of the variance ($K_{11} : \sigma_Y^2 = 5.16$, continuous line ; $K_{16} : \sigma_Y^2 = 9.16$, dashed line and $K_{17} : \sigma_Y^2 = 5.66$, dot-dashed line). b. Influence of the mean length ($K_{09} : L_{12} = 0.1$, continuous line ; $K_{10} : L_{12} = 0.5$, dashed line and $K_{11} : L_{12} = 1.0$, dot-dashed line). c. Influence of the orientation angle ($K_{11} : \theta = 0°$, continuous line ; $K_{12} : \theta = 30°$, dashed line and $K_{13} : \theta = 90°$, dot-dashed line) d. Influence of a third facies (K_{11} : no third facies, continuous line ; K_{14} : isotropic third facies, dashed line and K_{15} : anisotropic third facies, dot-dashed line).

|	[m]	K_{09}	K_{10}	K_{11}	K_{12}	K_{13}	K_{14}	K_{15}	K_{16}	K_{17}
$\alpha_{L,1}$	[m]	0.169	1.606	11.07	11.38	1.029	0.911	7.852	1.507	11.07
$\alpha_{L,2}$	[m]	1.102	15.32	40.84	41.51	6.341	21.00	19.77	40.31	40.84
$\alpha_{L,3}$	[m]	-	-	-	-	-	28182	21437	20122	-
α_L^*	[m]	0.563	8.026	23.48	23.70	3.266	2711	1918	2187	23.48
ϵ_u	[%]	33.3	2976	8421	3042	546	4242800	765430	456520	8668

Table 6.12: Results of the inclusion upscaling model.

The analytical solution for flow tilted with respect to the bedding was not implemented. Therefore, theoretical apparent dispersivity in cases K_{07}, K_{08}, K_{12} and K_{13} will be again determined by assuming $\theta = 30° \approx 0°$ and $\theta = 60° \approx 90°$. Table 6.12 show predicted asymptotic dispersivities for Markovian fields. Contribution of each facies is indicated, as well as total apparent dispersivity. As mentioned by Dagan and Lessoff [56] and by Dagan et al. [55], the apparent dispersivity computed for high permeability contrast (typically for $\kappa < 10^{-2}$) is limited by diffusion. Values indicated for the third facies are thus unrealistically high. Regarding ϵ_u values, apparent dispersivity is however exaggerated even for smaller permeability contrast. The only case in a relative agreement with predicted values is K_{09}, for which it must be moreover noted that the largest observed dispersivity values are about 0.57 m, which is close to the value obtained by the self-consistent method. Regarding the overall bad upscaling capacity of the method, no attempt to compute ΔRMS_u will be done.

6.5 Application of upscaled transport equations

6.5.1 Characterization using temporal FADE

A similar method as that used in Chapter 5 is applied. Local transport parameters are determined from the simultaneous analysis of two local-scale BTC's (observed respectively at $X = 0.1$ m and $X = 0.4$ m). Results are reported in Tables 6.13 and 6.14 for log-Gaussian and Markovian fields respectively. As done previously, characteristic velocities $1/C_1$ also obtained from the BTC analysis are expressed as $v_a = v_m C_1$, with v_m being a mean velocity computed from the observed geometric mean of the $\ln(K)$ field.

For log-Gaussian fields, β_t is found to be lower than observed for stratified cases, indicating a higher level of heterogeneity, even for low variance cases. It is moreover found to be constant and equal to 1, whatever be the values of variance, correlation length and orientation angle. This might indicate that transport is mainly controlled by advection and that local dispersion and diffusion play a negligible role. Unlike in the stratified case, v_a is found to be relatively constant too, and no clear correlation can be established between this parameter and the soil structure. ϵ_u values are also indicated in Table 6.13. For log-Gaussian fields, except for higher variance (> 1) and higher correlation lengths (> 0.5), they are found to be relatively high compared to other methods. On the contrary, for Markovian fields, ϵ_u is found to be particularly

	K_{01}	K_{02}	K_{03}	K_{04}	K_{05}	K_{06}	K_{07}	K_{08}
β_t [-]	1.05	1.01	1.01	1.01	1.01	1.02	1.01	0.99
v_a [-]	0.30	2.55	3.25	3.57	2.34	1.94	3.35	1.37
ϵ_u [%]	1642	293	36.7	75.5	146	52.8	291	702

Table 6.13: Results of TC for log-Gaussian fields.

	K_{09}	K_{10}	K_{11}	K_{12}	K_{13}	K_{14}	K_{15}	K_{16}	K_{17}
β_t [-]	1.03	1.07	1.07	0.97	0.92	1.33	1.09	1.09	1.08
v_a [-]	3.04	0.35	0.33	1.64	1.99	0.37	0.08	0.15	0.39
ϵ_u [%]	20.3	34.4	33.2	36.7	50.7	25.4	46.9	71.6	30.4

Table 6.14: Results of TC for Markovian fields.

low.

Figs. 6.19 and 6.18 show the values of ΔRMS_u. It is found to be negative for distances smaller than 40 cm (i.e. the scale at which transport parameters were determined) and positive for larger distances. This observation is comparable to what was obtained in stratified cases, where a scale limit was observed.

6.5.2   Characterization using spatial FADE

As similar method as in Chapter 5 is also used here. β_x is obtained from the comparison of apparent dispersivity at $X = 0.1$ and $X = 0.4$ and is reported in Tables 6.15 and 6.16. In this case, the characteristic length is computed according to $\lambda_B = (\mathcal{D}_x/v_m)^{1/(1-\beta_x)}$, v_m being defined similarly as in previous section. For log-Gaussian fields, contrary to β_t, β_x is found to be linked to heterogeneity : it is close to 2 for K_{01} and decreases for increasing variance and correlation length. It is also found to increase with the orientation angle. Characteristic lengths are found to increase with variance, but not with correlation length. Bias is most of the time close to zero. ϵ_u is found to be relatively low, in every case. For Markovian fields, β_x values are lower. Characteristic lengths are much more variable and bias is also negative

Values of ϵ_u are relatively low, and ΔRMS_u, shown in Figs. 6.21 and 6.22, are also relatively good. However, the analytical solution of the space-FADE (which is actually a semi-analytical solution involving integrals which have to be computed numerically) is prone to high numerical errors for $\beta_x < 1$ and was not computed for K_{09}, K_{10}, K_{12}, K_{13} and K_{14}.

6.6   Conclusion

The scale-effect of apparent longitudinal dispersivity was simulated using a numerical model, for various heterogeneous synthetic aquifers. Both log-Gaussian and Markovian permeability fields were tested. Log-Gaussian fields are widely investigated in the literature (e.g. Trefry et al. [184]) but relatively few results are presented for permeability fields exhibiting larger variance and preferential
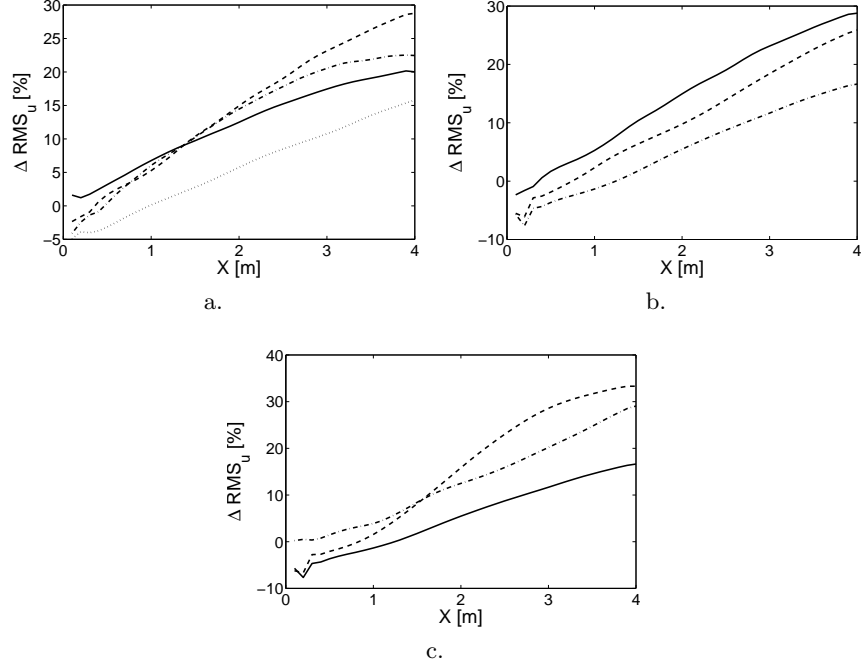
Figure 6.19: Improvement of TC compared to the classical ADE for log-Gaussian fields. a. Influence of the variance ($K_{01} : \sigma_Y^2 = 0.1$, continuous line ; $K_{02} : \sigma_Y^2 = 1.0$, dashed line ; K_{05} : $\sigma_Y^2 = 2.0$, dot-dashed line and $K_{06} : \sigma_Y^2 = 4.0$, dotted line). b. Influence of the correlation length ($K_{02} : \lambda_1 = 0.1$, continuous line ; $K_{03} : \lambda_1 = 0.5$, dashed line and $K_{04} : \lambda_1 = 1.0$, dot-dashed line). c. Influence of the orientation angle ($K_{04} : \theta = 0°$, continuous line ; K_{07} : $\theta = 30°$, dashed line and $K_{08} : \theta = 90°$, dot-dashed line).

	K_{01}	K_{02}	K_{03}	K_{04}	K_{05}	K_{06}	K_{07}	K_{08}
β_x [-]	1.94	1.37	1.16	1.15	1.44	1.41	1.25	1.43
λ_B [m]	44.4	198	294	116	196	342	241	520
γ_B [-]	0.99	−0.08	−0.19	−0.04	0.03	−0.53	0.09	−0.07
ϵ_u [%]	28.0	31.4	75.4	62.4	44.0	59.1	47.5	65.9

Table 6.15: Results of the spatial CTRW upscaling method for log-Gaussian fields.

	K_{09}	K_{10}	K_{11}	K_{12}	K_{13}	K_{14}	K_{15}	K_{16}	K_{17}
β_x [-]	0.89	1.02	1.43	0.98	0.65	0.52	1.34	1.39	1.37
λ_B [m]	-	-	27.4	-	-	-	0.99	11.8	44.6
γ_B [-]	-	-	−0.99	-	-	-	−0.99	−0.99	−0.99
ϵ_u [%]	-	-	76.4	-	-	-	323	25.4	70.7

Table 6.16: Results of the spatial CTRW upscaling method for Markovian fields.
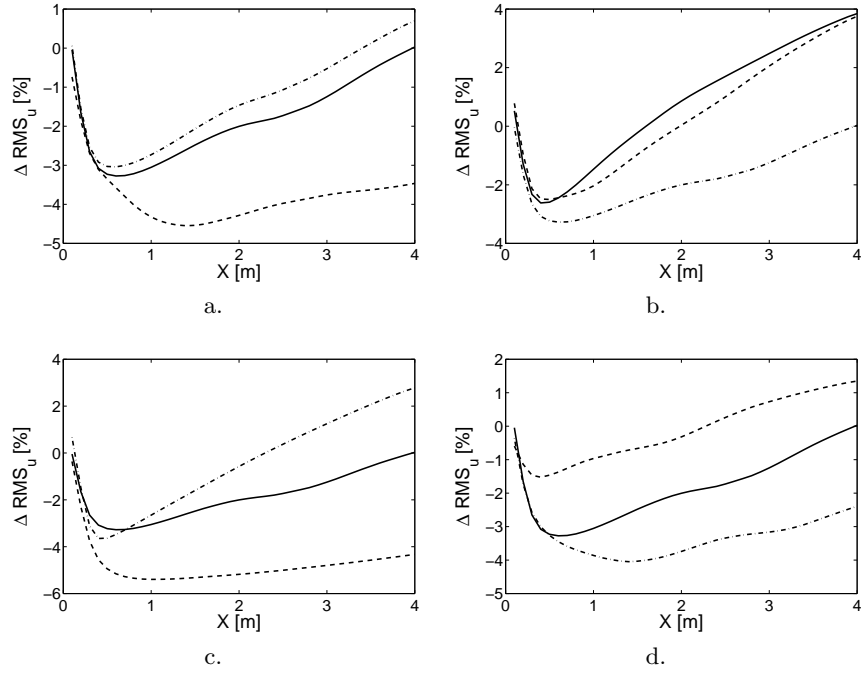
Figure 6.20: Improvement of TC compared to the classical ADE for Markovian fields. a. Influence of the variance ($K_{11} : \sigma_Y^2 = 5.16$, continuous line ; $K_{16} : \sigma_Y^2 = 9.16$, dashed line and $K_{17} : \sigma_Y^2 = 5.66$, dot-dashed line). b. Influence of the mean length ($K_{09} : L_{12} = 0.1$, continuous line ; $K_{10} : L_{12} = 0.5$, dashed line and $K_{11} : L_{12} = 1.0$, dot-dashed line). c. Influence of the orientation angle ($K_{11} : \theta = 0°$, continuous line ; $K_{12} : \theta = 30°$, dashed line and $K_{13} : \theta = 90°$, dot-dashed line) d. Influence of a third facies ($K_{11} :$ no third facies, continuous line ; $K_{14} :$ isotropic third facies, dashed line and $K_{15} :$ anisotropic third facies, dot-dashed line).
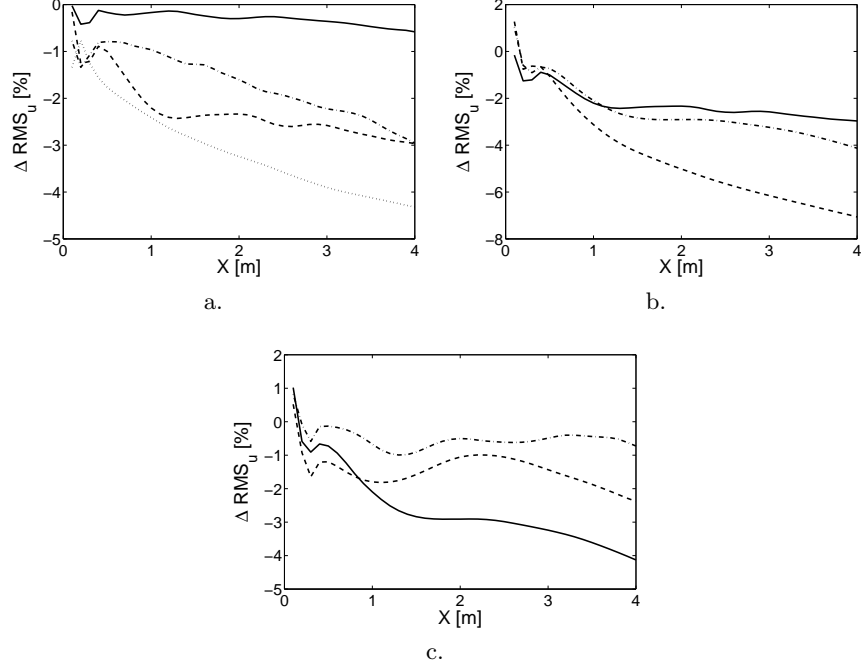
Figure 6.21: Improvement of the spatial CTRW upscaling method compared to the classical ADE for log-Gaussian fields. a. Influence of the variance ($K_{01} : \sigma_Y^2 = 0.1$, continuous line ; $K_{02} : \sigma_Y^2 = 1.0$, dashed line ; $K_{05} : \sigma_Y^2 = 2.0$, dot-dashed line and $K_{06} : \sigma_Y^2 = 4.0$, dotted line). b. Influence of the correlation length ($K_{02} : \lambda_1 = 0.1$, continuous line ; $K_{03} : \lambda_1 = 0.5$, dashed line and $K_{04} : \lambda_1 = 1.0$, dot-dashed line). c. Influence of the orientation angle ($K_{04} : \theta = 0°$, continuous line ; $K_{07} : \theta = 30°$, dashed line and $K_{08} : \theta = 90°$, dot-dashed line).
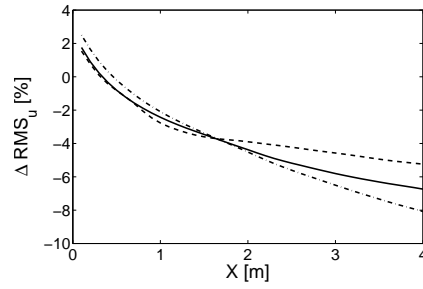

Figure 6.22: Improvement of the spatial CTRW upscaling method compared to the classical ADE for Markovian fields. Influence of the variance ($K_{11} : \sigma_Y^2 = 5.16$, continuous line ; $K_{16} : \sigma_Y^2 = 9.16$, dashed line and $K_{17} : \sigma_Y^2 = 5.66$, dot-dashed line).

	Log-Gaussian fields		Markovian fields	
	ϵ_u	ΔRMS_u	ϵ_u	ΔRMS_u
S	Correct upscaling in all cases		Correct upscaling in all cases	Non-optimal upscaling for tilted formations
F	Correct upscaling in all cases		Correct upscaling in all cases	Limit scale below which the quality of prediction decreases
I			Systematic over-estimation of longitudinal dispersivity	
TC	Non-optimal upscaling for low heterogeneity and tilted cases. Correct upscaling otherwise.	Systematic mis-prediction of concentration distributions	Correct upscaling in all cases	Limit scale beyond which the quality of prediction decreases
SC	Correct upscaling in all cases		Numerical instabilities in analytical solutions for $\beta_x < 1$. Correct upscaling otherwise.	

Table 6.17: Summary of main observations for upscaling methods and upscaled equations applied to 2D media.

pathways flow architecture (e.g. Elfeki et al. [68], Liu et al. [123] or Zinn and Harvey [206]). From this point of view, as well as regarding the range of structural parameters investigated (i.e. large correlation length), the simulations performed in this chapter are relatively original.

6.6.1   Comparison of methods and models

Results concerning upscaling of transport are summarized in Table 6.17. Main observations made when applying each model are recalled here, with an emphasis on the quality of predictions of apparent dispersivity (i.e. observations linked to ϵ_u) and of concentration distributions (i.e. observations linked to ΔRMS_u).

First, methods to predict effective permeability of log-Gaussian heterogeneous fields are relatively efficient. Even for high variance, high correlation length or tilted cases, the stochastic approach allowed a relatively correct upscaling of permeability. The method also yields good performance with respect to effective permeability of Markovian fields, provided flow is parallel to the bedding. Surprisingly, the self-consistent approach, which is theoretically better suited to situations where permeability distributions are multimodal, yielded less adequate effective permeability values, except in the particular case of flow occuring at an angle with respect to the bedding.

Although the prediction of apparent dispersivity generally reaches a reasonable precision, ΔRMS_u values are particularly low, and can even become positive in particular cases for several models (S, F and TC). This indicates that a bad prediction of advection transport might be the source of discrepancy. Indeed, even if a migration velocity corresponding to the breakthrough

curve at $X = 0.4$ m was adopted, this value might not be representative of the long-term velocity of the solute plume (which has to be constant since all investigated K fields are stationary random fields). For the range of correlation lengths used, flow and transport are not necessarily ergodic at such a small distance from injection and one does not expect the velocity experienced by the particle plume to be representative of the whole velocity distribution.

The non-optimal behavior of temporal CTRW is also linked to this issue. β_t values obtained from the joint analysis of $X = 0.1$ m and $X = 0.4$ m BTC mainly reflect the mean velocity difference between both curves rather than the rate of narrowing of concentration distributions. This is why β_t values were all found to be close to 1. The model then assumes a constant decrease in apparent velocity, and upscaling results degrade for large times as predicted BTC are more and more shifted compared to observed BTC. This is reflected by the increasing value of ΔRMS_u for this model. Such a result would plead for an explicit description of advection, like in other models.

Although space-FADE methods seem to have a higher upscaling efficiency, their analytical solutions are prone to numerical difficulties in highly heterogeneous cases. This indicates that upscaling methods for apparent dispersivity, to be used with well-known analytical solutions of the classical ADE, might be more interesting from a practical point of view. Moreover, regarding the general similarity between stochastic and fractal methods, and taking into account that part of the investigated examples are log-Gaussian fields typically suited for stochastic analysis, results obtained here would indicate that fractal methods should be considered with a regained interest. The fractal method seem to be general enough to depict with a sufficient accuracy any type of heterogeneity and to allow transport upscaling with a relative confidence.

6.6.2 Recommendation for further studies

In this section, several observations are made with respect to issues that could be potentially solved by further studies. In particular, recommendations are given to design the physical experiment performed in Part 3. This experiment could be indeed viewed as a 18th example, aimed at testing assumptions linked to the numerical code used to solve synthetic examples in this chapter and in Chapter 5.

First, if upscaling methods and upscaled models yield comparable results for two-dimensionsional log-Gaussian fields, strong differences appear for Markovian fields. This, added to the fact that relatively few laboratory-scale tracer tests have been performed using Markovian heterogeneous samples, tends to indicate that it would be interesting to further investigate transport in such conditions.

It was also shown that variance was not necessarily a parameter of high importance with respect to applicability of stochastic methods to transport in log-Gaussian permeability fields. For the range of variance values investigated with Markovian fields, typically higher than that of log-Gaussian fields, upscaling results remain of a good quality. A higher-variance case could help to draw conclusions regarding the applicability of S more confidently. High-correlation length and tilted cases were also observed to be more problematic.

Finally, inclusion models exhibited particularly poor performances. Such a result could be expected to a limited extent, as relatively high permeability contrasts were investigated, leading to a potentially high influence of diffusion and local-scale dispersion processes. It is proposed to further elucidate the effect of these local-scale processes on global transport in Part 3. In particular, it is proposed to study a situation where diffusion between zones of different permeability is known to have an influence. This will allow one to assess if diffusion is indeed highly limiting for inclusion models, and this will also allow one to introduce mobile-immobile models in the comparison.

Part III

Application to a laboratory experiment

Chapter 7

Transport in a highly heterogeneous medium

7.1 Introduction

Numerical models are relatively convenient when performing parametrical studies, in which a large number of different situations have to be evaluated and compared. However, they are rather artificial as they rely on a conceptual (theoretical) model that might be biased and as the whole information is theoretically known. Although they also rely on conceptual assumptions, physical experiments have to be performed in order to depart from these drawbacks and to assess flow and transport theories in field-like situations. Field experiments are expensive as a correct characterization of the subsoil over the scale of interest (involving the identification of the spatial distribution of permeabilities and the identification of appropriate boundary conditions) require an extensive characterization and measurement network. On the contrary, Intermediate-Scale Experiments (ISE) are performed in the laboratory at a smaller scale (usually of the order of a few meters), under known and identified boundary conditions and permeability distributions. They are cheaper to conduct due to the smaller volume of soil involved, the smaller duration and the reduced need for characterization.

This chapter must be considered as a continuation of the previous ones. In Chapter 5, highly conceptual transport situations were investigated in order to identify tendencies in model upscaling capacities with respect to variance and correlation length. In Chapter 6, 2D situations involving both log-Gaussian and Markovian permeability fields were investigated. Influence of other structural parameters, such as anisotropy and azimuth angle, was also studied. It came out of these numerical simulations that Markovian fields might require a deeper investigation, and that the influence of local-scale processes, such as diffusion, should be further examined. The example studied in this chapter must then be viewed as a 18th example, following the 17 cases investigated in Chapter 6. It is proposed to simulate the transport problem using a physical rather than a numerical model, in order to depart from limitations attached to numerical studies evoked before. It must be emphasized that the objective pursued in this section is not to validate the numerical code that was used in Chapter 5 and 6. This code was validated elsewhere and it is assumed to yield accurate results, within the limits of spatial, temporal and mass discretization adopted.

An important proportion of ISE have been designed by researchers to validate results of stochastic theories. These experiments involve a heterogeneous

synthetic aquifer characterized by a log-normal permeability distributions that is generated according to a given covariance function. The continuous permeability distribution is then discretized into a finite number of different materials and is usually characterized by a relatively small variance. For example, Danquigny et al. [59] investigated transport in a 3D heterogeneous media characterized by a variance $\sigma_Y^2 = 1.03$. Barth et al. [10] performed a 2D experiment on a synthetic aquifer characterized by a variance $\sigma_Y^2 = 1.22$. The 2D experiment of Silliman and Zheng [170] was characterized by a variance of 0.5. Jose et al. [109] performed a 2D experiment on a medium characterized by a higher variance ($\sigma_Y^2 \approx 2.4$). Welty and Elsner [196] performed tests on two 1D heterogeneous soil columns characterized by a variance of 0.25 and 1 respectively. Ursino et al. [185] performed 2D experiments in unsaturated conditions using three different materials. They did not indicate saturated permeability values but, based on d_{50} values, the maximum permeability ratio can be estimated at about 1/20. Levy and Berkowitz [121] aimed at validating temporal CTRW theories, but used three different sands with a maximum permeability ratio of 1/35, resulting in relatively mildly heterogeneous synthetic aquifers.

Tracer experiments involving discrete (bimodal) theoretical permeability distributions also generally involve mildly heterogeneous media. Silliman and Simpson [174] were among the first to perfom tracer tests on artificially reconstructed heterogeneous media, on order to give experimental evidence of the scale effect under controlled conditions. They used two materials with a permeability contrast of about 1/20, the finer one being in minor volumetric proportion (about 16 %). Silliman and Caswell [172] performed experiments on bimodal media of stochastic and fractal pattern. They however used materials with a relatively low permeability ratio (about 1/10).

Related transport problems are also usually investigated using low-variance heterogeneous media. Silliman [171] realized experiments using two realizations of a log-normal exponentially correlated K field to assess chemical transport to wells. The influence of heterogeneity on tracer test results has also been widely assessed using low-variance K field reconstructed in ISE [41, 70, 71]. Wood et al. [198] investigated biodegradation using a two-layer perfectly stratifed synthetic aquifer with a permeability ratio of 1/13. Murphy et al. [140] performed similar experiments in an heterogeneous medium composed of a background formation containing about 3 % of inclusions of a material about 50 times more permeable. Illangasekare et al. [104] performed experiments on movement and distribution of DNAPL in heterogeneous media using three sand types with a maximum permeability ratio 1/33. Schincariol and Schwartz [166] investigated density effects in perfectly stratified and lenticular heterogeneous media, with permeability ratio going up to 1/150 but did not consider diffusion processes in low permeability material.

On the contrary, laboratory studies involving highly heterogeneous medium are generally limited to very simple heterogeneous patterns. For example, Silliman et al. [173] investigated the effect of preferential pathways and impervious inclusions using hollow plastic tubes and impermeable disks buried in a porous medium. This experimental approach did not allow them to take into account mass transfer between zones of very different permeability. Su-

dicky et al. [177] investigated physical nonequilibrium models, but used a rather simple soil structure (a three-layer perfectly-stratified model : a thin layer of sand embedded between two thicker layers of silt). Other diffusion-dominated problems are typically investigated at the core scale, using column studies [9, 30, 32, 33, 44, 149, 190, 191].

To the author's knowledge, no detailed test (i.e. with a known permeability distribution) on diffusion-dominated problems has already been performed using a field-like highly heterogeneous medium. Besides attempting to answer to questions raised in Chapter 6 regarding efficiency of upscaling methodologies reviewed so far, the aim of this part of the study is thus to alleviate the lack of experimental data for this type of soil structure and to explore whether observations and conclusions obtained using a numerical study can be extrapolated to a physical model set up at the laboratory scale.

It is therefore proposed to create a highly heterogeneous 2D composite permeability field in an intermediate-scale laboratory tank and perform a tracer test. The permeability field will have to be carefully designed as (1) the structure of the velocity field must exhibit preferential pathways along which diffusion through low-permeability zones can occur and (2) flow through high-K zones must be, one one hand, fast enough to have a rapid breakthrough (so that total experiment duration remains reasonable) and, on the other hand, slow enough for transfer towards low-K zones to occur. A special attention will have to be dedicated to the choice of materials as (1) chemical interaction between tracer and the low-permeability material has to be minimized and (2) tracer must be used at low concentrations (in order to avoid density effects) but must still be detecteable over a wide range of concentrations. Another challenge lies in the preparation of the experiment as (1) the synthetic aquifer must be carefully packed in order to avoid undesired connexions between high-K zones and (2) the sampling program must be designed in order to minimize perturbation on the system (which can be critical when sampling in less mobile zones).

First, the experimental setup is presented in Section 7.2, and a special attention is drawn on the design of the synthetic aquifer. Then, experimental data collected are presented and a first analysis is conducted in Section 7.3. In Section 7.4, numerical models for flow and transport are set up in order to estimate actual soil parameters using various measurement data. In Section 7.5, upscaling theories are used to attempt to predict apparent longitudinal dispersivity and tailing behavior observed at the tank outlet.

7.2 Materials and methods

7.2.1 Experimental setup

The experimental setup consists of a 221.0 cm long, 8.0 cm wide, and 45.0 cm high plexiglas tank (Figs. 7.1 and C.1). It is equipped with inlet and outlet reservoirs, separated from the heterogeneous aquifer by a 3-cm thick filter made of very coarse sand ($d_{50} \approx 2$ mm) maintained with stainless steel screens covered with a geotextile. A peristaltic pump was used to impose a constant-
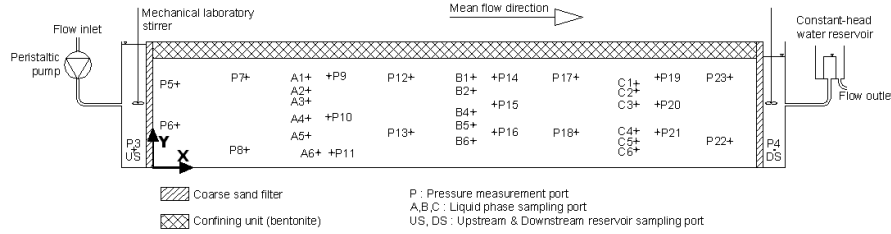
Figure 7.1: Schematic view of the experimental setup. Position of pressure measurement ports and sampling ports.

flux inlet hydraulic boundary condition (Fig. C.2) and a fixed-head condition was applied at the tank outlet (Fig. C.3). Deaired tap water was used for the whole experiment. Sample confinement was achieved using bentonite, separated from the soil using a plastic film to prevent physical and chemical interaction between tracer and bentonite.

A total of 21 pressure measurement ports were set evenly along the sample (including upstream and downstream reservoirs). Pressure ports installed in the aquifer were made of needles plugged into rubber septas installed in the tank wall (Fig. C.4). Needle diameter had to be small enough so that soil grains could not clog it. All pressure measurement ports were connected to a pressure transducer (Validyne P55) through a scanning fluid switch (Double Scanivalve System DSS-24C), allowing one to take measurements on a regular time basis for the whole experiment (Figs. C.6 and C.7). Fig. 7.1 and Table C.1 show the locations of the pressure ports.

Rhodamine WT (RWT) was used as tracer. Reasons justifying that choice are described in Section 7.2.3. As, in this study, a particular attention needs to be devoted to tail behavior, a high-concentration injection was performed in the upstream reservoir. Samples with higher concentration have then to be diluted in order to be analyzed. This was done in order to increase precision of late-time concentration data and obtain relative concentration curves extending over several orders of magnitude (i.e. over a larger range than allowed by the measurement device). Mixing in the upstream tank was maintained using a mechanical laboratory stirrer (Fig. C.8). In such conditions, concentration curve at injection decays exponentially and induces heavy-tailed concentration distributions. As this could potentially hide tailing effects due to local-scale processes in the sample, the upstream reservoir was flushed about 60 minutes later in order to create a Dirac-like injection condition.

Sampling ports were built similarly to pressure ports, but were equipped with a small tap allowing one to manually take samples (Fig. C.5). 2-ml samples (Fig. C.9) were taken at 17 different locations, shown in Figs. 7.1 and 7.2. Samples were diluted 6 to 216 times with deionized water and analyzed using a 10-AU Turner Designs Fluorometer (Figs. C.10 and C.11).

7.2.2 Design of the heterogeneous aquifer

The heterogeneous medium is composed of three different silica sands. A two-material model would have only allowed one to simulate properly either an advection-dominated problem (with mild permeability contrast) or a diffusion-dominated problem (with a high permeability contrast) and the conclusions to be drawn would have been straightforward according to the configuration adopted. Moreover, a two-material synthetic K field is thought to be a too simplified model for a real aquifer. On the contrary, multiplying the number of material would lead to a log-Gaussian-like aquifer (e.g. Fernandez-Garcia et al. [70] have discretized a log-normal distribution in 5 categories). Therefore, it is believed that a three-material model is a relatively good candidate to perform this study.

Materials with the highest permeability are silica sands corresponding to mesh #8 (high K inclusions - further referred to as material 1) and #30 (background formation of intermediate K - material 2) respectively. Some of the mechanical and hydraulic properties of these materials are summarized in Table 7.1. Sorption properties of Rhodamine WT with these materials are investigated in Section 7.2.3. Filters separating the sample from inlet and outlet reservoirs are actually made of material 1, from which the finer fraction was removed.

Two main criteria guided the choice of the third material (material 3). First, preliminary simulations showed that a permeability contrast of at least three orders of magnitude between intermediate and low permeability materials was required. This is in accordance with the results that Guswa and Freyberg [88] obtained in their numerical study of transport through a single ellipse. Using basic empirical formulae, this requirement could be converted into a constraint on particle size distribution. Then, a geotechnical stability criterion added a second constraint on particle size distribution. The material that was used resulted from the mixing of a #325 silica flour with #140 and #70 silica sands, respectively in 15 %, 45 % and 40 % weighing proportions. Permeability values based on column test ranged between 10^{-4} cm/s and $5\ 10^{-4}$ cm/s.

Transition probabilities were used to set up the spatial distribution of permeabilities [39, 40]. Target volumetric proportion of high (material 1) and low permeability (material 3) inclusions are respectively 10 % and 50 %. The synthetic aquifer is characterized by a relatively high level of anisotropy, as inclusions have a mean size of 20 cm × 2 cm. No preferential spatial sequences were considered by setting transitions probabilities from material 1 to 2, 1 to 3, 3 to 1 and 3 to 2 equal. The relatively high proportion of low permeability material and the high anisotropy ratio were chosen to ensure preferential pathways flow architecture, with rapid flow in high-K channels surrounded by low-K lenses, to stimulate diffusion-dominated transport. The permeability field was generated using T-Progs [38] for a larger domain (5 m × 2 m), from which the reference field to be used was extracted in order to avoid potential border effects. A packing unit of 2 cm × 2 cm was adopted, resulting in inclusions having a slab shape. Fig. 7.2 shows the distribution of permeability that was adopted for this study. Figs. C.12 and C.13 show corresponding transition probabilities as well as theoretical Markov chains models. Actual material proportions are 7.5 %,
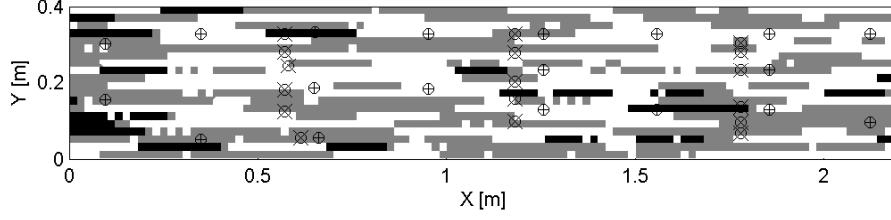
Figure 7.2: Spatial structure adopted for the heterogeneous aquifer. Background formation is gray, low-K inclusions are white and high K inclusions are black. Pressure ports (+-cross) and sampling ports (x-cross) are also represented.

Material	Bulk density [g/cm^3]	Porosity [%]	Permeability [cm/s]	Longitudinal dispersivity [cm]
1	$1.43 - 1.60^a$	$39.7 - 45.9^a$	$1.613 - 2.730^a$	$0.161 - 0.229^b$
2	$1.31 - 1.61^a$	$39.4 - 50.4^a$	$0.150 - 0.307^a$	$0.058 - 0.223^b$
3	-	-	$10^{-4} - 5\ 10^{-4}$	-

^{a}from Sakaki and Komatsu [156]

^{b}from Fernandez-Garcia et al. [70]. Dispersivity values determined for Br$^-$ and Li.

Table 7.1: Summary of the properties of the two sand types used as high- and medium-K material

42.5 % and 50.0 % for material 1, 2 and 3 respectively.

Packing was achieved under approximately 2 mm of standing water, so that air entrapment was minimized (i.e. saturation is maximized) during the packing process but fine particles (present in material 3) are not suspended. This could result in fine upward sequences that would strongly affect transport and that would be difficult to model. Vertical separation between regions of different material was maintained using thin metal dividers. Packing was achieved in a relatively loose way, as the tank was not vibrated due to potential disturbances that could have been induced at slab boundaries.

7.2.3 Tracer characterization

Sutton et al. [178] enumerate five reasons to justify the suitability of RWT as a groundwater tracer : (1) RWT can be detected at concentrations as low as 0.1 ppb using a sensitive flutorometer ; (2) RWT is considered the most stable of the fluorescent dyes and its main degradating agents are not naturally present in groundwater systems ; (3) fluorescence of RWT is not influenced by the pH provided it is higher than 6 ; (4) the U.S. Environmental Agency does not expect adverse health effects when RWT is used as tracer if sanitation guidelines are followed and (5) Sutton et al. [178] report from Field et al. that RWT is not an acute toxic threat above 1 mg/L.

However, for physical aquifer characterization, the ideal tracer should be conservative, and RWT is known to be a reactive tracer. For example, Ptak and Schmid [148] performed a tracer test in a highly heterogeneous and highly

conductive aquifer over a short distance and observed significant differences between RWT and fluoresceine (known to be less reactive). They obtained an effective retardation coefficient for RWT ranging between 1.26 and 1.40. Moreover, batch studies highlighted that RWT was sorptive even on mineral surfaces (alumina and silica) [154].

Actually, other tracers could have been considered for this study. For example, bromide (Br^-) is usually assumed to be an ideal conservative tracer [122]. It can however only be measured within relatively high concentration ranges (using e.g. a ion chromatograph), at which density effects can become important [11]. This limitation, added to the need for a wide measurement range at relatively low cost, constrains the choice of the tracing technique to fluorescence. Fluoresceine could then have been considered, as it is less sorptive than RWT [148, 155]. It is however known to be much more reactive to sunlight [155]. As the sandbox walls are made of plexiglas and as the tracer test is expected to last more than one month, the risk of exposure to sunlight was found too high to adopt this tracer.

Batch tests were performed in order to explore sorption effects of RWT on each of the materials that were used. The aim pursued by this orientation testing was not to derive sorption models to be used in the analysis of concentration series. In that case, column tests should have been preferred. The aim was only to verify whether one should expect sorption of RWT on soil grains or not. Material 3 was not investigated, but each of its three components were tested independently, which is though to be sufficient here.

As a reminder, equilibrium chemical interaction is quantified using partitioning coefficients K_d according to

$$C_s \quad = \quad K_d C \tag{7.1}$$

$$C_s \quad = \quad K_d C^n \tag{7.2}$$

where C [g/L] is the solute concentration in the liquid phase and C_s [g/kg] is the sorbed concentration. Eq. 7.1 is a linear model that is suited to described low-concentration situations. Eq. 7.2 is referred to as the Freundlich isotherm.

Table 7.2 shows the values of partitioning coefficients that were obtained and Figs 7.3 and 7.4 show the agreement of sorption models with experimental data. A linear model is usually adopted for concentrations lower than 100 ppb [122, 178]. However, for concentrations in the range investigated in this study (i.e. up to 2000 ppb), a Freundlich model is usually better suited [155]. Both models were fitted to experimental data and are reported here.

Except for silica sand #70, K_d values reported here are generally consistent with other results presented in the literature. For example, Sutton et al. [178] observed K_d values between 0.142 and 0.198 L/kg for isomers of RWT and a washed sand used for monitoring wells pack. For the range of bulk densities and porosities given in Table 7.1, one expects the linear retardation coefficient to range between 2.00 and 2.28 for material 1 and 1.23 and 1.37 for material 2. No desorption test was performed to assess the reversibility of chemical reaction. However, Sutton et al. [178] mention a mass recovery of about 80 % on column studies for their washed sand. Lin et al. [122] conducted batch experiments using natural soils with a relatively high organic content and indicate that only

		Material 1	Material 2	Material 3		
		#8	#30	#70	#140	#325 flour
Linear	K_d	0.32	0.09	1.34	0.38	0.16
Freundlich	K_d	0.41	0.12	1.51	0.53	0.14
	n	0.73	0.60	0.74	0.65	0.69

Table 7.2: Estimated partitioning coefficients and exponents for a Freundlich isotherm. K_d for the linear model is expressed in [l/kg] and similar units are used for the Freundlich isotherm.
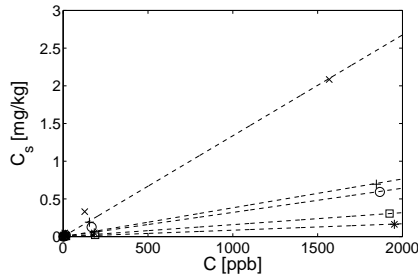

Figure 7.3: Linear adsorption isotherms for Rhodamine WT. #8 (squares), #30 (+-crosses), #70 (x-crosses), #140 (stars), silica flour (circles) and corresponding fit (dashed line).

Figure 7.4: Freundlich adsorption isotherms for Rhodamine WT. #8 (squares), #30 (+-crosses), #70 (x-crosses), #140 (stars), silica flour (circles) and corresponding fit (dashed line).
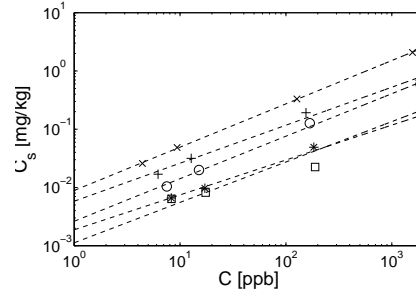
10 % of the sorption was reversible. K_d for silica sand #70 is extremely high and is suspected to be influenced by an experimental error.

The aqueous diffusion coefficient of RWT was not found in the literature, but Sabatini [154] estimates that of Sulforhodamine B at $4.7 \ 10^{-10}$ m^2/s. This value will be used here with a tortosity factor of 0.7 [72], leading to an estimated effective diffusion coefficient of $3.3 \ 10^{-10}$ m^2/s.

7.3   Experimental results

Bulk experimental data are presented in this section, as well as results from preliminary analyses. First, considerations linked to flow in the sample are summarized in Section 7.3.1. Then, concentration data recorded in the downstream reservoir is examined in Section 7.3.2 with respect to mass balance, and in Section 7.3.3 with respect to apparent transport parameters. Finally, local BTC (i.e. BTC recorded at sampling ports located in the tank) are presented in Section 7.3.4 and sets of apparent transport parameters are computed.

7.3.1   Head and discharge data

Liquid phase samples were initially taken every 3 hours at every sampling port for the first 5 days. This frequency was adopted in order to maintain the estimated perturbation on total discharge below 5 %. It was moreover
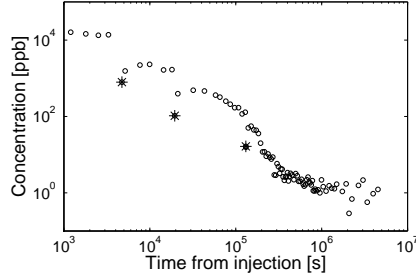
Figure 7.5: Concentration measured in the upstream tank. Stars indicate flushing.
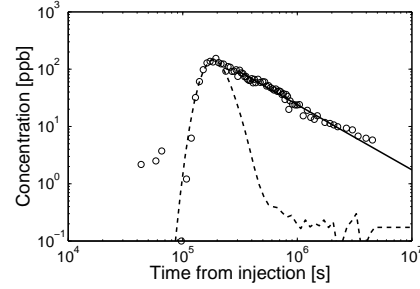

Figure 7.6: Concentration in the downstream tank. Experimental values (circles), late-time linear tailing behavior (continuous line) and ADE fit (dashed line).

checked using a preliminary numerical model that this design allowed a proper detection of concentration peaks. For the following 5 days, sampling frequency was decreased to one sampling sequence every 6 hours, and then progressively decreased to one sampling sequence every week. Besides daily variations due to temperature and pressure fluctuations, pressure drops due to sampling can be clearly observed (Fig. C.14). The reference gradient $i = 1.45$ % that is adopted throughout the remaining part of this analysis corresponds to the average value measured between 420 and 450 hours from injection (± 3.2 cm of head difference between upstream and downstream reservoirs). Numerical values adopted to perform the analysis of other results are reported in Table C.1.

Total discharge was measured using a weighing method. A volume of about 2 liters was collected at the tank outlet, over a duration of 4 to 5 hours. Data also reflect the influence of sampling, as the measured value increases when sampling frequency decreases (Fig. C.15). The total discharge for the last (supposed unperturbed) measurement is 4.988 ml/min, yielding an effective permeability of $1.830 \, 10^{-2}$ cm/s ± 2 % (95 % confidence interval estimated from the variance of the measured gradient). Whether this value could be expected or not is discussed in Section 7.4.2.

7.3.2 Mass recovery considerations

A perfect pulse injection condition could not be achieved, as the flushing could only decrease concentration by one order of magnitude in the upstream tank (Fig.7.5). It must be moreover observed that concentrations tend to recover just after flushing. Two explanations can be invoked for this phenomenon : back diffusion from the aquifer and desorption from bentonite residuals present in the upstream reservoir. A second and a third flushing were also performed at later times but had limited effects. Late-time behavior of the injection curve decays exponentially, at a rate controlled both by total discharge and upstream reservoir volume. Background concentration is about 1 ppb (as the fluorometer was calibrated using standard solutions made from deionized water and tap water is used in the tank). Integration of the curve yields a total injected tracer mass of 19.912 mg.

The total mass of tracer recuperated at the model outlet, obtained by integration of the outlet BTC (Fig. 7.6) up to 10^7 s, is 14.302 mg. As no leak appeared during the experiment, about 28.2 % of the tracer mass is still trapped in the tank after about 50 days. As the outlet BTC exhibits a strong tailing behavior, assuming that the observed log-log linear late-time trend remains unchanged until the background concentration is reached (e.g. 1 ppb at about $2\ 10^7$ s), it is possible to compute an additional mass of about 4.5 mg that could be potentially recuperated at the model outlet. The corresponding mass balance would then be verified within 5 %. Based on results obtained by other authors, irreversible sorption might be another explanation for incomplete mass recovery.

7.3.3 Outlet breakthrough curve

The outlet breakthrough curve, shown in Fig. 7.6, is representative of concentration distributions averaged over the whole sample cross-section. Therefore, apparent transport parameters for this curve could be characteristic of an homogeneous medium equivalent to the heterogeneous aquifer. It will be shown in this section that the definition of that equivalent homogeneous medium is not straightforward and that analysis of the outlet BTC can yield different sets of transport parameters, depending on the point of view adopted.

Similar tools as in previous chapters can be used to analyze temporal concentration series. It is first proposed to use curve-fitting to obtain apparent Fickian transport parameters for the outlet BTC. The analytical solution of the advection-dispersion equation (without retardation) corresponding to the actual injection curve was used. A convolution product was also added in the model to simulate mixing in the downstream reservoir. Mean migration velocity and apparent longitudinal dispersivity were found equal to $1.169\ 10^{-5}$ cm/s ± 121 % and 44.5 m ± 119 % (95 % confidence interval) respectively. These values are unrealistic, and both confidence intervals extent to non-physical negative values.

Instead, temporal moment analysis can be used. The value of apparent dispersivity that is obtained using this method better corresponds to its theoretical definition : it is computed as the spreading of the concentration distribution around its center of mass. Moreover, this method is more straightforward than curve-fitting (it does not require an optimization algorithm) and embodies a proper scaling for peak concentrations (as temporal moments are normalized by the zeroth moment). It is however recognized that this method might lead to biased results as (1) total recovery is not observed, (2) the injection condition is not a perfect Dirac point injection and (3) mixing in the downstream reservoir is not accounted for. The second effect is believed to have a minor influence. Flushing in the upstream reservoir induced sharp variations of injection concentrations, having a limited effect on apparent dispersion. Only a slight underestimation of apparent velocity is expected. The third effect is known to induce a higher apparent dispersion but, as distributions are already characterized by a high spreading, the relative increase is supposed to be of minor influence. Transport parameter values are $v = 1.829\ 10^{-4}$ cm/s and $\alpha_L^* = 1.02$ m.

As a reminder, Darcy velocity obtained from discharge measurements was $2.598 \ 10^{-4}$ cm/s. Assuming a reasonable value of porosity (e.g. 40 %), the mean retardation factor would be about 3.6. This value seems to be unrealistic regarding the set of K_d values obtained (assuming that the value obtained for sand # 70 is erroneous). As observed by Rovey and Niemann for a sensitively less heterogeneous sample [151], mean advective transport in heterogeneous media is slower than predicted using the effective permeability, even for conservative tracers, due to dispersion and diffusion towards less mobile zones which, in the average, prevent solute particles to concentrate in preferential pathways.

If diffusion is indeed a key process for the case under consideration, it controls late-time behavior of concentration distributions. Advection should then be estimated from early-time data instead of from the whole curve. Fitting of the analytical solution of the ADE (using actual injection condition and convolution to model mixing in the downstream tank) on the raising part of the outlet BTC yields a mean migration velocity of $1.431 \ 10^{-3}$ cm/s and an apparent longitudinal dispersivity of 3.57 cm. As mass balance does not apply when analyzing only part of the BTC, a scale factor was used in the curve-fitting process to match peak concentration. Assuming no retardation and an homogeneous sample, a value of 18.2 % can be calculated for the mean effective porosity, which is clearly outside the bounds showed in Table 7.1 for material 1 and 2 and seems to be too low to be explained by the presence of material 3. Accounting for retardation would decrease this value even more.

Actually, solute transport in heterogeneous media is controlled by connectivity rather than effective porosity [71]. Connectivity is the concept that contemplates the presence in an aquifer of high conductivity pathways between the point of injection and the measurement point [71]. For a flux-type injection, transport mainly occurs in these preferential pathways, at a velocity higher than the mean migration velocity (i.e. corresponding to the mean Darcy velocity divided by the mean porosity). Therefore, solute front is detected at the measurement point earlier than predicted by the mean migration velocity. The only way to account for this phenomenon assuming an equivalent homogeneous medium is to take a lower mean effective porosity value.

Comparing both apparent dispersivity values is a direct illustration of the scale effect. Dispersivity from early-time BTC data is representative of dispersion processes along preferential travel path in the high-K phase. This value could therefore be interpreted as a local (microscopic) longitudinal dispersivity. The apparent dispersivity of the whole BTC includes the full complexity of transport processes occuring in the sample : macroscopic differential advection, mass transfer between preferential pathways and low-K zones, and microscopic sorption processes. The ratio of macroscale to local longitudinal dispersivity is about 30, which is particularly high.

Finally, the strong linear tailing behavior exhibited by the outlet concentration curve typically highlights multiple-rate transfers between mobile and immobile phases (see Section 3.4). Spatial variability in sorption properties of the tracer might also contribute to the tailing behavior of the BTC [148, 165]. A linear model was fitted on the curve plotted on a log-log scals graph and the slope was found equal to -1.1366.

Port	X	Y	v	CV	α_L	C	$\langle t \rangle$	α_L^*	$1/\omega$
	[m]	[m]	[m/d]	[-]	[cm]	[-]	[d]	[m]	[d]
US	0.00	-	-	-	-	-	-	-	-
DS	2.26	-	1.236	0.017	3.57	0.14	14.3	1.02	54.1
A1	0.601	0.331	0.740	0.009	0.94	0.44	7.35	0.55	29.0
A2	0.601	0.283	1.751	$-^a$	0.18	0.44	4.43	1.12	21.5
A3	0.601	0.245	5.439	0.065	5.73	0.37	12.6	0.30	29.7
A4	0.601	0.181	7.777	0.047	1.13	0.08	13.6	0.21	37.2
A5	0.601	0.119	8.350	0.053	0.65	0.38	5.52	0.77	25.1
A6	0.643	0.055	1.077	0.204	4.34	0.38	3.99	1.10	28.1
B1	1.211	0.331	0.810	0.013	1.71	0.25	11.1	0.65	21.7
B2	1.211	0.281	0.841	0.035	3.78	0.32	11.6	0.65	27.7
B4	1.211	0.203	0.719	0.013	2.04	0.48	12.4	0.58	26.5
B5	1.211	0.157	0.473	0.019	4.65	0.39	15.0	0.48	43.3
B6	1.211	0.099	0.994	0.015	0.65	0.22	9.77	0.79	18.6
C1	1.809	0.307	0.543	0.008	3.96	0.33	17.3	0.69	81.4
C2	1.809	0.283	0.524	0.007	2.75	0.29	18.0	0.66	112.0
C3	1.809	0.233	0.576	0.013	4.06	0.22	17.1	0.71	96.4
C4	1.809	0.135	0.546	0.056	11.1	0.32	16.3	0.65	58.5
C5	1.809	0.097	1.042	0.014	4.51	0.29	10.9	1.02	29.0
C6	1.809	0.067	1.173	0.013	4.87	0.30	9.33	1.21	29.3

^{a}due to too fee early-time measurements

Table 7.3: Position of sampling ports. Apparent velocity v, corresponding coefficient of variation CV obtained from the confidence interval of v, local dispersivity α_L and scale parameter C are obtained from early-time behavior of BTC. Mean breakthrough time $\langle t \rangle$ and apparent dispersivity α_L^* are obtained from temporal moment analysis. Exchange rate ω is obtained from the fitting of a linear model on the semilog plot of the BTC.

7.3.4 Local concentration data

Local breakthrough curves recorded at sampling ports A to C are showed in Figs. 7.7 to 7.9. Again, early breakthroughs and late-time heavy tails are observed.

First, apparent transport parameters are determined for each BTC using entire curves. Temporal moment analysis was also used, with the limitations highlighted in previous section (except that the downstream reservoir has no influence here). Apparent velocities and longitudinal dispersivities are shown in Figs. 7.10 and 7.12, and are indicated in Table 7.3. Apparent dispersivity values, although smaller than observed for the outlet BTC, are of a similar order of magnitude and exhibit a scale-effect.

Local apparent velocities and dispersivities were then estimated by fitting of the ADE solution corresponding to the actual injection curve to the raising part of the BTC. Local apparent velocities and dispersivities are plotted in Figs. 7.11 and 7.13 respectively and their numerical values are indicated in Table 7.3. Dispersivities are about two orders of magnitude smaller and do not seem to exhibit a scale-effect. This tends to support the assumption that apparent dispersivities from early-time data (i.e. using the raising part of BTC) are local values, not necessarily influenced by heterogeneities.
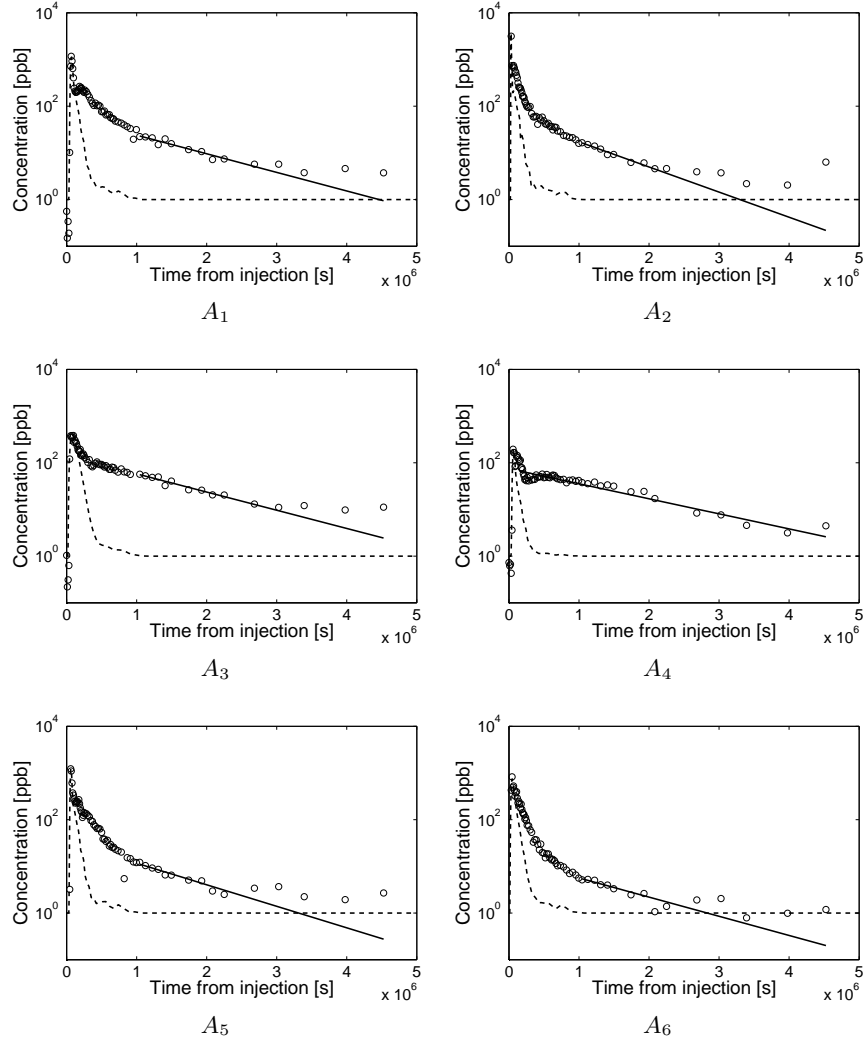
Figure 7.7: Concentration recorded in sampling ports A. Experimental values (circles), late-time linear tailing behavior (continuous line) and ADE fit (dashed line).
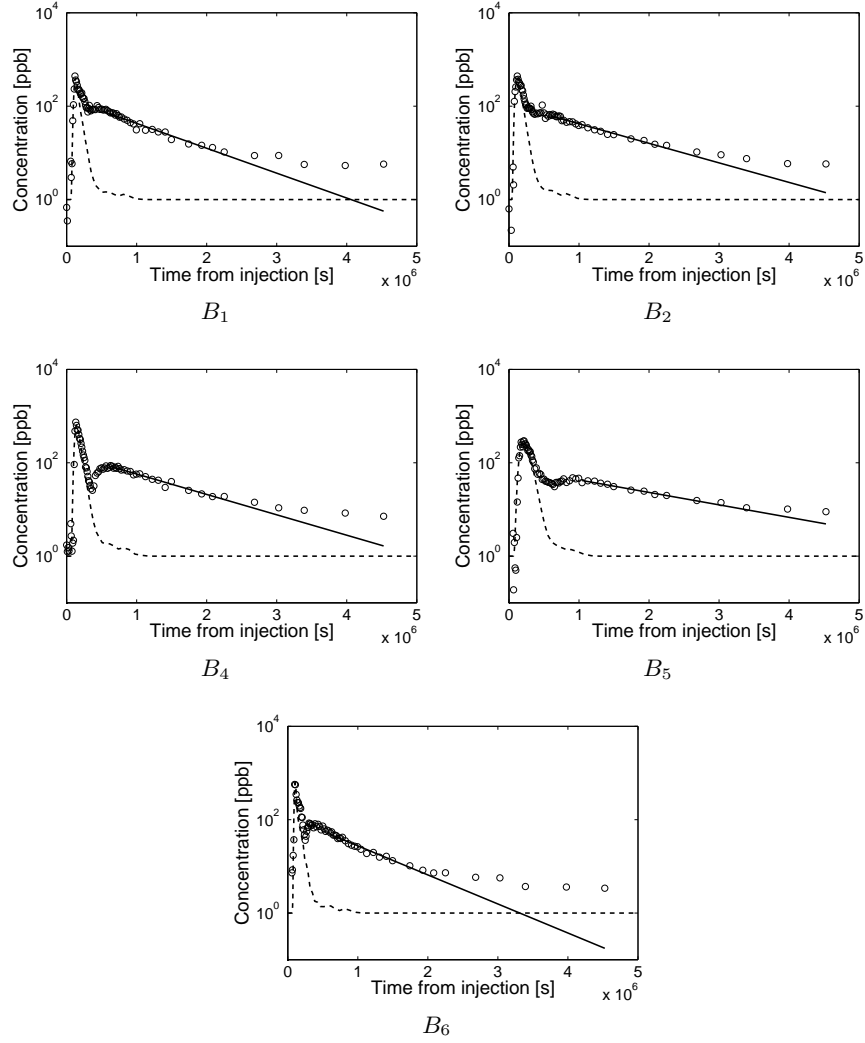
Figure 7.8: Concentration recorded in sampling ports B. Experimental values (circles), late-time linear tailing behavior (continuous line) and ADE fit (dashed line).
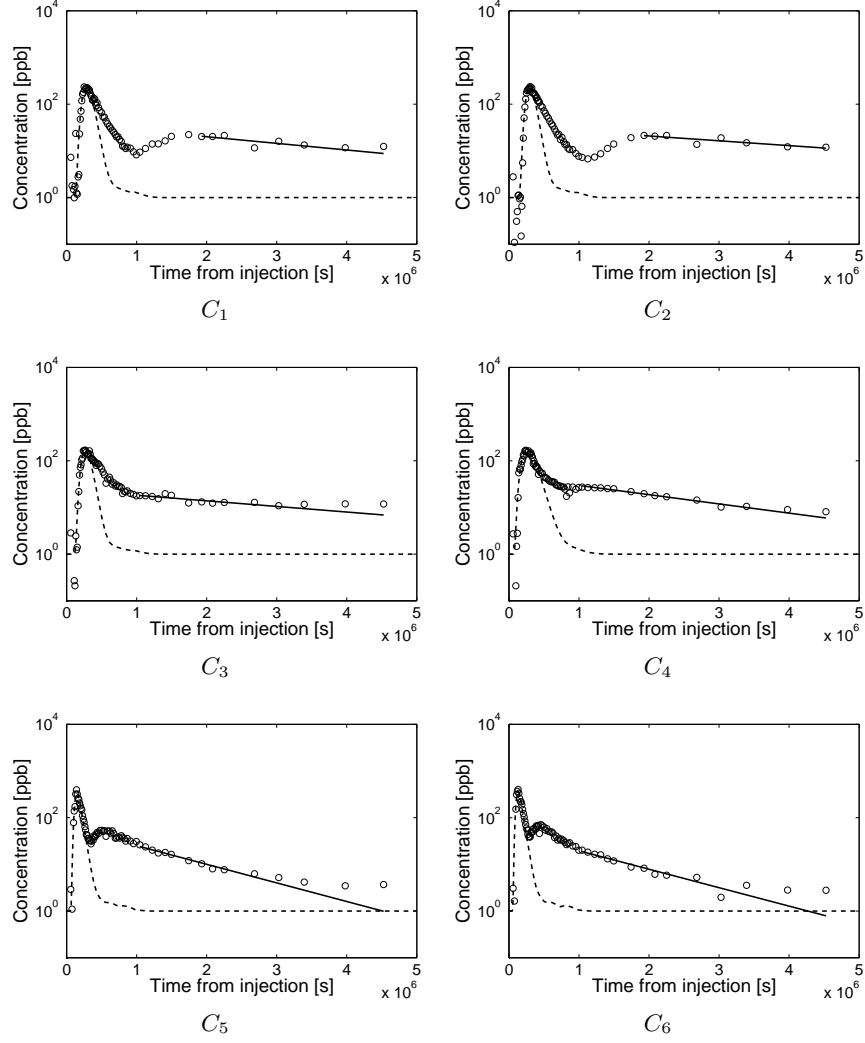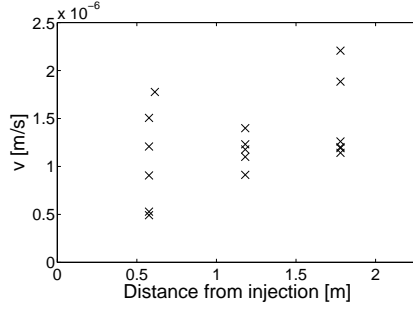
Figure 7.9: Concentration recorded in sampling ports C. Experimental values (circles), late-time linear tailing behavior (continuous line) and ADE fit (dashed line).

Figure 7.10: Apparent longitudinal velocity obtained from temporal moment analysis of local breakthrough curves
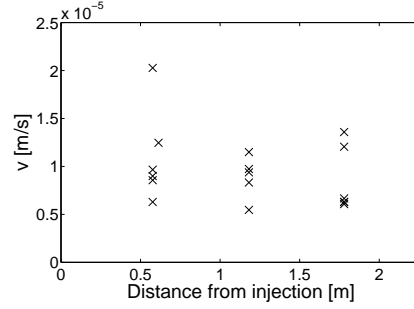
Figure 7.11: Apparent longitudinal velocity obtained from curve-fitting on early-time concentration data
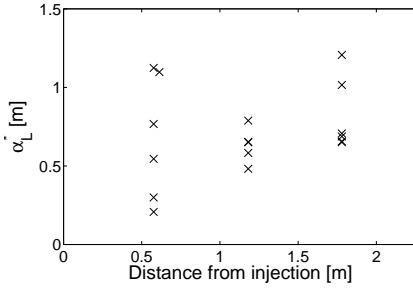
Figure 7.12: Apparent longitudinal dispersivity obtained from temporal moment analysis of local breakthrough curves
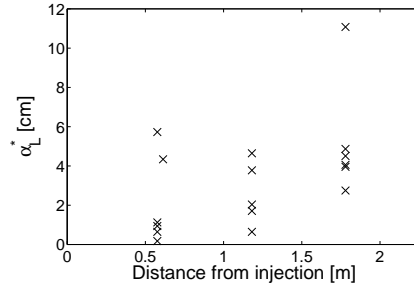
Figure 7.13: Apparent longitudinal dispersivity obtained from curve-fitting on early-time concentration data

Finally, assuming that a single-rate transfer model between mobile and immobile zones can be adopted, a linear model was fitted on the late-time semilog plot of concentration $\ln(C)$ vs t. However, since a perfect Dirac injection condition could not be achieved, concentration decays exponentially in the upstream tank. One expects this exponential behavior to control very late-time concentration curve and, therefore, only intermediate-time data (i.e. the part of the curve occuring after the peak, that behaves linearly except for the couple of last measurements) were analyzed to obtain local-scale transfer rates. Fig. 7.14 shows a smoothened distribution of exchange rates with a lognormal distribution fitted on the main peak. Its corresponding mean and standard deviation are respectively $\ln(\mu) = -14.681$ and $\sigma = 0.22$.

7.4   Numerical model

Actual physical properties of the synthetic aquifer build in the tank may differ from the range indicated in Table 7.1, due e.g. to settling and disturbances during the packing process. These values are however required in order to apply analytical methods presented in Part 1. Therefore, a numerical model corresponding to the heterogeneous configuration shown in Fig. 7.2 has to be set
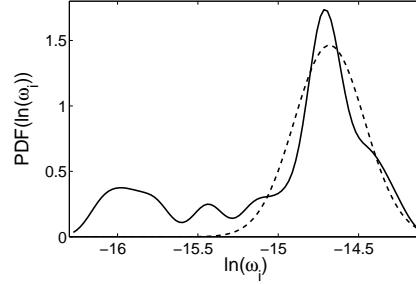
Figure 7.14: Distribution of the logarithm of the apparent exchange rate obtained from the late-time slope of local breakthrough curves. Smoothened experimental distribution (continuous line) and fitted normal distribution (dashed line).

up and validated against e.g. outlet concentrations (which is the data with which upscaling models will be confronted). It is then proposed to use inverse modelling to determine actual material properties based on local experimental data.

7.4.1 Numerical codes

It is proposed to use the same codes as in Chapter 5 and Chapter 6, MOD-FLOW 2000 [96] for flow and RWHet [115] for transport. RWHet does not embody the capacity to simulate reactive transport. However, linear retardation results in apparent lower velocities, which can be easily accounted for by using higher effective porosities. Transport codes able to simulate reactive transport are available (e.g. MT3D [203]). These codes are however based on numerical schemes prone to artificial dispersion. Regarding the range of local dispersivities evoked in Table 7.1, the numerical grid required to avoid numerical dispersion would lead to too high computational costs.

In a first step, only head and discharge measurements are used in this process to determine actual permeabilities of material 2 and 3, using an automated parameter estimation procedure implemented in MODFLOW 2000. Then, a simple trial-and-error method using outlet concentration data will be applied to estimate lumped effective porosities using RWHet.

Actuallly, two attempts to incorporate local concentration data in optimization algorithms combined with transport numerical codes were performed but did not yield valuable results. First, early-time (according to the definition already used) advective transport measurements were used in an automated parameter estimation procedure combined with a purely advective particle tracking algorithm [1, 2]. This highlighted that diffusion processes could not be neglected in the model. Then, mean advective transport measurements obtained from temporal moment analysis were used with an optimization algorithm and a numerical code solving the steady-state ADE, but no useful result could be
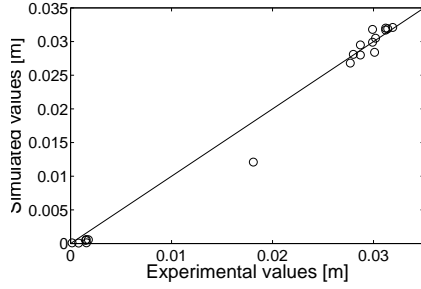
Figure 7.15: Comparison of experimental (circles) and simulated (continuous line) heads for optimal transport parameters.
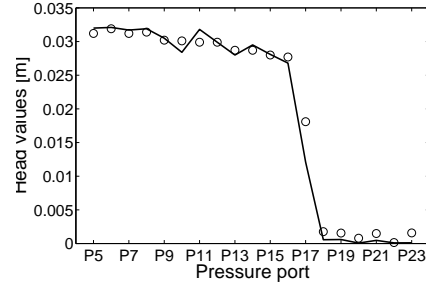

Figure 7.16: Comparison of experimental (circles) and simulated (continuous line) heads for optimal transport parameters.

obtained as well. The full transient numerical code for transport RWHet could not be used in an automated calibration procedure due to computational costs.

7.4.2 Estimation of permeabilities

A numerical model for the flow field was set up using a 1 cm $\times$ 1 cm two-dimensional square grid. The Parameter-Estimation package [99] was used to estimate actual permeability values corresponding to the spatial distribution shown in Fig. 7.2. As the sensitivity of heads to the permeability of material 1 was found to be very low, due to its low volumetric proportion, K value for material 1 could not be determined and was estimated from the range reported in Table 7.1. It must be noted that the filters isolating the sample from inlet and outlet reservoirs were explicitly incorporated in the numerical model. Their properties were set equal to those of material 1.

Weighted least-square fitting was used, and observation errors were estimated from the variability of head measurements during the corresponding discharge measurement. The latter was assigned a much higher weight, so that its simulated value is close to its measured value. Permeabilities of material 2 and 3 were determined for various K values of material 1 and were found to be relatively insensitive to it. Final values are $K_2 = 8.39\ 10^{-3}$ m/s ±59 % and $K_3 = 3.32\ 10^{-6}$ m/s ±26 %. Fig. 7.15 shows that the agreement between oberved and simulated heads is relatively good. Final discrepancy between observed and simulated total discharge is about 0.3 %.

Fig. 7.17 shows the computed head. The lack of connectivity of the permeability is clearly visible in the head field, as most of the total head drop happens between $X = 1.5$ m and $X = 1.6$ m.

7.4.3 Validation of the model

As previously stated, a trial-and-error method was performed using only outlet concentration data with the numerical code RWHet [115]. A similar grid to that of the flow model was used, but the flow domain was extended upwards by 20 cm in order to limit boundary effects (as already done in previous chapters). 1.000.000 particles were injected at time $t = 0$ over the boundary $X = 0$.
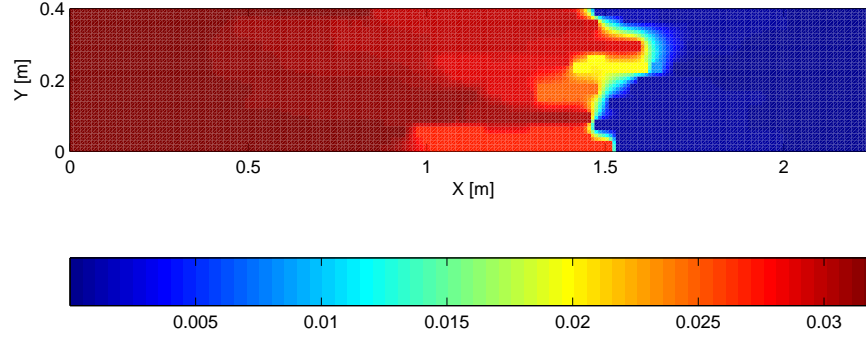
Figure 7.17: Head field. Heads are expressed in [m] relative to the head in the downstream tank.

In order to simulate a flux-type injection condition, the number of particles in a cell was set proportional to the velocity in that cell. The outlet BTC was calculated as the number of particles exiting the flow domain between two time steps, which is a measurement in flux. The curve was afterwards convoluted with the inlet concentration curve and mixing in the downstream tank was accounted for by convoluting the curve with a negative exponential (as done previously).

Local dispersivities were set constant and equal to $\alpha_L = 1$ cm and $\alpha_T = 1$ mm. Fig. 7.18 shows the predicted curve for effective porosities equal to 0.48, 0.52 and 0.42 for material 1, 2 and 3 respectively. These values are higher than the maximum values reported in Table 7.1, which highlights retardation processes. The agreement is only partially convincing : advective transport (i.e. the raising part of the curve) is correctly modelled, as well as peak concentrations. However, the tailing behavior could not be reproduced, whatever be the values of porosities and diffusion coefficient. Actually, the model did not reveal a high dependence of tailing behavior on diffusion, indicating that another explanation should be invoked for that observation. Enhanced tailing can also be attributed to variability in sorption processes [47, 148]. As different lumped porosities were estimated for each material, variability in retardation factor is incorporated within the numerical model. Therefore, one could wonder if sorption/desorption kinetic effect take place. More precisely, such a tail could be explained by a slow desorption process.

It must be emphasized that mobile-immobile processes should not be taken into account in the detailed numerical model of the aquifer. Indeed, no intraparticle diffusion can be considered for the silica sands used here. Mobile-immobile models can only be considered when attempting to replace the heterogeneous aquifer by an equivalent homogeneous one.

High lumped porosities are in agreement with the expected sorptive behavior of Rhodamine WT on soil grains. As the sample was packed in a relatively loose way, one estimates actual porosities to be in the higher part of the interval indicated in Table 7.1. Therefore, retardation coefficients probably range
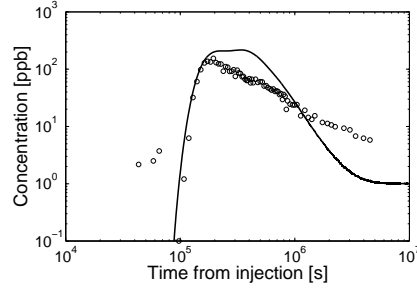
Figure 7.18: Comparison of experimental (circles) and simulated (continuous line) concentrations at the tank outlet.
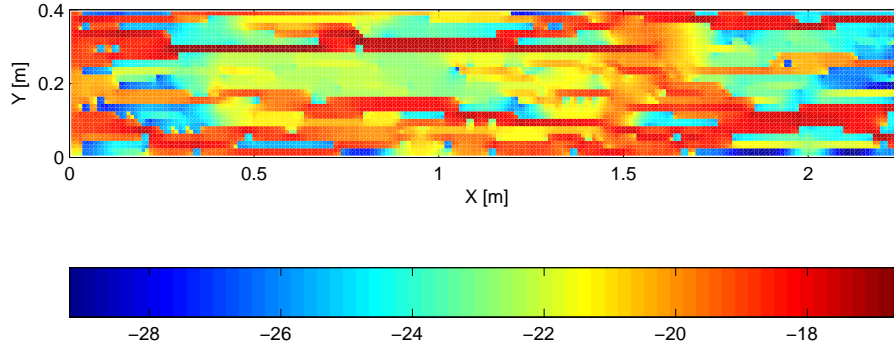

Figure 7.19: Natural logarithm of the velocity field. Velocities are expressed in [m/s].

between 1.05 and 1.21 for material 1 and 1.03 and 1.16 for material 2. For the latter material, results are smaller but close to values discussed in Section 7.2.3. The lower influence of material 1 on transport might account for the higher discrepancy.

Fig. 7.19 shows the spatial distribution of the norm of migration velocity. It indeed exhibits a preferential pathway architecture, with an important channel in the lower part of the sample and a smaller one in the upper part of the sample. The disconnected zone also appears between $X = 1.5$ m and $X = 1.6$ m.

7.5   Application of non-Fickian models

In previous sections, it was shown that transport was infuenced both by physical and chemical processes. This sensitively complicates the analysis and the links to draw with observations from Chapter 5 and Chapter 6. As upscaling methods for apparent dispersivity only account for physical processes originating from the presence of heterogeneity, one already expects them to yield poor results,

especially regarding the extremely high value of apparent dispersivity obtained. However, upscaled transport equations could account for chemical processes through lumped parameters and are expected to yield better results. It must be noted that filters, made of material 1, are supposed to be part of the synthetic aquifer.

7.5.1 Upscaling of flow

According to the methodology adopted in Chapter 6, results with respect to flow are first confronted to corresponding upscaling theories. As no measurement of the velocity distribution could be performed in the experimental tank, only effective permeability is considered in this analysis. As a reminder, a value of $1.830 \ 10^{-4}$ m/s was found for that parameter. That value could be correctly predicted using the numerical model presented in previous section, since adequate permeability values of each material were found to be close to measurements performed in column studies (values presented in Table 7.1). It will be verified in this section whether theories based on structural descriptions of the permeability field allows an efficient upscaling of permeability.

The variance of the $\ln K$ field can be computed using Eq. 6.12 and is about 16. This value is really high compared to other experimental investigation of transport in heterogeneous media at the laboratory scale. Similar assumptions as in Chapter 6 are made regarding the computation of equivalent correlation lengths. The material with the largest volumetric proportion (i.e. material 3) is supposed to control flow and transport and correlation lengths are computed from the mean facies length and from the volumetric proportion of other materials. This yields $\lambda_1 = 0.1$ m and $\lambda_2 = 0.01$ m.

The geometric mean of the permability field is computed using Eq. 6.11 and equals $1.81 \ 10^{-4}$ m/s. The effective permeability for a mean flow aligned with the X direction is computed from Eq. 6.13 and equals $1.37 \ 10^{-3}$ m/s. This value is one order of magnitude higher than the value actually measured . Moreover, the theoretical value of effective permeability for a mean flow parallel to the Y direction would be negative, making the stochastic theory of flow upscaling totally unadapted. In the self-consistent approach, the effective permeability for a mean flow aligned with the X direction is given by Eq. A.22 and equals $4.60 \ 10^{-3}$ m/s, which is a worse estimation than the stochastic result.

Analytical results from theories on solute transport in heterogeneous media generally assume a constant effective porosity. Therefore, permeability values will be corrected so that migration velocities correspond to a normalized constant effective porosity, that will be arbitrarily taken equal to 40 %.

7.5.2 Upscaling of longitudinal dispersivity

In this section, upscaling theories for apparent dispersivity are tested based on available data. The main difference with what was previously done is that parametrization methods cannot always be applied as presented in Chapter 4, due to the lack of necessary data. Moreover, apparent dispersivity values obtained from temporal moment analysis of the local breakthrough curves cannot be compared with upscaling results of non-Fickian theories as they do not
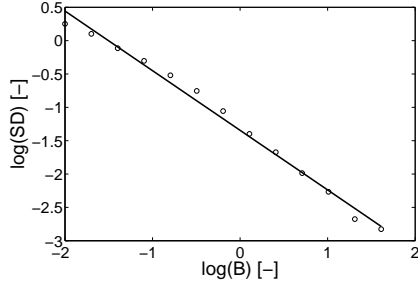
Figure 7.20: Dispersional analysis to determine Hurst coefficient in the longitudinal direction. B is the bin length and SD is the transscale statistic.
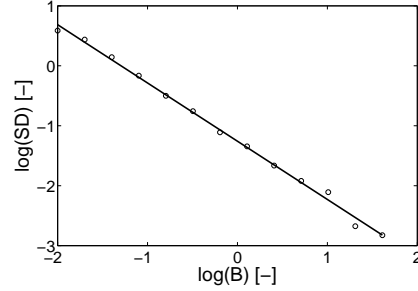
Figure 7.21: Dispersional analysis to determine Hurst coefficient in the transverse direction. B is the bin length and SD is the transscale statistic.

represent an average behavior over the full aquifer thickness. Therefore, non-Fickian models will only be compared based on outlet BTC data. The value of apparent dispersivity that was obtained from curve-fitting analysis $\alpha_L^* = 1.02$ m is the reference value that will be used in this section. Considering the low quality of the prediction of effective permeability, inclusion models will not be applied in this section.

In the stochastic approach, asymptotic longitudinal dispersivity can be calculated using Eqs. 2.29 and is equal to $3.2 \ 10^{-3}$ mm ! This value is about 6 orders of magnitude smaller than the measured one. Actually, for high anisotropy, the scale-effect in apparent dispersivity is generally of limited extension and decreases when variance increases (see Fig. 2.4). For high variance and high anisotropy, if flow is parallel to the bedding, solute transport mainly occurs in one single direction and velocity perturbations are of limited magnitude. Using the analytical expression derived for a bimodal medium (Eq. 6.15), assuming that material 1 is similar to material 3, a value $\alpha_L^* = 1.44$ m is found. This is in a better agreement with the observed value but, as this solution assumes isotropy, an anisotropic version of it would probably yield a value of a similar order of magnitude as the first estimation (i.e. $\approx 10^{-3}$ mm).

Figs. 7.20 and 7.21 show the results of the dispersional analysis conducted along X and the Y direction respectively. H_X is found equal to 0.11 ± 54 % and $H_Y = 0.03 \pm 135$ %. Using a similar method as in Chapter 6, one obtains $\hat{H} = 0.067$ and $\alpha_X/\alpha_Y = 1.93$. In this case, and contrary to Markovian fields investigated in Chapter 6, the ratio α_X/α_Y is positively correlated with λ_X/λ_Y. L_m is representative of a physical boundary of the flow system and will be taken equal to $L_m = 2.26$. Eq. 2.46 predicts an asymptotic value of macrodispersivity equal to $\alpha_L^* = 2.01$ m, which is of a correct order of magnitude. If transient dispersivity is computed assuming a perfectly stratified system and a transverse dispersivity of 1 mm, a value $\alpha_L^* = 1.09$ m is found, which is relatively close to the actual value.

Expectively, upscaling theories for apparent longitudinal dispersivity do not yield acceptable predictions, since reactive transport is believed to play an important role in observed tailing effects. The surprising result is that the fractal method exhibit a relatively high efficiency. As this model only accounts

for advective processes, which could indeed take place (as diffusion and slow advection in low-K zones have a similar effect on tailing behavior [88]), this result is believed to be a coincidence.

7.5.3 Application of upscaled transport equations

In this section, attempts to predict the outlet BTC using upscaled transport equations are performed. Temporal and spatial CTRW methods are used, as well as mobile-immobile models. Transport parameters are obtained from local BTC. Since transport is believed to be reactive, using information from local concentration data should highly improve the prediction of the outlet BTC through lumped transport parameters. As already done when analyzing local BTC in Section 7.3.4, non-ideal injection conditions are supposed to be of minor influence but predicted outlet BTC are convoluted with a decreasing exponential to account for mixing in the downstream reservoir.

It is not possible to use all 17 local BTC simultaneously in the parametrization process of the temporal CTRW model. As moreover BTC tailing behavior is believed to be the principal evidence of anomalous transport, β_t was obtained from the separate analysis of each BTC. As optimization procedures are found to work more efficiently for cumulative breakthrough curves, experimental curves were integrated. They were also normalized with respect to injected mass and corrected in order to ensure a convergence towards 1. The scale factor determined when fitting the ADE on the raising part of the BTC could not be used as correction factor, as it usually led to concentrations higher than 1.

The curve-fitting tools already used in Chapters 5 and 6 were applied to determine temporal CTRW transport parameters. The matching of experimental data was relatively good for most of the BTC. Fig C.16 shows a smoothened distribution of the 17 local β_t values. Two peaks of equal amplitude are observed, at values $\beta_t = 0.626$ and $\beta_t = 0.985$. Other transport parameters are computed in a similar fashion. The distribution of $\ln(C_1)$ is also found to exhibit two peaks (Fig. C.17). Actually, C_1 values for the smallest peak correspond to β_t values equal to 0.5, which might highlight numerical problems. The value corresponding to the other peak is $1/C_1 = 1.259 \ 10^{-6}$ m/s, which is close to the observed velocity from temporal moment analysis of the outlet BTC and is a more realistic value. The distribution of $\ln(C_\beta)$ exhibits two peaks as well, at $C_\beta = 5597$ and $C_\beta = 1.085 \ 10^6$, corresponding to the lowest and highest β_t peaks respectively (Fig. C.18).

Fig. 7.22 shows the outlet breakthrough curve, its best fit as well as the prediction using transport parameter values determined previously. The optimal β_t value is 0.5 and $1/C_1 = 8.42 \ 10^7$. It can be seen that the prediction corresponding to the higher β_t peak is relatively different than the actual concentration distribution. However, for $\beta_t = 0.62$, though concentration levels are a bit underestimated, the general shape of the curve is correctly predicted. The problem arising for such a low β_t value is that early-time concentration is overestimated (with an instantaneous transfer of about 20 % of the total mass.

The value of β_x obtained from the scale effect in apparent dispersivity (Fig. 7.12) is 1.53. $\mathcal{D}_x$ and γ_B were determined for each local BTC and their distribution are shown respectively in Figs. C.19 and C.20. The peak value for
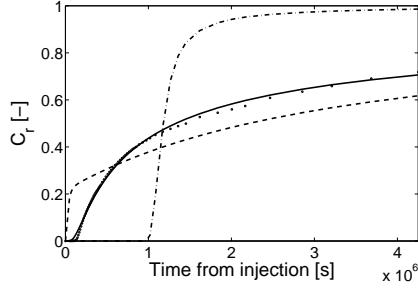
Figure 7.22: Outlet breakthrough curves and temporal CTRW solutions. Experimental data (circle), optimal fit (continuous line), prediction 1 ($\beta = 0.62$, $1/C_1 = 1.259 \ 10^{-6}$ m/s and $C_{beta} = 5557$: dashed line) and prediction 2 ($\beta = 0.98$, $1/C_1 = 1.259 \ 10^{-6}$ m/s and $C_{beta} = 1.085 \ 10^6$: dot-dashed line).
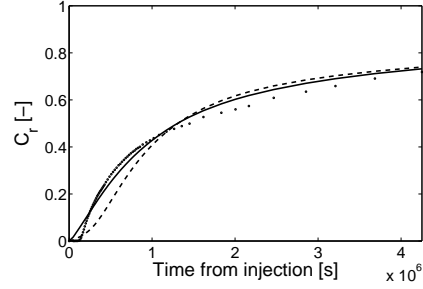
Figure 7.23: Outlet breakthrough curves and spatial CTRW solutions. Experimental data (circle), optimal fit (continuous line) and prediction (dashed line).

$\mathcal{D}_x$ is $2.79 \ 10^{-6}$. The distribution of γ_B is relatively uniform. The value that will be taken into consideration is the mean value -0.575. The problem arising with the outlet BTC is the prediction of the average migration velocity. It was concluded that upscaling methods for permeability failed to predict even a correct order of magnitude for K_e. Based on concentration data, the mean velocity from temporal moment analysis is $v = 1.243 \ 10^{-6}$ m/s. This value is in a good agreement with the observed velocity at the tank outlet and will be adopted for the prediction. The fitted values on the outlet BTC are respectively $\mathcal{D}_x = 4.38 \ 10^{-6}$ and $\gamma_B = 0.04$. Fig. 7.23 shows that the predicted distribution is in a relatively close agreement with the optimal curve. The overall discrepancy is also relatively small.

No methodology was introduced in Chapter 4 to determine mobile-immobile model parameters. A relatively straightforward way to do this is then to perform a curve-fitting analysis on local BTC, as done for fractional-order equations. Application of MIM to Markovian fields can be however less artificial, as a direct measure of the volumetric proportion of the immobile zone is available, and as transfert rate is expected to be inversely proportional to the square of the transversal size of the inclusions [202]. In this work, it is proposed to use exchange rate parameters obtained in Section 7.3 to simulate outlet concentration. θ_{im} is computed as the volumetric proportion of material 3, i.e. 50.0 %. Velocity and dispersivity are values obtained from early-time local concentration fit (local transport parameters) as well as from temporal analysis (global transport parameters) are tested.

Two different exchange models are tested here, but are not optimized. A single-rate model is compared to the multirate model corresponding to a lognormal distribution of exchange rates. Analytical solutions are computed using STAMMT-L [93]. Local parameters are unadapted to predict transport and lead to an overestimation of the rate of recovery. On the contrary, and as for the temporal CTRW model, global transport parameters lead to an underes-
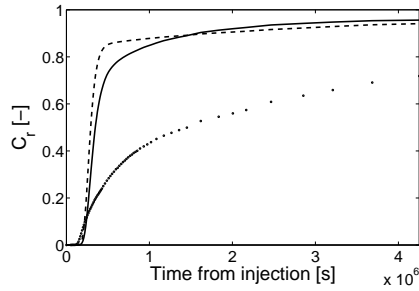
Figure 7.24: Outlet breakthrough curves and multi-domain solutions with local transport parameters. Experimental data (circle), single rate prediction (continuous line) and multirate prediction (dashed line).
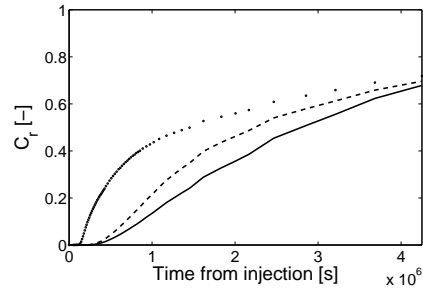
Figure 7.25: Outlet breakthrough curves and multi-domain solutions with global transport parameters. Experimental data (circle), single rate prediction (continuous line) and multirate prediction (dashed line).

timation of convergence. In general, one can consider that the use of global transport parameters and a multirate model yields a better prediction.

7.6   Conclusion

In this section, an original laboratory experiment involving a highly heterogeneous composite model aquifer has been performed. The experiment was carefully designed in order to ensure a preferential pathway flow architecture and stimulate diffusion processes through low-permeability zones. Rhodamine WT was used as a tracer in order to be able to measure a wide range of concentration distributions. However, batch tests revealed that it was sorptive onto soil grains, even though they were industrial silica sands. Concentration were monitored at 17 locations in the sample and at the tank outlet. Heavy concentration tails as well as a slow recovery were observed.

A numerical model accounting for both physical and chemical processes could not be set up due to complexity of transport. A model allowing simultaneously the correct simulation of local dispersion and diffusion processes (i.e. without numerical diffusion) and incorparating the possibility to simulate sorption processes (more complex than linear retardation) could not be identified. Instead, a particle-tracking algorithm was used, taking into account retardation through lumped porosities. Comparison of numerical concentration data with actual measurement at the model outlet showed that chemical transport was probably rate-controlled, with slow desorption processes.

Upscaling procedures were applied to predict apparent dispersivity. Using only information on aquifer properties or local concentration data, attempts were performed to predict the outlet concentration distribution. A direct comparison with results from Chapter 5 and Chapter 6 is not straightforward. In this case, transport is known to be reactive and parametrization methods used in this chapter are different. Several observations are however drawn here.

Contrary to previous simulations, it appeared that the stochastic method

failed to predict both effective permeability and apparent longitudinal dispersivity. It seems that the combination of a high anisotropy and a high variance is the cause of such a behavior. Application of a fractal model allowed a prediction of apparent dispersivity close to the actual measured value. This model was however incapable neither to simulate heavy concentration tails, nor to explicitly embody chemical interaction. Inclusion models yielded such a non-optimal estimation of effective permeability that no attempt to predict apparent dispersivity was performed.

As in Chapter 5 and 6, upscaled equations, although somehow difficult to parametrize based on the available data, revealed to be tools of a higher efficiency. Lumped parameters embodying physical and chemical processes could be estimated based on averaged parameters from local BTC. The spatial CTRW method yielded the best results and, as expected since they are basically equivalent, temporal CTRW and MIM produced upscaling results of a similar quality.

Chapter 8

Conclusions

The general objective of this study was to perform a comparison of existing theoretical transport models in field-like heterogeneous situations. The classical Fickian advection-dispersion model is indeed widely used but suffers from a lack of upscalability. Its transport parameters, when measured at a local scale, are most of the time upscaled using empirical relationships or using rules of thumb. Therefore, in a first stage, a collection of upscaling methods and non-Fickian models were identified in the literature and are reported in Chapter 2 and Chapter 3.

Upscaling methods provide tools to estimate a macroscale apparent dispersion coefficient based on a model of the soil structure, which can be incorporated in the standard ADE. As practitioners are used to deal with the ADE, which moreover has relatively simple analytical solutions, this method is usually preferred to non-Fickian models. Another advantage of upscaling methods is that numerical tools developed to solve the ADE under more complex heterogeneous conditions remain of use. However, apparent dispersivity is only part of the information needed to predict concentration levels. It may occur that concentration curves exhibit either early breakthrough or long tailing, due to heterogeneity at a scale that cannot be resolved by common field characterization techniques. In that case, the ADE, even with an upscaled apparent dispersivity, is useless and non-Fickian models have to be applied instead.

Two indicators have been defined in Chapter 4 to quantify the improvement brought by either upscaling methods or non-Fickian models to solute transport modelling. The first one (ϵ_u) focuses on apparent dispersivity. It measures the relative difference between observed and predicted dispersivity, averaged over the scale of interest. It is mainly aimed at evaluating upscaling methods for dispersion. A second indicator (ΔRMS_u) was defined in order to evaluate whether the whole concentration curves are better predicted. It is defined as the difference between the root-mean-square of the ADE residuals and that of the non-Fickian (or upscaled ADE) residuals. It therefore quantifies an improvement relative to the local ADE.

8.1 Transport in stratified formations

As a first approach to solute transport in heterogeneous media, the case of a perfectly stratified aquifer was investigated. Besides being a rather simple and conceptual case for which the structure of the K field can be characterized using a reduced parameter set, a variety of analytical solutions are available for the various transport models of interest.

In this study, 25 realizations of a log-normal permeability profile were investigated, characterized by an exponential covariance function with a variance and a relative correlation length (defined as the ratio of the correlation length divided by the aquifer thickness) ranging from 0.01 to 4 and 0.01 to 1 respectively. To the author's knowledge, no such detailed numerical computation of solute transport in perfectly stratified media has been performed so far, accounting for heterogeneous local longitudinal and transverse dispersion and over distances as far as 100 times the aquifer thickness.

Apparent longitudinal dispersivity was found to exhibit a large scale effect. Values up to 2000 times the local longitudinal dispersivity have been observed and no convergence to an asymptotic constant value seemed to happen. Considering upscaling methods for apparent dispersivity, it appeared that for larger correlation lengths (i.e. when the fulfilment of the ergodic condition becomes questionable), the fractal method yields the best results, whereas for intermediate correlation length, the stochastic method is the most efficient. For smaller correlation lengths, upscaling capacities of the stochastic method decrease because local dispersivity becomes of a similar order of magnitude as correlation length (which violates the assumptions under which stochastic analytical solutions are derived). A surprising result is that the variance does not seem to influence the capacities of the stochastic method.

Considering upscaling of concentration distributions, two models appeared to have the best upscaling capacities : the spatial CTRW model for large variance and the modal method (Scheidegger's telegraph equation) for large correlation length. Moreover, whereas temporally and spatially anomalous transport models were found to be relatively equivalent regarding upscaling of longitudinal dispersivity, temporal CTRW was found to have a limit scale beyond which upscaling capacities for solute transport decreased.

8.2   Transport in 2D heterogeneous formations

Transport in two-dimensional heterogeneous media was studied both using numerical and physical data. A similar numerical approach as for transport in stratified formations was first adopted to refine the parametric study and assess the influence of soil structure in more complex cases. Among others, that study allowed one to give recommendations for the design a original laboratory experiment. The latter was conducted to verify whether conclusions drawn from synthetic numerical examples could be extended to a physical situation at the laboratory scale.

8.2.1   Results from the numerical study

First, eight realizations of random log-normal permeability fields characterized by various variance, correlation lengths and inclination angle with respect to flow direction were studied. A scale-effect in apparent dispersivity could be observed and could be simulated with a relative quality by all methods (except the temporal CTRW). However, although methods for the prediction of effective flow parameters were in a close agreement with observed values of permeability

and velocity, a misprediction of advective transport revealed to be the main cause of discrepancy between numerical observations of concentration and non-Fickian models. This is due to the non-fulfilment of the ergodic condition for measurements close to the injection. In particular, this caused poor upscaling results for the temporal CTRW. It also highlighted the need for a separate (large-scale) estimation of advective transport, that can be obtained e.g. from head measurements. Globally, spatial CTRW yielded the best upscaling results

Then, eight realizations of bi- and tri-modal permeability fields were created from Markov chains models. They were all characterized with similar facies proportions and permeabilities, but various sets of correlation lengths and inclination angle were investigated. Finally, a last example was created from a bimodal field and two zero-mean log-Gaussian fields. This example was set up in order to introduce a multi-scale heterogeneous example in the analysis, and be able to discern the relative importance of small-scale variations on overall transport. Globally, due to the general higher level of heterogeneity for these examples, upscaling results were of a poorer quality. Difficulty of transport prediction even appeared through numerical problems for analytical solutions for some of the non-Fickian models.

8.2.2 Results from the laboratory study

A highly heterogeneous ($\sigma_Y^2 \approx 16$) composite aquifer was created in an intermediate-scale laboratory tank and a one-dimensional tracer test was performed using Rhodamine WT. Transport was monitored at 17 locations evenly set along the tank side, as well as in the downstream reservoir. BTC exhibited strong tailing behavior, enhanced by chemical interaction between tracer and soil grains.

Regarding upscaling methods, the fractal model predicted a value of apparent dispersivity at the model outlet resulting in a relative agreement with the observed value. Upscaled transport equations could be parametrized in a rather empirical fashion, but upscaling results were of an acceptable quality. The spatial CTRW model seemed again to yield the best prediction at model outlet using only smaller-scale information.

Two other general conclusions from this part of this study deal with current laboratory and numerical techniques. First, an accurate numerical model of the laboratory experiment could not be set up due to the complexity of physical and chemical processes. A model able to simulate both accurate local-scale diffusion and dispersion and complex kinetic sorption reaction could not be identified. Then, although the tracer was carefully chosen, some of its drawbacks increased modelling difficulties. Rhodamine WT is relatively stable to sunlight and can be detected over a wide range of concentrations. It is however reactive with soil grains, even with washed industrial silica sands, and may undergo irreversible sorption. This behavior significantly complicated the analysis of breakthrough curves. Moreover, liquid phase samples were manually taken. This induced a perturbation on the head field and the flow lines in the tank. Non-perturbative methods should be preferred, like geophysical methods. These methodes have moreover the advantage to allow one to perform a three-dimensional visualization of solute plumes. However, geophysical methods like electrical tomography

must be used with electrically conductive tracers (e.g. bromide) at relatively high concentration. If high concentrations are needed, it is then necessary to adapt density criteria (developped to assess the influence of density effects on advection-dominated transport) to diffusion-dominated situations.

8.3   Perspectives

This study was mainly a theoretical and conceptual study, performed under simple conditions (e.g. isothermal conditions, biphasic medium only, processed soils, ...). A lot of links are still missing in the chain between our conclusions and the practical implementation of efficient upscaling methods in the field. Some of them are evoked in this section.

First of all, a general trend emerging throughout this study is the need for better characterization methods. The stochastic method is widely developed in the literature and a non-negligible part of it is devoted to the estimation of the geostatistical parameters. However, as shown in this work, other non-Fickian models yield better performances and might be worth having more elaborate characterization methods. For example, for the set of examples investigated here, the estimation of the Hurst coefficient of fractal media was subject to a relatively high uncertainty. Similarly, research to link CTRW parameters directly to the soil structure is needed in order to depart from the requirement of concentration data (which has moreover to be obtained at different scales) to parametrize fractional-order equations.

The approach adopted in this study proceeded by successive increase of the complexity of the soil structure, starting from a simple perfectly stratified case and going to anisotropic two-dimensional situations with flow tilted with respected to the principal directions of the permeability field. Therefore, a natural extension of this study would be to investigate three-dimensional heterogeneous situations. Along the same lines, only log-Gaussian and Markovian fields were tested here. The definition of *field-like* aquifers adopted in this study could be extended to fractal aquifers, as well as permeability field exhibiting multiscale heterogeneity (similar to the K_{17} case investigated in Chapter 6).

The aim of this study was to assess solute transport in various situations, each of them being one realization of a given random field. As recommendations are given on the applicability of each model with respect to the parametric description of the aquifer, it could be of importance to verify whether conclusions drawn in this study can be extended to other realizations of the K fields investigated.

Only one-dimensional transport was investigated in this study, and one focused exclusively on longitudinal apparent dispersivity. However, transverse dispersivity is of primary importance too. It controls lateral mixing (see e.g. Chapter 5) which, for point source pollution, is directly linked to the spatial extension of the solute plume. Literature on transverse dispersivity is relatively scarce, and even reliable local-scale experimental values are difficult to obtain. Little work has focused on the prediction of transverse dispersivity in field situation, and the general rule of thumb is to take as value for transverse dispersivity one tenth of the longitudinal value. There is therefore a need to

perform an in-depth study of the influence of heterogeneity on apparent values of this parameter.

Finally, further on the way to the practical application of non-Fickian models, it is necessary to assess their capacities under conditions of non-uniform flow, likely to occur in situations of remediation. Recent studies have indeed revealed that apparent transport parameters are modified by flow conditions. This is a rather alarming observation as it implies that transport parameters obtained from different types of tracer tests would not be suited to situations were different flow conditions occurs. Non-Fickian models involving parameters that are not scale-dependent might solve this issue.

Appendices

Appendix A

Effective permeability of two-dimensional media

In this section, an analytical expression for longitudinal effective permeability of two-dimensional anistropic media is derived using the self-consistent approach. This derivation is already available in the literature for isotropic media [50] and for anisotropic three-dimensional media [53], but the two-dimensional anisotropic case was left as an exercise by Dagan in his reference textbook [53]. It will be resolved in this section by following step by step the methodology proposed by Dagan in his original paper [50].

In the self-consistent approximation, space-averaged gradient and specific discharge in the longitudinal direction consist of a sum of contributions from each block [50]

$$\langle J \rangle \quad = \quad J_0 + \Sigma_{i=1}^{N} \Sigma_{j=1}^{M} \Delta_{ij} J \qquad (A.1)$$

$$\langle q \rangle \quad = \quad -K_0 J_0 + \Sigma_{i=1}^{N} \Sigma_{i=j}^{M} \Delta_{ij} q \qquad (A.2)$$

where J_0 is the gradient corresponding uniform velocity at infinity, and $\Delta_{ij} J$ and $\Delta_{ij} q$ respectively correspond to gradient and specific discharge fluctuation caused by inclusion i of permeability K_j. Other parameters are defined in Section 2.4. Effective permeability in the longitudinal direction is found according to $K_e = -q/J$.

One will only consider in the remaining part of this section inclusions of elliptical shape with semi axes A_i and B_i (with $e_i = B_i/A_i$), described by

$$\frac{x^2}{A_i^2} + \frac{y^2}{B_i^2} = 1 \qquad (A.3)$$

Provided that the inclusions are rescaled so that a cylindrical coordinate system (ρ, θ) can be adopted, the solution of the head field ϕ_{ij}^{int} and ϕ_{ij}^{ext} inside and around an ellipse i of permeability K_j can be writtten as

$$\phi_{ij}^{int} \quad = \quad J_0 \frac{1+e_i}{1+e_i \kappa_j} \rho \cos(\theta) \quad r \leq a_i \qquad (A.4)$$

$$\phi_{ij}^{ext} \quad = \quad J_0 \left(1 + \mu \frac{a_i^2}{\rho^2} \right) \rho \cos(\theta) \quad r \geq a_i \qquad (A.5)$$

in which $\kappa_j = K_j/K_0$ and $\mu = \pm |e_i \kappa_j - 1|/(e_i \kappa_j + 1)$, and has to be evaluated as positive for $\kappa_j < 1/e_i$ and as negative for $\kappa_j > 1/e_i$. $a_i = A_i(1+e_i)/2$ is the radial coordinate of the ellipse boundary in the transformed reference system.

The physical cartesian coordinate system link with the tranformed cylindrical coordinate system using

$$x = (\rho + c_i^2/\rho)\cos(\theta) \tag{A.6}$$
$$y = (\rho - c_i^2/\rho)\sin(\theta) \tag{A.7}$$

with $c_i = A_i\sqrt{1 - e_i^2}/2$.

Space-averages of longitudinal components of head gradient $\langle J_{ij}\rangle$ and specific discharge $\langle q_{ij}\rangle$ due to a single inclusion are

$$
\begin{aligned}
\langle J_{ij}\rangle &= \frac{1}{v}\int \nabla\phi_{ij}dv \\
&= \frac{1}{\pi R^2}\int_{\rho=R}\cos(\theta)\phi_{ij}^{ext}dA \tag{A.8} \\
\langle q_{ij}\rangle &= -\frac{1}{v}\int K\nabla\phi_{ij}dv \\
&= -\frac{K_0}{v}\left[\int_{\rho=R}\cos(\theta)\phi_{ij}^{ext}dA\right. \\
&\quad \left. +(\kappa_j - 1)\int_{\rho=a}\cos(\theta)\phi_{ij}^{int}dA\right] \tag{A.9}
\end{aligned}
$$

where Green's theorem was used. Integration is performed over a circle of radius $R >> a$ and $dA = 2\pi\rho d\rho$. Subsituting Eqs. A.4 and A.5 into Eqs. A.8 and A.9 allows one to compute gradient and specific discharge fluctuation caused by an inclusion

$$
\begin{aligned}
\Delta_{ij}J &= \langle J_{ij}\rangle - J_0 = p_{ij}\mu J_0 \tag{A.10} \\
\Delta_{ij}q &= \langle q_{ij}\rangle + K_0 J_0 \\
&= -p_{ij}K_0\left(\frac{(\kappa_j - 1)(1 + e_i)}{1 + e_i\kappa_j} + \mu\right)J_0 \tag{A.11}
\end{aligned}
$$

where $p_{ij} = a_i^2/R^2$ is the total volumetric proportion of inclusions of shape i and permeability K_j in the flow domain. Substitution in Eqs. A.1 and A.2 and taking into account that $\Sigma_{i=1}^M p_{ij} = p_j$ is the total volumetric proportion of phase K_j, yields

$$
\begin{aligned}
\langle J\rangle &= J_0\left[1 + \Sigma_{j=1}^N \mu p_j\right] \tag{A.12} \\
\langle q\rangle &= -K_0 J_0\left[1 + \Sigma_{j=1}^N\left(\frac{(\kappa_j - 1)(1 + e_i)}{1 + e_i\kappa_j} + \mu\right)p_j\right] \tag{A.13}
\end{aligned}
$$

At the continous limit $N \to \infty$ and $K_j \to K$ is a continuous distribution, so that $p_j \to f(K)dK$. Eqs. A.12 and A.13 then become

$$
\begin{aligned}
\langle J\rangle &= J_0\int(\mu + 1)f(K)dK \tag{A.14} \\
\langle q\rangle &= -K_0 J_0\int\left(\frac{(\kappa - 1)(1 + e_i)}{1 + e_i\kappa} + (\mu + 1)\right)f(K)dK \tag{A.15}
\end{aligned}
$$

where κ is now equal to K/K_0. The effective permeability is finally obtained as

$$K_e = K_0 \frac{\int \left(\frac{(\kappa-1)(1+e_i)}{1+e_i\kappa} + (\mu + 1) \right) f(K)dK}{\int (\mu + 1)f(K)dK} \quad \text{(A.16)}$$

which can be simplified to

$$K_e - K_0 = K_0 \frac{\int \frac{(\kappa-1)(1+e_i)}{1+e_i\kappa} f(K)dK}{\int (\mu + 1)f(K)dK} \quad \text{(A.17)}$$

Eq. A.17 provides a value of K_e in terms of permeability distribution $f(K)$ and unknown K_0. Neither correlation of the permeability field, nor block size influence K_e, which is accordance with results from stochastic theories [53]. K_0 is an arbitrary reference permeability that is linked to K_e. In the self-consistent approach, one assumes that K_0 is precisely equal to K_e, i.e. that the matrix surrounding each inclusion has the same effective permeability as the matrix as a whole [50]. Hence, K_e can be found by solving

$$\int \frac{(\kappa - 1)(1 + e_i)}{1 + e_i\kappa} f(K)dK = 0 \quad \text{(A.18)}$$

with, in this case, $\kappa = K/K_e$. In the isotropic case, Eq. A.18 writes

$$\int \frac{K - K_e}{K + K_e} f(K)dK = 0 \quad \text{(A.19)}$$

which can be shown to be identical to the result obtained by Dagan [50]

$$K_e = \frac{1}{2} \left[\int \frac{f(K)dK}{K + K_e} \right]^{-1} \quad \text{(A.20)}$$

Analytical solutions can be easily obtained in the case of media composed of two and three facies of constant permeability. For a two facies medium, $f(K) = \delta(K - K_1)p_1 + \delta(K - K_2)p_2$ and it can be verified that the effective permeability is the positive root of the second-order polynomial

$$K_e^2 + (p_1(eK_2 - K_1) - p_2(K_2 - eK_1)) K_e - eK_1K_2 = 0 \quad \text{(A.21)}$$

Fig. A.1 shows the solution to Eq. A.21 for $e = 1/4$ and investigates the influence of inclusion volumetric proportion p_2 and permeability K_2 on the effective permeability. Expectively, the dependence of K_e on the inclusion permeability K_2 decreases with the volumetric proportion of inclusions $p_2 = 1 - p_1$. Two different type of behavior can however be identified for low-permeability inclusions. For low p_2, K_e will converge towards a constant value and will not be influenced by K_2 anymore. This corresponds to a situation where the flow bypasses the low permeability inclusions. However, for higher p_2, such an asymptotic behavior does not exist and K_e remains strongly influenced by K_2. This corresponds to a situation where the volumetric proportion of low permeability material is too high for a bypass to occur. For high K_2, the inverse situation occurs and flow remains strongly dependent on the permeability of the inclusions for the whole range of possible volumetric proportions.
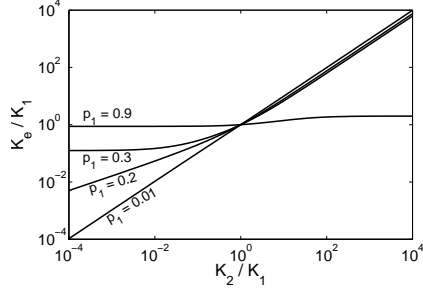
Figure A.1: Influence of volumetric proportion of inclusions on effective permeability of a two-facies medium. $e = 1/4$.
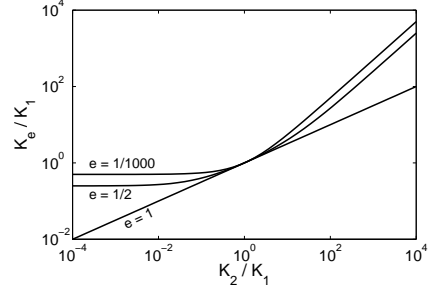
Figure A.2: Influence of anisotropy ratio of inclusions on effective permeability of a two-facies medium. $p_2 = 0.5$.
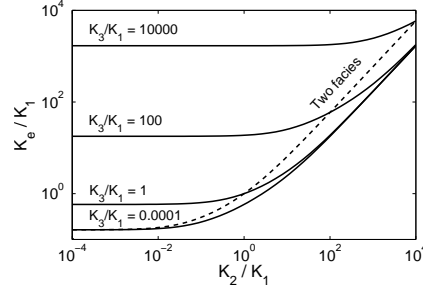

Figure A.3: Influence of the permeability of a third facies on effective permeability. $e = 1/4$, $p_1 = p_2 = p_3 = 0.33$.

The influence of anisotropy is illustrated in Fig. A.2 for $p_2 = 0.5$. In the isotropic case, $\log(K_e)$ and $\log(K_2)$ are linearly dependent. This is consistent with the well-known result $K_e = K_g$ in a two-dimensional geometry.

For a three-facies medium, $f(K) = \delta(K - K_1)p_1 + \delta(K - K_2)p_2 + \delta(K - K_3)p_3$ and the effective permeability is the only positive root of the third-order polynomial

$$
\begin{aligned}
K_e^3 &+ K_e^2 \left[e\left(K_1 + K_2 + K_3\right) - (1 + e)\left(p_1 K_1 + p_2 K_2 + p_3 K_3\right) \right] \\
&+ K_e e \left[(1 + e)\left(p_3 K_1 K_2 + p_2 K_1 K_3 + p_1 K_2 K_3\right) \right. \\
&\quad\left. - \left(K_1 K_2 + K_1 K_3 + K_2 K_3\right) \right] \\
&- e^2 K_1 K_2 K_3 \\
&= 0
\end{aligned}
\tag{A.22}
$$

Fig. A.3 shows the corresponding solution in the case of three facies present in equal volumetric proportion for an anisotropy ratio $e = 1/4$. It can be verified that the solution of a two facies system with $p_1 = 0.33$ and $p_2 = 0.67$ intersects the various curves at $K_3 = K_2$.

Appendix B

Perfectly stratified examples : Figures and tables

In this section, secondary data from the analysis performed in Chapter 5 are provided, either plotted under graphical form or given as numerical values in tables. For the sake of brevity, similar notations as in Chapter 5 are used to refer to upscaling methods and upscaled equations.
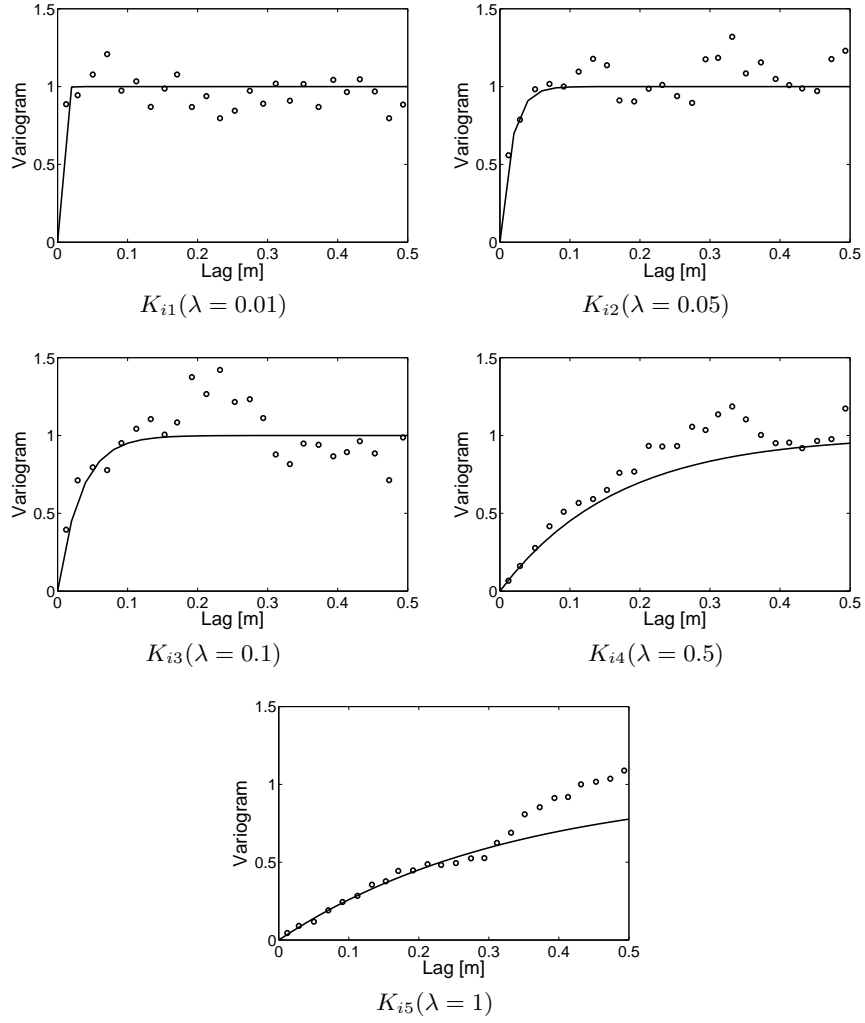
$K_{i1}(\lambda = 0.01)$

$K_{i2}(\lambda = 0.05)$

$K_{i3}(\lambda = 0.1)$

$K_{i4}(\lambda = 0.5)$

$K_{i5}(\lambda = 1)$

Figure B.1: Experimental (circles) and theoretical (continuous line) variograms corresponding to vertical $\ln(K)$ profiles adopted for stratified cases.
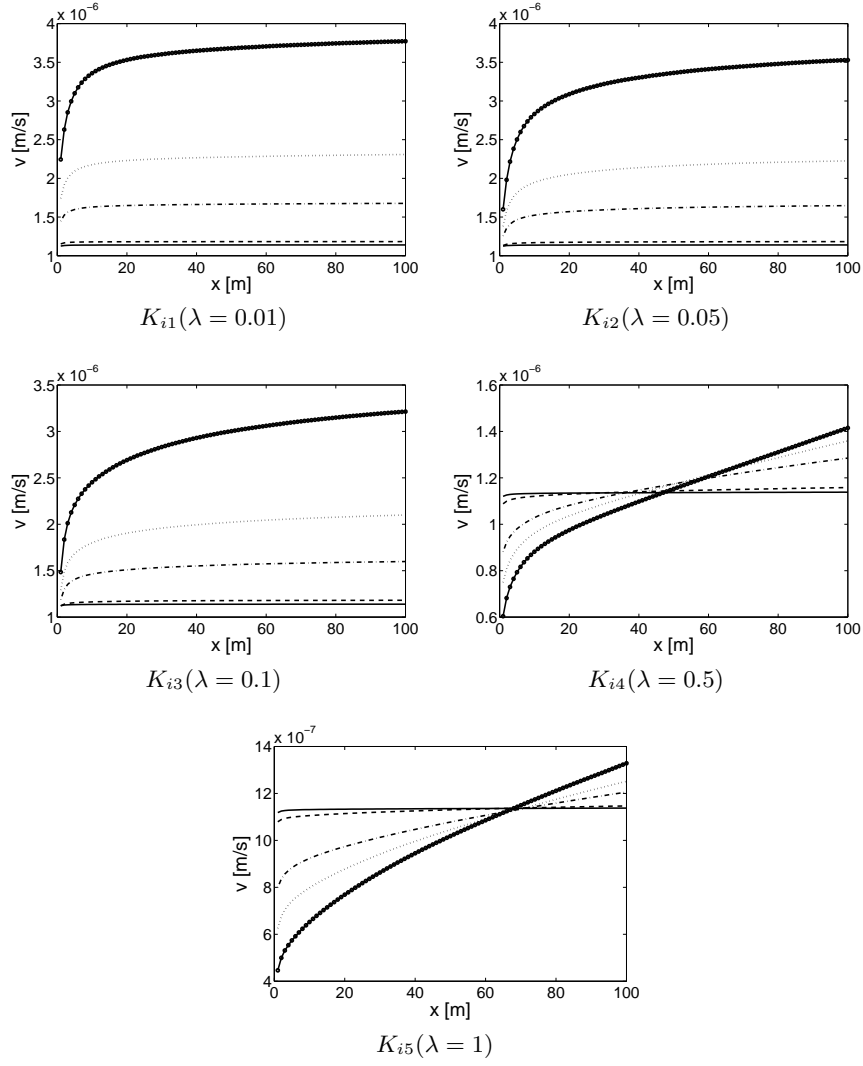
Figure B.2: Migration velocity values obtained from temporal moment analysis. $i = 1$ - $\sigma_Y^2 = 0.01$ (continuous line), $i = 2$ - $\sigma_Y^2 = 0.1$ (dashed line), $i = 3$ - $\sigma_Y^2 = 1$ (dot-dashed line), $i = 4$ - $\sigma_Y^2 = 2$ (small-dotted line) and $i = 5$ - $\sigma_Y^2 = 4$ (large-dotted line).
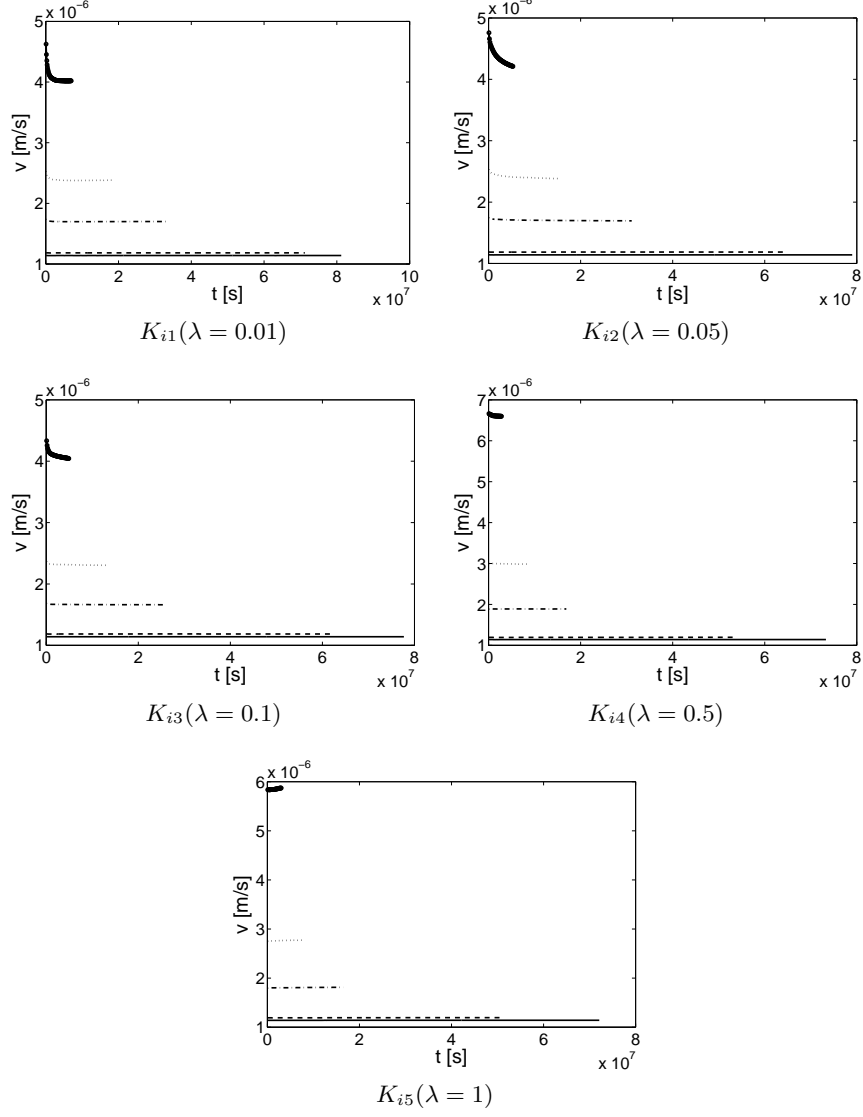
$K_{i1}(\lambda = 0.01)$

$K_{i2}(\lambda = 0.05)$

$K_{i3}(\lambda = 0.1)$

$K_{i4}(\lambda = 0.5)$

$K_{i5}(\lambda = 1)$

Figure B.3: Migration velocity values obtained from spatial moment analysis. $i = 1$ - $\sigma_Y^2 = 0.01$ (continuous line), $i = 2$ - $\sigma_Y^2 = 0.1$ (dashed line), $i = 3$ - $\sigma_Y^2 = 1$ (dot-dashed line), $i = 4$ - $\sigma_Y^2 = 2$ (small-dotted line) and $i = 5$ - $\sigma_Y^2 = 4$ (large-dotted line).

K_{ij}	$j=1$	$j=2$	$j=3$	$j=4$	$j=5$
$i=1$	$V_a = 0.010$	$\sigma_K^2 = 0.011$	$V_a = 0.010$	$V_a = 0.013$	$V_a = 0.019$
	$\lambda_K = 0.015$	$\lambda_K = 0.054$	$\lambda_K = 0.081$	$\lambda_K = 0.615$	$\lambda_K = 1.96$
	$\epsilon_u = 151.8$	$\epsilon_u = 31.94$	$\epsilon_u = 93.84$	$\epsilon_u = 160.9$	$\epsilon_u = 332.8$
$i=2$	$V_a = 0.100$	$V_a = 0.104$	$V_a = 0.089$	$V_a = 0.153$	$V_a = 0.183$
	$\lambda_K = 0.015$	$\lambda_K = 0.053$	$\lambda_K = 0.067$	$\lambda_K = 0.692$	$\lambda_K = 1.89$
	$\epsilon_u = 101.7$	$\epsilon_u = 88.56$	$\epsilon_u = 58.07$	$\epsilon_u = 182.5$	$\epsilon_u = 310.0$
$i=3$	$V_a = 1.046$	$\sigma_K^2 = 0.949$	$V_a = 0.817$	$V_a = 1.413$	$V_a = 1.246$
	$\lambda_K = 0.011$	$\lambda_K = 0.048$	$\lambda_K = 0.044$	$\lambda_K = 0.533$	$\lambda_K = 0.831$
	$\epsilon_u = 6.26$	$\epsilon_u = 93.81$	$\epsilon_u = 15.26$	$\epsilon_u = 146.9$	$\epsilon_u = 136.6$
$i=4$	$V_a = 2.136$	$\sigma_K^2 = 1.799$	$V_a = 1.722$	$V_a = 2.300$	$V_a = 2.121$
	$\lambda_K = 0.001$	$\lambda_K = 0.045$	$\lambda_K = 0.038$	$\lambda_K = 0.368$	$\lambda_K = 0.533$
	$\epsilon_u = 96.86$	$\epsilon_u = 99.40$	$\epsilon_u = 18.81$	$\epsilon_u = 115.5$	$\epsilon_u = 100.3$
$i=5$	$V_a = 4.368$	$\sigma_K^2 = 3.378$	$V_a = 3.799$	$V_a = 3.549$	$V_a = 3.501$
	$\lambda_K = 0.001$	$\lambda_K = 0.042$	$\lambda_K = 0.034$	$\lambda_K = 0.224$	$\lambda_K = 0.332$
	$\epsilon_u = 94.39$	$\epsilon_u = 104.0$	$\epsilon_u = 36.56$	$\epsilon_u = 94.89$	$\epsilon_u = 77.41$

Table B.1: Upcaling results for S. $V_a = \sigma_K^2/\langle K \rangle^2$ is an adimensional variance.

K_{ij}	$j=1$	$j=2$	$j=3$	$j=4$	$j=5$
$i=1$	$V_a = 0.008$	$V_a = 0.008$	$V_a = 0.007$	$V_a = 0.007$	$V_a = 0.006$
	$\lambda_K = 0.003$	$\lambda_K = 0.012$	$\lambda_K = 0.019$	$\lambda_K = 0.127$	$\lambda_K = 0.230$
	$\epsilon_c = 4.74$	$\epsilon_c = 5.69$	$\epsilon_c = 7.74$	$\epsilon_c = 5.19$	$\epsilon_c = 2.99$
$i=2$	$V_a = 0.075$	$V_a = 0.085$	$V_a = 0.068$	$V_a = 0.070$	$V_a = 0.060$
	$\lambda_K = 0.004$	$\lambda_K = 0.011$	$\lambda_K = 0.018$	$\lambda_K = 0.141$	$\lambda_K = 0.239$
	$\epsilon_c = 4.19$	$\epsilon_c = 3.77$	$\epsilon_c = 5.54$	$\epsilon_c = 3.81$	$\epsilon_c = 3.20$
$i=3$	$V_a = 0.394$	$V_a = 0.729$	$V_a = 0.406$	$V_a = 0.667$	$V_a = 0.574$
	$\lambda_K = 0.008$	$\lambda_K = 0.011$	$\lambda_K = 0.028$	$\lambda_K = 0.130$	$\lambda_K = 0.216$
	$\epsilon_c = 3.70$	$\epsilon_c = 1.78$	$\epsilon_c = 2.19$	$\epsilon_c = 3.97$	$\epsilon_c = 2.23$
$i=4$	$V_a = 0.921$	$V_a = 1.238$	$V_a = 1.048$	$V_a = 0.998$	$V_a = 0.972$
	$\lambda_K = 0.007$	$\lambda_K = 0.011$	$\lambda_K = 0.020$	$\lambda_K = 0.152$	$\lambda_K = 0.269$
	$\epsilon_c = 3.23$	$\epsilon_c = 1.28$	$\epsilon_c = 5.89$	$\epsilon_c = 1.45$	$\epsilon_c = 0.22$
$i=5$	$V_a = 3.316$	$V_a = 1.473$	$V_a = 0.998$	$V_a = 1.620$	$V_a = 1.663$
	$\lambda_K = 0.003$	$\lambda_K = 0.016$	$\lambda_K = 0.042$	$\lambda_K = 0.104$	$\lambda_K = 0.208$
	$\epsilon_c = 1.81$	$\epsilon_c = 1.03$	$\epsilon_c = 1.72$	$\epsilon_c = 2.45$	$\epsilon_c = 0.60$

Table B.2: Optimal geostatistical parameters for S. $V_a = V_{a,opt} = \sigma_K^2/\langle K \rangle^2$ is an adimensional variance. $\lambda_K = \lambda_{K,opt}$.
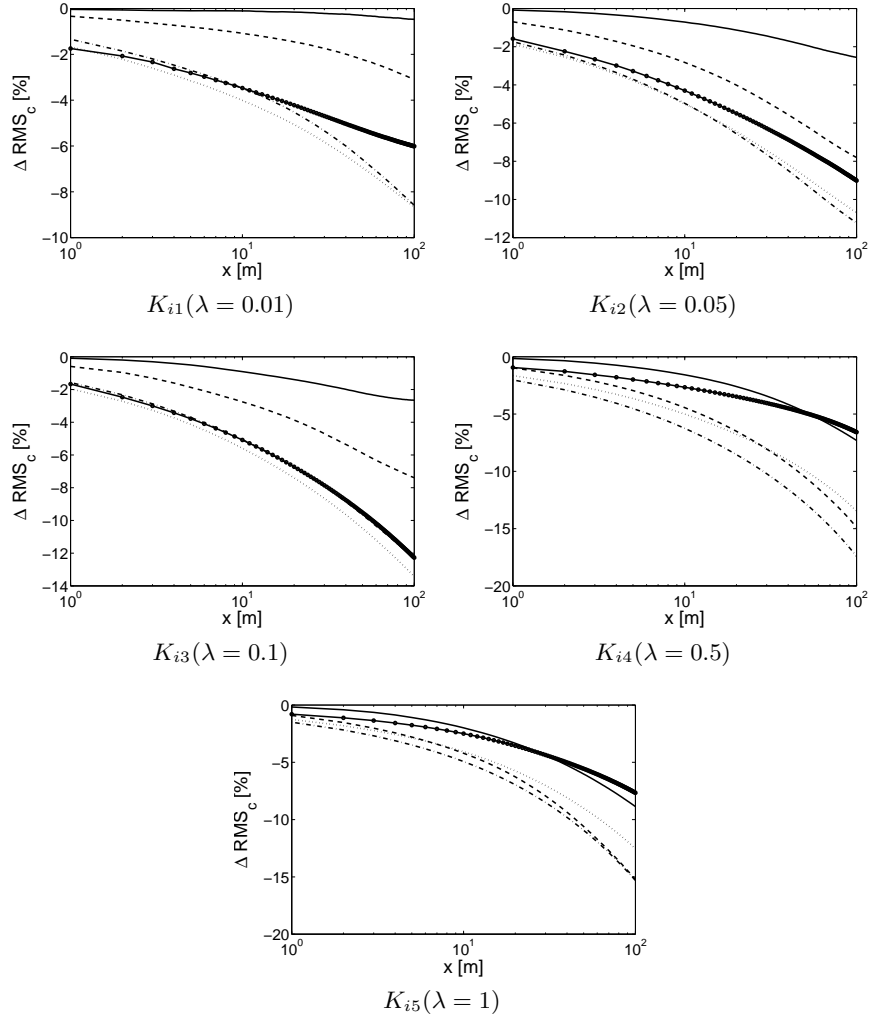
Figure B.4: Improvement of S with optimal parameters compared to the classical ADE. $i = 1$ - $\sigma_Y^2 = 0.01$ (continuous line), $i = 2$ - $\sigma_Y^2 = 0.1$ (dashed line), $i = 3$ - $\sigma_Y^2 = 1$ (dot-dashed line), $i = 4$ - $\sigma_Y^2 = 2$ (small-dotted line) and $i = 5$ - $\sigma_Y^2 = 4$ (large-dotted line).

K_{ij}	$j = 1$	$j = 2$	$j = 3$	$j = 4$	$j = 5$
	$H = 0.009$	$H = 0.041$	$H = 0.061$	$H = 0.091$	$H = 0.107$
$i = 1$	$L_m = 1.52$	$L_m = 1.80$	$L_m = 1.73$	$L_m = 6.86$	$L_m = 8.36$
	$\epsilon_c = 7.63$	$\epsilon_c = 1.11$	$\epsilon_c = 0.33$	$\epsilon_c = 0.78$	$\epsilon_c = 2.20$
	$H = 0.009$	$H = 0.038$	$H = 0.051$	$H = 0.109$	$H = 0.097$
$i = 2$	$L_m = 1.68$	$L_m = 1.84$	$L_m = 1.79$	$L_m = 6.11$	$L_m = 10.3$
	$\epsilon_c = 7.56$	$\epsilon_c = 1.65$	$\epsilon_c = 0.34$	$\epsilon_c = 0.66$	$\epsilon_c = 1.88$
	$H = 0.011$	$H = 0.033$	$H = 0.035$	$H = 0.096$	$H = 0.085$
$i = 3$	$L_m = 1.86$	$L_m = 1.66$	$L_m = 2.10$	$L_m = 7.11$	$L_m = 11.8$
	$\epsilon_c = 7.10$	$\epsilon_c = 2.49$	$\epsilon_c = 0.98$	$\epsilon_c = 0.36$	$\epsilon_c = 1.35$
	$H = 0.014$	$H = 0.032$	$H = 0.033$	$H = 0.071$	$H = 0.062$
$i = 4$	$L_m = 1.45$	$L_m = 1.43$	$L_m = 2.10$	$L_m = 8.03$	$L_m = 24.1$
	$\epsilon_c = 6.92$	$\epsilon_c = 2.68$	$\epsilon_c = 1.62$	$\epsilon_c = 0.25$	$\epsilon_c = 0.99$
	$H = 0.017$	$H = 0.031$	$H = 0.034$	$H = 0.049$	$H = 0.050$
$i = 5$	$L_m = 1.01$	$L_m = 1.25$	$L_m = 1.80$	$L_m = 7.48$	$L_m = 19.2$
	$\epsilon_c = 5.62$	$\epsilon_c = 1.69$	$\epsilon_c = 2.27$	$\epsilon_c = 0.11$	$\epsilon_c = 0.79$

Table B.3: Optimal parameters for F.

| K_{ij}	$j = 1$	$j = 2$	$j = 3$	$j = 4$	$j = 5$
	$V_a = 0.001$	$V_a = 0.001$	$V_a = 0.002$	$V_a = 0.004$	$V_a = 0.004$
$i = 1$	$\lambda_e = 3.24$	$\lambda_e = 22.0$	$\lambda_e = 17.8$	$\lambda_e = 41.1$	$\lambda_e = 96.9$
	$\epsilon_c = 17.6$	$\epsilon_c = 5.31$	$\epsilon_c = 4.81$	$\epsilon_c = 2.47$	$\epsilon_c = 1.21$
	$V_a = 0.002$	$V_a = 0.010$	$V_a = 0.013$	$V_a = 0.040$	$V_a = 0.042$
$i = 2$	$\lambda_e = 19.0$	$\lambda_e = 21.6$	$\lambda_e = 20.7$	$\lambda_e = 67.8$	$\lambda_e = 89.4$
	$\epsilon_c = 10.9$	$\epsilon_c = 5.80$	$\epsilon_c = 4.68$	$\epsilon_c = 2.73$	$\epsilon_c = 1.15$
	$V_a = 0.032$	$V_a = 0.089$	$V_a = 0.111$	$V_a = 0.426$	$V_a = 0.446$
$i = 3$	$\lambda_e = 23.3$	$\lambda_e = 19.4$	$\lambda_e = 22.1$	$\lambda_e = 49.8$	$\lambda_e = 55.7$
	$\epsilon_c = 10.6$	$\epsilon_c = 6.64$	$\epsilon_c = 5.23$	$\epsilon_c = 2.46$	$\epsilon_c = 1.02$
	$V_a = 0.078$	$V_a = 0.185$	$V_a = 0.231$	$V_a = 0.740$	$V_a = 0.869$
$i = 4$	$\lambda_e = 18.3$	$\lambda_e = 16.0$	$\lambda_e = 20.5$	$\lambda_e = 44.2$	$\lambda_e = 38.5$
	$\epsilon_c = 10.5$	$\epsilon_c = 6.81$	$\epsilon_c = 5.54$	$\epsilon_c = 2.42$	$\epsilon_c = 0.73$
	$V_a = 0.186$	$V_a = 0.388$	$V_a = 0.499$	$V_a = 1.139$	$V_a = 1.412$
$i = 5$	$\lambda_e = 12.6$	$\lambda_e = 13.3$	$\lambda_e = 16.5$	$\lambda_e = 34.5$	$\lambda_e = 45.8$
	$\epsilon_c = 9.25$	$\epsilon_c = 5.71$	$\epsilon_c = 5.79$	$\epsilon_c = 2.34$	$\epsilon_c = 1.10$

Table B.4: Optimal parameters for TE.
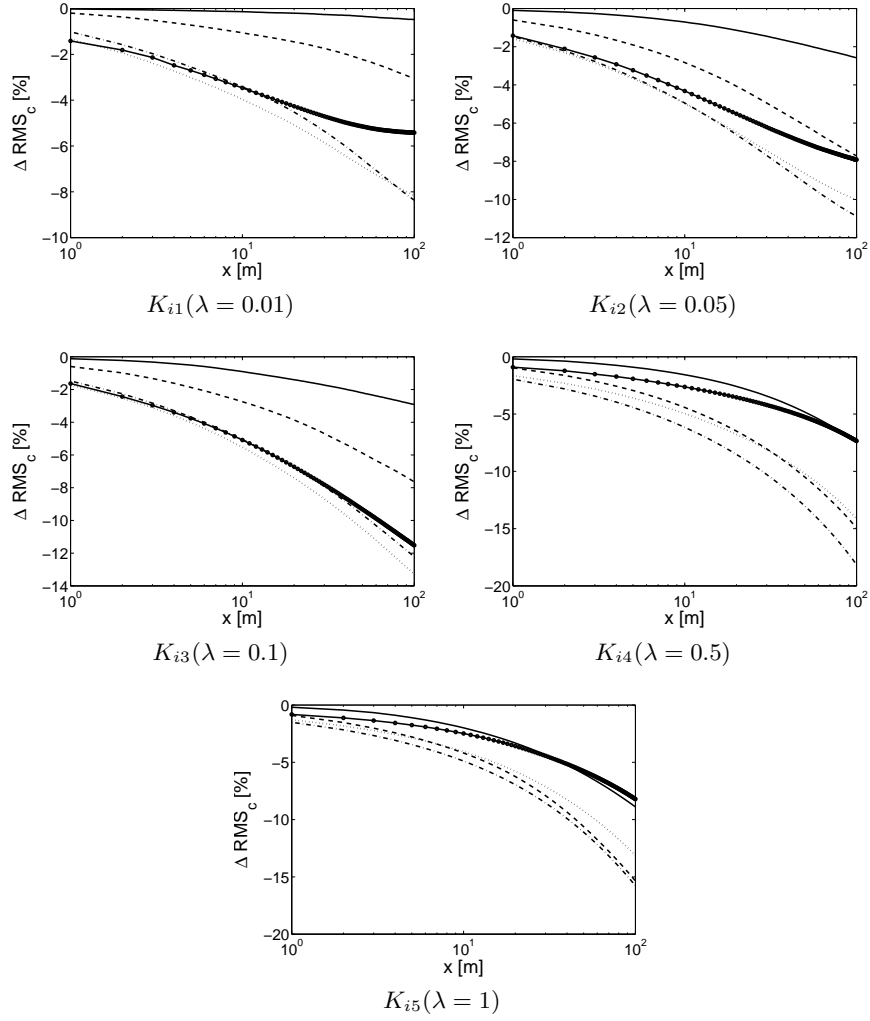
Figure B.5: Improvement of F with optimal parameters compared to the classical ADE. $i = 1$ - $\sigma_Y^2 = 0.01$ (continuous line), $i = 2$ - $\sigma_Y^2 = 0.1$ (dashed line), $i = 3$ - $\sigma_Y^2 = 1$ (dot-dashed line), $i = 4$ - $\sigma_Y^2 = 2$ (small-dotted line) and $i = 5$ - $\sigma_Y^2 = 4$ (large-dotted line).
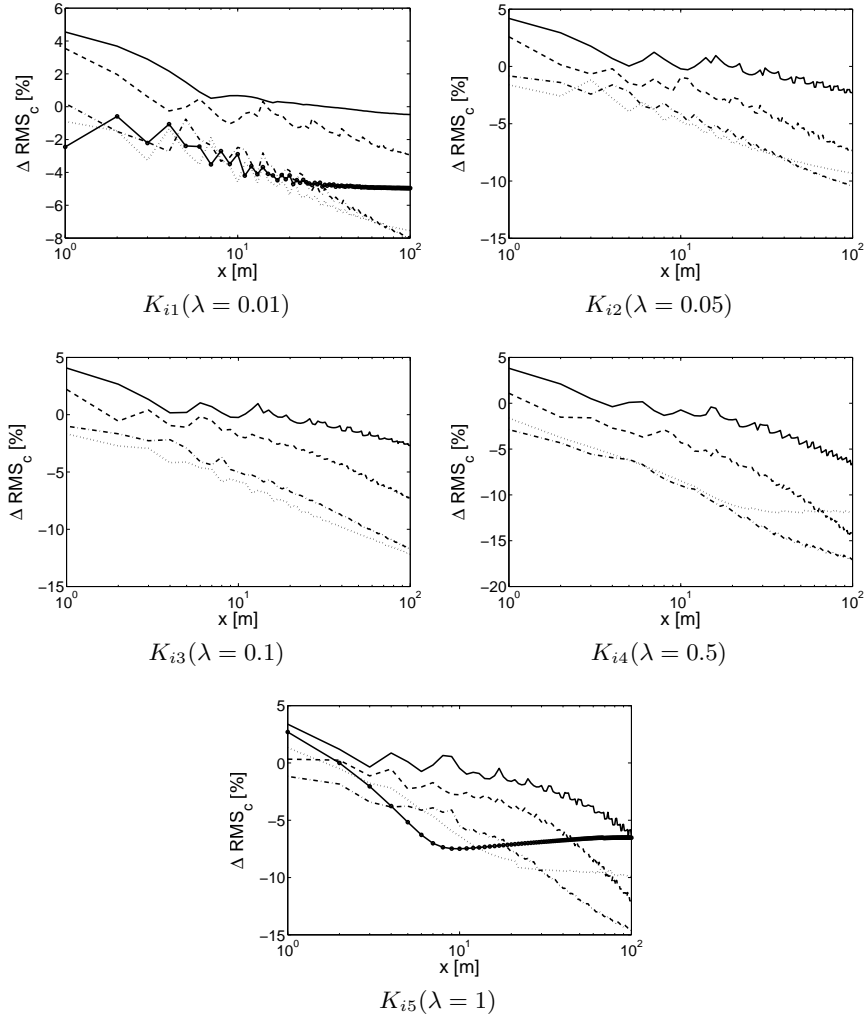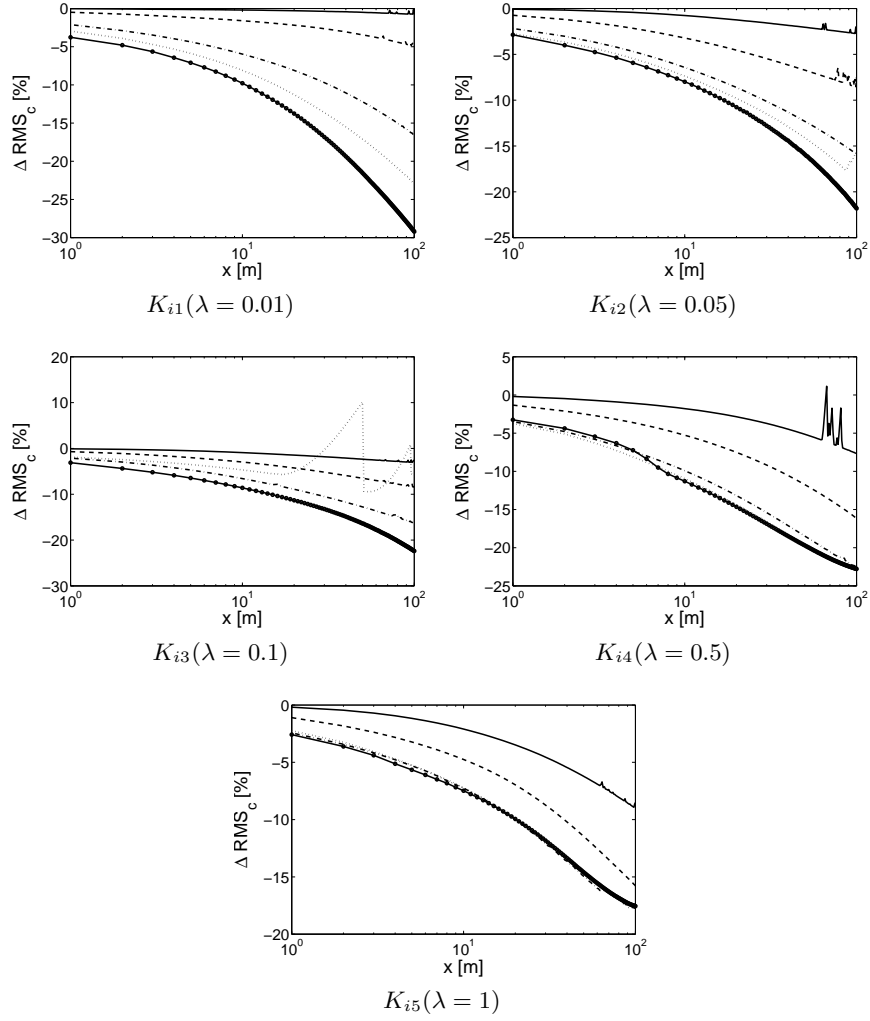
Figure B.6: Improvement of TE with optimal parameters compared to the classical ADE. $i = 1$ - $\sigma_Y^2 = 0.01$ (continuous line), $i = 2$ - $\sigma_Y^2 = 0.1$ (dashed line), $i = 3$ - $\sigma_Y^2 = 1$ (dot-dashed line), $i = 4$ - $\sigma_Y^2 = 2$ (small-dotted line) and $i = 5$ - $\sigma_Y^2 = 4$ (large-dotted line).
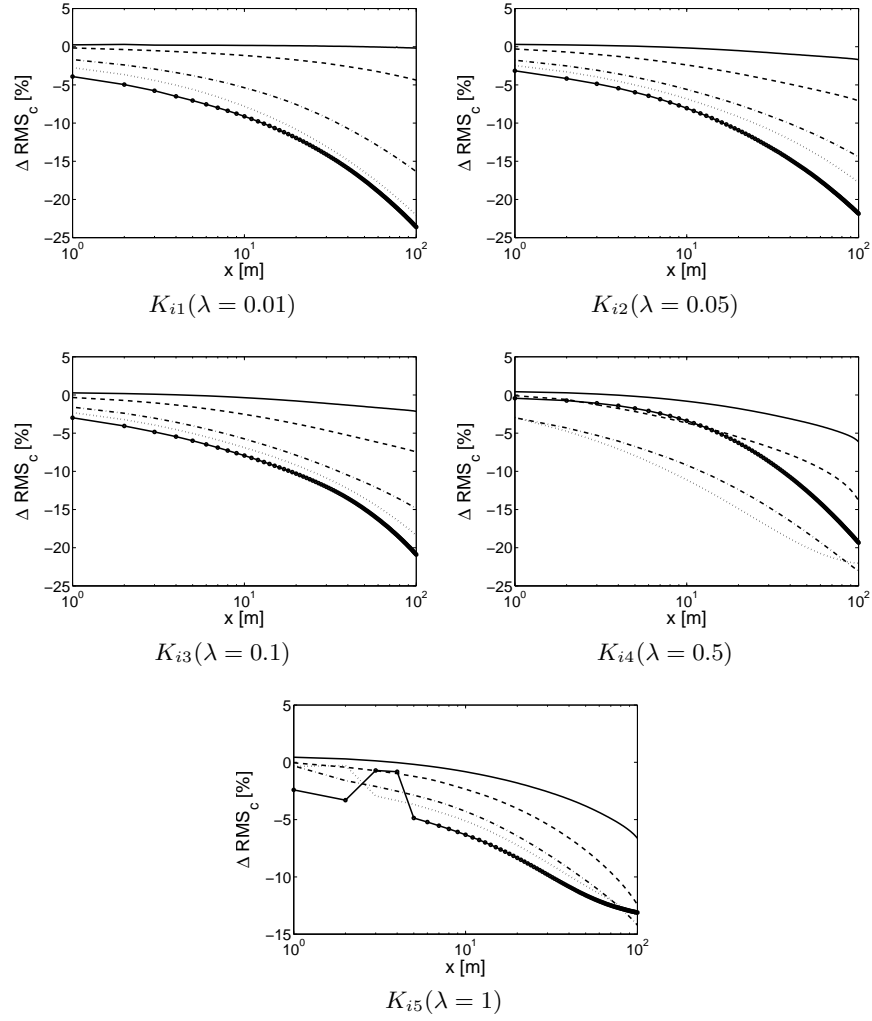
Figure B.7: Improvement of TC with optimal parameters compared to the classical ADE. $i = 1$ - $\sigma_Y^2 = 0.01$ (continuous line), $i = 2$ - $\sigma_Y^2 = 0.1$ (dashed line), $i = 3$ - $\sigma_Y^2 = 1$ (dot-dashed line), $i = 4$ - $\sigma_Y^2 = 2$ (small-dotted line) and $i = 5$ - $\sigma_Y^2 = 4$ (large-dotted line).

Figure B.8: Improvement of SC with optimal parameters compared to the classical ADE. $i = 1$ - $\sigma_Y^2 = 0.01$ (continuous line), $i = 2$ - $\sigma_Y^2 = 0.1$ (dashed line), $i = 3$ - $\sigma_Y^2 = 1$ (dot-dashed line), $i = 4$ - $\sigma_Y^2 = 2$ (small-dotted line) and $i = 5$ - $\sigma_Y^2 = 4$ (large-dotted line).

Appendix C

Laboratory experiment : Figures and tables

In this section, secondary data from the analysis performed in Chapter 7 are provided, either plotted under graphical form or given as numerical values in tables.

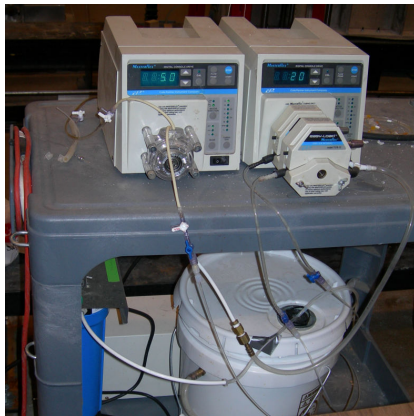**Figure C.1:** Overall view of the experimental setup

Figure C.2: View of the tap water filtering system and the pump

Figure C.3: View of the downstream fixed-head system

Figure C.4: Pressure measurement port. The scale is given by the size of the material 1 layer (≈ 2 cm).

Figure C.5: Liquid phase sampling port. The scale is given by the size of the material 3 layer (≈ 4 cm).
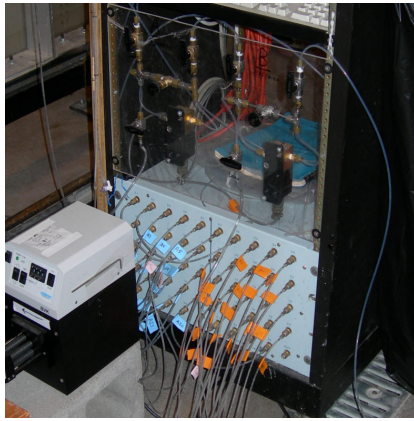

Figure C.6: Pressure measurement system. Mechanical multiplexer (down), pressure transducer (middle) and acquisition computer (up, not shown).
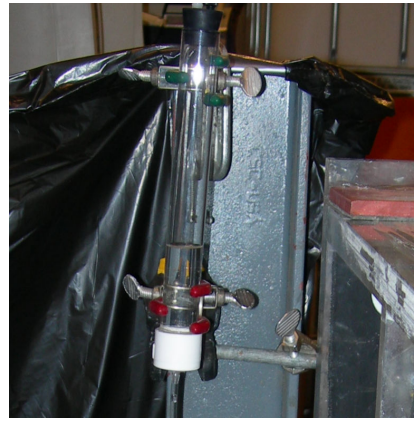

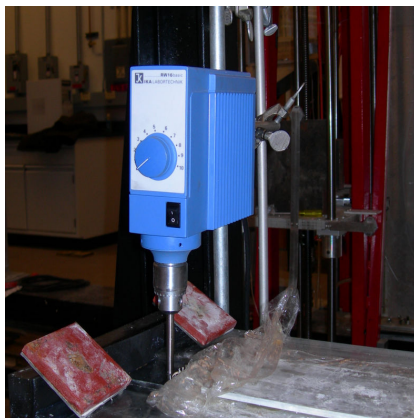**Figure C.7:** Pressure measurement system. Constant pressure reference point.

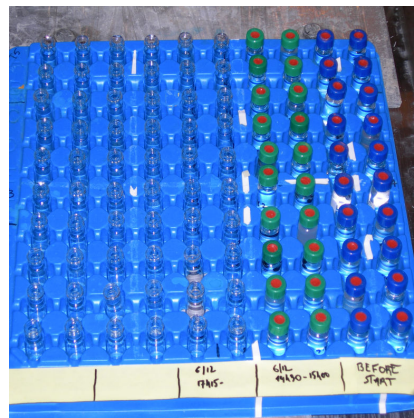**Figure C.8:** View of mechanical stirrer installed in the upstream reservoir
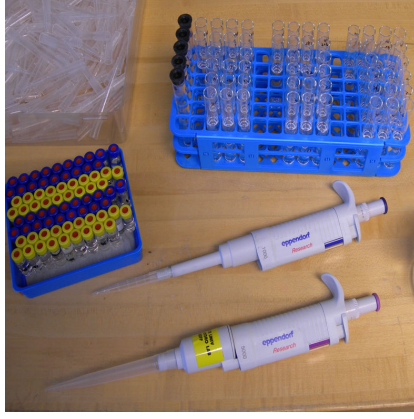

Figure C.9: Sampling bottles

Figure C.10: Material used to perform sample dilution

Figure C.11: View of the fluorometer

Port	X [m]	Y [m]	Head [m]	CV [-]
P3	2.26	-	0	0
P4	0.00	-	0.0321	0
P5	0.096	0.305	0.0312	0.012
P6	0.096	0.155	0.0319	0.010
P7	0.350	0.331	0.0312	0.009
P8	0.350	0.050	0.0314	0.010
P9	0.652	0.335	0.0302	0.115
P10	0.650	0.185	0.0301	0.082
P11	0.662	0.055	0.0299	0.010
P12	0.953	0.331	0.0299	0.009
P13	0.953	0.184	0.0287	0.009
P14	1.258	0.331	0.0287	0.009
P15	1.258	0.232	0.0280	0.009
P16	1.258	0.130	0.0277	0.008
P17	1.558	0.331	0.0181	0.020
P18	1.558	0.130	0.0018	0.031
P19	1.856	0.331	0.0016	0.022
P20	1.856	0.232	0.0008	0.123
P21	1.856	0.130	0.0015	0.049
P22	2.122	0.097	0.0002	0.403
P23	2.122	0.331	0.0016	0.077

Table C.1: Position of head measurement ports, mean measured value between 420 and 450 hours after injection and corresponding coefficient of variation (defined as the ratio of the standard deviation of the measurements divided by the mean value.)
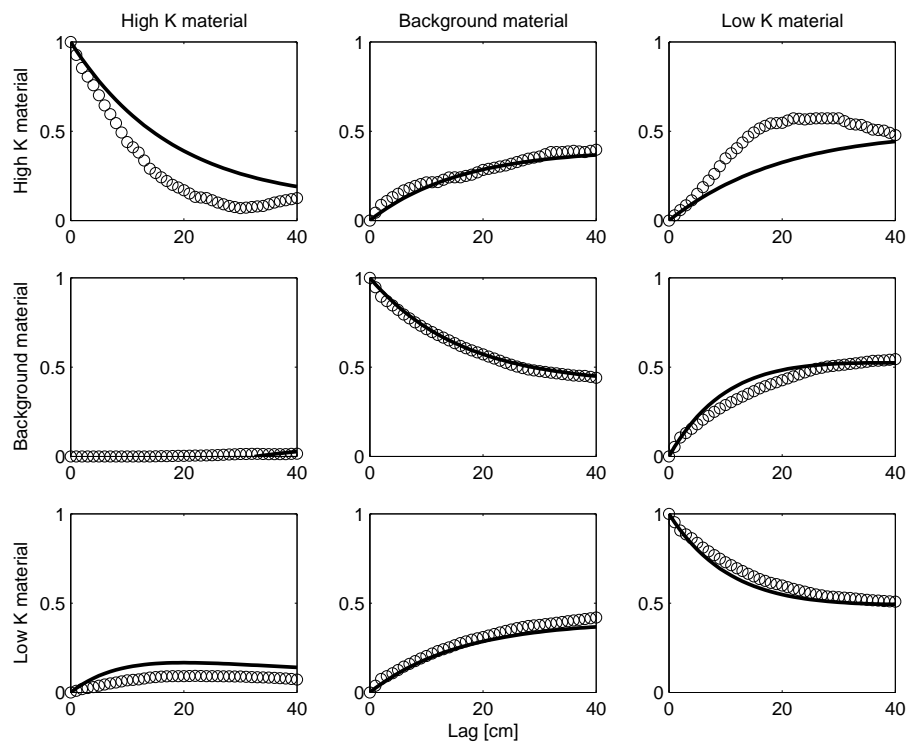
Figure C.12: Measured (circle) and Markov chains model (continuous line) transition probabilities in the longitudinal direction.
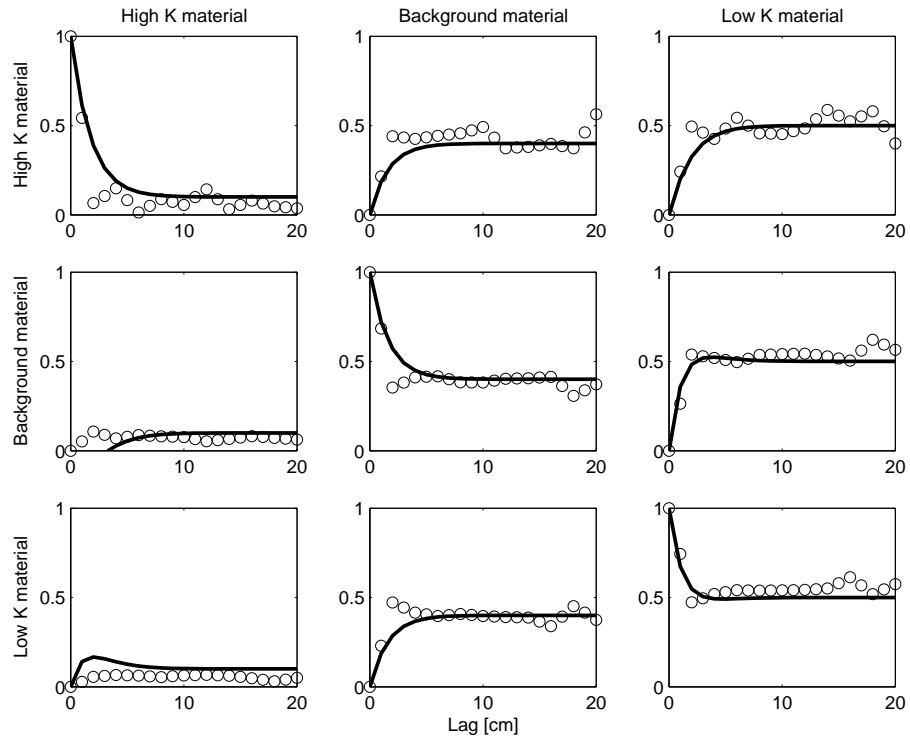
Figure C.13: Measured (circle) and Markov chains model (continuous line) transition probabilities in the transverse (vertical) direction.
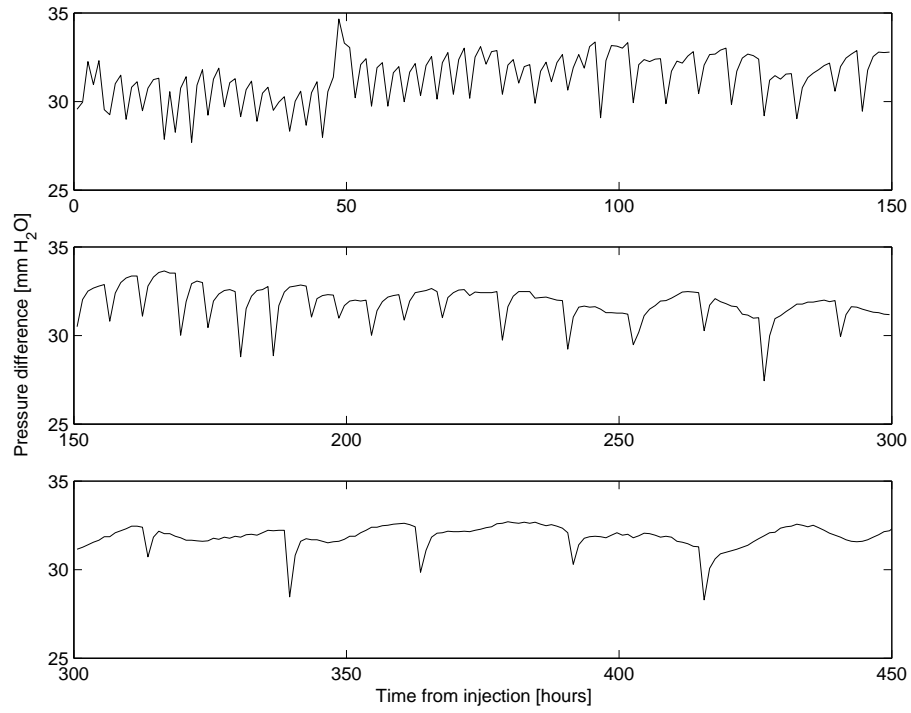
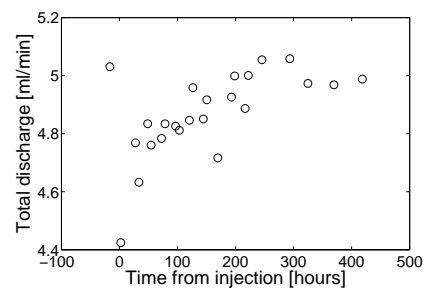**Figure C.14:** Measured total head difference accross the tank (P4-P3).

Figure C.15: Measured total discharge at the tank outlet

Figure C.16: Distribution of observed β_t values for the local breakthrough curves.
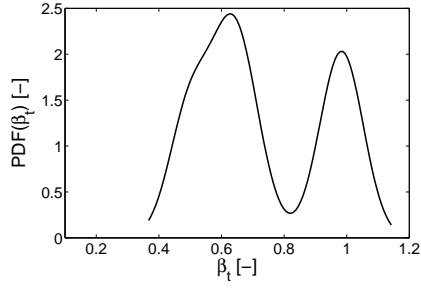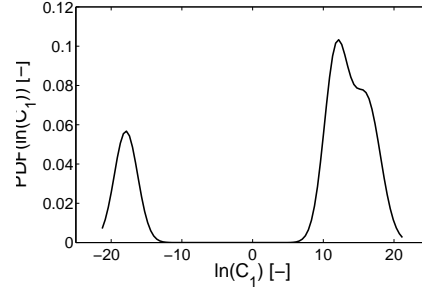

Figure C.17: Distribution of observed C_1 values for the local breakthrough curves.

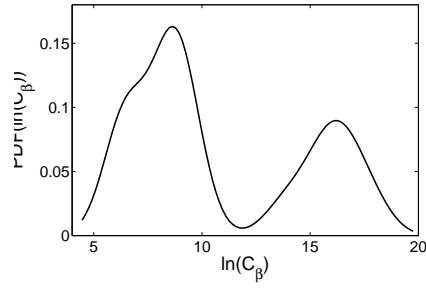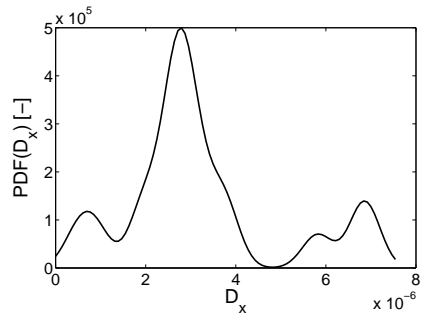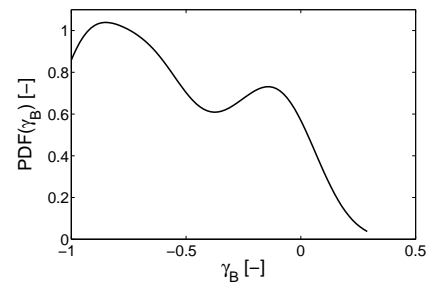**Figure C.18:** Distribution of observed C values for the local breakthrough curves.

Figure C.19: Distribution of observed $\mathcal{D}_x$ values for the local breakthrough curves.

Figure C.20: Distribution of observed γ_B values for the local breakthrough curves.

Bibliography

[1] ANDERMAN, E. R., AND HILL, M. C. Modflow-2000, the U.S. Geological Survey modular ground-water model. Documentation of the advective-transport observation (ADV2) package, version 2. Tech. Rep. 01-54, U.S. Geological Survey, 2001.

[2] ANDERMAN, E. R., AND HILL, M. C. Modflow-2000, the U.S. Geological Survey modular ground-water model. Documentation of effective porosity parameters in the advective-transport observation (ADV2) package. Tech. rep., U. S. Geological Survey, 2003.

[3] ANDERSON, M. P. Using models to simulate the movement of contaminants through groundwater flow systems. *Critical Reviews in Environmental Control*, 2 (1979), 97–156.

[4] ARAL, M. M., AND LIAO, B. Analytical solutions for two-dimensional transport equation with time-dependent dispersion coefficients. *Journal of Hydrologic Engineering 1*, 1 (1996), 20–32.

[5] ARIS, R. On the dispersion of a solute in a fluid flowing through a tube. *Proc. Royal Soc. London A235* (1956), 67–77.

[6] BAEUMER, B., BENSON, D. A., AND MEERSCHAERT, M. M. Advection and dispersion in time and in space. *Physica A 350* (2005), 245–262.

[7] BAEUMER, B., BENSON, D. A., MEERSCHAERT, M. M., AND WHEATCRAFT, S. W. Subordinated advection-dispersion equation for contaminant transport. *Water Resources Research 37*, 6 (2001), 1543–1550.

[8] BAHR, J. M., AND RUBIN, J. Direct comparison of kinetic and local equilibrium formulations for solute transport affected by surface reactions. *Water Resources Research 23*, 3 (1987), 438–452.

[9] BAJRACHARYA, K., AND BARRY, D. A. Nonequilibrium solute transport parameters and their physical significance : numerical and experimental results. *Journal of Contaminant Hydrology 24* (1997), 185–204.

[10] BARTH, G. R., HILL, M. C., ILLANGASEKARE, T. H., AND RAJARAM, H. Predictive modeling of flow and transport in a two-dimensional intermediate-scale, heterogeneous medium. *Water Resources Research 37*, 10 (2001), 2503–2512.

[11] BARTH, G. R., ILLANGASEKARE, T. H., HILL, M. C., AND RAJARAM, H. A new tracer-density criterion for heterogeneous porous media. *Water Resources Research 37*, 1 (2001), 21–31.

[12] BAVEYE, P., JACOBSON, A., ALLAIRE, S., TANDARICH, J., AND BRYANT, R. Whither goes soil science in the us and canada? Survey results and analysis. *Soil Science in press* (2006).

[13] BEAR, J. *Dynamics of fluids in porous media.* American Elsevier Publishing Company, 1972.

[14] BELLIN, A., SALANDIN, P., AND RINALDO, A. Simulation of dispersion in heterogeneous porous formations : statistics, first-order theories, convergence of computations. *Water Resources Research 28*, 9 (1992), 2211–2227.

[15] BENSON, D. A., , MEERSCHAERT, M. M., BAEUMER, B., AND SCHEFFLER, H.-P. Aquifer operator scaling and the effect on solute mixing and dispersion. *Water Resources Research 42* (2006), doi:10.1029/2004WR003755.

[16] BENSON, D. A. *The fractional advection-dispersion equation : development and application.* PhD thesis, University of Nevada, Belgium, May 1998.

[17] BENSON, D. A., TADJERAN, C., MEERSCHAERT, M. M., FARNHAM, I., AND POHLL, G. Radial fractional-order dispersion trough fractured rocks. *Water Resources Research 40* (2004), doi:10.1029/2004WR003314.

[18] BENSON, D. A., WHEATCRAFT, S. W., AND MEERSCHAERT, M. M. Application of a fractional advection-dispersion equation. *Water Resources Research 36*, 6 (2000), 1403–1412.

[19] BENSON, D. A., WHEATCRAFT, S. W., AND MEERSCHAERT, M. M. The fractional-order governing equation of Lévy motion. *Water Resources Research 36*, 6 (2000), 1413–1423.

[20] BERENTSEN, C. *Upscaling of flow in porous media from a tracer perspective.* PhD thesis, T. U. Delft, The Netherlands, 2003.

[21] BERENTSEN, C. W. J., VERLAAN, M. L., AND VAN KRUIJSDIJK, C. P. J. W. Upscaling and reversibility of Taylor dispersion in heterogeneous porous media. *Physical Review E 71* (2005), doi:10.1103/PhysRevE.71.046308.

[22] BERKOWITZ, B., KLAFTER, J., METZLER, R., AND SCHER, H. Physical pictures of transport in heterogeneous media : advection-dispersion, random walk and fractional derivatives formulations. *Water Resources Research 38*, 10 (2002).

[23] BERKOWITZ, B., KOSAKOWSKI, G., MARGOLIN, G., AND SCHER, H. Application of continuous time random walk theory to tracer test measurements in fractured and heterogeneous porous media. *Groundwater 39*, 4 (2001), 593–604.

[24] BERKOWITZ, B., AND SCHER, H. On characterization of anomalous dispersion in porous and fractured media. *Water Resources Research 31*, 6 (1995), 1461–1466.

[25] BERKOWITZ, B., AND SCHER, H. The role of probabilistic approaches to transport theory in heterogeneous media. *Tranport in Porous Media 42* (2001), 241–263.

[26] BERKOWITZ, B., SCHER, H., AND SILLIMAN, S. E. Anomalous transport in laboratory-scale, heterogeneous porous media. *Water Resources Research 36*, 1 (2000), 149–158.

[27] BERKOWITZ, B., SCHER, H., AND SILLIMAN, S. E. Correction to : Anomalous transport in laboratory-scale, heterogeneous porous media. *Water Resources Research 36*, 5 (2000), 1371.

[28] BOGAERT, P. *Introduction à la géostatistique.* Université catholique de Louvain, Louvain-la-Neuve, Belgium, 2003.

[29] BRIDGE, J. S., AND LEEDER, M. R. A simulation model for alluvial stratigraphy. *Sedimentology 26* (1979), 617–644.

[30] BROMLY, M., AND HINZ, C. Non-fickian transport in homogeneous unsaturated repacked sand. *Water Resources Research 40* (2004), doi:10.1029/2003WR002579.

[31] BRUSSEAU, M. L. Application of a multiprocess nonequilibrium sorption model to solute transport in a stratified porous medium. *Water Resources Research 27*, 4 (1991), 589–595.

[32] BRUSSEAU, M. L., GERSTL, Z., AUGUSTIJN, D., AND RAO, P. S. C. Simulating solute transport in an aggregated soil with the dual-porosity model: measured and optimized parameter values. *Journal of Hydrology 163* (1994), 187–193.

[33] BRUSSEAU, M. L., HU, Q., AND SRIVASTAVA, R. Using flow interruption to identify factors causing nonideal contaminant transport. *Journal of Contaminant Hydrology 24* (1997), 205–219.

[34] CACCIA, D. C., PERCIVAL, D., CANNON, M. J., RAYMOND, G., AND BASSINGTHWAIGHTE, J. B. Analyzing exact fractal time series: evaluating dispersional analysis and rescaled range methods. *Physica A 246* (1997), 609–632.

[35] CAMACHO, J. Purely global model for Taylor dispersion. *Physical Review E 48*, 1 (1993), 310–321.

[36] CAMACHO, J. Thermodynamic functions for Taylor dispersion. *Physical Review E 48*, 3 (1993), 1844–1849.

[37] CAMACHO, J. Thermodynamics of Taylor dispersion : Constitutive equations. *Physical Review E 47*, 2 (1993), 1049–1053.

[38] CARLE, S. F. *T-Progs : Transition probability geostatistical software version 2.1.* University of Carlifornia, Davis, 1999.

[39] CARLE, S. F., AND FOGG, G. E. Transition probability-based indicator geostatistics. *Mathematical Geology 28*, 4 (1996), 453–476.

[40] CARLE, S. F., AND FOGG, G. E. Modeling spatial variability with one and multidimensional continuous-lag Markov chains. *Mathematical Geology 29*, 7 (1997), 891–918.

[41] CHAO, H.-C., RAJARAM, H., AND ILLANGASEKARE, T. Intermediate scale experiments and numerical simulations of transport under radial flow in two-dimensional heterogeneous porous medium. *Water Resources Research 36*, 10 (2000), 2869–2878.

[42] CHRISTAKOS, G., BOGAERT, P., AND SERRE, M. *Temporal GIS: Advanced Functions for Field-Based Applications.* Springer-Verlag, New York, 2002.

[43] CIRPKA, O. A. Spectral methods for flow and transport in heterogeneous formations. In 20th *Course on Groundwater Management : Stochastic tools for groundwater modelling* (ETH-Zürich, March 10-14 2003).

[44] COATS, K. H., AND SMITH, B. D. Dead-end pore volume and dispersion in porous media. *Society of Petroleum Engineering Journal 4* (1964), 73–84.

[45] CORTIS, A., AND BERKOWITZ, B. Computing anomalous contaminant transport in porous media : The CTRW Matlab toolbox. *Groundwater 43*, 6 (2005), 947–950.

[46] CORTIS, A., GALLO, C., SCHER, H., AND BERKOWITZ, B. Numerical simulation of non-Fickian transport in geological formations with multiple-scale heterogeneities. *Water Resources Research 40* (2004), doi:10.1029/2003WR002750.

[47] CURTIS, G. P., DAVIS, J. A., AND NAFTZ, D. L. Simulation of reactive transport of uranium(VI) in groundwater with variable chemical conditions. *Water Resources Research 42* (2006), doi:10.1029/2005WR003979.

[48] CUSHMAN, J. H., AND GINN, T. R. Fractional advection-dispersion equation : a classical mass-balance with convolution-Fickian flux. *Water Resources Research 36*, 12 (2000).

[49] CVETKOVIC, V., AND HAGGERTY, R. Transport with multiple-rate exchange in disordered media. *Physical Review E 65* (2002), doi:10.1103/PhysRevE.65.051308.

[50] DAGAN, G. Models of groundwater flow in statistically homogeneous porous formations. *Water Resources Research 15*, 1 (1979), 47–63.

[51] DAGAN, G. Solute transport in heterogeneous formations. *Journal of Fluid Mechanics 145* (1984), 151–177.

[52] DAGAN, G. Time-dependent macrodispersion for solute transport in anisotropic heterogeneous aquifer. *Water Resources Research 24*, 9 (1988), 1491–1500.

[53] DAGAN, G. *Flow and Transport in porous formations*. Springer, New-York, 1989.

[54] DAGAN, G., AND FIORI, A. Time-dependent transport in heterogeneous formations of bimodal structure. 1. The model. *Water Resources Research 39*, 5 (2003), doi:10.1029/2002WR001396.

[55] DAGAN, G., FIORI, A., AND JANKOVIC, I. Flow and transport in highly heterogeneous formations. 1. Conceptual framework and validity of first-order approximations. *Water Resources Research 39*, 9 (2003), doi:10.1029/2002WR001717.

[56] DAGAN, G., AND LESSOFF, S. C. Solute transport in heterogeneous formations of bimodal conductivity distribution. 1. Theory. *Water Resources Research 37*, 3 (2001), 465–472.

[57] DAI, Z., RITZI, R. W., AND DOMINIC, D. F. Improving permeability semivariograms with transition probability models of hierarchical sedimentary architecture derived from outcrop analog studies. *Water Resources Research 41* (2005), doi:10.1029/2004WR003515.

[58] DAI, Z., RITZI, R. W., HUAND, C., RUBIN, Y. N., AND DOMINIC, D. F. Transport in heterogeneous sediments with multimodal conductivity and hierarchical organization across scales. *Journal of Hydrology 294* (2004), 68–86.

[59] DANQUIGNY, C., ACKERER, P., AND CARLIER, J.-P. Laboratory tracer tests on 3d heterogeneous porous media. *Journal of Hydrology 294* (2004), 196–212.

[60] DE MARSILY, G., DELAY, F., TELES, V., AND SCHAFMEISTER, M. T. Some current methods to represent the heterogeneity of natural media in hydrogeology. *Hydrogeology Journal*, 6 (1998), 115–130.

[61] DENTZ, M., AND BERKOWITZ, B. Transport behavior of a passive solute in continuous time random walks and multirate mass transfer. *Water Resources Research 39*, 5 (2003), doi:10.1029/2001WR001163.

[62] DESBARATS, A. J. Macrodispersion in sand-shale sequences. *Water Resources Research 26*, 1 (1990), 153–163.

[63] DEUTSCH, C. V., AND JOURNEL, A. G. *GSLIB : Geostatistical software library and user's guide*, 2nd ed. Applied Geostatistics Series. Oxford University Press, New-York, 1998.

[64] DEUTSCH, C. V., AND WANG, L. Hierarchical object-based stochastic modeling of fluvial reservoirs. *Mathematical Geology 28*, 7 (1996), 857–880.

[65] DOMENICO, P. A., AND ROBBINS, G. A. A dispersion scale effect in model calibration and field tracer experiments. *Journal of Hydrology*, 70 (1984), 123–132.

[66] DOMENICO, P. A., AND SCHWARTZ, F. W. *Physical and Chemical hydrogeology*. J. Wiley and sons, 1998.

[67] EAMES, I., AND BUSH, J. W. M. Longitudinal dispersion by bodies fixed in a potential flow. *Proc. Royal Soc. London 455* (1999), 3665–3686.

[68] ELFEKI, A. M. M., UFFINK, G. J. M., AND BARENDS, F. B. J. *Groundwater contaminant transport: impact of heterogeneous characterization.* Balkema, Rotterdam, 1997.

[69] FEEHLEY, C. E., ZHENG, C., AND MOLZ, F. J. A dual-domain mass transfer approach for modeling solute transport in heterogeneous aquifers : application to the Macrodispersion Experiment (MADE) site. *Water Resources Research 36*, 9 (2000), 2501–2515.

[70] FERNANDEZ-GARCIA, D., ILLANGASEKARE, T. H., AND RAJARAM, H. Conservative and sorptive forced-gradient and uniform flow tracer tests in a three-dimensional laboratory test aquifer. *Water Resources Research 40* (2004), doi:10.1029/2004WR003112.

[71] FERNANDEZ-GARCIA, D., SANCHEZ-VILA, X., AND ILLANGASEKARE, T. H. Convergent-flow tracer tests in heterogeneous media : combined experimental-numerical analysis for determination of equivalent transport parameters. *Journal of Contaminant Hydrology 57* (2002), 129–145.

[72] FETTER, C. W. *Contaminant Hydrology*, 2nd ed. Prentice Hall, Englewood Cliffs, New-Jersey, 1999.

[73] FIORI, A., AND DAGAN, G. Time-dependent transport in heterogeneous formations of bimodal structure. 2. Results. *Water Resources Research 39*, 5 (2003), doi:10.1029/2002WR001398.

[74] FIORI, A., JANKOVIC, I., AND DAGAN, G. Flow and transport in highly heterogeneous formations. 2. Semianalytical results for isotropic media. *Water Resources Research 39*, 9 (2003), doi:10.1029/2002WR001719.

[75] FIORI, A., JANKOVIC, I., AND DAGAN, G. Flow and transport through two-dimensional isotropic media of binary conductivity distribution. Part 1 : Numerical methodology and semi-analytical solutions. *Stochastic Environmental Research and Risk Assessment 17* (2003), 370–383.

[76] FREEZE, R. A., AND CHERRY, J. A. *Groundwater.* Prentice Hall, 1979.

[77] FRIED, J. J. *Groundwater Pollution.* Elsevier, 1975.

[78] FRIPPIAT, C. C., AND HOLEYMAN, A. E. Upscaling of solute transport in mildly heterogeneous media: comparison of Fickian and non-Fickian approaches. In *Calibration and Reliability in Groundwater Modelling: From Uncertainty to Decision Making*, vol. 304. International Association of Hydrological Science, 2006, pp. 167–173.

[79] GELHAR, L. W. *Stochastic subsurface hydrology.* Prentice Hall, Englewood Cliffs, New-Jersey, 1993.

[80] GELHAR, L. W., AND AXNESS, C. L. Three-dimensional stochastic analysis of macrodispersion in aquifers. *Water Resources Research 19*, 1 (1983), 161–180.

[81] GELHAR, L. W., GUTJAHR, A. L., AND NAFF, R. L. Stochastic analysis of macrodispersion in a stratified aquifer. *Water Resources Research 15*, 6 (1979), 1387–1397.

[82] GELHAR, L. W., WELTY, C., AND REHFELDT, K. R. A critical review of data on field-scale dispersion in aquifers. *Water Resources Research 28*, 7 (1992), 1955–1974.

[83] GERKE, H. H., AND VAN GENUCHTEN, M. T. A dual-porosity model for simulating the preferential movement of water and solutes in structured porous media. *Water Resources Research 29*, 2 (1993), 305–319.

[84] GOMEZ-HERNANDEZ, J. J., AND WEN, X.-H. To be or not to be multi-Gaussian ? A reflection on stochastic hydrogeology. *Advances in Water Resources 21*, 1 (1998), 47–61.

[85] GREENKORN, R. A. *Flow phenomena in porous media.* Marcel Dekker, 1983.

[86] GRIFFIOEN, J. Suitability of the first-order mass transfer concept for describing cyclic diffusive mass transfer in stagnant zones. *Journal of Contaminant Hydrology 34* (1998), 155–165.

[87] GRIFFIOEN, J. W., BARRY, D. A., AND PARLANGE, J.-Y. Interpretation of two-region model parameter. *Water Resources Research 34*, 3 (1998), 373–384.

[88] GUSWA, A. J., AND FREYBERG, D. L. Slow advection and diffusion through low permeability inclusions. *Journal of Contaminant Hydrology 46* (2000), 205–232.

[89] GÜVEN, O., AND MOLZ, F. J. Deterministic and stochastic analyses of dispersion in an unbounded stratified porous medium. *Water Resources Research 22*, 11 (1986), 1565–1574.

[90] GÜVEN, O., MOLZ, F. J., AND MELVILLE, J. G. An analysis of dispersion in a stratified aquifer. *Water Resources Research 20*, 10 (1984), 1337–1354.

[91] HAGGERTY, R., AND GORELICK, S. M. Multiple-rate mas transfer for modeling diffusion and surface reactions in media with pore-scale heterogeneity. *Water Resources Research 31*, 10 (1995), 2383–2400.

[92] HAGGERTY, R., MCKENNA, S., AND MEIGS, L. C. On the late-time behavior of tracer test breakthrough curves. *Water Resources Research 36*, 12 (2000), 3467–3479.

[93] HAGGERTY, R., AND REEVES, P. C. Stammt-l 1.0, formulation and user's guide. Tech. Rep. 520308, Sandia National Laboratories, 2002.

[94] HANTUSH, M. M., AND MARINO, M. A. Interlayer diffusive transfer and transport of contaminants in stratified formations. I. Theory. *Journal of Hydrologic Engineering 3*, 4 (1998), 232–240.

[95] HANTUSH, M. M., AND MARINO, M. A. Interlayer diffusive transfer and transport of contaminants in stratified formations. II. Analytical solutions. *Journal of Hydrologic Engineering 3*, 4 (1998), 241–246.

[96] HARBAUGH, A. W., BANTA, E. R., HILL, M. C., AND MCDONALD, M. G. Modflow-2000, the U.S. Geological Survey modular ground-water model. User guide to modularization concepts and the ground-water flow process. Tech. Rep. 00-92, USGS, 2000.

[97] HARVEY, C., AND GORELICK, S. M. Rate-limited mass transfer or macrodispersion: which dominates plume evolution at the Macrodispersion Experiment (MADE) site ? *Water Resources Research 36*, 3 (2000), 637–650.

[98] HASSANIZADEH, S. M. On the transient non-Fickian dispersion theory. *Tranport in Porous Media 23* (1996), 107–124.

[99] HILL, M. C., BANTA, E. R., HARBAUGH, A. W., AND ANDERMAN, E. R. Modflow-2000, the U.S. Geological Survey modular ground-water model. User guide to the observation, sensitivity and parameter-estimation processes and three post-porcessing programs. Tech. Rep. 00-184, USGS, 2000.

[100] Hsu, K.-C. The influence of the log-conductivity autocovariance structure on macrodispersion coefficients. *Journal of Contaminant Hydrology 65* (2003), 65–77.

[101] Huang, K., van Genuchten, M. T., and Zhang, R. Exact solutions for one-dimensional transport with asymptotic scale-dependent dispersion. *Appl. Math. Modelling 20* (1996), 298–308.

[102] Hunt, B. Contaminant sources solutions with scale-dependent dispersivities. *Journal of Hydrologic Engineering 3*, 4 (1998), 268–275.

[103] Hunt, B. Scale-dependent dispersion from a pit. *Journal of Hydrologic Engineering 7*, 2 (2002), doi:10.1061/(ASCE)1084–0699(2002)7:2(168).

[104] Illangasekare, T. H., Ramsey, J. L., Jensen, K. H., and Butts, M. B. Experimental study of movement and distribution of dense organic contaminants in heterogeneous aquifers. *Journal of Contaminant Hydrology 20* (1995), 1–25.

[105] Jankovic, I., Fiori, A., and Dagan, G. Flow and transport in highly heterogeneous formations. 3. Numerical simulations and comparison with theoretical results. *Water Resources Research 39*, 9 (2003), doi:10.1029/2002WR001721.

[106] Jankovic, I., Fiori, A., and Dagan, G. Flow and transport through two-dimensional isotropic media of binary conductivity distribution. Part 2 : Numerical simulations and comparison with theoretical results. *Stochastic Environmental Research and Risk Assessment 17* (2003), 384–393.

[107] Jarvis, N. J., Jansson, P.-E., Dk, P. E., and Messing, I. Modelling water and solute transport in macroporous soil. I. Model description and sensitivity analysis. *Journal of Soil Science 42* (1991), 59–70.

[108] Javaux, M., and Vanclooster, M. Scale- and rate-dependent solute transport within an unsaturated sandy monolith. *Soil Science Society of America Journal 67*, 5 (2003), 1334–1343.

[109] Jose, S. C., Rahman, A., and Cirpka, O. A. Large-scale sandbox experiment on longitudinal effective dispersion in heterogeneous porous media. *Water Resources Research 40* (2004), doi:10.1029/2004WR003363.

[110] Journel, A. G., and Isaaks, E. H. Conditional indicator simulation : Application to a Saskatchewan uranium deposit. *Mathematical Geology 16*, 7 (1984), 685–718.

[111] Klotz, D., Seiler, K.-P., Moser, H., and Neumaier, F. Dispersivity and velocity relationship from laboratory and field experiments. *Journal of Hydrology 45* (1980), 169–184.

[112] Koltermann, C. E., and Gorelick, S. M. Paleoclimatic signature in terrestrial flood deposit. *Science 256* (1992), 1775–1782.

[113] Koltermann, C. E., and Gorelick, S. M. Heterogeneity in sedimentary deposits : a review of structure-imitating, process-imitating and descriptive approaches. *Water Resources Research 32*, 9 (1996), 2617–2658.

[114] Kreft, A., and Zuber, A. On the physical meaning of the dispersion equation and its solutions for different initial and boundary conditions. *Chemical Engineering Science 33* (1978), 1471–1480.

[115] Labolle, E. M. *RWHet : random walk particle model for simulating transport in heterogeneous permeable media version 2.0.* University of California, Davis, 2000.

[116] LALLEMAND-BARRÈS, A., AND PEAUDECERF, P. Recherche des relations entre la valeur de la dispersivité macroscopique d'un milieu aquifère, ses autres caractéristiques et les conditions de mesure. Etude bibliographique. *Bulletin du BRGM 2e série - section III*, 4 (1992), 277–284.

[117] LAMBOT, S., SLOB, E. C., VAN DEN BOSCH, I., STOCKBROECKX, B., SCHEERS, B., AND VANCLOOSTER, M. Estimating soil electric properties from monostatic ground-penetrating radar signal inversion in the frequency domain. *Water Resources Research 40* (2004), doi:10.1029/2003WR002095.

[118] LANDMAN, A.-J. *unpublished*. PhD thesis, TU Delft, The Netherlands, 2004.

[119] LEIJ, F. J., AND DANE, J. H. Solute transport in a two-layer medium investigated with time moments. *Soil Science Society of America Journal 55* (1991), 1529–1535.

[120] LESSOFF, S. C., AND DAGAN, G. Solute transport in heterogeneous formations of bimodal conductivity distribution. 2. Applications. *Water Resources Research 37*, 3 (2001), 473–480.

[121] LEVY, M., AND BERKOWITZ, B. Measurement and analysis of non-Fickian dispersion in heterogeneous porous media. *Journal of Contaminant Hydrology 64* (2003), 203–226.

[122] LIN, A. Y.-C., DEBROUX, J.-F., CUNNINGHAM, J. A., AND REINHARD, M. Comparison of Rhodamine WT and bromide in the determination of hydraulic characteristics of constructed wetlands. *Ecological Engineering 20* (2003), 75–88.

[123] LIU, G., ZHENG, C., AND GORELICK, S. M. Limits of applicability of the advection-dispersion model in aquifers containing connected high-conductivity channels. *Water Resources Research 40* (2004), doi:10.1029/2003WR002735.

[124] LOGAN, J. D. Solute transport in porous media with scale-dependent dispersion and periodic boundary conditions. *Journal of Hydrology*, 184 (1996), 261–276.

[125] LU, S., MOLZ, F. J., AND FIX, G. J. Possible problems of scale dependency in applications of the three-dimensional fractional advection-dispersion equation to natural porous media. *Water Resources Research 38*, 9 (2002).

[126] LU, S., MOLZ, F. J., FOGG, G. E., AND CASTLE, J. W. Combining stochastic facies and fractal models for representing natural heterogeneity. *Hydrogeology Journal*, 10 (2002), 475–482.

[127] MARGOLIN, G., AND BERKOWITZ, B. Application of continuous time random walk to transport in porous media. *Journal of Physical Chemistry B 104* (2000), 3942–3947.

[128] MARGOLIN, G., AND BERKOWITZ, B. Correction to : Application of continuous time random walk to transport in porous media. *Journal of Physical Chemistry B 104* (2000), 3942.

[129] MARGOLIN, G., AND BERKOWITZ, B. Spatial behavior of anomalous transport. *Physical Review E 65* (2002).

[130] MARGOLIN, G., AND BERKOWITZ, B. Continuous time random walk revisited : first passage time and spatial distributions. *Physica A 334* (2004), 46–66.

[131] MARLE, C., SIMANDOUX, P., PACSIRSZKY, J., AND GAULIER, C. Etude du déplacement de fluides miscibles en milieu poreux stratifié. *Rue de l'Institut Français du Pétrole 22*, 2 (1967), 272–294.

[132] MATHERON, G., AND DE MARSILY, G. Is transport in porous media always diffusive ? A counterexample. *Water Resources Research 16*, 5 (1980), 901–917.

[133] MEERSCHAERT, M. M., BENSON, D. A., AND BAEUMER, B. Multidimensional advection and fractional dispersion. *Physical Review E 59*, 5 (1999), 5026–5028.

[134] MEERSCHAERT, M. M., BENSON, D. A., AND BAEUMER, B. Operator Lévy motion and multiscaling anomalous diffusion. *Physical Review E 63* (2001), 1112–1117.

[135] MEERSCHAERT, M. M., BENSON, D. A., SCHEFFLER, H.-P., AND BAEUMER, B. Stochastic solution of space-time fractional diffusion equations. *Physical Review E 65*, 4 (2002), 102–105.

[136] MERCADO, A. The spreading pattern of injected water in a permeability stratified aquifer. In *Artifical recharge and management of aquifers* (1967), IAHS-AIHS, Ed., vol. 72, pp. 23–36.

[137] METZLER, R., AND KLAFTER, J. The random walk's guide to anomalous diffusion : a fractional dynamics approach. *Physics Reports 339* (2000), 1–77.

[138] MOLZ, F. J., GÜVEN, O., AND MELVILLE, J. G. An examination of scale-dependent dispersion coefficient. *Groundwater 21*, 6 (1983), 715–725.

[139] MONTROLL, E. W., AND WEISS, G. H. Random walks on lattices. II. *Journal of Mathematical Physics 6*, 2 (1965), 167–181.

[140] MURPHY, E. M., GINN, T. R., CHILAKAPATI, A., RESCH, T., PHILLIPS, J., WIETSMA, T., AND SPADONI, C. M. The influence of physical heterogeneity on microbial degradation and distribution in porous media. *Water Resources Research 33* (1997), 1087–1104.

[141] NEUMAN, S. P., WINTER, C. L., AND NEWMAN, C. M. Stochastic theory of field-scale Fickian dispersion in anistropic porous media. *Water Resources Research 23*, 3 (1987), 453–466.

[142] NKEDI-KIZZA, P., BIGGAR, J. W., SELIM, H. M., VAN GENUCHTEN, M. T., WIERENGA, P. J., DAVIDSON, J. M., AND NIELSEN, D. R. On the equivalence of two conceptual models for describing ion exchange during transport through an aggregated oxisol. *Water Resources Research 20*, 8 (1984), 1123–1130.

[143] PANG, L., AND HUNT, B. Solutions and verification of a scale-dependent dispersion model. *Journal of Contaminant Hydrology*, 53 (2001), 21–39.

[144] PARKER, J. C., AND VALOCCHI, A. J. Constraints on the validity of equilibrium and first-order kinetic models in structured soils. *Water Resources Research 22*, 3 (1986), 399–407.

[145] PETERS, G. P., AND SMITH, D. W. Spatially and temporally varying dispersivity. In *GeoEng 2000 Conference Proceedings* (2000).

[146] PICKENS, J. F., AND GRISAK, G. E. Modeling of scale-dependent dispersion in hydrogeologic systems. *Water Resources Research 17*, 6 (1981), 1701–1711.

[147] PICKENS, J. F., AND GRISAK, G. E. Scale-dependent dispersion in a stratified granular aquifer. *Water Resources Research 17*, 4 (1981), 1191–1211.

[148] PTAK, T., AND SCHMID, G. Dual-tracer transport experiments in a physically and chemically heterogeneous porous aquifer : effective transport parameters and spatial variability. *Journal of Hydrology 183* (1996), 117–138.

[149] RAO, P. S. C., ROLSTON, D. E., JESSUP, R. E., AND DAVIDSON, J. M. Solute transport in aggregated porous media : theoretical and experimental evaluation. *Soil Science Society of America Journal 44* (1980), 1139–1146.

[150] RENTIER, C. *Méthode stochastique de délimitation des zones de protection autour des captages d'eau.* PhD thesis, Université de Liège, Belgium, November 2002.

[151] ROVEY, C. W., AND NIEMANN, W. L. Do conservative solutes migrate at average pore-water velocity ? *Groundwater 43*, 1 (2005), 52–62.

[152] RUBIN, Y. Flow and transport in bimodal heterogeneous formations. *Water Resources Research 31*, 10 (1995), 2461–2468.

[153] RUBIN, Y., AND DAGAN, G. Stochastic analysis of the effects of boundaries on spatial variability in groundwater flows: 2. Impervious boundary. *Water Resources Research 25*, 4 (1989), 707–712.

[154] SABATINI, D. A. Sorption and intraparticule diffusion of fluorescent dyes with consolidated aquifer media. *Groundwater 38*, 5 (2000), 651–656.

[155] SABATINI, D. A., AND AL AUSTIN, T. Characteristics of Rhodamine WT and Fluorescein as adsorbing ground-water tracers. *Groundwater 29*, 3 (1991), 341–349.

[156] SAKAKI, T., AND KOMATSU, M. Physical properties of silica sands for laboratory experiments. Colorado School of Mines, ESE division, internal report, April 2005.

[157] SALANDIN, P., AND FIOROTTO, V. Solute transport in highly heterogeneous aquifers. *Water Resources Research 34*, 5 (1998), 949–961.

[158] SALANDIN, P., RINALDO, A., AND DAGAN, G. A note on transport in stratified formations by flow tilded with respect to the bedding. *Water Resources Research 27*, 11 (1991), 3009–3017.

[159] SAUPE, D., AND PEITGEN, H. *The Science of Fractal Images.* Springer-Verlag, 1988, p. 312 p.

[160] SAUTY, J. Mise au point et utilisation d'abaques pour l'interprétation des expériences de traçages dans les nappes d'eau souterraine. *Bulletin du BRGM 2e série - section III*, 4 (1978), 285–291.

[161] SAUTY, J. An analysis of hydrodispersive transfer in aquifers. *Water Resources Research 16*, 1 (1980), 145–158.

[162] SCHEIDEGGER, A. E. Typical solutions of the differential equations of statistical theories of flow through porous media. *Transactions, American Geophysical Union 39*, 5 (1958), 929–932.

[163] SCHEIDEGGER, A. E. *The physics of flow through porous media.* Mac Millan Company, 1960.

[164] SCHER, H., AND LAX, M. Stochastic transport in a disordered solids. II Impurity conduction. *Physical Review B 7* (1973), 4502–4519.

[165] SCHÄFER, W., AND KINZELBACH, W. K. H. Transport of reactive species in heterogeneous porous media. *Journal of Hydrology 183* (1996), 151–168.

[166] SCHINCARIOL, R. A., AND SCHWARTZ, F. An experimental investigation of variable density flow and mixing in homogeneous and heterogeneous media. *Water Resources Research 26*, 10 (1990), 2317–2329.

[167] SCHUMER, R., BENSO, D. A., MEERSCHAERT, M. M., AND BAEUMER, B. Fractal mobile/immobile solute transport. *Water Resources Research 39*, 10 (2003), doi:10.1029/2003WR002141.

[168] Schumer, R., Benson, D. A., Meerschaert, M. M., and Baeumer, B. Multiscaling fractional advection-dispersion equations and their solutions. *Water Resources Research 39*, 1 (2003).

[169] Schumer, R., Benson, D. A., Meerschaert, M. M., and Wheatcraft, S. W. Eulerian derivation of the fractional advection-dispersion equation. *Journal of Contaminant Hydrology*, 48 (2001), 69–88.

[170] Silliamn, S. E., and Zheng, L. Comparison of observations from a laboratory model with stochastic theory: Initial analysis of hydraulic and tracer experiments. *Tranport in Porous Media 42*, 1/2 (2001), 85–107.

[171] Silliman, S. E. Laboratory study of chemical transport to wells within heterogeneous porous media. *Water Resources Research 37*, 7 (2001), 1883–1892.

[172] Silliman, S. E., and Caswell, S. Observations of measured hydraulic conductivity in two artificial, confined aquifers with boundaries. *Water Resources Research 34*, 9 (1998), 2203–2213.

[173] Silliman, S. E., Konikow, L., and Voss, C. Laboratory investigation of longitudinal dispersion in anisotropic porous media. *Water Resources Research 23*, 11 (1987), 2145–2151.

[174] Silliman, S. E., and Simpson, E. S. Laboratory evidence of the scale effect in dispersion of solutes in porous media. *Water Resources Research 23*, 8 (1987), 1667–1673.

[175] Sposito, G., and Weeks, S. W. Tracer advection by steady groundwater flow in a stratified aquifer. *Water Resources Research 34*, 5 (1998), 1051–1059.

[176] Strack, O. D. L. A mathematical model for dispersion with a moving front in groundwater. *Water Resources Research 28*, 11 (1992), 2973–2980.

[177] Sudicky, E. A., Gillham, R. W., and Frind, E. O. Experimental investigation of solute transport in stratified porous media. 1. The non-reactive case. *Water Resources Research 21* (1985), 1035–1041.

[178] Sutton, D. J., Kabala, Z. J., Francisco, A., and Vasudevan, D. Limitations and potential of commercially available Rhodamine WT as a groundwater tracer. *Water Resources Research 37*, 6 (2001), 1641–1656.

[179] Taylor, G. I. Dispersion of soluble matter in solvent flowing slowly through a tube. *Proc. Royal Soc. London A219* (1953), 186–203.

[180] Taylor, G. I. Conditions under which dispersion of a solute in a stream of solvent can be used to measure molecular diffusion. *Proc. Royal Soc. London A225* (1954), 473–477.

[181] Teles, V., Delay, F., and de Marsily, G. Comparison of genesis and geostatistical methods for characterizing the heterogeneity of alluvial media : groundwater flow and transport simulations. *Journal of Hydrology 294* (2004), 103–121.

[182] Tompson, A. F. B. On a new functional form for the dispersive flux in porous media. *Water Resources Research 24*, 11 (1988), 1939–1947.

[183] Tompson, A. F. B., and Gray, W. G. A 2nd-order approach for the modelling of dispersive transport in porous media. 1. Theoretical development. *Water Resources Research 22*, 5 (1986), 591–599.

[184] Trefry, M. G., Ruan, F. P., and McLaughlin, D. Numerical simulations of preasymptotic transport in heterogeneous porous media : departures from the Gaussian limit. *Water Resources Research 39*, 3 (2003), doi:10.1029/2001WR001101.

[185] URSINO, N., GIMMI, T., AND FLÜHLER, H. Combined effects of heterogeneity, anisotropy, and saturation on steady state flow and transport: a laboratory sand tank experiment. *Water Resources Research 2* (37), 201–208.

[186] VALOCCHI, A. J. Validity of the local equilibrium assumption for modeling sorbing solute transport through homogeneous soils. *Water Resources Research 21*, 6 (1985), 808–820.

[187] VAN GENUCHTEN, M. T., TANG, D. H., AND GUENNELON, R. Some exact solutions for solute transport through soils containing large cylindrical macropores. *Water Resources Research 20*, 3 (1984), 335–346.

[188] VAN GENUCHTEN, M. T., AND WAGENET, R. J. Two-site/two-region models for pesticide transport and degradation : theoretical development and analytical solutions. *Soil Science Society of America Journal 53*, 5 (1989), 1303–1310.

[189] VAN GENUCHTEN, M. T., AND WIERENGA, P. J. Mass transfer studies in sorbing porous media. I. Analytical solutions. *Soil Science Society of America Journal 40*, 4 (1976), 473–480.

[190] VAN GENUCHTEN, M. T., AND WIERENGA, P. J. Mass transfer studies in sorbing porous media. II. Experimental evaluation with tritium (3H2O)., volume = 41, year = 1977. *Soil Science Society of America Journal* (1977), 272–278.

[191] VAN GENUCHTEN, M. T., WIERENGA, P. J., AND O'CONNOR, G. A. Mass transfer studies in sorbing porous media. III. Experimental evaluation with 2,4,5T.,. *Soil Science Society of America Journal 41* (1977), 278–285.

[192] VANCLOOSTER, M., JAVAUX, M., AND VANDERBORGHT, J. *Solute transport in soils.* Encyclopedia of Hydrological Sciences. John Wiley and sons, 2005.

[193] WANG, P. P., ZHENG, C., AND GORELICK, S. M. A general approach to advective-dispersive transport with multirate mass transfer. *Advances in Water Resources 28* (2005), 33–42.

[194] WEISSMANN, G. S., CARLE, S. F., AND FOGG, G. E. Three-dimensional hydrofacies modeling based on soil surveys and transition probability geostatistics. *Water Resources Research 35*, 6 (1999), 1761–1770.

[195] WEISSMANN, G. S., AND FOGG, G. E. Multi-scale alluvial fan heterogeneity modeled with transition probability geostatistics in a sequence stratigraphic framework. *Journal of Hydrology 226* (1999), 48–65.

[196] WELTY, C., AND ELSNER, M. Construction of random fields in the laboratory for observations of fluid flow and mass transport. *Journal of Hydrology 202* (1997), 192–211.

[197] WHEATCRAFT, S. W., AND TYLER, S. W. An explanation of scale-dependent dispersivity using concepts of fractal geometry. *Water Resources Research 24*, 4 (1988), 566–578.

[198] WOOD, B. D., DAWSON, C. N., SZECSODY, J. E., AND STREILE, G. P. Modeling contaminant transport and biodegradation in a layered porous media system. *Water Resources Research 30*, 6 (1994), 1833–1845.

[199] YATES, S. R. An analytical solution for one-dimensional transport in heterogeneous porous media. *Water Resources Research 26*, 10 (1990), 2331–2338.

[200] YU, C., WARRICK, A. W., AND CONKLIN, M. H. A moment method for analysing breakthrough curves of step inputs. *Water Resources Research 35*, 11 (1999), 3567–3572.

[201] ZHAN, H., AND WHEATCRAFT, S. W. Macrodispersivity tensor for nonreactive solute transport in isotropic and anisotropic fractal porous media: analytical solutions. *Water Resources Research 32*, 12 (1996), 3461–3474.

[202] ZHANG, Y., AND BENSON, D. A. Anomalous transport in regional-scale alluvial quifers : can we predict the tails of breakthrough curves ? Preprint submitted to Elsevier Science, July 2005.

[203] ZHENG, C., AND WANG, P. P. Mt3dms, a modular three-dimensional multispecies transport model for simulation of advection, dispersion and chemical reactions of contaminants in groundwater systems. Documentation and user guide. Tech. Rep. SERDP-99-1, U.S. Army Engineer Research and Development Center, 1999.

[204] ZHOU, L., AND SELIM, H. M. A conceptual fractal model for describing time-dependent dispersivity. *Soil Science 167*, 3 (2002), 173–183.

[205] ZHOU, L., AND SELIM, H. M. Application of the fractional advection dispersion equation in porous media. *Soil Science Society of America Journal 67* (2003), 1079–1084.

[206] ZINN, B., AND HARVEY, C. F. When good statistical models of aquifer heterogeneity go bad : a comparison of flow, dispersion, and mass transfer in connected and multivariate Gaussian hydraulic conductivity fields. *Water Resources Research 39* (2003), doi:10.1029/2001WR001146.

[207] ZOU, S., XIA, J., AND KOUSSIS, A. D. Analytical solutions to non-Fickian subsurface dispersion in uniform groundwater flow. *Journal of Hydrology*, 179 (1996), 237–258.